

RELATIVISTIC CALCULATION OF NUCLEAR MATTER AND THE NUCLEAR SURFACE[†]

J. BOGUTA ^{††}

Argonne National Laboratory, Argonne, Illinois 60439

and

A. R. BODMER

Argonne National Laboratory, Argonne, Illinois 60439

and

University of Illinois at Chicago Circle, Chicago, Illinois 60680

Received 15 July 1977

Abstract: Relativistic mean field Hartree and Thomas-Fermi calculations are made for infinite and semi-infinite symmetric nuclear matter. Cubic and quartic scalar meson self-interactions are included. The strength of these self-interactions, the scalar and vector meson coupling constants, and the scalar meson mass are considered as parameters chosen to fit the empirical properties of nuclear matter and of the nuclear surface. Acceptable fits imply large self-interactions. No abnormal nuclear matter solutions are found. The best fit of the nuclear surface yields a compressibility coefficient of 150 ± 50 MeV. The Hartree and TF results are in good agreement for larger surface thicknesses.

1. Introduction

Recently there has been considerable interest in relativistic Hartree calculations of nuclear matter and finite nuclei¹⁻¹²). In particular, a relativistic approach may be necessary for the calculation and prediction of the properties of nuclear matter at very high densities. The simplest relativistic model capable of giving the saturation properties of nuclear matter for $N = Z$ involves two isoscalar meson fields with Yukawa couplings to the nucleon; a scalar field which gives the long-range attraction and a vector field which gives the short-range repulsion. A model of this type has been considered by Duerr and later by Walecka⁴⁻⁵). Lee and Wick have considered a scalar field model involving the specific quartic self-interactions appropriate for the sigma model⁶). With a suitably chosen additional repulsive contribution they obtained, for the energy/nucleon, a minimum which is deeper and at a higher density than the normal one. Such possible new "abnormal" states of nuclear matter are clearly of great interest¹³⁻¹⁷).

[†] Work performed under the auspices of US ERDA, Division of Physical Research.

^{††} Also supported by the NSF under grant GP-39014 while at the University of Illinois at Chicago Circle.

A number of investigations have been made using the sigma and related meson models^{6-9, 18)}. A fundamental problem is the uncertainty in the self-interaction terms due to the renormalization corrections. It is thus of interest to consider more phenomenological models with scalar meson self-interactions, the strength of these interactions being considered as adjustable parameters. Moszkowski and Källman¹²⁾ have studied a model with self-interactions which has only one free parameter and which has as its limits the sigma model and the Walecka model. They determine this parameter from the symmetry energy. They do not find a second minimum, i.e. an abnormal state.

In this paper, we use both the Hartree and the Thomas-Fermi (TF) approximations. The latter is an approximation to the former, but for infinite nuclear matter they are the same. We consider only the $N = Z$ case and neglect the Coulomb forces. We need then consider only isoscalar mesons and our Lagrangian involves a scalar field σ and a vector field ν_μ , both with Yukawa couplings to the nucleon field; in addition, our Lagrangian has the most general self-interaction involving cubic and quartic terms for the scalar field. The coefficients of these self-interaction terms are taken to be parameters to be determined by the properties of normal nuclear matter and of the nuclear surface.

The "empirical" properties¹⁹⁾ of nuclear matter that we fit are the energy/nucleon $e(\rho_0)$ as determined from the semi-empirical mass formula, the saturation density ρ_0 as determined from the central density of heavy nuclei and the condition that $e(\rho_0)$ corresponds to a local minimum:

$$e(\rho_0) - m_N = -15.75 \text{ MeV}, \quad \rho_0 = 0.192 \text{ fm}^{-3}, \quad (1)$$

$$[de(\rho)/d\rho]_{\rho=\rho_0} = 0, \quad (2)$$

where m_N is the nucleon mass. The energy density is denoted by $e(\rho) = \rho e(\rho)$.

A central part of our work is the Hartree and TF calculations of the nuclear surface. The surface provides additional constraints to those provided by the above bulk properties of nuclear matter. Thus the self-interactions are expected to lead to additional dependences of $e(\rho)$ on ρ to those due to only the Yukawa couplings²⁰⁾ and one may then expect these self-interactions to be significantly constrained by nuclear properties at densities different from ρ_0 . However such properties are just provided, for $\rho \leq \rho_0$, by those of the nuclear surface.

For the nuclear surface we consider the well-known idealization of semi-infinite nuclear matter with a single free surface. This is the nuclear surface analog of nuclear matter. Its properties are characterized by two quantities: (i) The surface energy which is obtained from the surface energy term $u_s A^{\frac{1}{2}}$ in the semi-empirical mass formula. Thus u_s is the surface energy appropriate to a surface area of $4\pi r_0^2$ where $r_0 = 1.1 \text{ fm}$. The value of u_s is $19 \pm 1 \text{ MeV}$ [ref. 19)]. (ii) The "90 %–10 %" surface thickness t which is the distance between the points where $\rho = 0.9\rho_0$ and $\rho = 0.1\rho_0$. From the density distribution of heavy nuclei one obtains $t = 2.2 \pm 0.1$

fm [ref. ²¹]). These properties are assumed to represent the average properties of the nuclear surface for $N = Z$, in the limit $A \rightarrow \infty$ (i.e. in the limit of zero curvature) and in the absence of Coulomb forces; in particular, shell effects are assumed to be averaged out.

From a comparison of our results for semi-infinite nuclear matter obtained with the self-consistent Hartree and TF calculations we can, in particular, obtain the conditions for which the latter is an adequate approximation to the former. For such conditions one may then use the TF approximation which is considerably easier to use than the Hartree approximation.

It should be noted that knowledge of the compressibility coefficient of nuclear matter, defined by

$$K = \left[\frac{1}{9} \rho_0^2 \frac{d^2 e}{d \rho^2} \right]_{\rho=\rho_0}, \quad (3)$$

would also provide information about $e(\rho)$ for $\rho \neq \rho_0$. However, K is difficult to determine empirically and in fact the most reliable values are probably determined from analysis of the nuclear surface properties ^{25, 26}); K is probably about 200 MeV. An important result of our work is to give support for this conclusion together with a value of K . The value of K obtained by Walecka is quite large, about 500 MeV.

Our approach may be considered a relativistic analog of non-relativistic Hartree calculations which use Skyrme-type interactions. Thus the density dependent terms of the latter correspond to the self-interactions of the present approach. Finite range effects are taken into account in our calculation by the explicit inclusion of the meson fields. Our TF calculations are thus close in spirit to the TF approximations as used for atoms where the Coulomb potential is explicitly included. They therefore differ from some nuclear TF calculations which do not explicitly include finite range effects of the nuclear forces ²³⁻²⁴). However, other nuclear TF calculations do include finite range effects through the Weiszäcker-type gradient terms [refs. ²⁵⁻²⁸].

2. Relativistic Hartree and Thomas-Fermi calculations

As mentioned in the introduction, our Lagrangian is a generalization of that used by Walecka. It is given by

$$\mathcal{L} = -\bar{\psi} (\gamma_\lambda \partial_\lambda + m_N) \psi - \frac{1}{2} (\partial_\lambda \sigma)^2 - U(\sigma) - g_v \bar{\psi} \psi \sigma - \frac{1}{4} F_{\lambda\mu} F_{\lambda\mu} - \frac{1}{2} m_v^2 V_\lambda V_\lambda + i g_v \bar{\psi} \gamma_\lambda \psi V_\lambda, \quad (4a)$$

with

$$F_{\mu\nu} = \partial_\mu V_\nu - \partial_\nu V_\mu, \quad (4b)$$

$$U(\sigma) = \frac{1}{2} m_\sigma^2 \sigma^2 + \frac{1}{3} b \sigma^3 + \frac{1}{4} c \sigma^4. \quad (4c)$$

Here σ and V_μ are the scalar and vector fields (μ is the space-time index), ψ is the

(four-component spinor) nucleon field and γ_λ are the usual γ -matrices; g_s and g_v are the Yukawa coupling constants, and m_s and m_v are the scalar and vector meson masses. The Walecka model is obtained for $b = c = 0$ and the sigma model for $b = 1.5m_s^2(g_s/m_N)$, $c = 0.5m_s^2(g_s/m_N)^2$.

The time-independent Hartree equations corresponding to the above Lagrangian are

$$\nabla^2\sigma - m_s^2\sigma = b\sigma^2 + c\sigma^3 + g_s\rho_s, \quad (5)$$

$$\nabla^2V - m_v^2V = -g_v\rho, \quad (6)$$

$$(\alpha \cdot p + \beta m^*)\psi_i = (E_i - g_v V)\psi_p \quad (7)$$

with

$$m^* = m_N + g_s\sigma. \quad (8)$$

These equations are just the classical time-independent field equations, but with the meson-field quantities now interpreted as the ground state expectation values of the respective field operators²⁹⁾; E_i and ψ_i are the energy and Dirac wave function for the i th nucleon state; $V_4 = iV$, and α are the usual Dirac matrices. Only the dependence on the spatial position x remains. For semi-infinite nuclear matter these states ψ_i belong to a continuum and are labelled by a momentum quantum number k (see below). Thus the scalar and vector densities, ρ_s and ρ respectively, are given by

$$\rho_s(x) = 4 \int^{k_F} \frac{d^3k}{(2\pi)^3} \bar{\psi}_k(x)\psi_k(x), \quad (9)$$

$$\rho(x) = 4 \int^{k_F} \frac{d^3k}{(2\pi)^3} \bar{\psi}_k^+(x)\psi_k(x). \quad (10)$$

For the ground state the nucleon states are occupied up to the Fermi level (with quantum number k_F); equal number of neutrons and protons and equal number of spin-up and spin-down nucleons are assumed.

For semi-infinite nuclear matter, translational invariance is assumed for directions transverse to the normal to the surface. The only dependence of ρ_s , ρ , σ , V and of the energy density e is then on the coordinate z normal to the surface. For convenience the origin is taken in the surface. For $z \rightarrow -\infty$ conditions are required to approach those of normal infinite nuclear matter of density ρ_0 satisfying the saturation conditions (1) and (2). Thus the nucleon states may be labelled by the momentum k of the states of the nuclear-matter Fermi gas with Fermi momentum k_F , where

$$k_F^3 = \frac{3}{2}\pi^2\rho_0. \quad (11)$$

For $z \rightarrow \infty$, appropriate to free space, the fields and densities must vanish. The fields σ and V depend only on z and are obtained from the following integral equations, that for σ being non-linear. These equations have been obtained by use of the Green functions appropriate to the linear differential operators on the left-hand sides of eqs. (5) and (6) and for the desired boundary conditions. Thus

$$\sigma = -\frac{1}{2m_s} \int_{-\infty}^{\infty} \exp(-m_s|z-z'|)[g_s\rho_s + b\sigma^2 + c\sigma^3]dz', \quad (12a)$$

$$V = +\frac{1}{2m_v} \int_{-\infty}^{\infty} \exp(-m_v|z-z'|)g_v\rho(z')dz'. \quad (12b)$$

Eq. (12b) gives V explicitly in terms of ρ . Eq. (12a) becomes explicitly linear for $b = c = 0$, i.e. for the Walecka model and σ is then explicitly given in terms of ρ_s .

In the Hartree approximation the nuclear wave function ψ_k must be calculated from eq. (7). Because of the assumed translational invariance in the transverse direction x_\perp one may write

$$\psi_k(x) = \exp(ik_\perp \cdot x_\perp)\psi_k(z), \quad (13)$$

where $k^2 = k_\perp^2 + k_z^2$. Here k_\perp is the magnitude of the transverse momentum and k_z is the momentum-like quantum number for the z -direction. The index k for $\psi_k(z)$ is a short hand notation for the pair of quantum numbers k_\perp, k_z . One then obtains the following equation for $\psi_k(z)$,

$$\left(\hat{K} + \frac{\alpha_3}{i} \frac{d}{dz}\right) \psi_k(z) = [E - g_v V(z)] \psi_k(z), \quad (14)$$

where

$$\hat{K} = \alpha + \beta m^*.$$

The operator \hat{K} is hermitian and \hat{K}^2 is diagonal. Eq. (14) can then be simplified by means of a unitary transformation to a representation in which \hat{K} itself is diagonal. The transformed equations are

$$\begin{aligned} \frac{d\tilde{\psi}_k^A}{dz} &= i(E - g_v V - \omega) \tilde{\psi}_k^B, \\ \frac{d\tilde{\psi}_k^B}{dz} &= i(E - g_v V + \omega) \tilde{\psi}_k^A, \end{aligned} \quad (15)$$

with

$$\omega = [k_\perp^2 + m^*(z)^2]^{\frac{1}{2}}. \quad (16)$$

The functions $\tilde{\psi}^A$ and $\tilde{\psi}^B$ are then related to $\psi_{\mathbf{k}}(z)$ by the unitary transformation

$$\psi_{\mathbf{k}}(z) = \begin{pmatrix} \chi^A \tilde{\psi}_{\mathbf{k}}^A \\ \frac{k_x \sigma_3 - ik_y}{k_{\perp}} \chi^A \tilde{\psi}_{\mathbf{k}}^B \end{pmatrix}, \quad (17)$$

where χ^A are the usual two component spin wave functions ($\lambda = 1, 2$ for spin up and spin down, respectively). The boundary conditions are

$$\begin{aligned} \psi_{\mathbf{k}}(z) &\rightarrow 0 \quad \text{for } z \rightarrow +\infty, \\ \tilde{\psi}_{\mathbf{k}}^A(z) &\rightarrow \sqrt{\frac{1}{2}} [\exp(ik_z z) + B(k_{\perp}, k_z) \exp(-ik_z z)] \quad \text{for } z \rightarrow -\infty. \end{aligned} \quad (18)$$

The solutions of eq. (15) for a set of values k_{\perp} , k_z , and subject to the above boundary conditions, then determine the reflection coefficient $B(k_{\perp}, k_z)$, where $|B| = 1$ because of complete internal reflection at the surface.

The energy density in the Hartree approximation is given by

$$\epsilon(z) = 4 \int^{k_F} \frac{d^3 k}{(2\pi)^3} \psi_{\mathbf{k}}^+(z) \psi_{\mathbf{k}}(z) ([k^2 + m^{*2}(-\infty)]^{\frac{1}{2}} + g_v V(-\infty)) - \frac{1}{2} g_v \rho(z) - \frac{1}{2} g_s \rho_s(z) \sigma(z). \quad (19)$$

The surface energy u_s is obtained from the value of the energy density appropriate to the self-consistent solution by use of eq. (24) as discussed below.

2.1. THOMAS-FERMI APPROXIMATION

The time consuming calculation of the nucleon wave functions is avoided in the TF approximation by use of the local density approximation. This assumes that for the calculation of the *kinetic energy density* the conditions at any point z correspond to those of infinite nuclear matter with density $\rho(z)$. Then

$$\rho(z) = (2/3\pi^2)k_F^3(z), \quad (20)$$

$$\begin{aligned} \rho_s(z) &= 4 \int^{k_F(z)} \frac{d^3 k}{(2\pi)^3} \frac{m^*(z)}{(k^2 + m^*(z)^2)^{\frac{1}{2}}} \\ &= m^*(z)(k_F(z)^2/\pi^2) \left[(1 + \lambda^2)^{\frac{1}{2}} - \frac{1}{2}\lambda^2 \ln \left[\frac{(1 + \lambda^2)^{\frac{1}{2}} + 1}{(1 + \lambda^2)^{\frac{1}{2}} - 1} \right] \right], \end{aligned} \quad (21)$$

with

$$\lambda = m^*(z)/k_F(z).$$

Here $k_F(z)$ is the local Fermi momentum and is obtained from

$$E_F = g_v V(z) + [k_F^2(z) + m^{*2}(z)]^{\frac{1}{2}}. \quad (22)$$

The Fermi energy E_F is given by that of the asymptotic nuclear matter and $m^*(z)$ is given in terms of σ by eq. (8).

The equations which relate ρ_s to σ and ρ to V , i.e. eqs. (12), remain the same as for the Hartree approximation. Since in the TF approximation $\rho(z)$ and $\rho_s(z)$ are given in terms of $k_F(z)$ and $\sigma(z)$ by eqs. (20) and (21), the solution of the TF equations does not involve the calculation of the individual nucleon wave functions. These are also not needed for the calculation of the energy density, which is given by

$$\begin{aligned} \epsilon(z) = 4 \int_{-\infty}^{k_F(z)} \frac{d^3 k}{(2\pi)^3} [k^2 + m^{*2}(z)]^{1/2} \\ + \frac{1}{2} g_v \rho(z) V_0(z) - \frac{1}{2} g_s \rho_s \sigma(z). \end{aligned} \quad (23)$$

The validity of the TF approximation implies that the effect of the variation of the density on the kinetic energy can be neglected. Thus, in particular the TF approximation is expected to be better for thicker surfaces. This is confirmed by our numerical results and is discussed in more detail below.

2.2. SURFACE ENERGY

From the self-consistent solutions and the corresponding energy densities the surface energy for both Hartree and TF approximations is obtained in the same standard manner, namely, by use of

$$u_s = 4\pi r_0^2 \int_{-L}^{\infty} [\epsilon(z) - Ne(\rho)] dz,$$

with

$$N = \int_{-L}^{\infty} \rho(z) dz. \quad (24)$$

Here L is a suitably large length (about 10 fm) such that conditions at $-L$ are to a good approximation those of infinite nuclear matter; N is the corresponding number of nucleons per unit area and $Ne(\rho_0)$ is thus just the energy which the nucleons between $z = -L$ and $z = \infty$ would have if they were all at the uniform density ρ_0 of infinite nuclear matter.

2.3. SOLUTION OF THE HARTREE AND TF EQUATIONS

The Hartree equations for semi-infinite nuclear matter are solved numerically by iteration to obtain satisfactory self-consistency. We start with reasonable values for σ and $V(z)$: with these the Dirac eqs. (15) are solved for a suitable grid of values of k_\perp and k_z . The resulting wave functions $\psi_k(z)$ are used to compute $\rho(z)$ and $\rho_s(z)$ with use of eqs. (9) and (10). These densities then determine new values of $\sigma(z)$ and $V(z)$ through eqs. (12). These equations could in principle be solved for each iteration to determine σ and V explicitly in terms of ρ_s and ρ_v appropriate to that iteration. It is in fact more convenient to solve eqs. (12) as part of the iterative

procedure. Thus for the $(k+1)$ th iteration the values of $\sigma^{(k+1)}$ and $V^{(k+1)}$ are obtained by use, in the right-hand side of eq. (12), of the values $\rho_s^{(k)}$, $\rho^{(k)}$, $\sigma^{(k)}$ and $V^{(k)}$ obtained in the previous iteration. This iterative process converges quite rapidly. For each iteration the values of $\rho_s^{(k)}(z)$, $\rho^{(k)}(z)$, $\sigma_s^{(k)}(z)$ and $V^{(k)}(z)$ for large and negative values of z are readjusted to their prescribed infinite nuclear matter values. In principle these boundary conditions are built in, but in practice, rounding errors and truncation errors make it necessary to perform this readjustment. This is particularly necessary for the Hartree approximation. Satisfactory convergence (successive iterations are required to agree within 0.1 %) is usually achieved in about ten iterations.

The self-consistent densities and fields obtained in the Hartree calculation show a damped oscillatory behavior as a function of z as one moves into the interior. Such behavior is in fact expected in the Hartree approximation because of the interference between the "incident" and "reflected" waves in eq. (18). Even after summing over all the occupied states there is still a residual oscillation with a wavelength of order $2\pi/k_F$ which, however, damps out like z^{-1} as one moves away from the nuclear surface.

For the TF calculation the computational problems are less than for the Hartree approximation. It is only necessary to have reasonable starting values for the first iteration; these values are obtained by trial and error.

For both the Hartree and TF calculations of semi-infinite nuclear matter it is important that the interactions be such that the saturation conditions, i.e. eqs. (1) and (2), for nuclear matter are satisfied. Otherwise, instabilities occur and the iterative process does not converge. (Such instabilities are to be expected if the interactions are such that nuclear matter does not saturate at ρ_0 since the self-consistent Hartree or TF calculations try to seek the solution which minimizes the energy and which for nuclear matter no longer corresponds to $\rho = \rho_0$.)

We have made Hartree and TF calculations both for the Walecka model and with nonlinear self-interactions. The solutions, for semi-infinite nuclear matter, for

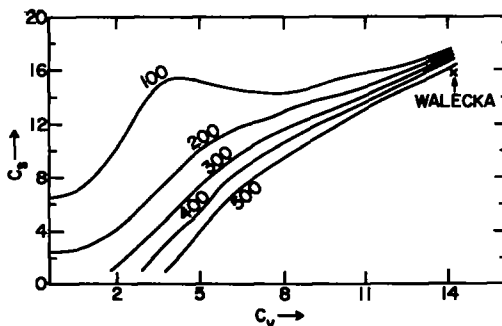


Fig. 1. Contours of constant compressibility coefficient K (MeV) as a function of the scalar and vector coupling constants C_s and C_v .

non-zero self-interactions *cannot* be obtained by starting from the self-consistent solution for zero self-interactions (the Walecka model) and using this as the starting point for a sequence of self-consistent calculations for (slowly) increasing self-interactions. (The self-consistent solution for some particular value of the self-interactions is used as the starting point for a self-consistent calculation for a larger value of the self-interactions.) The reason why this does not work is that (as illustrated by fig. 1 and as discussed further below) the *infinite nuclear-matter solutions* in the neighborhood of the Walecka solution depend strongly on the compressibility coefficient K . This has the result that for the semi-infinite case the above sequence of self-consistent calculations is quite unstable. In fact we were first able to obtain self-consistent solutions for large self-interactions corresponding to small values of K . These solutions were then used as the starting point for a sequence of self-consistent calculations for different self-interactions. In particular one can approach the solution for the Walecka model in this way. This sequence of self-consistent calculations is generated by increasing the values of C_s and C_v defined below in eq. (25). This procedure amounts in effect to an analytic continuation of the solution in these coupling constants and is a very useful procedure once a particular solution has been found.

For infinite nuclear matter the Hartree and TF approximations are identical. One now has just the TF equations but without any z -dependence. The derivative terms are zero and the relation between the fields σ , V and the densities ρ_s , ρ is given directly by eqs. (5) and (6) with the derivative terms equal to zero.

3. Results and discussion

3.1. NUCLEAR MATTER

In general, our interaction depends on six parameters, namely: g_s , g_v , m_s , m_v , b , c . However, for infinite nuclear matter only the following four parameters enter:

$$C_s = m_N(g_v/m_s), \quad C_v = m_N(g_s/m_v), \quad b/g_s^3, \quad c/g_s^4. \quad (25)$$

Only the ratios g_s/m_s , g_v/m_v enter, but not m_s and m_v separately, because for translationally invariant nuclear matter there is no length scale in the Hartree (or equivalently TF) approximation.

The empirical saturation properties of nuclear matter, as given by eqs. (1) and (2), provide two constraints and allow b/g_s^3 and c/g_s^4 to be determined as functions of C_s and C_v . All other nuclear-matter properties, in particular the compressibility coefficient K , are then also determined as functions of C_s and C_v . The equilibrium condition [eq. (2)] leads to the following expression for the effective mass:

$$m^* = [(e(\rho_0) - (C_v/m_N)^2 \rho_0)^2 - k_F^2]^{\frac{1}{2}}. \quad (26)$$

For the Walecka model, for which $b = c = 0$, the values of C_s and C_v , and hence

of K and m^* , are uniquely determined and are

$$\begin{aligned} C_s &= 16.34, & C_v &= 13.99, \\ K &= 550 \text{ MeV}, & m^*/m_N &= 0.56. \end{aligned} \tag{27}$$

The value of K is seen to be very large.

For the general case when self-interactions are included, fig. 1 shows the contours of constant compressibility K in the C_s , C_v plane. For C_s fixed, K is seen to increase rapidly with increasing C_v , i.e., as the repulsive contribution due to the vector meson field increases. On the other hand, eq. (26) shows that m^* decreases as C_v increases. For $K \approx 200$ MeV one has $m^*/m \approx 0.8-0.9$ ($C_v \approx 2$, $V_s \approx 8$). It should be noted that conventional nonrelativistic G -matrix calculations which use two-body nuclear forces give $m^*/m \approx 0.6$ [ref. 23)].

These results, when non-linear self-interactions are included, can be understood as a consequence of a repulsive contribution to the energy coming from the quartic self-interaction term. Such a repulsive contribution then requires a correspondingly smaller repulsive contribution from the vector field, corresponding to a reduced value of C_v as compared with the value for the Walecka model. In fact, saturation of nuclear matter and fairly reasonable nuclear surface properties can be obtained without any vector field.

3.2. NUCLEAR SURFACE

The nuclear surface, in contrast to nuclear matter in the Hartree or TF approximations, involves a length scale, namely, the surface thickness t , which characterizes the variation of ρ through the surface. Thus the meson masses m_s and

TABLE I
Comparison of the Hartree and Thomas-Fermi approximations for semi-infinite nuclear matter

C_s	C_v	m_s (MeV)	Hartree		Thomas-Fermi	
			u_s (MeV)	t (fm)	u_s (MeV)	t (fm)
8.0	0.0	100	34.5	4.48	37.5	4.80
		150	27.5	3.60	26.6	3.30
		400	14.4	2.00	10.2	1.30
		700	10.6	1.76	5.9	0.60
		950	6.4	1.60	4.7	0.50
16.34	13.99	400	44.1	3.50	NC	NC
		450	28.5	2.00	NC	NC
		500	26.4	1.85	28.9	2.20
		600	15.2	1.46	20.7	1.30
		650	3.6	1.32	17.0	1.00
		700	NC	NC	13.5	0.66
		800	NC	NC	7.5	0.29

NC denotes that the iteration did not converge and no solution was obtained.

m_v now become additional parameters. Since the nuclear matter calculations determine b/g_s^3 and c/g_s^4 in terms of C_s and C_v , the surface properties depend on four parameters, namely, C_s , C_v , m_s and m_v . For m_v we mostly used $m_v = 780$ MeV appropriate to the ω -meson mass, although a few calculations were made with other values of m_v . The surface thickness is then effectively determined by m_s as discussed below. For the Walecka model there then remains only one free parameter m_s to fit the surface properties.

We have made both Hartree and TF calculations for the Walecka model and also with non-linear self-interactions included. Table I shows Hartree and TF results for u_s and t as a function of m_s for several values of C_s and C_v . Fig. 2 shows some of these

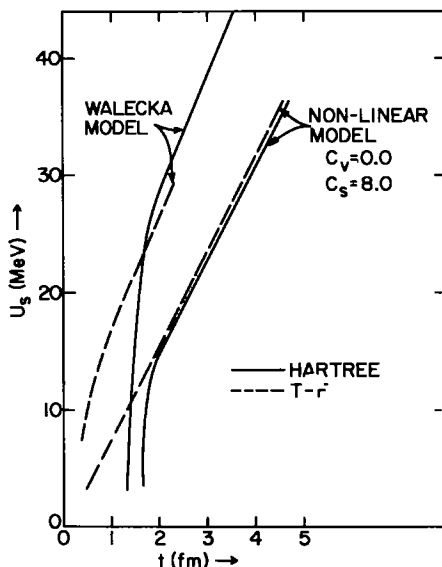


Fig. 2. The surface energy u_s versus surface thickness t . The solid lines are for the Hartree approximation, the broken lines for the Thomas-Fermi approximation.

results in the form of u_s versus t . For $1.7 \leq t \leq 4.4$ fm the Hartree and TF results, for the same value of the parameters, are within about 5 % of each other when non-linear interactions are included. For the Walecka model there is similar agreement for $1.7 \leq t \leq 2.4$ fm. Thus both with and without self-interactions, the Hartree and TF approximations agree well for values of t of about the empirical value.

Such agreement between the Hartree and TF approximations for larger values of t is perhaps not too surprising. This is because in both calculations the meson fields are obtained in the same way from their sources and finite range effects for the interaction energy are as fully included in the TF as in the Hartree calculation. The main difference is that in the TF approximation the kinetic energy is calculated with the use of the local density approximation and is thus all Fermi energy, whereas in

the Hartree approximation there will be additional contributions from the z -dependence of the wave function. However, for the empirical value of t the usual non-relativistic calculations indicate that this latter contribution to the kinetic energy is quite small. Since the TF calculation is much less time consuming than the Hartree calculation, most of our results for non-zero values of b and c were obtained with the TF approximation.

For the Hartree calculations, both for the Walecka model and with non-linear interactions, t becomes almost independent of m_s for $t \leq 1.7$ fm, corresponding to $m_s \leq 600$ MeV, whereas the surface energy continues to decrease (fig. 2). There is thus a nonzero value of m_s^{-1} , i.e. of the range of the scalar interaction, for which the surface energy becomes zero. Associated with this is a peaking of the density in the surface illustrated in fig. 3 for the Walecka model with $m_s \approx 700$ MeV. These features

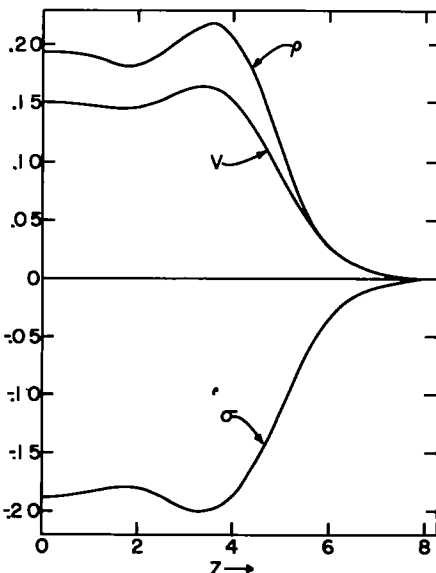


Fig. 3. The particle density ρ (fm^{-3}), the vector potential V and the scalar potential σ (both in fm) for the Walecka model as functions of the coordinate z normal to the nuclear surface. The values are for the Hartree approximation for a scalar meson mass $m_s = 700$ MeV.

may be an indication that the translationally invariant state of nuclear matter may not be the lowest one for very short ranges m_s^{-1} . For the TF calculations for the Walecka model the surface shrinks to zero for $m_s \approx 800$ MeV, whereas for the Hartree calculation this occurs for $m_s \approx 750$ MeV. For the Walecka model we were unable to obtain a solution in the Hartree approximation for $t \geq 2.5$ fm. The solution then becomes numerically unstable.

Fig. 2 and table 1 show that to a good approximation there is a linear relationship between m_s^{-1} and the surface thickness t as well as between the surface energy

u_s and m_s . Thus, to a good approximation

$$u_s = Am_s^{-1}, \quad t = Bm_s^{-1}, \quad (28)$$

where A and B may be obtained from the results of table 1 and 2. Although A and B are somewhat different in the Hartree and TF approximations, the ratio B/A is almost the same for both approximations. (For $C_s = 8, C_v = 0$ one has $B/A = 12.5$.) This ratio is, however, not a function only (or even mainly) of the compressibility coefficient K .

TABLE 2
Thomas-Fermi results

C_s	C_v	$b/(g_s^3 m_N)$	c/g_s^4	m_s (MeV)	u_s (MeV)	t (fm)
8.0	2.0	0.361	6.896	150	32.3	3.3
				200	24.6	2.5
				300	16.6	1.6
				400	12.4	1.1
				500	10.1	0.8
8.0	1.0	0.445	9.465	150	28.0	3.2
				200	21.2	2.4
				300	14.2	1.6
				400	10.6	1.2
				500	8.5	0.8
8.0	0.0	0.482	10.164	150	26.6	3.2
				200	19.1	2.4
				300	13.0	1.6
				400	10.2	1.2
				500	7.5	0.9

TF results for u_s and t are given in table 2. Fig. 4, which shows u_s versus t , also depicts some of these results. The acceptable empirical values are inside the rectangle. These results are all for interactions for which the coefficients b and c of the non-linear terms have been obtained in terms of C_s and C_v from the empirical properties of nuclear matter as described above.

The Walecka model, for which only m_s is available to fit the surface properties, cannot adequately describe these empirical surface properties. Thus the empirical value of the surface thickness t requires $m_s \approx 250$ MeV and gives $u_s \approx 30$ MeV (see fig. 2). This large value of u_s is a result of the large value of K required for the Walecka model by the nuclear matter properties. The Walecka model is thus not able to describe the empirical surface properties and hence, as is also reflected by the large value of K , cannot be considered as giving an adequate description of nuclear matter properties for $\rho \neq \rho_0$.

With the inclusion of non-linear self-interactions, the range of values of C_s and C_v which are consistent with the empirical values of u_s and t is in fact rather limited.

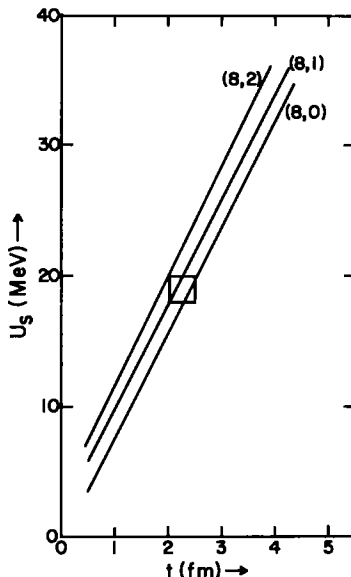


Fig. 4. Results for the surface energy u_s versus the surface thickness t calculated in the Thomas-Fermi approximation. The bracketed numbers are the values of (C_s, C_v) . The rectangle covers the empirically acceptable range of values of u_s and t .

Thus corresponding to $u_s = 19 \pm 1$ MeV, $t = 2.2 \pm 0.1$ fm we obtain as acceptable values

$$C_s = 8 \pm 1, \quad C_v = 1 \pm 1, \quad m_s = 250 \text{ MeV}. \quad (29)$$

These values of C_s and C_v imply

$$K = 150 \pm 50 \text{ MeV}, \quad m^*/m_N = 0.85 \pm 0.05. \quad (30)$$

The value of K is very reasonable and is much less than the large value for the Walecka model. It is significant and is satisfactory that a similar value of about 140 MeV is also obtained by Meyers²²⁾ as a result of a phenomenological non-relativistic TF calculation. Earlier semi-phenomenological calculations also give similar values for K [refs. ^{25, 26}]. A value of $K \approx 150$ MeV as determined by the nuclear surface properties may, most probably, be considered as the best available semi-phenomenological value.

The reasonable value of K , obtained when self-interactions are included, is a result of shifting a large part of the repulsive contribution to the energy from the vector field to the scalar self-interactions. In fact, a reasonable fit to the surface properties can be obtained with $C_v = 0$, i.e. when all the repulsion is due to the scalar self-interaction. The large self-interactions required by the surface properties are then also responsible for the large value of m^* as compared with that obtained for the Walecka model.

The large non-linear self-interactions which are required for a satisfactory description of both nuclear matter and the nuclear surface have implications also for other nuclear properties. We have considered only $N = Z$ and thus did not include isovector mesons. Consequently, with our Lagrangian and in the Hartree approximation, the symmetry energy, i.e. the term $u_s(N-Z)^2/A$ in the semi-empirical mass formula, is entirely due to the difference in the effective (Fermi) kinetic energy between the neutrons and protons as obtained with use of the effective mass m^* . Thus the calculated value of u_s is proportional to m^{*-1} . Because of the small value of m^* for the Walecka model this gives $u_s \approx 23$ MeV, quite close to the empirical value of 25 MeV [ref. ¹⁹]. However, for the value of $m^*/M_N = 0.9$ obtained when self-interactions are included, we obtain only $u_s \approx 15$ MeV. Since the rather large values of m^* are associated with the small values of K required by the surface properties, it is necessary, at least in the Hartree approximation, to include isovector mesons in order to obtain agreement with the empirical symmetry energy. In particular, it will thus be necessary to include such isovector fields if relativistic Hartree calculations are to be meaningful for neutron star matter.

Another implication of the large non-linear self-interactions and of the correspondingly reduced value of C_v of the vector meson coupling is for the spin-orbit splitting in finite nuclei. It will be of interest to see what the non-linear model would predict for this.

3.3. ABNORMAL STATES

Fig. 5 shows the energy/nucleon as a function of the Fermi momentum k_F for the (central) values of C_s and C_v of eq. (29) which are consistent with the empirical nuclear matter and surface properties. Apart from the normal minimum at $k_F = 1.42 \text{ fm}^{-1}$ (which we require at the outset), there is no other minimum, no abnormal state. In fact, even more strongly, if we require only consistency with the

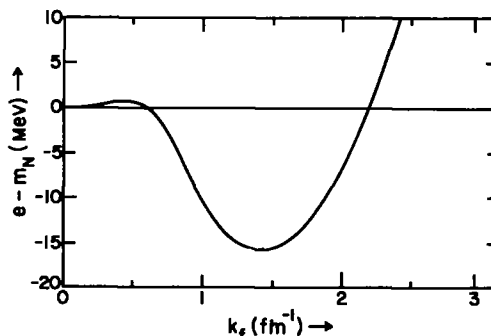


Fig. 5. Energy per particle for nuclear matter as a function of the Fermi momentum k_F for $C_s = 8.0$ and $C_v = 1.0$. There is only the normal minimum corresponding to $k_F = 1.42 \text{ fm}^{-1}$ and $e - m_N = -15.75$ MeV.

empirical nuclear matter properties and "reasonable" compressibilities (less than 1000 MeV) we do not obtain a second minimum, even though we no longer require that the empirical *surface* properties be correctly reproduced. A detailed analysis of the possibility of abnormal nuclear matter states is given elsewhere by one of us (JB)³⁰. The essence of the analysis depends on the observation that in theories with non-linear self-interactions, the self-consistency requirement of eq. (2) implies that $e(\rho)$ must be a multi-valued function of the density. In general, there will be bifurcation points among the different branches. This bifurcation can be avoided when the potential function $U(\sigma)$ has an extremum at $m^* = 0$, i.e. at the Lee-Wick point.

References

- 1) A. E. S. Green and T. Sawada, Rev. Mod. Phys. **39** (1967) 594
- 2) L. D. Miller and A. E. S. Green, Phys. Rev. **C5** (1972) 241
- 3) G. Kalman, Phys. Rev. **D9** (1974) 9
- 4) H. P. Duerr, Phys. Rev. **103** (1956) 469
- 5) J. D. Walecka, Ann. of Phys. **83** (1974) 491;
S. A. Chin and J. D. Walecka, Phys. Lett. **52B** (1974) 24
- 6) T. D. Lee and G. C. Wick, Phys. Rev. **D9** (1974) 2291;
T. D. Lee, Rev. Mod. Phys. **47** (1975) 267;
T. D. Lee and M. Margulies, Phys. Rev. **D11** (1975) 1591
- 7) A. K. Kerman and L. D. Miller, Contribution to the relativistic heavy ion summer study, Berkeley, July 1974, MIT-CTP PUB 449
- 8) C. G. Källman and S. A. Moszkowski, Phys. Lett. **57B** (1975);
C. G. Källman, Phys. Lett. **55B** (1975) 178
- 9) E. M. Nyman and M. Rho, Phys. Lett. **60B** (1976) 134; Nucl. Phys. **A268** (1976) 408;
E. M. Nyman, Nucl. Phys. **A285** (1977) 368
- 10) V. R. Pandharipande and R. A. Smith, Phys. Lett. **59B** (1975) 15
- 11) J. C. Collin and M. J. Perry, Phys. Rev. Lett. **34** (1975) 1353
- 12) S. A. Moszkowski and G. C. Källman, Nucl. Phys. **A287** (1977) 495
- 13) A. R. Bodmer, Phys. Rev. **D4** (1971) 1601; in The nuclear many-body problem, ed. F. Calogero and C. Ciofidegli Atti (Editrice Compositori, Bologna, 1973) p. 509
- 14) A. B. Migdal, ZhETF (USSR) **63** (1972) 1993
- 15) R. F. Sawyer, Phys. Rev. Lett. **29** (1972) 383
- 16) D. J. Scalapino, Phys. Rev. Lett. **29** (1972) 386
- 17) J. Hofmann, H. Stocker, U. Heinz, W. Scheid and W. Greiner, Phys. Rev. Lett. **36** (1974) 88
- 18) L. I. Schiff, Phys. Rev. **84** (1951) 1; **84** (1951) 10
- 19) W. D. Meyers and W. J. Swiatecki, Ann. of Phys. **35** (1969) 395
- 20) S. Barshay and G. E. Brown, Phys. Rev. Lett. **34** (1975) 1106
- 21) J. L. Friar and J. W. Negele, Adv. in Nucl. Phys. **8** (1975) 219
- 22) W. D. Meyers, private communication
- 23) H. A. Bethe, Ann. Rev. Nucl. Sci. **21** (1971) 93
- 24) P. J. Siemens, Phys. Rev. **C1** (1970) 98
- 25) L. Wilets, Rev. Mod. Phys. **30** (1958) 542
- 26) A. R. Bodmer, Nucl. Phys. **17** (1960) 388
- 27) K. A. Bruckner, J. R. Buchler, S. Jorna and R. J. Lombard, Phys. Rev. **171** (1968) 1188
- 28) M. Beiner and R. J. Lombard, Ann. of Phys. **86** (1974) 262
- 29) A. K. Kerman and A. Klein, Phys. Rev. **132** (1963) 1326; **138** (1965) B1323
- 30) J. Boguta, Remarks on nuclear density isomers in infinite nuclear matter, ANL preprint, 1977



ELSEVIER

Nuclear Physics A 606 (1996) 508–537

NUCLEAR
PHYSICS A

Relativistic mean-field theory and the high-density nuclear equation of state

Horst Müller, Brian D. Serot

Physics Department and Nuclear Theory Center, Indiana University, Bloomington, IN 47405, USA

Received 13 March 1996; revised 8 May 1996

Abstract

The properties of high-density nuclear and neutron matter are studied using a relativistic mean-field approximation to the nuclear matter energy functional. Based on ideas of effective field theory, nonlinear interactions between the fields are introduced to parametrize the density dependence of the energy functional. Various types of nonlinearities involving scalar-isoscalar (σ), vector-isoscalar (ω) and vector-isovector (ρ) fields are studied. After calibrating the model parameters at equilibrium nuclear matter density, the model and parameter dependence of the resulting equation of state is examined in the neutron-rich and high-density regime. It is possible to build different models that reproduce the same observed properties at normal nuclear densities, but which yield maximum neutron star masses that differ by more than one solar mass. Implications for the existence of kaon condensates or quark cores in neutron stars are discussed.

PACS: 21.65.+f, 26.60.+c, 97.60.Jd

1. Introduction

Numerous calculations have established that relativistic mean-field models provide a realistic description of the bulk properties of finite nuclei and nuclear matter [1,2]. In addition to this successful low-energy phenomenology, these models are often extrapolated into regimes of high density and temperature to extract the nuclear equation of state (EOS), which is the basic ingredient in many astrophysical applications and in microscopic models of energetic nucleus–nucleus collisions.

Based on the original version of Walecka [3] and its extensions [4,5], relativistic mean-field models generally involve the interaction of Dirac nucleons with neutral scalar and vector mesons and with isovector ρ mesons. One of the key observations in their success is that to provide sufficient flexibility, nonlinear self-interactions for the scalar

meson must be included [2,4,6–11]. Since these models were proposed to be renormalizable, the scalar self-interactions are limited to a quartic polynomial, and scalar–vector and vector–vector interactions are not allowed [12]. One of the motivations for renormalizability, as discussed in Walecka’s seminal paper, is that once the model parameters are calibrated to observed nuclear properties, one can extrapolate into regimes of high density or temperature without the appearance of new, unknown parameters.

An alternative approach is inspired by *effective field theories*, such as chiral perturbation theory [13,14], which successfully describes the low-energy phenomenology of hadronic Goldstone bosons [15,16]. Although a Lagrangian usually serves as the starting point, the meson and baryon fields are no longer considered elementary, and the constraint of renormalizability is dropped. This has several important consequences. First, there is no reason to restrict meson self-interactions to a simple quartic polynomial in the scalar field; on the contrary, one should include all interaction terms that are consistent with the underlying symmetries of QCD. Second, since there is an infinite number of coupling constants, one must find suitable expansion parameters for the systems under consideration, and one must develop a systematic truncation scheme for the effective theory to have any predictive power. Third, extrapolation of calculated results into new regimes of the physical parameters becomes problematic, because the truncation scheme may break down, and predictions can become sensitive to unknown parameters.

Within the framework of effective field theory, mean-field models of nuclear structure and the EOS must be interpreted in a new context. One important observation is that near normal nuclear density, the mean scalar and vector fields (or nucleon self-energies), which we denote as Φ and W , are large on nuclear energy scales but are small compared to the nucleon mass M and vary slowly in finite nuclei. This implies that the ratios Φ/M and W/M and the gradients $|\nabla\Phi|/M^2$ and $|\nabla W|/M^2$ are useful expansion parameters. The assumption of “naturalness” in effective field theory is also important. Naturalness implies that the coefficients of the various terms in the Lagrangian, when expressed in appropriate dimensionless form, should all be of order unity. When combined with meaningful expansion parameters, this means that one can anticipate the approximate magnitude of mean-field contributions to the energy (at least up to moderate nuclear densities) and thereby motivate a suitable truncation scheme; if the coefficients are natural, the omitted terms will be numerically unimportant¹. Naturalness also implies that one should include *all* possible terms (that is, those allowed by the symmetries) through a given order of truncation; it is *unnatural* for some coefficients to vanish without a relevant symmetry argument.

From this point of view, it is difficult to justify nuclear mean-field models that include only scalar self-interactions [4,6,7,10], and recently, generalizations that also include quartic self-interactions for the neutral vector meson have been discussed [9,19,20]. Moreover, a new analysis involving all meson self-interactions through fourth order

¹ It has also been shown recently that the naturalness assumption is consistent with power counting in chiral effective field theory [17,18].

in the isoscalar scalar and vector fields has been performed [21]. These extensions give rise to additional model parameters (coupling constants) that must be constrained by calibrating to observed nuclear properties. For the truncation at fourth order to be sensible, the parameters so obtained should exhibit naturalness.

Although it is possible to discuss effective hadronic field theory from the point of view of a Lagrangian, as above, the expansion in powers of the mean fields is a low-density expansion, and it is hard to justify the neglect of many-body corrections, which are known to be relevant in nuclear structure and in the EOS. Alternatively, one can consider this expansion at the level of an energy functional or effective action [21]. In such a formulation of the relativistic nuclear many-body problem, the central object is an energy functional of scalar and vector densities (or more generally, vector four-currents) [22–24]. Extremization of the functional gives rise to Dirac equations for occupied orbitals with *local* scalar and vector potentials, not only in the Hartree approximation, but in the general case as well. Rather than work solely with the densities, one can introduce auxiliary variables corresponding to the local potentials, so that the functional depends also on mean meson fields. The resulting field equations have the same form as in a Dirac–Hartree calculation [21], but correlation effects can be included, if the proper energy functional can be found. This procedure is analogous to the well-known Kohn–Sham [25] approach in density-functional theory, with the local meson fields playing the role of (relativistic) Kohn–Sham potentials; by introducing nonlinear couplings between these fields, one can implicitly include additional density dependence in the potentials. Thus the nonlinear meson interaction terms simulate more complicated physics, such as one- and two-pion exchange or vacuum-loop corrections, which might be calculated directly in a more microscopic many-body approach [20,24]. The fields (and their gradients) again serve as useful expansion parameters at moderate density, so the nonlinear interaction terms can be truncated, leaving a finite number of unknown couplings.

Rather than focus on the calculation of the nonlinear couplings from an underlying effective Lagrangian, we wish to concentrate instead on how well the energy functional can be calibrated by fitting the couplings to observed nuclear properties, and on the limitations on the extrapolation of the resulting EOS into the high-density regime. In general, even with a significant truncation, the number of unknown couplings exceeds the number of normalization conditions, which we take to be five properties of infinite nuclear matter: the equilibrium density and binding energy (ρ_0 , $-e_0$), the nucleon effective (or Dirac) mass at equilibrium (M_0^*), the compression modulus (K_0) and the bulk symmetry energy (a_4). (Experience has shown that an accurate reproduction of these five properties leads to realistic results when the calculations are extended to finite nuclei [6,7,10,11,21].) Thus families of models can be generated which describe exactly the same nuclear matter properties at equilibrium [19]. We then investigate the differences in the high-density EOS predicted by models within a given family. This question is important for astrophysical applications, particularly in the study of neutron stars; it will be difficult to deduce the existence of “exotic” neutron-star structure (for example, hyperonic matter, kaon condensates or quark cores) unless the EOS of the

more mundane components (neutrons, protons and electrons) is well constrained.

If our truncation of the energy functional is motivated by low-density behavior, why should we have any confidence at all in a high-density extrapolation? This is indeed the crucial question, and we are not attempting here to justify such an extrapolation; we are merely recognizing that this procedure is often used in neutron-star calculations, even recent ones, without any mention of the implicit assumptions about the absence of additional contributions at high density [26–32]. We therefore feel it is timely to investigate quantitatively the uncertainties in the extrapolated equation of state.

We begin the theoretical analysis with a model that contains meson–meson and meson self-interactions described by an *arbitrary* finite polynomial in the fields. We find that both the asymptotic (high-density) limit of the EOS and the approach to this limit (i.e., the “stiffness”) are model dependent. In particular, one can construct models with the *same* equilibrium nuclear matter properties that yield high-density equations of state ranging all the way from the causal limit ($p = \mathcal{E}$) to one that resembles a free relativistic gas ($p = \mathcal{E}/3$) [9,19]. (Here p is the pressure and \mathcal{E} is the energy density.)

As an explicit example, we consider a model that includes self-interactions for the isoscalar scalar and vector mesons and for the ρ meson up to fourth order in the fields. To our knowledge, this is the first time nonlinear terms in the ρ meson mean field have been included. (Note that the ρ field enters here as an *effective* field whose purpose is to parametrize the isospin dependence; thus, fundamental questions about causal propagation [33,34] and spin mixing [35] are not relevant.) To provide a quantitative measure of the variations in the EOS, we compute neutron star masses, which turn out to be sensitive to the model types and to changes in the parametrizations, *even for models that reproduce the same equilibrium nuclear matter properties*. In some cases, variations in the calculated maximum mass are more than one solar mass.

These results lead us to two basic conclusions. First, existing methods for calibration of the EOS at normal density are *not* sufficient to provide a satisfactory extrapolation into the density regime relevant for neutron stars. The basic problem rests with the quartic neutral vector meson (ω) interaction, which produces major modifications in the high-density behavior. We discuss the existing situation regarding the specification of this term and prospects for improved calibration. Second, we find that if the quartic ω term can be accurately determined, additional higher-order terms (and the quartic ρ term) produce relatively minor changes in the neutron star mass. This occurs because the W^4 term softens the high-density EOS so completely that additional interactions have little effect, at least in the density regime relevant for neutron stars.

These conclusions have important implications, because the contributions to the EOS from the neutrons and protons are commonly believed to be the best understood part of the physical input necessary to describe a dense stellar object. Without well-constrained results from this part of the EOS, it will be impossible to determine the importance of additional dynamics, for example, the transition from nuclear matter to quark matter in the interiors of neutron stars [36,37,27] or the role of strangeness in the form of hyperons [38,39] or a kaon condensate [40]. As an example of how uncertainties in the basic nuclear EOS can influence these interesting effects, we study the transition from

hadronic matter to quark matter using a simple model [37,1] and show the possible variations in the results.

The outline of this paper is as follows: In Section 2 we present the general model, which involves an arbitrary number of nonlinear meson interactions and derive the EOS. Based on this general model, Section 3 is devoted to the high-density limit of the EOS. In Section 4 we apply our model to neutron stars. For the quantitative analysis, we initially include self-interactions up to fourth order in the ρ and ω fields and then investigate the consequences of sixth-order and eighth-order ω self-interactions. We also briefly discuss the parameter and model dependence of the transition to quark matter in the central region of the star. Section 5 contains a short summary and our conclusions.

2. The nuclear equation of state

We describe the nuclear equation of state using a relativistic approach involving valence Dirac nucleons and effective mesonic degrees of freedom, which are taken to be neutral scalar and vector fields, plus the isovector ρ meson field. Rather than focus directly on a Lagrangian, we consider instead as a starting point an *effective action*

$$\Gamma = \Gamma[\phi, V_\mu, b_\mu], \quad (1)$$

which is a functional of the meson fields denoted by ϕ , V_μ and b_μ for the scalar, vector-isoscalar and vector-isovector field, respectively. In principle, this functional can be calculated in a many-body approach based on a Lagrangian for the nucleon-nucleon interaction, or its general form might be obtained from an underlying theory. Here we will be satisfied to parametrize the effective action, calibrate it as accurately as we can to observed nuclear properties, and then examine the predicted high-density equation of state.

The effective action is related to the thermodynamic potential Ω [41] by

$$i\beta\Omega = \Gamma[\phi, V_\mu, b_\mu], \quad (2)$$

where the fields are determined by the general thermodynamic principle that they should make Ω stationary:

$$\frac{\partial\Gamma}{\partial\phi} = \frac{\partial\Gamma}{\partial V_\mu} = \frac{\partial\Gamma}{\partial b_\mu} = 0. \quad (3)$$

A basic property of the functional is that it reflects the underlying symmetries [42]. Thus, if we assume that the system possesses two conserved charges, namely, baryon number B and the third component of total isospin I_3 , this gives rise to two chemical potentials μ and ν :

$$\Omega \equiv \Omega(\beta, \mu, \nu), \quad (4)$$

with

$$B = \int d^3x \rho = -\frac{\partial \Omega}{\partial \mu}, \quad (5)$$

$$I_3 = \frac{1}{2} \int d^3x \rho_3 = -\frac{\partial \Omega}{\partial \nu}, \quad (6)$$

β the inverse temperature and $\rho_3 \equiv \rho_p - \rho_n$. Note that the fields can be held fixed in evaluating the partial derivatives in Eqs. (5) and (6) by virtue of the extremization conditions (3).

In the field theoretical context [43], one can show that the effective action can be expanded as a power series in gradients of the fields. Thus, after taking the zero-temperature limit, one usually writes

$$\Gamma[\phi, V_\mu, b_\mu] = \int d^4x \left[-\mathcal{V}_{\text{eff}}(\phi, V_\mu, b_\mu) + \mathcal{Z}(\phi, V_\mu, b_\mu, \partial_\nu \phi, \partial_\nu V_\mu, \partial_\nu b_\mu) \right], \quad (7)$$

where the second term vanishes in a uniform system and the dependence on the chemical potentials has been suppressed. For the effective potential, we make the following ansatz:

$$\begin{aligned} \mathcal{V}_{\text{eff}}(\phi, V_\mu, b_\mu; \mu, \nu) = & \frac{1}{2} m_s^2 \phi^2 - \frac{1}{2} m_v^2 V_\mu V^\mu - \frac{1}{2} m_\rho^2 b_\mu \cdot b^\mu + i \text{tr} \ln Z_\psi(\mu, \nu) \\ & - i \text{tr} \ln Z_\psi(0, 0) + \Delta \mathcal{V}(\phi, V_\mu V^\mu, b_\nu \cdot b^\nu; \mu, \nu), \end{aligned} \quad (8)$$

with a nonlinear potential

$$\Delta \mathcal{V}(\phi, V_\mu V^\mu, b_\nu \cdot b^\nu; \mu, \nu) \equiv - \sum_{i,j,k} a_{ijk}(\mu, \nu) \phi^i (V_\mu V^\mu)^j (b_\nu \cdot b^\nu)^k \quad (9)$$

that contains at least three powers of the fields: $i + 2j + 2k \geq 3$. The fermionic contributions are represented by a one-body term $\text{tr} \ln Z_\psi$ (with the appropriate zero-density subtraction [44]) and by terms where the fermions have been “integrated out”, which results in a (generally nonanalytic) dependence of the mesonic coefficients a_{ijk} on the chemical potentials μ and ν . There will also be contributions to the a_{ijk} that are independent of the chemical potentials; these arise from integrating out heavy degrees of freedom and vacuum loops. Thus \mathcal{V}_{eff} contains explicit contributions only from valence nucleons and classical meson fields.

The fermionic part $\text{tr} \ln Z_\psi$ is obtained by evaluating the trace of the kernel

$$K(\mu, \nu) = (i\partial^\mu - g_v V^\mu - \frac{1}{2} g_\rho \tau \cdot b^\mu) \gamma_\mu + \mu \gamma^0 + \frac{1}{2} \nu \tau_3 \gamma^0 - (M - g_s \phi), \quad (10)$$

using Dirac wave functions calculated in the presence of static background fields. The subtraction removes contributions from negative-energy states, which are already included implicitly in the nonlinear parameters a_{ijk} . (See Ref. [44] for an analogous calculation.) The values of the fields are determined by extremization at the given values of μ and ν .

The potential of Eq. (8) represents an effective field theory for the interacting nucleons. Although the exact form of the effective potential is not known, we introduce the meson mean fields as relativistic Kohn–Sham potentials [25] and consider the valence nucleons moving in the resulting local fields. The nonlinear interactions of the fields

generate implicit density dependence above and beyond that arising from the couplings in Eq. (10). Thus the series in Eq. (9) can be interpreted as a Taylor series parametrization of the unknown part of the effective potential, which includes the effects of nucleon exchange and correlations, as well as contributions from other mesons and the quantum vacuum. (See the discussion in Refs. [21,44].)

Although the couplings a_{ijk} generally depend on the chemical potentials, experience with calculations for finite nuclei and nuclear matter, together with explicit computations of exchange and correlation corrections [45], implies that mean fields and *constant* couplings a_{ijk} provide an adequate (albeit approximate) parametrization of these many-body effects. Thus we consider the a_{ijk} as constants in the sequel and leave the study of their dependence on μ and ν as a topic for future investigation. Moreover, at low densities and temperatures, the mean meson fields are small compared to the nucleon mass, and so provide useful expansion parameters [21]. Thus, in practice, the series in Eq. (9) can be truncated at some reasonable order, and the relevant question in this paper is how far one can extrapolate the truncated potential into the high-density regime.

In principle, the unknown coefficients (coupling constants) can be constrained by imposing chiral symmetry and other symmetries of the underlying QCD, such as broken scale invariance. (Lorentz covariance and isospin symmetry are already incorporated explicitly².) As has been discussed recently, however [11,21], if one assumes a *nonlinear* realization of the chiral symmetry for the pions and nucleons [46], the meson interaction terms are essentially unconstrained³. We therefore take the couplings as free model parameters in our approach. Obviously, an infinite number of normalization conditions is generally needed to fix their values. Since this is not feasible in practice, we terminate the summation at the finite values i_{\max} , j_{\max} and k_{\max} .

According to Eq. (3), the thermodynamic potential Ω must be stationary with respect to changes in the fields for fixed values of the proton and neutron chemical potentials

$$\mu_p \equiv \mu + \frac{1}{2}\nu = (k_{Fp}^2 + M^{*2})^{1/2} + W + \frac{1}{2}R, \quad (11)$$

$$\mu_n \equiv \mu - \frac{1}{2}\nu = (k_{Fn}^2 + M^{*2})^{1/2} + W - \frac{1}{2}R. \quad (12)$$

Here, following Bodmer [19], we define the scaled meson fields $\Phi \equiv g_s \phi$, $W \equiv g_v V_0$ and $R \equiv g_\rho b_0$, with b_0 the time-like, neutral part of the ρ meson field; the effective nucleon mass is $M^* \equiv M - \Phi$. (We work in the rest frame of the infinite matter, where the spatial parts of the vector fields vanish.) The Fermi momenta for protons (k_{Fp}) and neutrons (k_{Fn}) are related to the conserved baryon density

$$\rho = \frac{1}{3\pi^2} \left(k_{Fp}^3 + k_{Fn}^3 \right) \quad (13)$$

² Note that since the energy functional is an effective functional, we presently know of no reason to exclude terms that explicitly contain the medium four-velocity u^μ , such as $u^\mu V_\mu V^\nu V_\nu$. This issue will be considered in a later publication.

³ Broken scale invariance leads to restrictions on the purely scalar interactions, as shown in Refs. [47,44], but we will not consider these limitations here. As discussed in the next section, the details of the scalar dynamics do not play a major role in our analysis.

and isovector density

$$\rho_3 = \frac{1}{3\pi^2} \left(k_{\text{Fp}}^3 - k_{\text{Fn}}^3 \right). \quad (14)$$

Using Eqs. (2), (5) and (6), together with relations (11) and (12) for the chemical potentials, it is straightforward to eliminate the chemical potentials in favor of the densities and to compute the pressure p and the energy density $\mathcal{E} = -p + \mu\rho + \frac{1}{2}\nu\rho_3$:

$$\begin{aligned} p &= \frac{1}{3\pi^2} \int_0^{k_{\text{Fp}}} dk \frac{k^4}{(k^2 + M^{*2})^{1/2}} + \frac{1}{3\pi^2} \int_0^{k_{\text{Fn}}} dk \frac{k^4}{(k^2 + M^{*2})^{1/2}} \\ &\quad + \frac{1}{2c_v^2} W^2 + \frac{1}{2c_\rho^2} R^2 - \frac{1}{2c_s^2} \Phi^2 + \sum_{i,j,k} \bar{a}_{ijk} \Phi^i W^{2j} R^{2k}, \end{aligned} \quad (15)$$

$$\begin{aligned} \mathcal{E} &= \frac{1}{\pi^2} \int_0^{k_{\text{Fp}}} dk k^2 (k^2 + M^{*2})^{1/2} + \frac{1}{\pi^2} \int_0^{k_{\text{Fn}}} dk k^2 (k^2 + M^{*2})^{1/2} \\ &\quad + W\rho + \frac{1}{2} R\rho_3 - \frac{1}{2c_v^2} W^2 - \frac{1}{2c_\rho^2} R^2 + \frac{1}{2c_s^2} \Phi^2 - \sum_{i,j,k} \bar{a}_{ijk} \Phi^i W^{2j} R^{2k}. \end{aligned} \quad (16)$$

Here the ratios $c_i^2 = g_i^2/m_i^2$ and $\bar{a}_{ijk} \equiv a_{ijk}/g_s g_v^i g_\rho^{2k}$ have been introduced for convenience.

As noted earlier, the pressure in Eq. (15) and the energy density in Eq. (16) also contain vacuum contributions arising from the partition function of the nucleons. However, at least at the one-baryon-loop level, these vacuum terms can be absorbed in the definition of the nonlinear couplings in Eq. (9) [44], and thus we include explicitly only the contributions from valence nucleons.

At zero temperature, the stationarity conditions of Eq. (3) with fixed chemical potentials are equivalent to an extremization of the energy at fixed baryon and isovector density. This leads to the self-consistency equations

$$\frac{1}{c_s^2} \Phi - \sum_{i,j,k} i \bar{a}_{ijk} \Phi^{i-1} W^{2j} R^{2k} = \rho_s, \quad (17)$$

$$\frac{1}{c_v^2} W + \sum_{i,j,k} 2j \bar{a}_{ijk} \Phi^i W^{2j-1} R^{2k} = \rho, \quad (18)$$

$$\frac{1}{c_\rho^2} R + \sum_{i,j,k} 2k \bar{a}_{ijk} \Phi^i W^{2j} R^{2k-1} = \frac{1}{2} \rho_3, \quad (19)$$

where the scalar density is given by

$$\rho_s = \frac{M^*}{\pi^2} \int_0^{k_{\text{Fp}}} dk \frac{k^2}{(k^2 + M^{*2})^{1/2}} + \frac{M^*}{\pi^2} \int_0^{k_{\text{Fn}}} dk \frac{k^2}{(k^2 + M^{*2})^{1/2}}. \quad (20)$$

Because of the factor of 1/2 on the right-hand side of Eq. (19), it follows that the relevant expansion parameters for the energy density are Φ/M , W/M and $2R/M$. Moreover, by dividing \mathcal{E} by M^4 and expressing the result in terms of these expansion parameters, one can identify the scaled couplings that should all be of roughly the same size if they are “natural”, namely,

$$\frac{1}{2c_s^2 M^2}, \quad \frac{1}{2c_v^2 M^2}, \quad \frac{1}{8c_\rho^2 M^2} \quad \text{and} \quad \frac{\bar{a}_{ijk} M^{i+2j+2k-4}}{2^{2k}}.$$

3. The high-density limit

The coupling constants c_v^2 , c_s^2 , c_ρ^2 and \bar{a}_{ijk} in Eqs. (15) and (16) enter as unknown model parameters. According to the generally accepted procedure, these parameters will be chosen to reproduce the properties of nuclear matter near equilibrium. The basic ingredient in many astrophysical problems, e.g., neutron-star calculations, is the EOS

$$p = p(\mathcal{E}), \quad (21)$$

which is then extrapolated into the neutron-rich and high-density regime. Anticipating the results of the next section, one can expect that different parameter sets that lead to identical equilibrium properties produce qualitatively similar equations of state at low densities. The relevant question is whether this qualitatively similar behavior persists at high densities, particularly in the regime important for neutron stars. As a first step in this direction, we investigate the high-density limit of the EOS generated by the model introduced in the previous section.

To make the discussion more transparent, we focus here on pure neutron matter ($k_{Fp} = 0$, $k_{Fn} \equiv k_F$), although nuclear matter in β -decay equilibrium with a finite proton to neutron ratio is necessary to achieve accurate results for maximum neutron star masses. We will return to this issue in the next section.

It is clear that a sufficiently large number of couplings introduces a high degree of flexibility. Due to the nonlinearity of the problem, not all families of parameter sets lead to physically acceptable results, which provides one way to restrict the parameter space. Classes of models can be ruled out if basic physical requirements are violated. For example, one certainly requires that the pressure p be a smooth function of the energy density \mathcal{E} . Moreover, it is necessary that the speed of (first) sound c_1 respect causality and also be real, to ensure stability. That is,

$$0 \leq c_1^2 = \frac{\partial p}{\partial \mathcal{E}} \leq 1.$$

In addition to these general principles, we require a positive and bounded value of the nucleon effective mass, i.e.,

$$0 \leq M^* \leq M. \quad (22)$$

This is motivated by the expectation that physically reasonable models will demonstrate some degree of chiral-symmetry restoration at finite density, leading to a reduction in the nucleon mass, with the most extreme situation corresponding to total restoration of the symmetry. The consequences of Eq. (22) will become more transparent in the following.

By specializing the formalism of the preceding section to pure neutron matter and by using the self-consistency equations (17)–(19), the pressure and energy density can be expressed as

$$\begin{aligned} p &\equiv p_0(k_F, M^*) + \Delta p(\Phi, W, R) \\ &= \frac{1}{3\pi^2} \int_0^{k_F} dk \frac{k^4}{(k^2 + M^{*2})^{1/2}} + \frac{1}{2c_v^2} W^2 + \frac{1}{2c_\rho^2} R^2 - \frac{1}{2c_s^2} \Phi^2 + \sum_{i,j,k} \bar{a}_{ijk} \Phi^i W^{2j} R^{2k}, \end{aligned} \quad (23)$$

$$\begin{aligned} \mathcal{E} &\equiv \mathcal{E}_0(k_F, M^*) + \Delta \mathcal{E}(\Phi, W, R) \\ &= \frac{1}{\pi^2} \int_0^{k_F} dk k^2 (k^2 + M^{*2})^{1/2} + \frac{1}{2c_v^2} W^2 + \frac{1}{2c_\rho^2} R^2 + \frac{1}{2c_s^2} \Phi^2 \\ &\quad + \sum_{i,j,k} (2j + 2k - 1) \bar{a}_{ijk} \Phi^i W^{2j} R^{2k}, \end{aligned} \quad (24)$$

where p_0 and \mathcal{E}_0 denote the results for a relativistic, noninteracting gas of spin-1/2 baryons with mass M^* . Note that these expressions include, as a special case, models where only the \bar{a}_{0jk} are nonzero, so that there are no scalar–vector couplings. Moreover, the isovector density in Eq. (19) is replaced by

$$\rho_3 = -\rho = -\frac{1}{3\pi^2} k_F^3. \quad (25)$$

At high densities, the left-hand sides of the self-consistency equations (18) and (19) must grow linearly in ρ , and thus we start with the ansatz

$$\lim_{\rho \rightarrow \infty} W = w_0 \rho^\alpha, \quad \lim_{\rho \rightarrow \infty} R = r_0 \rho^\beta, \quad (26)$$

where $0 < \alpha, \beta \leq 1$, $w_0 > 0$ and $r_0 < 0$. Since we assume that the effective mass is bounded, we can replace the scalar field by the limit

$$\Phi_\infty \equiv \lim_{\rho \rightarrow \infty} (M - M^*) \leq M. \quad (27)$$

To fulfill the resulting self-consistency equations:

$$\frac{1}{c_v^2} W + \sum_{i,j,k} 2j \bar{a}_{ijk} \Phi_\infty^i W^{2j-1} R^{2k} = \rho, \quad (28)$$

$$\frac{1}{c_\rho^2} R + \sum_{i,j,k} 2k \bar{a}_{ijk} \Phi_\infty^i W^{2j} R^{2k-1} = \frac{1}{2} \rho_3 = -\frac{1}{2} \rho, \quad (29)$$

there must be integers (j_m, k_m) and (j'_m, k'_m) with

$$(2j_m - 1)\alpha + 2k_m\beta = 1 > (2j - 1)\alpha + 2k\beta \quad \text{for all } j \neq j_m, k \neq k_m, \quad (30)$$

$$2j'_m\alpha + (2k'_m - 1)\beta = 1 > 2j\alpha + (2k - 1)\beta \quad \text{for all } j \neq j'_m, k \neq k'_m. \quad (31)$$

(This assumes that only one term in each sum produces the leading asymptotic behavior; if this actually happens for more than one term in a sum, the conclusions below are unchanged.) Using

$$\lim_{\rho \rightarrow \infty} p_0 = \frac{(3\pi^2)^{1/3}}{4} \rho^{4/3} + O(\rho^{2/3}), \quad \lim_{\rho \rightarrow \infty} \mathcal{E}_0 = \frac{3(3\pi^2)^{1/3}}{4} \rho^{4/3} + O(\rho^{2/3}), \quad (32)$$

the leading contributions to the pressure and the energy density are found to be

$$\begin{aligned} \lim_{\rho \rightarrow \infty} p &= \frac{(3\pi^2)^{1/3}}{4} \rho^{4/3} + \frac{1}{2c_v^2} w_0^2 \rho^{2\alpha} + \frac{1}{2c_\rho^2} r_0^2 \rho^{2\beta} \\ &\quad + w_0^{2j_m} r_0^{2k_m} \rho^{1+\alpha} \sum_i \bar{a}_{ij_m k_m} \Phi_\infty^i + w_0^{2j'_m} r_0^{2k'_m} \rho^{1+\beta} \sum_i \bar{a}_{ij'_m k'_m} \Phi_\infty^i, \end{aligned} \quad (33)$$

$$\begin{aligned} \lim_{\rho \rightarrow \infty} \mathcal{E} &= \frac{3(3\pi^2)^{1/3}}{4} \rho^{4/3} + \frac{1}{2c_v^2} w_0^2 \rho^{2\alpha} + \frac{1}{2c_\rho^2} r_0^2 \rho^{2\beta} \\ &\quad + w_0^{2j_m} r_0^{2k_m} \rho^{1+\alpha} (2j_m + 2k_m - 1) \sum_i \bar{a}_{ij_m k_m} \Phi_\infty^i \\ &\quad + w_0^{2j'_m} r_0^{2k'_m} \rho^{1+\beta} (2j'_m + 2k'_m - 1) \sum_i \bar{a}_{ij'_m k'_m} \Phi_\infty^i. \end{aligned} \quad (34)$$

To this point, the discussion is rather general. To make the conclusions more concrete, we discuss two distinct situations separately:

- (i) No coupling between W and R . In this special case, the asymptotic behavior of the fields is governed by their highest powers in the potential (9). From Eqs. (30) and (31), we obtain

$$\alpha = \frac{1}{2j_{\max} - 1}, \quad \beta = \frac{1}{2k_{\max} - 1}.$$

For $j_{\max} = 1$, $k_{\max} \geq 1$ or $j_{\max} \geq 1$, $k_{\max} = 1$, the quadratic terms dominate the right-hand sides of Eqs. (33) and (34), so that

$$\lim_{\rho \rightarrow \infty} \frac{1}{c_v^2} W^2 \propto \rho^2 \quad \text{or} \quad \lim_{\rho \rightarrow \infty} \frac{1}{c_\rho^2} R^2 \propto \rho^2.$$

This case includes the original version of the Walecka model [3] and generates the limiting behavior

$$\lim_{\rho \rightarrow \infty} p = \mathcal{E}. \quad (35)$$

The sums in Δp and $\Delta \mathcal{E}$ contribute to the leading order only if $j_{\max} = 2$, $k_{\max} \geq 2$ or $j_{\max} \geq 2$, $k_{\max} = 2$. In this case, the quadratic terms can be neglected, and Δp

and $\Delta\mathcal{E}$ are of the same order as the contributions from the ideal Fermi-gas terms. However, the factors in Eq. (34) conspire such that

$$\lim_{\rho \rightarrow \infty} \Delta p = \frac{1}{3} \Delta \mathcal{E}, \quad (36)$$

and the functional form of the limiting EOS resembles that of an ideal Fermi gas:

$$\lim_{\rho \rightarrow \infty} p = \frac{1}{3} \mathcal{E}. \quad (37)$$

In the remaining cases ($j_{\max} > 2, k_{\max} > 2$), the dominant contributions arise solely from p_0 and \mathcal{E}_0 , which also leads to Eq. (37). Note here the importance of Eq. (22), which implies that in the high-density limit, M^* becomes negligible, at least to leading order.

- (ii) At least one coupling between W and R . From Eqs (30) and (31), it follows directly that

$$\alpha \leq \frac{1}{3} \quad \text{and} \quad \beta \leq \frac{1}{3}.$$

The quadratic contributions in the fields are negligible, and Δp and $\Delta\mathcal{E}$ contribute to the leading term only if $\alpha = \beta = 1/3$, where again Eq. (36) holds. In any event, this leads to the limit of Eq. (37).

To summarize, we conclude that the high-density limit of the EOS is strongly influenced by nonlinear meson-meson interactions, which agrees with the conclusion of Bodmer and Price [9,19]. The limit in Eq. (35) obtained in the original version of the Walecka model [3] is a special case; in the more general situation, the nuclear matter EOS approaches that of an ideal Fermi gas, given by Eq. (37). We will show in the next section that these two limits can be achieved using different models with parameter sets that reproduce the same equilibrium properties of nuclear matter.

4. Consequences for neutron stars

The high-density limit of the EOS and the way in which the matter approaches the asymptotic regime have important consequences in neutron star calculations. The masses and radii of stars are sensitive to the stiffness of the EOS, thus providing a quantitative measure for studying the impact of the nonlinear interaction terms in Eq. (9).

To be specific, it is necessary to choose an explicit potential, and we begin with the form

$$\sum_{i,j,k} a_{ijk} \phi^i (V_\mu V^\mu)^j (\mathbf{b}_\mu \cdot \mathbf{b}^\mu)^k = -\frac{\kappa}{3!} \phi^3 - \frac{\lambda}{4!} \phi^4 + \frac{\zeta}{4!} g_v^4 (V_\mu V^\mu)^2 + \frac{\xi}{4!} g_\rho^4 (\mathbf{b}_\mu \cdot \mathbf{b}^\mu)^2, \quad (38)$$

which includes a subset of the meson self-interactions up to fourth order in the fields. As discussed in the Introduction, setting some of the allowed cubic and quartic couplings

Table 1
Equilibrium properties of nuclear matter

$(k_F)_0$ (fm $^{-1}$)	ρ_0 (fm $^{-3}$)	M_0^*/M	e_0 (MeV)	K_0 (MeV)	a_4 (MeV)
1.30	0.1484	0.60	-15.75	250	35

to zero is “unnatural”, but as we will discover, the model defined by Eq. (38) is already general enough to produce significant differences in predicted neutron star masses, and restoring the omitted couplings will lead to even more variation in the results. Moreover, the present model can be related to the most common models discussed in the literature, and it generalizes them to include a nonlinear isovector interaction. The motivation for adding the quartic rho-meson term is that one expects this coupling to be essentially unconstrained by normal nuclear observables, where the neutron–proton asymmetry is low, but it may have significant impact on the neutron-rich matter in neutron stars. As noted earlier, since the meson fields are effective (Kohn–Sham) potentials, we are not concerned here with their elementary excitations, and considerations of causality [33,34] are unimportant.

In nuclear matter calculations, this model contains seven free parameters. The polynomial in Eq. (38) contains four couplings that we may write as $\bar{\kappa} \equiv \kappa/g_s^3$, $\bar{\lambda} \equiv \lambda/g_s^4$, ζ and ξ ; in addition, values for the three ratios $c_i^2 = g_i^2/m_i^2$ ($i = s, v, \rho$) are needed. Five of the seven parameters can be chosen to reproduce the equilibrium properties of symmetric nuclear matter, which we take as the equilibrium density and binding energy (ρ_0 , $-e_0$), the nucleon effective (or Dirac) mass at equilibrium (M_0^*), the compression modulus (K_0) and the bulk symmetry energy (a_4). The first three of these are tightly constrained [11], whereas the latter two are not. In principle, the sensitivity of the high-density EOS to reasonable variations in K_0 and a_4 could be examined, but for simplicity, we keep their values fixed in most of our calculations. The “standard” set of equilibrium properties used here are listed in Table 1; these are motivated by successful descriptions of bulk and single-particle nuclear properties [11,44,21]. The nucleon mass is fixed at its empirical value ($M = 939$ MeV).

Our primary goal is to study the influence of the nonlinear vector-meson interactions on neutron star masses. Since there are more free couplings than normalization conditions, we proceed as follows: We choose values for the couplings ζ and ξ and determine the remaining couplings by requiring that they reproduce the desired equilibrium properties. This is achieved by solving a set of transcendental equations that relate the parameters directly to the nuclear matter properties [19,21]. Although we have no specific guidance on the allowed values of ζ and ξ , we rely on the assumption of naturalness, and based on the discussion at the end of Section 2, we observe that the following parameter combinations should all be of roughly equal size:

$$\frac{1}{2c_s^2 M^2}, \quad \frac{1}{2c_v^2 M^2}, \quad \frac{1}{8c_\rho^2 M^2}, \quad \frac{\bar{\kappa}}{6M}, \quad \frac{\bar{\lambda}}{24}, \quad \frac{\zeta}{24} \quad \text{and} \quad \frac{\xi}{384}.$$

Typical values for the first three parameters are between 0.001 and 0.002, so that the natural values of ζ and ξ are roughly limited to $0 \leq \zeta \lesssim 0.06$ and $0 \leq \xi \lesssim 1.5$. (To avoid abnormal solutions of the vector field equations, i.e., those with finite mean fields at zero density, ζ and ξ must be positive ⁴.) We will include results for vanishing ζ and ξ , which are in a strict sense unnatural, in order to make contact with earlier calculations. For a more thorough discussion of naturalness and its implications, see Ref. [21].

Using the notation of Section 2, the self-consistency equations (17)–(19) can be written as

$$\frac{1}{c_s^2} \Phi + \frac{\bar{\kappa}}{2} \Phi^2 + \frac{\bar{\lambda}}{6} \Phi^3 = \rho_s, \quad (39)$$

$$W \left(\frac{1}{c_v^2} + \frac{\zeta}{6} W^2 \right) = \rho, \quad (40)$$

$$R \left(\frac{1}{c_\rho^2} + \frac{\xi}{6} R^2 \right) = \frac{1}{2} \rho_3 = -\frac{1}{2} \rho. \quad (41)$$

The expressions for the pressure and the energy density follow as

$$p = \frac{1}{3\pi^2} \int_0^{k_F} dk \frac{k^4}{(k^2 + M^{*2})^{1/2}} + \frac{1}{2c_v^2} W^2 + \frac{\zeta}{24} W^4 + \frac{1}{2c_\rho^2} R^2 + \frac{\xi}{24} R^4 - \frac{1}{2c_s^2} \Phi^2 - \frac{\bar{\kappa}}{6} \Phi^3 - \frac{\bar{\lambda}}{24} \Phi^4, \quad (42)$$

$$\mathcal{E} = \frac{1}{\pi^2} \int_0^{k_F} dk k^2 (k^2 + M^{*2})^{1/2} + \frac{1}{2c_v^2} W^2 + \frac{\zeta}{8} W^4 + \frac{1}{2c_\rho^2} R^2 + \frac{\xi}{8} R^4 + \frac{1}{2c_s^2} \Phi^2 + \frac{\bar{\kappa}}{6} \Phi^3 + \frac{\bar{\lambda}}{24} \Phi^4. \quad (43)$$

We begin our discussion with the model introduced by Bodmer and Price [9], which corresponds to $\xi = 0$. According to the discussion in the preceding section, this model has the interesting feature that the high-density EOS of pure neutron matter approaches $p = \mathcal{E}$, while in symmetric matter, where the mean-field of the ρ meson vanishes, the EOS approaches the massless Fermi-gas limit, given by Eq. (37). In Fig. 1, we show the binding energy curves for symmetric and pure neutron matter for different values of the nonlinear coupling ζ . We emphasize that all parametrizations reproduce the same equilibrium properties listed in Table 1.

At low densities, all the curves approach a common limit, because the nonlinear terms do not contribute at leading order in a low-density expansion. At higher densities, the

⁴ Note that positive ζ and ξ imply that the resulting nonlinear interactions are *attractive*. This constraint on the highest-order vector interactions appears to be general and explains why our earlier analysis finds that nonlinear interactions soften the equation of state.

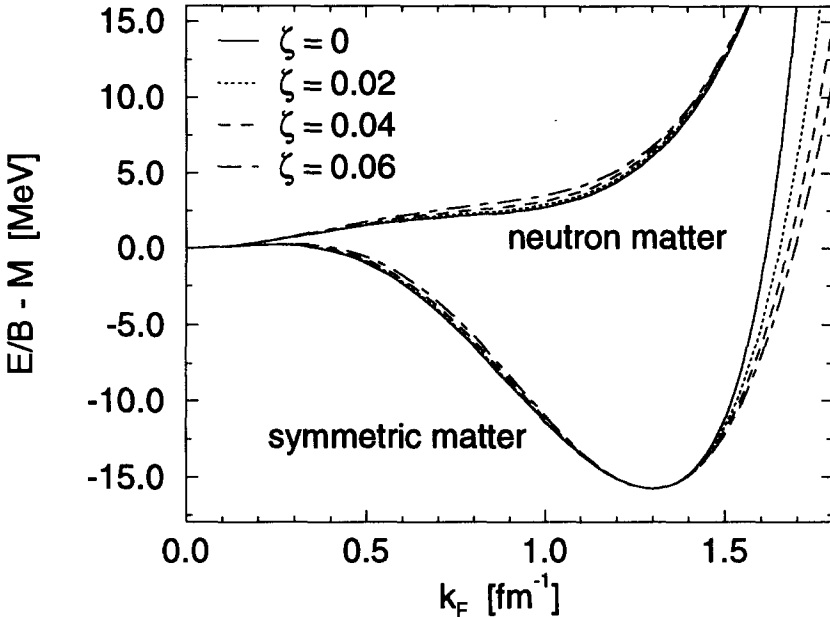


Fig. 1. Binding energy of symmetric and neutron matter.

softening of the EOS as ζ increases is clearly visible, at least for symmetric matter. The softening in neutron matter is more apparent in Fig. 2. In the regime of intermediate density, $200 \lesssim \mathcal{E} \lesssim 1000$ MeV/fm 3 , the EOS becomes softer with increasing values of ζ [19]. To study the approach to the asymptotic limit, we examine the nonleading terms in the high-density expansion:

$$\lim_{\mathcal{E} \rightarrow \infty} p = \mathcal{E} - \frac{1}{6\pi^2} \left(\frac{72\pi^4}{4c_v^2 + c_\rho^2} \right)^{2/3} \mathcal{E}^{2/3} + O(\mathcal{E}^{1/3}) \quad \text{for } \zeta = 0, \quad (44)$$

$$\lim_{\mathcal{E} \rightarrow \infty} p = \mathcal{E} - \frac{1}{6\pi^2} \left(\frac{72\pi^4}{c_\rho^2} \right)^{2/3} \left[1 + \left(\frac{2}{\pi^2 \zeta} \right)^{1/3} \right] \mathcal{E}^{2/3} + O(\mathcal{E}^{1/3}) \quad \text{for } \zeta \neq 0, \quad (45)$$

which reveals two important features. First, the $\zeta \neq 0$ results are *nonanalytic* in ζ . Thus one cannot reproduce Eq. (44) by taking the $\zeta \rightarrow 0$ limit of Eq. (45); at least as far as ζ is concerned, the high-density expansion is essentially a strong coupling expansion. Second, we observe that the coefficient of the nonleading term is smaller for $\zeta = 0$ for two reasons: the appearance of the isoscalar coupling c_v^2 in the denominator and the absence of the multiplicative factor containing ζ . (Note that c_ρ^2 is independent of ζ .) These two features produce a coefficient that is roughly an order of magnitude smaller for $\zeta = 0$ than for $\zeta \neq 0$, which explains the relatively slow approach to the asymptotic limit in the latter case, as is evident from Fig. 2.

The consequences for neutron stars can be studied in Fig. 3, where the star masses are shown as a function of the central mass density ρ_c . For a given value of ρ_c ,

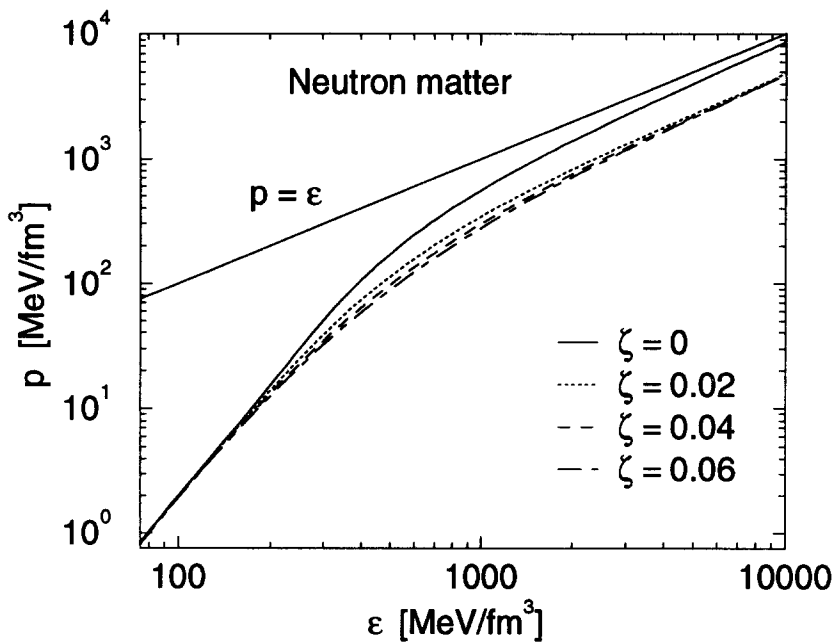
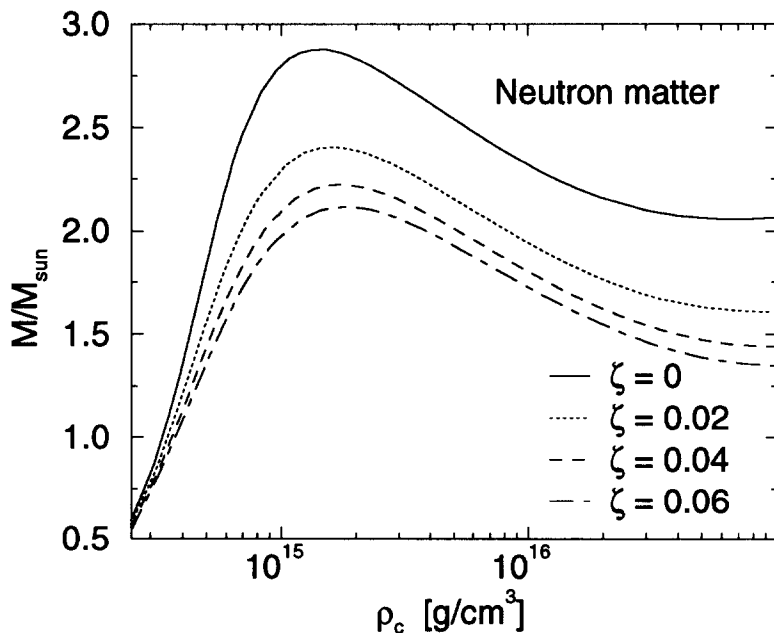


Fig. 2. Equation of state of neutron matter.

Fig. 3. Neutron star masses for different nonlinear couplings ζ . Pure neutron matter is assumed.

the mass is obtained by integrating the Tolman–Oppenheimer–Volkoff (TOV) equation, which follows from hydrostatic equilibrium in strong gravitational fields and the Einstein equations [48].

As expected from Fig. 2, the maximum mass decreases with increasing ζ . This decrease is substantial: from $M_{\max} = 2.9M_{\odot}$ for $\zeta = 0$ to $M_{\max} = 2.1M_{\odot}$ for $\zeta = 0.06$, which is roughly 30%. The shifts in the maximum mass are most dramatic for small couplings; for larger couplings, the softening effects begin to saturate.

To understand this result, it is useful to identify the regime of energy density that is most important in determining the mass of the star. This regime can be deduced from Fig. 4, where we show the radial mass density distributions for several neutron stars, as well as the corresponding energy densities. Observe that most of the mass is generated at radii between 6 and 12 km, which corresponds to energy densities of several hundred MeV/fm³. As can be seen from Fig. 2, this includes the regime where the EOS is sensitive to ζ , because this is where the W^4 contribution to the EOS begins to become important. Note, however, that the contribution of the W^4 term in this regime is still smaller than that of the W^2 term; the quartic term does not begin to dominate until the energy density reaches several thousand MeV/fm³, as indicated by the coalescence of the dashed and dotted curves in Fig. 2.

We now return to the general form in Eq. (38) and allow nonlinear self-interactions of the ρ meson. In contrast to the isoscalar coupling ζ , the new quantity ξ does not enter in the calculation of our five “standard” equilibrium properties of nuclear matter, and the other parameters are determined independently. This is true even for the symmetry energy, because the new coupling ξ first appears at order $(N - Z)^4$ in an expansion around symmetric nuclear matter. In principle, ξ could be constrained by fits to liquid-drop expansions of the energy, but in most such fits this parameter is set to zero. (We found only one nonzero value in the literature [49].) Thus, at present, contributions to the symmetry energy beyond terms of order $(N - Z)^2$ are practically unconstrained.

Fig. 5 shows the energy density of nuclear matter as a function of the proton fraction y for two different baryon densities. The curves are calculated for various values of ξ with ζ held fixed. For clarity, we plot the fractional shift in \mathcal{E} relative to its value with $\xi = 0$. At normal nuclear density, results for different ξ are virtually indistinguishable, but at high density, the curves differ by a few percent when the proton fraction becomes very small. This demonstrates that it is possible to generate families of models that reproduce identical properties of nuclear matter at low and normal densities, but which generate different predictions at high densities.

According to the analysis in the preceding section, the EOS asymptotically approaches the massless Fermi-gas limit for both symmetric and neutron matter. The high-density expansion for neutron matter corresponding to Eq. (45) is

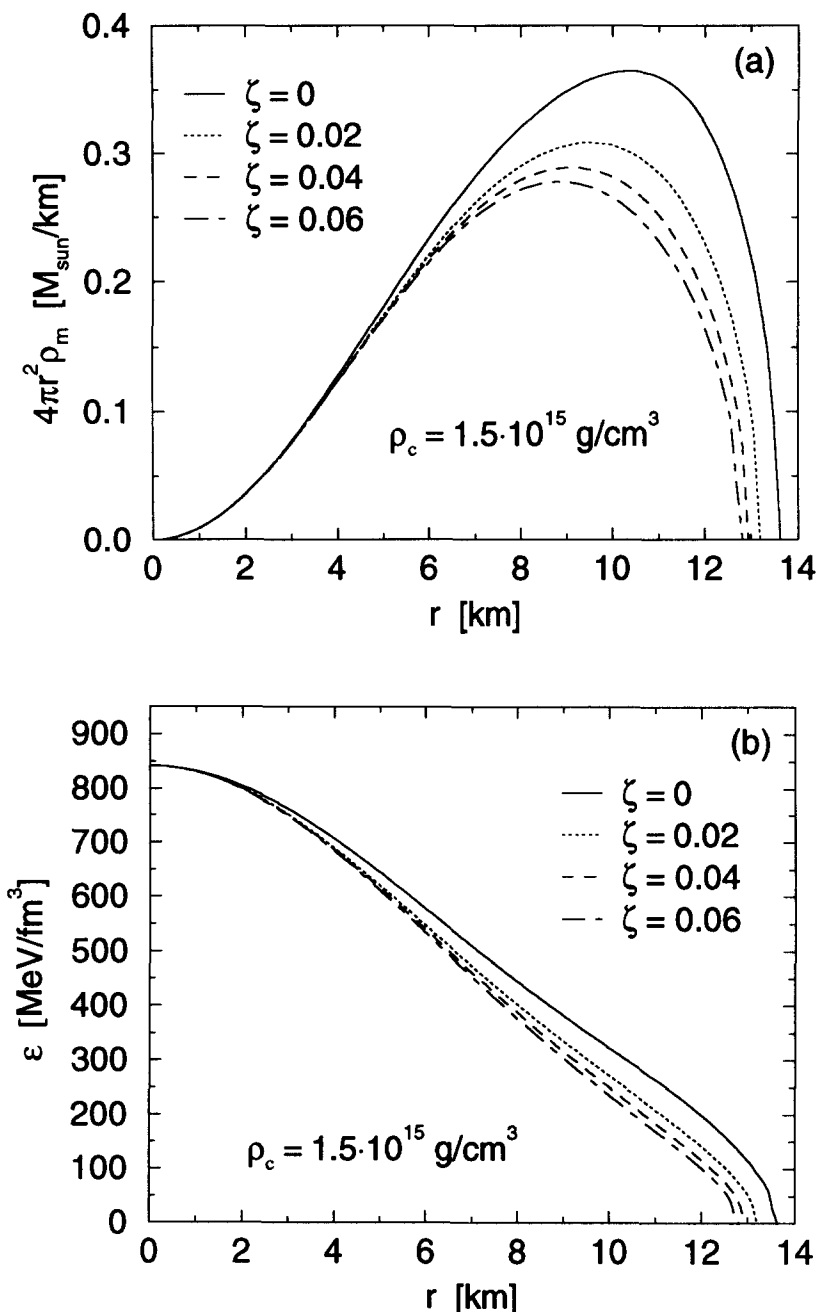


Fig. 4. Density distributions of neutron stars as a function of the radius, calculated with different parameters ζ . The central mass density $\rho_c = 1.5 \times 10^{15} \text{ g/cm}^3$ is the same for all curves. Part (a) shows the radial mass densities and part (b) the corresponding energy densities. The stars acquire most of their mass from the region $100 \lesssim \epsilon \lesssim 500 \text{ MeV/fm}^3$.

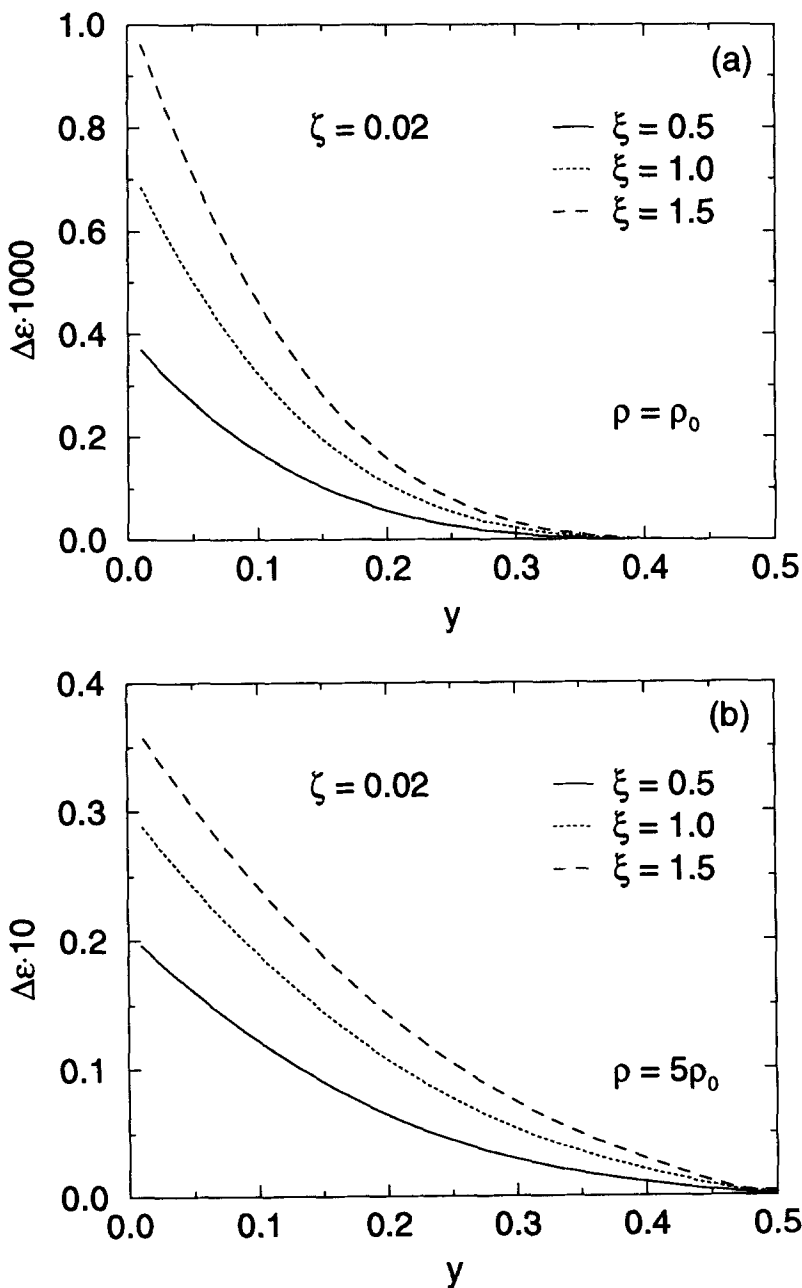


Fig. 5. Energy difference $\Delta\epsilon = [\mathcal{E}(\xi = 0) - \mathcal{E}(\xi)]/\mathcal{E}(\xi = 0)$ of nuclear matter as a function of the proton fraction y calculated at constant baryon density. In part (a) the density is fixed at its equilibrium value ρ_0 and part (b) shows the results at $5\rho_0$. Note the different vertical scales in (a) and (b).

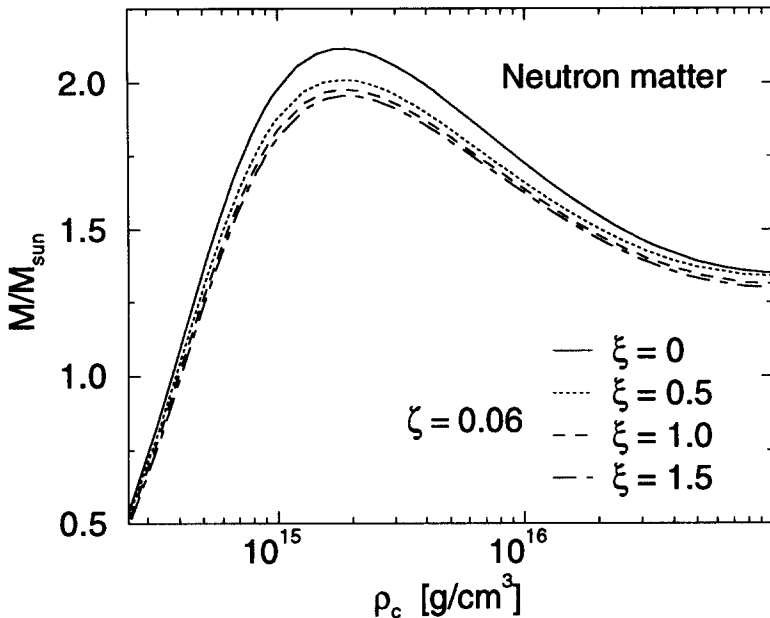


Fig. 6. Neutron star mass for different values of ξ at fixed ζ . Pure neutron matter is assumed.

$$\lim_{\mathcal{E} \rightarrow \infty} p = \frac{1}{3}\mathcal{E} + \frac{2\pi}{3} \frac{\left[\frac{1}{c_v^2} \left(\frac{2}{\pi^2 \zeta} \right)^{2/3} + \frac{1}{c_p^2} \left(\frac{1}{\pi^2 \xi} \right)^{2/3} \right]}{\left[1 + \left(\frac{2}{\pi^2 \zeta} \right)^{1/3} + \left(\frac{1}{\pi^2 \xi} \right)^{1/3} \right]^{1/2}} \mathcal{E}^{1/2} + O(\mathcal{E}^0) . \quad (46)$$

In contrast to the previous case, the asymptotic limit is now approached from above. Moreover, the analytical form has changed, since Eq. (46) indicates a series in powers of $\mathcal{E}^{1/2}$.

The dependence of the neutron star masses on ξ follows the same trend as found for ζ . This can be gleaned from Fig. 6, which shows results for pure neutron matter. For fixed ζ , the maximum mass decreases with increasing ξ , although the effect of this new parameter is smaller (less than a 10% change in the maximum mass), given the limitation on parameter values imposed by naturalness.

A more complete picture of M_{\max} is given in Fig. 7, where the variations with both ζ and ξ are shown. It is apparent that parameter sets that yield identical properties near nuclear equilibrium can still generate values of the maximum mass that differ by as much as one solar mass. We find variations between $M_{\max} = 2.9M_{\odot}$ and $1.9M_{\odot}$ for stars composed of pure neutron matter. The masses are most sensitive to changes at small values of the couplings, particularly for $\zeta \approx 0$, which can be related to the nonanalytic form of the EOS in terms of ζ and ξ . [See Eqs. (44)–(46).] As seen earlier, the effect of ξ is smaller than that of ζ .

So far, we have considered pure neutron matter, which gives only a qualitative picture of neutron star properties. For a more realistic description, it is necessary to consider

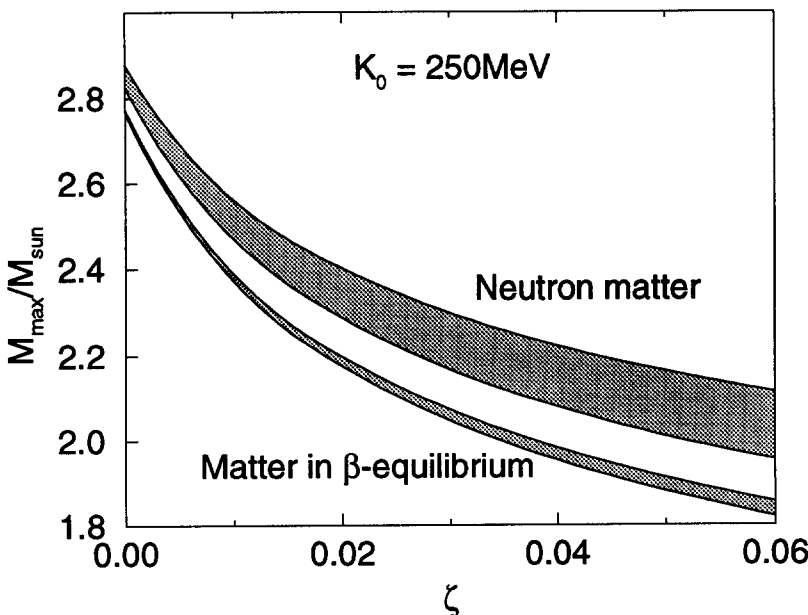


Fig. 7. Maximum neutron star mass as function of ζ and ξ . Results for pure neutron matter and for matter in β -equilibrium are displayed. The shaded areas show the mass range obtained when ξ is varied; the upper boundaries correspond to $\xi = 0$ and the lower boundaries to $\xi = 1.5$.

beta-stable matter, i.e., matter composed of neutrons, protons and electrons in beta-decay equilibrium. This situation was realized by adding the contribution of free, relativistic electrons to the nuclear EOS and by imposing the equilibrium condition

$$\mu_n = \mu_p + \mu_e .$$

The TOV equation is then integrated under the constraint of total charge neutrality. Maximum neutron star masses for beta-stable matter are also shown in Fig. 7. The dependence on the isoscalar coupling ζ is similar to that obtained earlier (the maximum mass varies between $M_{\max} = 2.8M_{\odot}$ and $1.8M_{\odot}$), but the influence of the isovector coupling ξ is less drastic, since the matter becomes significantly more symmetric in the region that gives the largest contribution to the mass.

In Fig. 8, we examine the dependence of the maximum mass on the compression modulus at equilibrium, which is not particularly well known. (Relativistic mean-field models with $200 \lesssim K_0 \lesssim 350$ MeV can produce accurate nuclear binding-energy systematics and surface energetics [21].) The shaded band shows the total predicted variation in maximum mass when both ζ and ξ are varied within the bounds imposed by naturalness. The dashed curve shows the predicted variation when K_0 is varied at fixed ζ and ξ . Evidently, the variations in the maximum mass arising from the possibility of nonlinear vector meson interactions is much greater than that arising from the uncertainty in the nuclear compressibility.

We also studied the dependence of the maximum mass on the ratio S/K_0 , where S

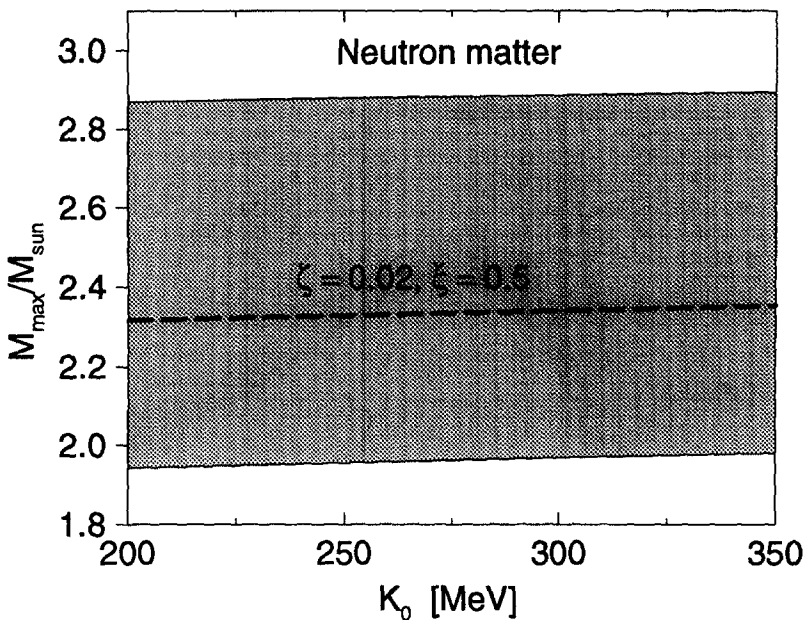


Fig. 8. Maximum neutron star mass as a function of the compression modulus K_0 . (All other nuclear matter inputs are held fixed.) The shaded area marks the covered range of masses. The upper boundary corresponds to $\zeta = 0$, $\xi = 0$ and the lower boundary to $\zeta = 0.06$, $\xi = 1.5$. For fixed values of the nonlinear couplings, the mass changes marginally with the compression modulus. This can be seen from the dashed line inside the shaded area, which corresponds to $\zeta = 0.02$, $\xi = 0.5$.

is the “skewness” defined by $S \equiv k_F^3 [d^3(\mathcal{E}/\rho)/dk_F^3]$ evaluated at equilibrium. Consider again Fig. 8. At $K_0 = 350$ MeV, S/K_0 varies by a factor of three (from 2.66 to 7.75) from the bottom to the top of the shaded region, indicating that this ratio could be correlated to the maximum mass. However, at $K_0 = 200$ MeV, there is a similar change in the maximum star mass, but S/K_0 varies by only 20% between the boundaries of the shaded region. Moreover, along the heavy dashed curve, there is a similar 10% variation in S/K_0 , but virtually no change in the maximum mass. We conclude that there is no strong correlation between S/K_0 and M_{\max} . This agrees with the results of Ref. [21], where little correlation was found between S/K_0 and the ground-state properties of finite nuclei.

These results raise the interesting question of whether the only significant nonlinearity is the quartic, isoscalar vector interaction. In other words, once one takes $\zeta \neq 0$ to soften the EOS at high densities, does the addition of further nonlinearities produce only small effects? To examine this question, we extend the model of Eq. (38) to include sixth-order and eighth-order terms involving the vector-isoscalar meson:

$$\Delta V' = -\frac{\zeta'}{6!} g_v^6 (V_\mu V^\mu)^3 - \frac{\zeta''}{8!} g_v^8 (V_\mu V^\mu)^4. \quad (47)$$

Thus $\zeta'/6!$ and $\zeta''/8!$ are the relevant ratios to be included in the parameter list given earlier, and we will initially set ξ to zero and examine the consequences of varying ζ ,

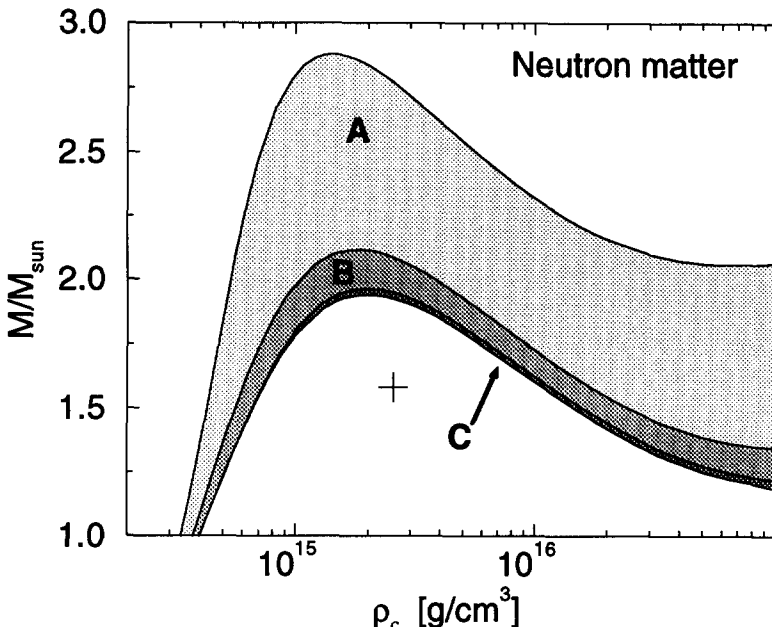


Fig. 9. Neutron star masses for models with different nonlinear couplings for the neutral vector meson. The uppermost curve corresponds to the Walecka model, including cubic and quartic couplings for the scalar meson. Region A shows the range of masses obtained when the quartic vector coupling is turned on. Regions A and B correspond to models with up to sixth-order terms, and regions A, B and C include an eighth-order term. The values of the nonlinear couplings are chosen within a natural range, as described in the text. The cross indicates the maximum mass ($1.58M_{\odot}$) obtained for beta-stable matter in a calculation that includes the ζ , ζ' , ζ'' and ξ couplings (see the text).

ζ' and ζ'' within the bounds imposed by naturalness.

Fig. 9 shows neutron star masses as higher-order vector nonlinearities are included sequentially. Evidently, the quartic interactions are the most important, producing a roughly 30% variation in the maximum. The effects of the sixth-order term are quite modest (roughly 10%), while the eighth-order contributions are essentially negligible (roughly 2%). Here the parameters are varied within the natural ranges $0 \leq \zeta \leq 0.06$, $0 \leq \zeta' \leq 1.2$ and $0 \leq \zeta'' \leq 60$. Thus we have the encouraging result that once the W^4 interaction has been accurately calibrated, contributions from higher-order nonlinearities are relatively unimportant. To indicate the most extreme reduction in maximum mass possible in the present model, the cross in Fig. 9 shows $M_{\max} = 1.58M_{\odot}$, which is obtained for *beta-stable matter* when the couplings $\zeta = 0.06$, $\zeta' = 1.2$, $\zeta'' = 60$ and $\xi = 1.5$ are included. Note that this value of M_{\max} is only slightly ($\approx 10\%$) larger than that of the most massive observed neutron stars.

Our analysis to this point has revealed significant model and parameter dependence in the high-density EOS. It is therefore of interest to see if these variations influence predictions arising from other relevant dynamics in systems with high densities. As an example, we study the effect of the high-density hadronic EOS on the existence of quark-matter cores in neutron stars. We adopt a simple two-phase model [37,1] based

on a first-order (Van der Waals) phase transition between the hadronic and quark phase. Although there are indications from QCD lattice calculations that the hadron–quark phase transition is second-order at vanishing chemical potential [50,51] (for massless quarks), the true behavior of the transition at finite density (and indeed, whether one actually exists) is unknown at present. Until more reliable information is available, one must resort to a separate description of the quark phase and the hadronic phase. Moreover, whereas a detailed description involving beta-stable matter requires a careful treatment of the phase transition in systems with two conserved charges (baryon number and isospin) [27,52], here we will be satisfied with a qualitative discussion based on pure neutron matter. This is certainly reasonable, given the large uncertainties we have already found in the hadronic EOS at high density.

We adopt the simple EOS involving massless u and d quarks given by

$$p = \frac{1}{3}\mathcal{E} - \frac{4}{3}b, \quad (48)$$

where the confinement property of QCD (or alternatively, the anomaly in the trace of the energy-momentum tensor) is modeled by a positive constant b , which represents the energy per unit volume in the vacuum.

We return to the hadronic model of Eq. (38), which leads to the high-density expansion in Eq. (46). Our discussion is based on the simple observation that independent of the actual nature of the transition, it is driven purely by the energetics in the two phases.

By comparing Eq. (48) with the expansion in Eq. (46), one observes that in the quark phase, the limit $p = \mathcal{E}/3$ is approached from below, whereas in neutron matter, for the general case $\zeta > 0$ and $\xi > 0$, the limit is approached from above. To decide whether a transition takes place, it is necessary to compare the energy/baryon in both phases. For the quark phase it is expressed as [37]

$$\mathcal{E}/\rho = \frac{3}{4}\pi^{2/3} f(\alpha_s)\rho^{1/3} + b/\rho, \quad (49)$$

with

$$f(\alpha_s) = (1 + 2^{4/3}) \left(1 + \frac{2\alpha_s}{3\pi} \right),$$

which includes the lowest-order contribution in α_s (the exchange energy). As discussed in the preceding section, in hadronic models that are characterized by Eqs. (44) and (45), the quadratic terms dominate at high densities, so that

$$\lim_{\mathcal{E} \rightarrow \infty} \mathcal{E}/\rho \propto \rho, \quad (50)$$

for $\zeta \geq 0$ and $\xi = 0$. This is also true if $\zeta = 0$ and $\xi \geq 0$. Thus, at sufficiently high densities, neutron matter always has higher energy compared to the quark phase [37], and the two phases can be connected by a Maxwell construction, which signals the transition from hadron to quark matter.

The situation is different in the general case $\zeta > 0$, $\xi > 0$. For the asymptotic form of the energy corresponding to Eq. (46), one obtains

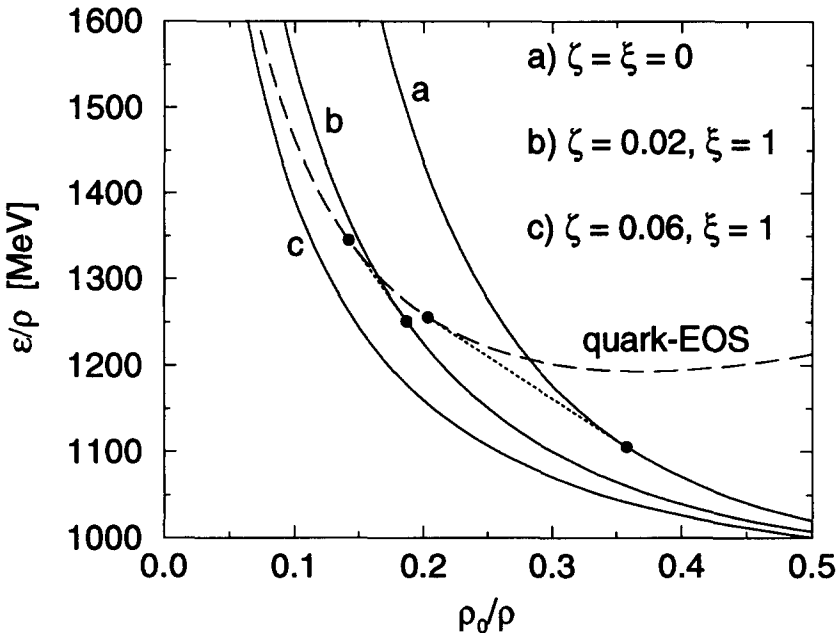


Fig. 10. Energy per baryon for neutron matter (solid) and quark matter (dashed). The quark matter results are calculated using $b = 120 \text{ MeV/fm}^3$ and $\alpha_s = 0.4$ [53].

$$\lim_{\varepsilon \rightarrow \infty} \varepsilon/\rho = \frac{3}{4} (3\pi^2)^{1/3} \left[1 + \left(\frac{2}{\pi^2 \zeta} \right)^{1/3} + \frac{1}{2} \left(\frac{1}{\pi^2 \xi} \right)^{1/3} \right] \rho^{1/3} + O(\rho^{-1/3}), \quad (51)$$

which is, up to the prefactor, the same leading behavior as in Eq. (49) for the quark phase. Therefore a phase transition is possible, i.e., neutron matter has higher energy, only if

$$3^{1/3} \left[1 + \left(\frac{2}{\pi^2 \zeta} \right)^{1/3} + \frac{1}{2} \left(\frac{1}{\pi^2 \xi} \right)^{1/3} \right] > f(\alpha_s). \quad (52)$$

This remarkable observation implies that for sufficiently large values of the nonlinear couplings, the matter remains in the hadron (neutron) phase, at least in the simple model discussed here. More generally, one observes that independent of the asymptotic form, increasing the couplings ζ and ξ increases the density at which the phase transition occurs (if it does), since the hadronic EOS becomes softer as the nonlinear couplings increase.

The different possibilities are illustrated in Fig. 10. The curve labeled *a* corresponds to Eq. (50); the asymptotic behavior is clearly different from the quark EOS. The phase transition occurs at roughly $3\rho_0$, and the Maxwell construction is indicated by the dotted line. In the situation described by curve *b*, neutron matter and quark matter have a similar asymptotic behavior, but the condition (52) remains true, and the two curves cross, leading to a phase transition at roughly $6\rho_0$. Finally, curve *c* lies completely below the quark EOS and a transition is not possible; neutron matter is stable at all densities.

If one introduces interaction terms of higher than fourth order in the fields, for example, $(V_\mu V^\mu)^3$, the hadronic energy is dominated by the Fermi-gas contribution, and Eq. (51) must be replaced by

$$\lim_{\mathcal{E} \rightarrow \infty} \mathcal{E}/\rho = \frac{3}{4}(3\pi^2)^{1/3}\rho^{1/3} + O(\rho^{-1/3}). \quad (53)$$

Since $3^{1/3} < f(\alpha_s)$, no transition is possible in the asymptotic regime for any choice of hadronic parameters in this case. On the other hand, the transition regime also depends on the model and parameters used for the description of the quark phase. In our model, the vacuum constant b and strong coupling α_s can be used to shift the transition point substantially [53,54], so that a transition may occur outside the asymptotic regime. It is clear, however, that the strong model dependence in the hadronic EOS introduces large uncertainties in any attempted prediction of these values.

The consequences for neutron stars in this model follow straightforwardly. Nonlinear vector meson interactions soften the hadronic EOS, which lowers the maximum neutron star mass and increases the density of the transition to quark matter. In contrast, a stiff hadronic EOS lowers the density of the phase transition, and since the quark matter EOS is soft, also tends to decrease the maximum star mass. Thus it may be impossible to decide, from neutron star masses alone, whether quark matter cores exist in neutron stars, and similar conclusions may be drawn about other exotic phenomena that soften the EOS. (The situation is complicated further by the continuous nature of the transition when two conserved charges are involved, which is the more physical case [27].) Whereas it might be possible, using the results of more advanced calculations of the finite-density hadron–quark phase transition, to rule out certain parametrizations of the hadronic EOS, existing uncertainties in both the nature of the phase transition and in the high-density hadronic EOS preclude any definite conclusions at this time.

5. Summary

In this paper we study the equation of state of nuclear and neutron-star matter based on relativistic mean-field theory. Our starting point is an effective action (or energy functional) containing Dirac nucleons and local scalar and vector fields. These fields are interpreted as relativistic Kohn–Sham potentials, and nonlinear interactions between the fields are introduced to parametrize the density dependence of the energy functional. We calibrate the energy functional by observing that at normal nuclear densities, the ratios of the mean fields to the nucleon mass are small, and thus the nonlinear interactions can be truncated at some low order in the fields. The unknown parameters can then be fit to properties of nuclear matter near equilibrium that are known to be characteristic of the observed bulk and single-particle properties of nuclei.

We then extrapolate the resulting equation of state into the neutron-rich, high-density regime to calculate the properties of neutron stars. Two problems arise in the extrapolation: First, even with a significant truncation of the energy functional, the unknown

parameters are underdetermined. Thus there exist families of parameters that reproduce exactly the same nuclear matter properties near equilibrium, but which produce potentially different high-density equations of state. Second, terms omitted from the functional because they are negligible at normal density may become important at densities relevant for neutron stars. This is true even if we assume that the coupling parameters are “natural”, which means that they are all of roughly the same size when expressed in appropriate dimensionless ratios.

Our basic goal is to determine, in light of these two problems, whether the calibration at equilibrium nuclear matter density is sufficient to predict a maximum neutron star mass within a reasonably small range. This is relevant in view of recent calculations that hope to see evidence for “new” physics in neutron stars (such as quark cores, strange matter or kaon condensates) based on the need for a softer high-density equation of state than that provided by neutrons, protons and electrons alone. These calculations assume that the high-density behavior of these more mundane components is well known, and in particular, that the contributions of many-nucleon forces are negligible [27–32]. These many-body, density-dependent forces are precisely the ones that are difficult to calibrate using observed nuclear properties; the question is whether one can build nuclear equations of state with different types of many-body forces that all reproduce the observed properties near equilibrium, but which yield significantly different results at high density.

By beginning with a meson self-interaction potential containing arbitrary powers of scalar-isoscalar (σ), vector-isoscalar (ω) and vector-isovector (ρ) fields, we show that the meson nonlinearities can have a profound effect on the high-density equation of state. In models where the vector mesons enter the potential at most quadratically, the equation of state is stiff and asymptotically approaches $p = \mathcal{E}$. (The Walecka model is a special case.) In models where the vector fields enter with high powers, these fields become negligible at high density, and the asymptotic equation of state resembles that of a free, relativistic gas: $p = \mathcal{E}/3$. The intermediate case occurs when the vector fields enter quartically; the asymptotic equation of state is still soft ($p = \mathcal{E}/3$), but the approach to the asymptotic limit is determined by the coupling parameters.

We illustrate these results using specific models containing quartic ω and ρ meson couplings and also sixth- and eighth-order ω couplings. All models are calibrated to exactly the same nuclear properties at equilibrium, for all choices of parameters. We find that by far the most important coupling constant is that of the quartic ω term; even when restricted by the requirements of naturalness, variations in this parameter can produce variations of nearly one solar mass in the predicted maximum neutron star mass. (This is true for both pure neutron matter and for beta-stable matter.) This uncertainty is clearly relevant on the scale on which one hopes to identify new, exotic effects. Moreover, increasing the strength of the quartic coupling softens the equation of state, which is precisely the effect sought from the exotica. The impact of a quartic ρ meson coupling is smaller, and its effects are only appreciable in stars made of pure neutron matter; the maximum masses of stars computed with beta-stable matter show little change when this parameter is varied within the bounds imposed by naturalness.

Similarly, sixth-order ω interactions have only a modest effect on the predicted maximum mass, and by the time the eighth-order terms are included, the high-density equation of state is already so soft that these terms are negligible.

We emphasize that the importance of these many-body effects is not limited to the domain of relativistic mean-field theories; equations of state based on nonrelativistic potentials [26] use interactions that are calibrated to few-body systems and that are insensitive to possible six- or eight-body forces that may be relevant at high density. This is especially important because a mean-field calculation with four-component spinors and just *two-body* Lorentz scalar forces already implicitly contains an infinite string of many-body forces if it is recast in terms of two-component spinors.

To illustrate these difficulties more concretely, we also study the role of the hadron-quark phase transition in a simple two-phase model with a first-order transition. We find that with couplings well within the bounds of naturalness, it is possible to push the phase transition to arbitrarily high density, and even to make it disappear altogether. Although the absence of a phase transition is probably unrealistic and could serve to exclude some values of the hadronic parameters, there are still too many uncertainties on both sides of the transition (as well as in the nature of the transition itself!) to make any definitive statements.

We therefore conclude that existing methods for calibrating the nuclear equation of state for extrapolation into the neutron-rich, high-density regime appropriate for neutron stars cannot constrain the predicted maximum star mass well enough to make reliable statements about the existence of “new” physics beyond the dynamics of neutrons, protons and electrons. We show that the uncertainties arising from an incomplete knowledge of the hadronic many-body forces are much larger than those arising from an imperfect knowledge of the properties of nuclear matter near equilibrium, such as the nuclear matter compression modulus. Even the old question of the role of the hadron-quark phase transition is problematic, since the high-density hadronic equation of state can be made essentially as soft as desired by the addition of nonlinear interactions that are still consistent with equilibrium nuclear matter properties.

One positive conclusion is that the most important nonlinear parameter is that of the quartic ω interaction. If this term could be accurately calibrated, the uncertainties introduced by other nonlinear interactions are likely to be tolerable. (One caveat: we do not study carefully the sensitivity to variations in mixed scalar–vector interactions because of the overwhelming sensitivity to the quartic ω term; if the latter were well constrained, the role of scalar–vector interactions should be examined in more detail.) Although this coupling has not been extensively studied in mean-field calculations, there are several possibilities for determining it reasonably well. First, since a quartic ω interaction leads to a nonlinear density dependence in the vector part of the baryon self-energy, one could calibrate this interaction by fitting to the self-energy obtained in a Dirac–Brueckner–Hartree–Fock calculation, for example. Although some initial attempts at this procedure have been made [20], the resulting parameters are not always natural; it is probably necessary to repeat the procedure using all possible scalar and vector self-interactions through fourth order and to fit both the scalar and vector part of the

self-energy simultaneously. Second, the nonlinearities in the energy functional can be interpreted in terms of effective masses for the vector and scalar mesons (defined by diagonalizing the matrix of appropriate second derivatives of the energy functional). This may provide useful constraints in the future, if concrete empirical information on these effective masses becomes available. Third, it is possible that additional observables in finite nuclei could constrain the nonlinear interactions. For example, some recent work suggests that the ratio of the nuclear matter “skewness” (which is related to the third derivative of the energy with respect to density at equilibrium) to the compression modulus K is constrained by monopole vibrations. Although a recent calculation of nuclear ground-state properties shows little correlation with this ratio [21], a more detailed examination of dynamical effects could provide meaningful constraints.

To summarize, precise predictions of the properties of neutron stars apparently require more accurate calibrations of the nuclear equation of state than are currently available. It is especially important to have the high-density behavior of the “standard” components (neutrons, protons and electrons) under control before one can make reliable statements about the existence of “new” physics. Since the window on experimentally observable nuclear properties is a narrow one, producing an equation of state that can be extrapolated with confidence remains a major challenge.

Acknowledgements

We thank R. J. Furnstahl and H.-B. Tang for useful comments. This work was supported in part by the Department of Energy under Contract No. DE-FG02-87ER40365.

References

- [1] B.D. Serot and J.D. Walecka, *Adv. Nucl. Phys.* 16 (1986) 1.
- [2] B.D. Serot, *Rep. Prog. Phys.* 55 (1992) 1855.
- [3] J.D. Walecka, *Ann. Phys. (N.Y.)* 83 (1974) 491.
- [4] J. Boguta and A.R. Bodmer, *Nucl. Phys. A* 292 (1977) 413.
- [5] B.D. Serot, *Phys. Lett. B* 86 (1979) 146; *B* 87 (1979) 403 (E).
- [6] P.G. Reinhard, M. Rufa, J. Maruhn, W. Greiner and J. Friedrich, *Z. Phys. A* 323 (1986) 13.
- [7] R.J. Furnstahl, C.E. Price and G.E. Walker, *Phys. Rev. C* 36 (1987) 2590.
- [8] R.J. Furnstahl and C.E. Price, *Phys. Rev. C* 40 (1989) 1398.
- [9] A.R. Bodmer and C.E. Price, *Nucl. Phys. A* 505 (1989) 123.
- [10] Y.K. Gambhir, P. Ring and A. Thimet, *Ann. Phys. (N.Y.)* 198 (1990) 132.
- [11] R.J. Furnstahl and B.D. Serot, *Phys. Rev. C* 47 (1993) 2338.
- [12] D.G. Boulware, *Ann. Phys. (N.Y.)* 56 (1970) 140.
- [13] S. Weinberg, *Phys. Rev.* 166 (1968) 1568; *Physica A* 96 (1979) 327.
- [14] R. Dashen and M. Weinstein, *Phys. Rev.* 183 (1969) 1261.
- [15] J. Gasser and H. Leutwyler, *Ann. Phys. (N.Y.)* 158 (1984) 142; *Nucl. Phys. B* 250 (1985) 465, 517, 539.
- [16] H. Leutwyler, *Ann. Phys. (N.Y.)* 235 (1994) 165.
- [17] J.L. Friar, D.G. Madland and B.W. Lynn, *Phys. Rev. C* 53 (1996) 3085.
- [18] R.J. Furnstahl, B.D. Serot and H.-B. Tang, in preparation.
- [19] A.R. Bodmer, *Nucl. Phys. A* 526 (1991) 703.

- [20] S. Gmuca, Z. Phys. A 342 (1992) 387; Nucl. Phys. A 547 (1992) 447.
- [21] R.J. Furnstahl, B.D. Serot and H.-B. Tang, Nucl. Phys. A 598 (1996) 539.
- [22] R.M. Dreizler and E.K.U. Gross, Density functional theory (Springer, Berlin, 1990).
- [23] C. Speicher, R.M. Dreizler and E. Engel, Ann. Phys. (N.Y.) 213 (1992) 312.
- [24] R.N. Schmid, E. Engel and R.M. Dreizler, Phys. Rev. C 52 (1995) 164.
- [25] W. Kohn and L.J. Sham, Phys. Rev. A 140 (1965) 1133.
- [26] B. Friedman and V.R. Pandharipande, Nucl. Phys. A 361 (1981) 502.
- [27] N.K. Glendenning, Phys. Rev. D 46 (1992) 1274.
- [28] T. Maruyama, H. Fujii, T. Muto, T. Tatsumi, Phys. Lett. B 337 (1994) 19.
- [29] R. Knorren, M. Prakash and P.J. Ellis, Phys. Rev. C 52 (1995) 3470.
- [30] M. Prakash, J. Cooke and J.M. Lattimer, Phys. Rev. D 52 (1995) 661.
- [31] M. Prakash, I. Bombaci, M. Prakash, P.J. Ellis, J.M. Lattimer and R. Knorren, Phys. Reports (in press).
- [32] H. Fujii, T. Maruyama, T. Moto and T. Tatsumi, Nucl. Phys. A 597 (1996) 645.
- [33] G. Velo and D. Zwanzinger, Phys. Rev. 188 (1969) 2218.
- [34] G. Velo, Nucl. Phys. B 65 (1973) 427.
- [35] V.I. Ogievetskij and I.V. Polubarinov, Ann. Phys. (N.Y.) 25 (1963) 358.
- [36] J.C. Collins and M.J. Perry, Phys. Rev. Lett. 34 (1975) 1353.
- [37] G. Baym and S.A. Chin, Phys. Lett. 62 B (1976) 241.
- [38] N.K. Glendenning, Ap. J. 293 (1985) 470; Nucl. Phys. A 493 (1989) 521.
- [39] J. Ellis, J.I. Kapusta and K.A. Olive, Nucl. Phys. B 348 (1991) 345.
- [40] H.D. Politzer and M.B. Wise, Phys. Lett. B 273 (1991) 156.
- [41] A.L. Fetter and J.D. Walecka, Quantum theory of many-particle systems (McGraw-Hill, New York, 1971).
- [42] C. Itzykson and J.B. Zuber, Quantum field theory (McGraw-Hill, New York, 1980) sec. 11–4–2.
- [43] J. Iliopoulos, C. Itzykson and A. Martin, Rev. Mod. Phys. 47 (1975) 165.
- [44] R.J. Furnstahl, H.-B. Tang and B.D. Serot, Phys. Rev. C 52 (1995) 1368.
- [45] C.J. Horowitz and B.D. Serot, Nucl. Phys. A 399 (1983) 529; A 464 (1987) 613; A 473 (1987) 760 (E).
- [46] H. Georgi, Weak interactions and modern particle theory (Benjamin/Cummings, Menlo Park, CA, 1984).
- [47] E.K. Heide, S. Rudaz and P.J. Ellis, Nucl. Phys. A 571 (1994) 713.
- [48] S. Weinberg, Gravitation and cosmology (Wiley, New York, 1972).
- [49] W.D. Myers and W.J. Swiatecki, Nucl. Phys. A 601 (1996) 141.
- [50] F.R. Brown, F.P. Butler, H. Chen, N.H. Christ, Z. Dong, W. Schaffer, L.I. Unger and A. Vaccarino, Phys. Rev. Lett. 65 (1990) 2491.
- [51] N.H. Christ, Nucl. Phys. A 544 (1992) 81c.
- [52] H. Müller and B.D. Serot, Phys. Rev. C 52 (1995) 2072.
- [53] B.D. Serot and H. Uechi, Ann. Phys. (N.Y.) 179 (1987) 272.
- [54] H.A. Bethe, G.E. Brown and J. Cooperstein, Nucl. Phys. A 462 (1987) 791.

New parametrization for the Lagrangian density of relativistic mean field theory

G. A. Lalazissis,^{1,2} J. König,¹ and P. Ring¹

¹Physik Department, Technische Universität München, D-85747 Garching, Germany

²Department of Theoretical Physics, Aristotle University of Thessaloniki, GR-54006 Thessaloniki, Greece

(Received 18 July 1996)

A new parametrization for an effective nonlinear Lagrangian density of relativistic mean field (RMF) theory is proposed, which is able to provide a very good description not only for the properties of stable nuclei but also for those far from the valley of beta stability. In addition the recently measured superdeformed minimum in the ¹⁹⁴Hg nucleus is reproduced with high accuracy. [S0556-2813(97)06101-3]

PACS number(s): 21.60.-n, 11.10.Ef, 21.10.-k, 21.30.Fe

Relativistic mean field (RMF) [1] theory has recently gained considerable success in describing various facets of nuclear structure properties. With a very limited number of parameters, RMF theory is able to give a quantitative description of ground-state properties of spherical and deformed nuclei [2,3] at and away from the stability line. Recently it has been shown that RMF theory is successful in reproducing the anomalous kink in the isotope shifts of Pb nuclei [4] and a first-ever microscopic description of anomalous isotopic shifts in Sr and Kr chains [5] has been provided. Such an anomalous behavior is a generic feature of deformed nuclei that include almost all isotopic chains in the rare-earth region [6] where RMF theory has been shown to have remarkable success. Moreover, good agreement with experimental data has been found recently for collective excitations such as giant resonances [7], and for twin bands in rotating superdeformed nuclei [8]. It is also noted that cranked RMF theory provides an excellent description of superdeformed rotational bands in the $A=140-150$ region [9], in the Sr region [10], and in the Hg region [11].

The starting point of RMF theory is a standard Lagrangian density [2]

$$\begin{aligned} \mathcal{L} = & \bar{\psi}(\gamma(i\partial - g_\omega \omega - g_\rho \vec{\rho} \cdot \vec{\tau} - eA) - m - g_\sigma \sigma)\psi + \frac{1}{2}(\partial\sigma)^2 \\ & - U(\sigma) - \frac{1}{4}\Omega_{\mu\nu}\Omega^{\mu\nu} + \frac{1}{2}m_\omega^2\omega^2 - \frac{1}{4}\vec{R}_{\mu\nu}\vec{R}^{\mu\nu} + \frac{1}{2}m_\rho^2\vec{\rho}^2 \\ & - \frac{1}{4}F_{\mu\nu}F^{\mu\nu}, \end{aligned} \quad (1)$$

which contains nucleons ψ with mass m ; σ , ω , ρ mesons; the electromagnetic field; and nonlinear self-interactions of the σ field,

$$U(\sigma) = \frac{1}{2}m_\sigma^2\sigma^2 + \frac{1}{3}g_2\sigma^3 + \frac{1}{4}g_3\sigma^4. \quad (2)$$

The Lagrangian parameters are usually obtained by a fitting procedure to some bulk properties of a set of spherical nuclei [12]. Among the existing parametrizations the most frequently used are NL1 [13], NL-SH [14], and the parameter set PL-40 [15], which has been proved to provide reasonable fission barriers. NL1 and NL-SH sets give good results in most of the cases. Along the beta stability line NL1 gives very good results for binding energies and charge radii; in addition it provides a reliable description of the superdeformed bands [9,11]. However, in going away from the stability line the results are less satisfactory. This can be partly

attributed to the large asymmetry energy $J=44$ MeV predicted by this force. In addition, the calculated neutron skin thickness shows systematic deviations from the experimental values for the set NL1 [13]. In the parameter set NL-SH this problem was treated in a better way and improved isovector properties have been obtained with an asymmetry energy of $J=36$ MeV. Moreover, NL-SH seems to describe the deformation properties in a better way than NL1. However, the NL-SH parametrization produces a slight overbinding along the line of beta stability and in addition it fails to reproduce successfully the superdeformed minima in Hg isotopes and in the actinides. A remarkable difference between the two parametrizations are the quite different values predicted for the nuclear matter incompressibility. NL1 predicts a small value ($K=212$ MeV) while with NL-SH a very large value ($K=355$ MeV) is obtained. Both forces fail to reproduce the experimental values for the isoscalar giant monopole resonances for Pb and Zr nuclei. The NL1 parametrization underestimates the empirical data, while NL-SH overestimates it.

The aim of the present investigation is to provide a new improved set of Lagrangian parameters, which to some extent cures the deficiencies of the existing parametrizations. For this reason a multiparameter fit was performed in the same way as with the other parametrizations [12,14]. The nucleon mass was fixed to 939 MeV. The Lagrangian parameters are the meson masses m_σ , m_ω , m_ρ , the corresponding coupling constants g_σ , g_ω , g_ρ and the parameters g_2 , g_3 of the nonlinear potential $U(\sigma)$. Apart from the mass of the ρ meson, which was fixed to the empirical value (763 MeV), all the others were taken as free parameters. The nuclear properties fitted are the charge radii, the binding energies, and the available neutron radii of several spherical nuclei. The experimental input for finite nuclei used in the fitting procedure is shown in Table I in parentheses. We recall that for the determination of NL-SH parameters six nuclei were used in the fit, namely ¹⁶O, ⁴⁰Ca, ⁹⁰Zr, ¹¹⁶Sn, ¹²⁴Sn, and ²⁰⁸Pb while for NL1 ⁴⁸Ca and ⁵⁸Ni were also taken into account. It is noted that for NL1 the experimental information used was the total binding energies, the diffraction radii, and the surface thickness. For NL-SH charge radii and neutron radii were used instead of the diffraction radii and the surface thickness. In the present work the number of nuclei used in the fit was increased to ten. In order to take into account a larger variation in isospin, in addition to the eight

TABLE I. The total binding energies charge radii, and neutron radii used in the fit (values in parentheses) together with the NL3 predictions.

Nucleus	BE (MeV)	r_{ch} (fm)	r_n (fm)
^{16}O	-128.83 (-127.62)	2.730 (2.730)	2.580
^{40}Ca	-342.02 (-342.06)	3.469 (3.450)	3.328 (3.370)
^{48}Ca	-415.15 (-416.00)	3.470 (3.451)	3.603 (3.625)
^{58}Ni	-503.15 (-506.50)	3.740 (3.769)	3.740 (3.700)
^{90}Zr	-782.63 (-783.90)	4.287 (4.258)	4.306 (4.289)
^{116}Sn	-987.67 (-988.69)	4.611 (4.627)	4.735 (4.692)
^{124}Sn	-1050.18 (-1049.97)	4.661 (4.677)	4.900 (4.851)
^{132}Sn	-1105.44 (-1102.90)	4.709	4.985
^{208}Pb	-1639.54 (-1636.47)	5.520 (5.503)	5.741 (5.593)
^{214}Pb	-1661.62 (-1663.30)	5.581 (5.558)	5.855

nuclei, used for NL1 the doubly closed shell nucleus ^{132}Sn as well as the heavier lead isotope ^{214}Pb were also included in the fit. The experimental values for the total binding energies were taken from the experimental mass tables [16], the charge radii from Ref. [17]. The available neutron radii are from Ref. [18]. In the case of open shell nuclei pairing was considered in the BCS formalism. The gap parameters $\Delta_{n(p)}$ were determined from the observed odd-even mass differences [16]. Specifically, for ^{58}Ni , $\Delta_n=1.4$ MeV, for ^{90}Zr , $\Delta_p=1.12$ MeV, for the two Sn isotopes ($A=116,124$) the Δ_n values are 1.17 and 1.32 MeV, respectively, and finally for ^{214}Pb , $\Delta_n=0.7$ MeV. The binding energies and charge radii were taken within an accuracy of 0.1% and 0.2%, respectively. For the neutron radii, however, due to existing uncertainties the experimental error taken into account was 2%. In addition in the fitting procedure some nuclear matter properties were also considered. As “experimental input” the following values were used: $E/A=-16.0$ MeV (5%), $\rho=0.153$ fm $^{-3}$ (10%), $K=250$ (MeV) (10%), $J=33$ MeV (10%). The values in parentheses correspond to the error bars used in the fit.

In Table I we list the predictions of NL3 for the ground-state properties of the nuclei used in the fit. It is seen that they are in very good agreement with the empirical values.

In Table II we show the values for the new parameter set. Adopting the convention introduced by Reinhard [12,13,15] for the nonlinear parametrizations the set is named NL3.

In order to check the influence of the nuclear matter “data” on the final results of the fit, we have also performed a fitting procedure using as the only input the experimental data of finite nuclei. The resulting parameters (NL3-II) are also shown in Table II together with the corresponding nuclear matter properties. Comparing the values of the two parameter sets one can easily see that they differ very little. The same holds for the nuclear matter properties. This suggests that one does not have to take into account nuclear matter “experimental input,” as long as one considers data from a sufficiently large set of finite nuclei. The contributions of the nuclear matter data to the χ^2 are small. The total χ^2 divided by the number of parameters for NL3 is 20.6, while for NL3-II it is 26.9. Because of the slightly better quality of the fit for NL3 we adopt this force in the follow-

TABLE II. Parameters of the Lagrangian NL3, NL3-II, NL1, and NL-SH together with the nuclear matter properties obtained with these effective forces.

	NL3	NL3-II	NL1	NL-SH
M (MeV)	939	939	938	939
m_σ (MeV)	508.194	507.680	492.250	526.059
m_ω (MeV)	782.501	781.869	783.000	783.000
m_ρ (MeV)	763.000	763.000	763.000	763.000
g_σ	10.217	10.202	10.138	10.4444
g_ω	12.868	12.854	13.285	12.945
g_ρ	4.474	4.480	4.976	4.383
g_2 (fm $^{-1}$)	-10.431	-10.391	-12.172	-6.9099
g_3	-28.885	-28.939	-36.265	-15.8337
Nuclear matter properties				
ρ_0 (fm $^{-3}$)	0.148	0.149	0.153	0.146
$(E/A)_\infty$ (MeV)	16.299	16.280	16.488	16.346
K (MeV)	271.76	272.15	211.29	355.36
J (MeV)	37.4	37.7	43.7	36.1
m^*/m	0.60	0.59	0.57	0.60

ing. For the sake of comparison the NL1 and the NL-SH parametrizations are also listed in Table II together with their nuclear matter properties.

In the following we present some applications of the new parameter set NL3 using the various RMF codes developed by the Munich group. We performed detailed calculations for the chain of Sn isotopes solving the relativistic Hartree-Bogoliubov (RHB) equations [19,20].

$$\begin{pmatrix} h & \Delta \\ -\Delta^* & -h^* \end{pmatrix} \begin{pmatrix} U \\ V \end{pmatrix}_k = E_k \begin{pmatrix} U \\ V \end{pmatrix}_k, \quad (3)$$

E_k are quasiparticle energies and the coefficients U_k and V_k are four-dimensional Dirac spinors normalized in the following way:

$$\int U_k^+ U_{k'} + V_k^+ V_{k'} d^3 r = \delta_{kk'}, \quad (4)$$

h is the Dirac operator

$$h = \alpha p + g_\omega \omega + \beta (M + g_\sigma \sigma) - \lambda, \quad (5)$$

where σ and ω are the meson fields determined self-consistently from the Klein Gordon equations:

$$\{-\Delta + m_\sigma^2\} \sigma = -g_\sigma \rho_s - g_2 \sigma^2 - g_3 \sigma^3, \quad (6)$$

$$\{-\Delta + m_\omega^2\} \omega = g_\omega \rho_B \quad (7)$$

with the scalar density ρ_s and the baryon density ρ_B ,

$$\rho_s = \sum_k \bar{V}_k V_k, \quad \rho_B = \sum_k V_k^+ V_k, \quad (8)$$

where the sum over k runs only over all the particle states in the *no-sea approximation*.

The pairing potential Δ in Eq. (3) is given by

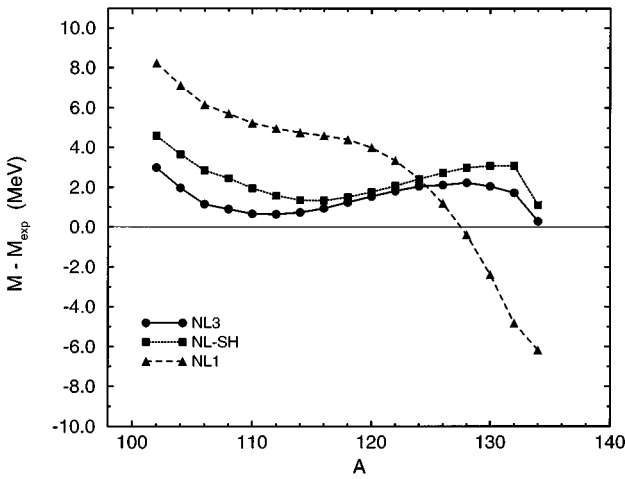


FIG. 1. The deviation of the theoretical masses of Sn isotopes, calculated in RMF with NL1, NL-SH, and NL3, from the experimental values.

$$\Delta_{ab} = \frac{1}{2} \sum_{cd} V_{abcd}^{pp} \kappa_{cd} \quad (9)$$

It is obtained from the pairing tensor $\kappa = U^* V^T$ and the effective interaction V_{abcd}^{pp} in the pp channel. More details are given in Ref. [19]. Since Walecka forces are not able to reproduce even in a semiquantitative way proper pairing in the realistic nuclear many-body problem, we replace V_{abcd}^{pp} in Eq. (9) by a two-body force of finite range of Gogny type,

$$V^{pp}(1,2) = \sum_{i=1,2} e^{-(r_1 - r_2 / \mu_i)^2} (W_i + B_i P^\sigma - H_i P^\tau - M_i P^\sigma P^\tau), \quad (10)$$

with the parameters μ_i , W_i , B_i , H_i , and M_i ($i=1,2$) taken from the Gogny parametrization D1S [21]. In fact this replacement does not violate the variational principle, because we could have obtained identical equations by just subtracting a pairing energy of the form

$$E_{\text{pair}} = \frac{1}{4} \sum_{abcd} \kappa_{ab}^* V_{abcd}^{pp} \kappa_{cd} \quad (11)$$

from the Lagrangian (1) and using standard variational techniques for HFB equations as they are discussed for instance in Chap. 7 of Ref. [22].

In Fig. 1 we show the isotopic dependence of the deviation of the theoretical mass calculated in RMF theory from the experimental values [16] for Sn nuclei. The theoretical results were obtained using the parameter sets NL1, NL-SH, and NL3. It is seen that all parametrizations give a very good description of the experimental masses. It is also seen, however, that the new force NL3 is able to provide improved results over the NL1 and NL-SH, reducing the rms deviation of the masses.

Axially symmetric calculations using a code in the oscillator basis [23] have been performed for some well-deformed rare-earth and actinide nuclei. Here, the pairing correlations are taken into account within the BCS formalism. The pairing parameters $\Delta_{n(p)}$ were taken from Tables XI and XIII of

TABLE III. Total binding energies (BE) (in MeV), charge radii r_c (in fm), quadrupole deformation parameters β_2 , proton quadrupole moments Q_p (in barns), and proton hexadecupole (H_p) moments (in barns²) for some deformed rare-earth and actinide nuclei with the parametrization NL3. The values in parentheses correspond to the empirical data. For details see the text.

A	BE	r_c	β_2	Q_p	H_p
^{152}Sm					
	-1294.49 (-1294.05)	5.177 (5.099)	0.301 (0.306)	5.63 (5.78)	0.48 (0.46(2))
^{158}Gd	-1296.40 (-1295.90)	5.176 (5.172)	0.342 (0.348)	7.14 (7.36)	0.48 (0.39(9))
^{162}Dy	-1324.09 (-1324.11)	5.227 (5.210)	0.347 (0.341)	7.54 (7.36)	0.45 (0.27(10))
^{166}Er	-1351.06 (-1351.57)	5.272 (5.303)	0.349 (0.342)	7.87 (7.70)	0.36 (0.32(16))
^{174}Yb	-1406.15 (-1406.60)	5.336 (5.410)	0.328 (0.325)	7.77 (7.58)	0.04 (0.22 ^{+0.14} _{-0.18})
^{232}Th					
	-1766.29 (-1766.69)	5.825 (5.790)	0.251 (0.261)	9.23 (9.62)	1.06 (1.22)
^{236}U	-1790.67 (-1790.42)	5.873 (0.282)	0.275 (0.282)	10.60 (10.80)	1.16 (1.30)
^{238}U	-1801.39 (-1801.69)	5.892 (5.854)	0.283 (0.286)	10.93 (11.12)	1.07 (1.38)

Ref. [2]. In Table III we give the results of our calculations together with the experimental information whenever available. It is seen that NL3 gives excellent results for the ground-state properties of rare-earth and actinide nuclei. The experimental masses [16] are reproduced within an accuracy of less than one MeV. The charge radii are in very good agreement with the experiment [17]. The deformation properties are also in excellent agreement with the empirical values. The absolute values of the empirical β_2 were obtained from the compilation of Raman *et al.* [24]. The experimental data for the hexadecupole moments of rare-earth nuclei are from a very recent compilation by Löbner [25]. Finally the experimental data for the proton quadrupole moments were taken from Tables XII and XIV or Ref [2].

Next we report some preliminary results for the giant monopole breathing energies of ^{208}Pb and ^{90}Zr nuclei obtained from relativistic generator coordinate (GCM) calculations based on constrained RMF wave functions. A detailed study including also dynamic RMF calculations will appear in a forthcoming publication [26]. In Table IV we show results of calculations using the new parameter set NL3 and compare it with experimental results and calculations obtained from the sets NL-SH and NL1. It is seen that NL3 is able to reproduce nicely the experimental values while the other two forces fail, either underestimating (NL1) or over-

TABLE IV. Isoscalar giant monopole energies in MeV calculated with the effective interactions NL3, NL1, NL-SH along with the empirical values.

<i>A</i>	Expt.	NL3	NL1	NL-SH
^{208}Pb	13.8 ± 0.5	13.0	11.0	15.0
^{90}Zr	16.2 ± 0.5	16.9	14.1	19.5

estimating (NL-SH), the experiment by almost 2 MeV. This is an indication that NL3 has a correct value for the nuclear incompressibility.

Recently, the excitation energy between the ground-state band and the superdeformed band in ^{194}Hg was measured for the first time [27]. Extrapolating to zero angular momentum the superdeformed minimum was found to be 6.02 MeV above the ground state. Performing RMF calculations with the parameter set NL3 and mapping the energy surface by a quadratic constraint we found the superdeformed minimum at an excitation energy of 5.99 MeV above the ground state.

The parameter set NL1 gives also a satisfactory value, namely (5.62 MeV). A detailed study will be published elsewhere [28].

In conclusion, our calculations with the new RMF parameterization NL3 give very good results in all cases considered so far. It is in excellent agreement with experimental nuclear masses, as well as the deformation properties. Moreover the RMF parametrization reproduces the isoscalar monopole energies in rather different regions of the periodic table such as Pb and Zr nuclei. This is very satisfactory and gives us confidence that NL3 can be used successfully also in future investigations.

One of the authors (G.A.L) acknowledges support by the European Union under Contract No. TMR-EU/ERB FMBCICT-950216. This work is also supported in part by the Bundesministerium für Bildung und Forschung under the project 06 TM 743 (6). We thank Professor K.E.G. Löbner for supplying us with his compilation on hexadecupole moments prior to its publication.

-
- [1] B. D. Serot and J. D. Walecka, *Adv. Nucl. Phys.* **16**, 1 (1986).
 - [2] Y. K. Gambhir, P. Ring, and A. Thimet, *Ann. Phys. (N.Y.)* **198**, 132 (1990).
 - [3] P. Ring, *Prog. Part. Nucl. Phys.* **37**, 193 (1996).
 - [4] M. M. Sharma, G. A. Lalazissis, and P. Ring, *Phys. Lett. B* **317**, 9 (1993).
 - [5] G. A. Lalazissis and M. M. Sharma, *Nucl. Phys.* **A586**, 201 (1995).
 - [6] G. Lalazissis, M. M. Sharma, and P. Ring, *Nucl. Phys.* **A597**, 35 (1996).
 - [7] D. Vretenar, H. Berghammer, and P. Ring, *Nucl. Phys.* **A581**, 679 (1994).
 - [8] J. König and P. Ring, *Phys. Rev. Lett.* **71**, 3079 (1993).
 - [9] A. V. Afanasjev, J. König, and P. Ring, *Nucl. Phys.* **A608**, 107 (1996).
 - [10] A. V. Afanasjev, J. König, and P. Ring, *Phys. Lett. B* **367**, 11 (1996).
 - [11] J. König and P. Ring, Technical University Munich report, 1996.
 - [12] P.-G. Reinhard, *Rep. Prog. Phys.* **52**, 439 (1989).
 - [13] P. G. Reinhard, M. Rufa, J. Maruhn, W. Greiner, and J. Friedrich, *Z. Phys. A* **323**, 13 (1986).
 - [14] M. M. Sharma, M. A. Nagarajan, and P. Ring, *Phys. Lett. B* **312**, 377 (1993).
 - [15] P.-G. Reinhard, *Z. Phys. A* **329**, 257 (1988); M. Sharma and P. Ring, *Phys. Rev. C* **45**, 2514 (1992).
 - [16] G. Audi and A. H. Wapstra, *Nucl. Phys.* **A565**, 1 (1993).
 - [17] H. de Vries, C. W. de Jager, and C. de Vries, *At. Data Nucl. Data Tables* **36**, 495 (1987).
 - [18] C. J. Batty, E. Friedman, H. J. Gils, and H. Rebel, *Adv. Nucl. Phys.* **19**, 1 (1989).
 - [19] H. Kucharek and P. Ring, *Z. Phys. A* **339**, 23 (1991).
 - [20] T. Gonzalez-Llarenar, J. L. Egido, G. A. Lalazissis, and P. Ring, *Phys. Lett. B* **379**, 13 (1996).
 - [21] J. F. Berger, M. Girod, and D. Gogny, *Nucl. Phys.* **A428**, 32c (1984).
 - [22] P. Ring and P. Schuck, *The Nuclear Many-body Problem* (Springer-Verlag, Heidelberg, 1980).
 - [23] P. Ring, Y. K. Gambhir, and G. A. Lalazissis, *Comput. Phys. Commun.* (to be published)
 - [24] S. Raman, C. H. Malarkey, W. T. Milner, C. W. Nestor, and P. H. Stelson, *At. Data Nucl. Data Tables* **36**, 1 (1987).
 - [25] K. E. G. Löbner (private communication).
 - [26] D. Vretenar *et al.* (to be published).
 - [27] T. L. Khoo *et al.*, *Phys. Rev. Lett.* **76**, 1583 (1996).
 - [28] G. A. Lalazissis *et al.* (to be published).

Neutron radii of ^{208}Pb and neutron stars

C. J. Horowitz

Nuclear Theory Center and Department of Physics, Indiana University, Bloomington, Indiana 47405

J. Piekarewicz

Department of Physics, Florida State University, Tallahassee, Florida 32306

(Received 14 August 2001; published 20 November 2001)

A new relation between the neutron skin of a heavy nucleus and the radius of a neutron star is proposed: the larger the neutron skin of the nucleus the larger the radius of the star. Relativistic models that reproduce a variety of ground-state observables cannot determine uniquely the neutron skin of a heavy nucleus. Thus, a large range of neutron skins is generated by supplementing the models with nonlinear couplings between isoscalar and isovector mesons. We illustrate how the correlation between the neutron skin and the radius of the star can be used to place important constraints on the equation of state and how it may help elucidate the existence of a phase transition in the interior of the neutron star.

DOI: 10.1103/PhysRevC.64.062802

PACS number(s): 26.60.+c, 21.10.Gv

What determines the size of a neutron star? For spherical, static stars in hydrostatic equilibrium, the so-called Schwarzschild stars, the sole feature responsible for their size is the equation of state of neutron-rich matter. The skin of a heavy nucleus—a system 18 orders of magnitude smaller and 55 orders of magnitudes lighter than a neutron star—is also composed of neutron-rich matter, although at a lower density.

In a recent publication we studied the relation between the neutron skin of ^{208}Pb and the nonuniform solid crust of a neutron star [1]. For models with a stiff equation of state it is energetically unfavorable to separate uniform nuclear matter into regions of high and low densities. Thus models with a stiff equation of state predict low transition densities from nonuniform to uniform neutron-rich matter and consequently thinner crusts. The thickness of the neutron skin in ^{208}Pb also depends on the equation of state of neutron-rich matter. The stiffer the equation of state the thicker the neutron skin. Thus, an inverse relationship was established: the thicker the neutron skin of a heavy nucleus the lower the transition from nonuniform to uniform neutron-rich matter.

In this work we study the relation between the neutron skin of a heavy nucleus and the radius of a neutron star. Indeed, we will show that models with thicker neutron skins produce neutron stars with larger radii. Such a study is particularly timely as it complements important advances in both experimental physics and observational astronomy. Indeed, a proposal now exists at the Jefferson Laboratory to measure the neutron radius of ^{208}Pb via parity-violating electron scattering [2,3]. Moreover, a number of improved radii measurements on isolated neutron stars, such as Geminga [4], RX J185635-3754 [5–7], Vela [8,9], and CXOU 132619.7-472910.8 [10] are now available. While these measurements are not yet accurate enough to set stringent limits on the equation of state, they represent an important first step in that direction [11].

Our starting point will be the relativistic effective-field theory of Ref. [12] supplemented with new couplings between the isoscalar and the isovector mesons. The interacting Lagrangian density for this model is given by [1,12]

$$\begin{aligned} \mathcal{L}_{\text{int}} = & \bar{\psi} \left[g_s \phi - \left(g_v V_\mu + \frac{g_\rho}{2} \boldsymbol{\tau} \cdot \mathbf{b}_\mu + \frac{e}{2} (1 + \tau_3) A_\mu \right) \gamma^\mu \right] \psi \\ & - \frac{\kappa}{3!} (g_s \phi)^3 - \frac{\lambda}{4!} (g_s \phi)^4 + \frac{\zeta}{4!} g_v^4 (V_\mu V^\mu)^2 \\ & + g_\rho^2 \mathbf{b}_\mu \cdot \mathbf{b}^\mu [\Lambda_s g_s^2 \phi^2 + \Lambda_v g_v^2 V_\mu V^\mu]. \end{aligned} \quad (1)$$

The model contains an isodoublet nucleon field (ψ) interacting via the exchange of two isoscalar mesons, the scalar sigma (ϕ) and the vector omega (V^μ), one isovector meson, the rho (\mathbf{b}^μ), and the photon (A^μ). In addition to meson-nucleon interactions the Lagrangian density includes scalar and vector self-interactions. (Note that while the original model allows for ρ -meson self-interactions [12], their phenomenological impact has been documented to be small so they will not be considered in this contribution.) The scalar self-interaction is responsible for reducing the compression modulus of nuclear matter from the unrealistically large value of $K=545$ MeV [13,14], all the way down to about $K=230$ MeV. This latter value appears to be consistent with the isoscalar giant-monopole resonance (GMR) in ^{208}Pb [15,16]. Omega-meson self-interactions have proven essential for the softening of the equation of state at high density. Indeed, without them large limiting masses for neutron stars (of about $2.8M_\odot$) are predicted, even for the softer models that provide a good description of the giant-monopole resonance [16]. This is because the GMR constrains the equation of state around saturation density but leaves the high-density behavior practically undetermined. Models that include omega-meson self-interactions soften the high-density equation of state to such a degree that limiting masses of $1.8M_\odot$ become possible [12]. Finally, the nonlinear couplings Λ_s and Λ_v are included to modify the density-dependence of the symmetry energy [1].

We compute the neutron radius of ^{208}Pb and the radius of a “canonical” 1.4 solar-mass neutron star for all the parameter sets listed in Ref. [1]. One of these is the very successful NL3-model of Lalazissis, König, and Ring [17]. The other models (S271 and Z271) were introduced in Ref. [1]. All the

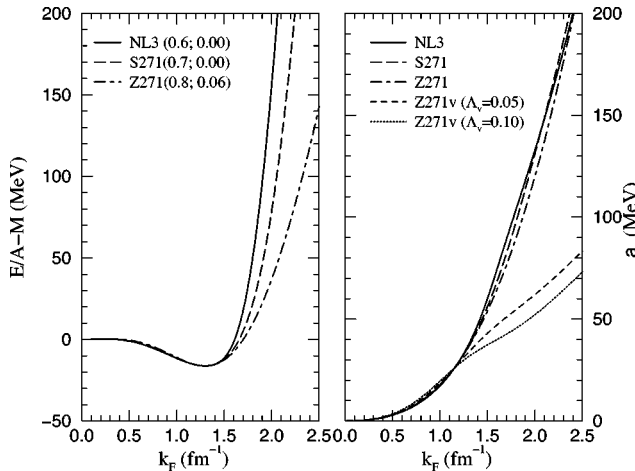


FIG. 1. Binding energy per nucleon in symmetric nuclear matter (left panel) and symmetry energy (right panel) in the various models discussed in the text. In the left-hand panel the first number in parentheses is M^*/M and the second one is ζ .

sets have been constrained to reproduce three important properties of symmetric nuclear matter at saturation: the saturation density (1.3 fm^{-3}), the binding energy per nucleon (-16.25 MeV), and the compression modulus (271 MeV). The value of the effective nucleon mass at saturation, which is not accurately known, as well as the strength of the omega-meson self-coupling coupling (ζ) differ in the various models [1]. This in turn permits a modification of the high-density component of the equation of state in the different models.

The energy density of symmetric nuclear matter can be computed in a mean-field approximation by solving the classical equations of motion for the meson fields. In the mean-field limit it is given by [12]

$$\begin{aligned} \mathcal{E}(\rho) = & \frac{2}{\pi^2} \int_0^{k_F} dk k^2 \sqrt{k^2 + M^{*2}} + \frac{1}{2} \left(\frac{m_s^2}{g_s^2} \right) \Phi_0^2 + \frac{\kappa}{6} \Phi_0^3 + \frac{\lambda}{24} \Phi_0^4 \\ & + \frac{1}{2} \left(\frac{m_v^2}{g_v^2} \right) W_0^2 + \frac{\zeta}{8} W_0^4. \end{aligned} \quad (2)$$

Note that the following definitions have been introduced: $\Phi_0 = g_s \phi_0$ and $W_0 = g_v V_0$. The equation of state for symmetric nuclear matter is displayed on the left panel of Fig. 1. As advertised ζ , and to a lesser extent M^* , are responsible for a softening of the equation of state at high density.

However, in order to compute the equation of state for neutron-rich matter one must supplement the equation of state for symmetric nuclear matter with the symmetry energy. The symmetry energy, a positive-definite quantity, is imposed as a penalty on the system for upsetting the $N=Z$ balance. It is given by

$$a_{\text{sym}}(\rho) = \frac{k_F^2}{6E_F^*} + \frac{g_\rho^2}{12\pi^2} \frac{k_F^3}{m_\rho^{*2}}, \quad (3)$$

where $E_F^* = \sqrt{k_F^2 + M^{*2}}$ and the “effective” rho-meson mass has been defined as

$$m_\rho^{*2} = m_\rho^2 + 2g_\rho^2(\Lambda_s \Phi_0^2 + \Lambda_v W_0^2). \quad (4)$$

In this manner, the equation of state of neutron-rich matter may be written as

$$\frac{E}{A}(\rho, t) = \frac{\mathcal{E}(\rho)}{\rho} + t^2 a_{\text{sym}}(\rho) + \mathcal{O}(t^4), \quad (5)$$

where the neutron excess has been defined as

$$t \equiv \frac{\rho_n - \rho_p}{\rho_n + \rho_p}. \quad (6)$$

The symmetry energy is given as a sum of two contributions. The first term in Eq. (3) represents the increase in the kinetic energy of the system due to the displacement of the Fermi levels of the two species (neutrons and protons). This contribution has been fixed by the properties of symmetric nuclear matter as it only depends on the nucleon effective mass M^* . By itself, it leads to an unrealistically low value for the symmetry energy; for example, at saturation density this contribution yields $\sim 15 \text{ MeV}$, rather than the most realistic value of $\sim 37 \text{ MeV}$. The second contribution is due to the coupling of the rho meson to an isovector-vector current that no longer vanishes in the $N \neq Z$ system. It is by adjusting the strength of the $NN\rho$ coupling constant that one can now fit the empirical value of the symmetry energy at saturation density. However, the symmetry energy at saturation is not well constrained experimentally. Yet an average of the symmetry energy at saturation density and the surface symmetry energy is constrained by the binding energy of nuclei. Thus, the following prescription is adopted: the value of the $NN\rho$ coupling constant is adjusted so that all parameter sets have a symmetry energy of 25.7 MeV at $k_F = 1.15 \text{ fm}^{-1}$ [1]. Following this prescription the symmetry energy at saturation density is predicted to be 37.3 , 36.6 , and 36.3 MeV in the NL3, S271, and Z271 models, respectively (for $\Lambda_s = \Lambda_v = 0$).

The simplicity of the symmetry energy is remarkable indeed. The contribution from the nucleon kinetic energy displays a weak model dependence through the effective nucleon mass and this dependence disappears in the high-density limit. The second term in Eq. (3) is also weakly model dependent, at least in the $\Lambda_s = \Lambda_v = 0$ limit. The reason is simple: models constrained to reproduce the symmetry energy of nuclear matter at some average density, while maintaining the effective nucleon mass within the “acceptable” range of $0.6 \leq M^*/M \leq 0.8$, yield values for the $NN\rho$ coupling constant within 15% of each other. The weak model dependence of the symmetry energy can be observed in the right panel of Fig. 1. Note that the high-density behavior of the symmetry energy is given by

$$a_{\text{sym}}(\rho) \xrightarrow[k_F \rightarrow \infty]{} \frac{g_\rho^2}{12\pi^2} \frac{k_F^3}{m_\rho^2}. \quad (7)$$

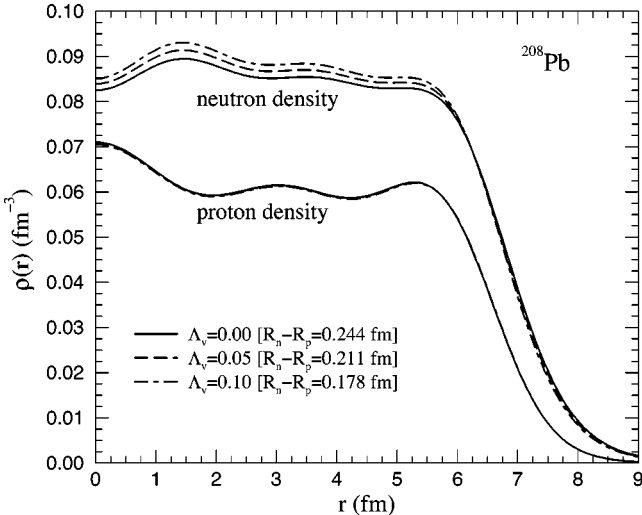


FIG. 2. Neutron and proton densities in ^{208}Pb in the Z271v model for three different values of the nonlinear ω - ρ coupling Λ_v . In all cases the root-mean-square charge radius is predicted to be $R_{\text{ch}}=5.51$ fm.

As they stand now, the models lack enough leverage to significantly modify the symmetry energy. In order to remedy this deficiency one must rely on the two nonlinear couplings between the isoscalar and isovector mesons (Λ_s and Λ_v). These couplings change the density dependence of the symmetry energy by modifying the rho-meson mass as is indicated in Eq. (4). For example, for $\Lambda_v \neq 0$ the high-density behavior of the omega-meson field becomes [12]

$$W_0 \xrightarrow[k_F \rightarrow \infty]{} \begin{cases} \left(\frac{g_v^2}{m_v^2}\right)\rho & \text{if } \zeta=0; \\ \left(\frac{6\rho}{\zeta}\right)^{1/3} & \text{if } \zeta \neq 0. \end{cases} \quad (8)$$

In either case ($\zeta=0$ or $\zeta \neq 0$) the modifications are significant enough to change the qualitative behavior of the symmetry energy; the symmetry energy now grows linearly with $k_F \propto \rho^{1/3}$ rather than as k_F^3 . This change in the qualitative behavior of the symmetry energy can be seen in the right panel of Fig. 1. Note that with $\Lambda_s \neq 0$ or $\Lambda_v \neq 0$ an adjustment of the $NN\rho$ coupling constant is necessary to maintain the symmetry energy unchanged from its fixed value of 25.7 MeV at $k_F=1.15$ fm $^{-1}$. Further, the inclusion of these nonlinear terms does not affect the properties of symmetric nuclear matter as $\mathbf{b}_\mu \equiv 0$ in the $N=Z$ limit.

The procedure described above is robust in another important way. While our goal is to induce changes in the neutron radius of ^{208}Pb through a modification of the symmetry energy, we want to do so without sacrificing the success of the models in describing the binding energy and charge radius of ^{208}Pb , both of them well known experimentally (B.E.=7.868 MeV and $R_{\text{ch}}=5.51$ fm) [18–20]. That this is possible may be seen in Fig. 2. In this figure the neutron and proton ground-state densities have been computed in the Z271 model for three different values of the nonlinear ω - ρ coupling Λ_v . While the softening of the symmetry energy

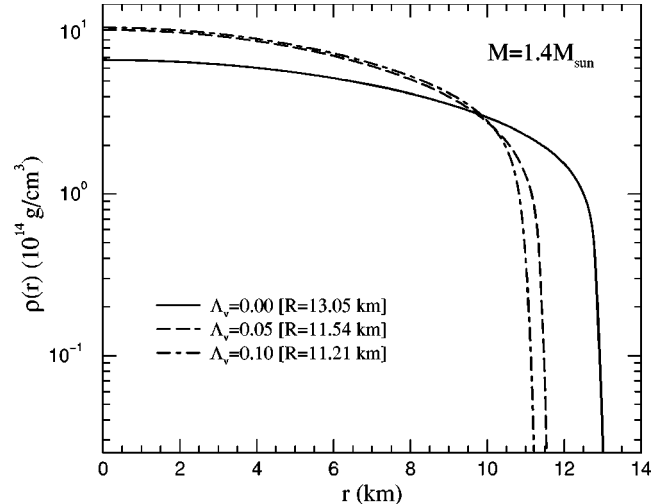


FIG. 3. Density profile for a $M=1.4M_\odot$ neutron star in the Z271v model for three different values of the nonlinear ω - ρ coupling Λ_v .

has reduced the neutron skin of ^{208}Pb appreciably, the charge radius has changed by less than 0.005 fm.

In Fig. 3 we show the equivalent plot but for an object 55 orders of magnitude heavier than ^{208}Pb : a 1.4 solar-mass neutron star. The density profile of such a neutron star correlates nicely with the neutron skin of ^{208}Pb . Models with a softer symmetry energy tolerate regions of large central densities thereby generating smaller radii.

Finally, the radius R of a 1.4 solar-mass neutron star as a function of the neutron skin $R_n - R_p$ in ^{208}Pb is displayed in Fig. 4 for the various models described in the text. All neutron-star radii were computed using the Oppenheimer-Volkoff equations for neutron-rich matter in beta equilibrium. Since this figure was generated using an equation of state for uniform matter, it may contain small errors due to an inappropriate treatment of the surface region. Note that whereas the Z271 model has been extended to include both

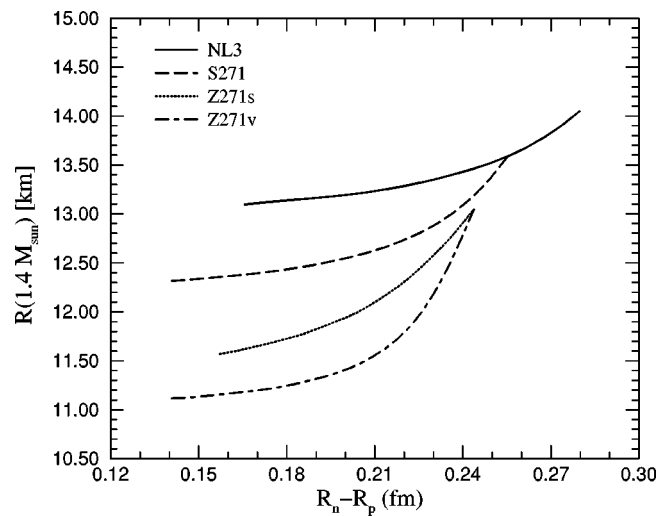


FIG. 4. Radius of a $M=1.4M_\odot$ neutron star as a function of the neutron-minus-proton radius in ^{208}Pb for the four parameter sets described in the text.

$\Lambda_s \neq 0$ (Z271s) and $\Lambda_v \neq 0$ (Z271v), the other two models have the σ - ρ coupling fixed at $\Lambda_s = 0$. The strong correlation between the neutron-star radius and the neutron skin in ^{208}Pb is evident: for a given parameter set R increases with $R_n - R_p$. However, as one modifies the parameter set to increase M^* or the ω -meson self-coupling ζ , the equation of state becomes softer so the pressure decreases at high density. As a result, the radius of the star becomes smaller for fixed $R_n - R_p$. For example, for a neutron skin of $R_n - R_p = 0.18$ fm, the radius of the star varies from $R \approx 13$ km in the NL3 model all the way down to $R \approx 11$ km in the Z271v model. Thus, we conclude that the radius of a $1.4M_\odot$ neutron star is not uniquely constrained by a measurement of the neutron-skin thickness because $R_n - R_p$ depends only on the equation of state at or below saturation density while R is mostly sensitive to the equation of state at higher densities. Yet one may be able to combine separate measurements of $R_n - R_p$ and R to obtain considerable information about the equation of state at low and high densities. For example, if $R_n - R_p$ is relatively large while R is small, this could indicate a phase transition. A large $R_n - R_p$ implies that the low-density equation of state is stiff while a small R suggests a soft high-density equation of state. The change from stiff to soft could be accompanied by a phase transition.

In conclusion, relativistic effective field theories that reproduce a variety of ground-state observables have been used to correlate the radius of a 1.4 solar-mass neutron star to the neutron skin of ^{208}Pb . Nonlinear couplings between isoscalar and isovector mesons have been introduced to modify the density dependence of the symmetry energy. Models with a softer symmetry energy tolerate larger central densities and produce systems with smaller radii. Thus an important correlation is revealed: the smaller the skin-thickness of ^{208}Pb the smaller the size of the neutron star. Yet the radius of the neutron star is not uniquely constrained by a measurement of the neutron skin in ^{208}Pb . This is because the ^{208}Pb measurement constraints the equation of state only for densities between the transition density to nonuniform matter and saturation density. In contrast, the radius of a $1.4M_\odot$ neutron star is mostly sensitive to the equation of state at high density. Yet together they provide considerable information on the equation of state. If these combined measurements reveal a large value of the neutron skin together with a small value of the star radius, this may provide strong evidence in support of a phase transition in the interior of the neutron star.

This work was supported in part by U.S. DOE Grant Nos. DE-FG02-87ER40365 and DE-FG05-92ER40750.

-
- [1] C.J. Horowitz and J. Piekarewicz, Phys. Rev. Lett. **86**, 5647 (2001).
 - [2] Jefferson Laboratory Experiment No. E-00-003, R. Michaels, P.A. Souder, and G.M. Urciuoli, spokespersons.
 - [3] C.J. Horowitz, S.J. Pollock, P.A. Souder, and R. Michaels, Phys. Rev. C **63**, 025501 (2001).
 - [4] A. Golden and A. Shearer, Astron. Astrophys. **342**, L5 (1999).
 - [5] Frederick M. Walter and Lynn D. Matthews, Nature (London) **389**, 358 (1997).
 - [6] Frederick M. Walter, Astrophys. J. **549**, 433 (2001).
 - [7] Jose A. Pons, Frederick M. Walter, James M. Lattimer, Madappa Prakash, Ralph Neuhäuser, and Penghui An, astro-ph/0107404.
 - [8] B. Link, R.I. Epstein, and J.M. Lattimer, Phys. Rev. Lett. **83**, 3362 (1999).
 - [9] G.G. Pavlov, V.E. Zavlin, D. Sanwal, V. Burwitz, and G.P. Garmire, astro-ph/0103171.
 - [10] Robert E. Rutledge, Lars Bildsten, Edward F. Brown, George G. Pavlov, and Vyacheslav E. Zavlin, astro-ph/0105405.
 - [11] P. Haensel, astro-ph/0105485.
 - [12] H. Müller and B.D. Serot, Nucl. Phys. **A606**, 508 (1996).
 - [13] J.D. Walecka, Ann. Phys. (N.Y.) **83**, 491 (1974).
 - [14] B.D. Serot and J.D. Walecka, Adv. Nucl. Phys. **16** (1986); Int. J. Mod. Phys. E **6**, 515 (1997).
 - [15] D.H. Youngblood, H.L. Clark, and Y.-W. Lui, Phys. Rev. Lett. **82**, 691 (1999).
 - [16] J. Piekarewicz, Phys. Rev. C **62**, 051304(R) (2000); **64**, 024307 (2001).
 - [17] G.A. Lalazissis, J. König, and P. Ring, Phys. Rev. C **55**, 540 (1997).
 - [18] G. Audi and A.H. Wapstra, Nucl. Phys. **A595**, 409 (1995).
 - [19] B. Frois *et al.*, Phys. Rev. Lett. **38**, 152 (1977).
 - [20] H. de Vries, C.W. de Jager, and C. De Vries, At. Data Nucl. Data Tables **36**, 495 (1987).

Neutron-Rich Nuclei and Neutron Stars: A New Accurately Calibrated Interaction for the Study of Neutron-Rich Matter

B. G. Todd-Rutel and J. Piekarewicz

Department of Physics, Florida State University, Tallahassee, Florida 32306, USA

(Received 11 April 2005; published 13 September 2005)

An accurately calibrated relativistic parametrization is introduced to compute the ground state properties of finite nuclei, their linear response, and the structure of neutron stars. While similar in spirit to the successful NL3 parameter set, it produces an equation of state that is considerably softer—both for symmetric nuclear matter and for the symmetry energy. This softening appears to be required for an accurate description of several collective modes having different neutron-to-proton ratios. Among the predictions of this model are a symmetric nuclear-matter incompressibility of $K = 230$ MeV and a neutron skin thickness in ^{208}Pb of $R_n - R_p = 0.21$ fm. The impact of such a softening on various neutron-star properties is also examined.

DOI: 10.1103/PhysRevLett.95.122501

PACS numbers: 21.10.-k, 21.60.Jz, 21.65.+f, 26.60.+c

The quest for the equation of state (EOS) of neutron-rich matter—which is likely to lead to the discovery of exotic phases of matter—is an exciting problem that permeates over many areas of physics. While the search for novel phenomena has long been at the forefront of science, learning about “neutron-rich nuclei in heaven and earth” has experienced a recent revitalization due to remarkable advances in both terrestrial experiments and space observations. These developments, coupled to the promise of new *facilities for the future of science*, guarantee continuing discoveries for many years to come. Figuring prominently among the facilities for the future is the Rare Isotope Accelerator (RIA), a facility that by defining the limits of nuclear existence, will constrain the EOS at large neutron-proton asymmetries. In addition, new telescopes operating at a variety of wavelengths have turned neutron stars from theoretical curiosities into powerful diagnostic tools. For some recent excellent reviews on the relevance of the EOS on a variety of phenomena, such as the dynamics of heavy-ion collisions, the structure of neutron stars, and the simulation of core-collapse supernova, see Refs. [1–4] and references contained therein.

Our aim in this Letter is to construct an accurately calibrated parameter set that, while constrained only by the ground-state properties and the linear response of a variety of nuclei, may still be used to predict some neutron-star observables. Such a successful paradigm is the relativistic NL3 parameter set of Lalazissis, Konig, and Ring [5]. The NL3 parametrization has been used with enormous success in the description of a variety of ground-state properties of spherical, deformed, and exotic nuclei. For some special cases, it has also been used successfully to compute the linear response of the mean-field ground state. In the particular case of the giant monopole resonance (GMR) in ^{208}Pb —the so-called *breathing mode*—the predicted distribution of strength is in close agreement with the experimental data [6]. Thus, it has come as a surprise that to reproduce the GMR in ^{208}Pb , accurately fit non-

relativistic and relativistic models predict compressional moduli in symmetric nuclear matter (K) that differ by about 25%. Indeed, while nonrelativistic models predict $K \approx 220\text{--}235$ MeV [7–9], relativistic models argue for a significantly larger value $K \approx 250\text{--}270$ MeV [5,10,11].

In an earlier work, the density dependence of the symmetry energy, which at present is poorly known, has been proposed as the culprit for the above discrepancy [12]. (Note that the symmetry energy equals, to an excellent approximation, the difference between the energy of pure neutron matter and that of symmetric nuclear matter.) Since first proposed, other groups have tested this assertion reaching similar conclusions [11,13–15]. In particular, in Refs. [12,13] it has been argued that a good description of the breathing mode in ^{208}Pb may be obtained using a large value of K —provided one compensates with an appropriately stiff symmetry energy, namely, one that rises rapidly with baryon density. Thus, it was suggested that ^{90}Zr , a nucleus with both a well-developed breathing mode and a small neutron-proton asymmetry, should be used (rather than ^{208}Pb) to constrain K . With the advent of unprecedented experimental accuracy in the determination of the breathing mode in ^{90}Zr [6], it now appears that the NL3 interaction overestimates the value of K [14]. Moreover, the alluded correlation between K and the density dependence of the symmetry energy serves as a telltale of a further problem with most relativistic parametrizations: an underestimation of the frequency of oscillations of neutrons against protons—the so-called isovector giant dipole resonance (IVGDR)—in ^{208}Pb [11,13].

In this Letter we introduce a new, accurately calibrated relativistic parametrization that simultaneously describes the GMR in ^{90}Zr and ^{208}Pb , and the IVGDR in ^{208}Pb , without compromising the success in reproducing ground-state observables. To do so, however, two additional coupling constants must be introduced. Without these additional coupling constants one cannot describe the various modes without seriously compromising the quality of the fit

TABLE I. Model parameters used in the calculations. The parameter κ and the inverse scalar range m_s are given in MeV. The nucleon, omega, and rho masses are kept fixed at $M = 939$ MeV, $m_\omega = 782.5$ MeV, and $m_\rho = 763$ MeV, respectively.

Model	m_s	g_s^2	g_v^2	g_ρ^2	κ	λ	ζ	Λ_v
NL3	508.1940	104.3871	165.5854	79.6000	3.8599	-0.0159	0.0000	0.0000
FSUGold	491.5000	112.1996	204.5469	138.4701	1.4203	+0.0238	0.0600	0.0300

[11,16]. The effective field theoretical model is based on an interacting Lagrangian that provides an accurate description of finite nuclei and a Lorentz covariant extrapolation for the equation of state of dense matter. It has the following form [17–19]:

$$\begin{aligned} \mathcal{L}_{\text{int}} = & \bar{\psi} \left[g_s \phi - \left(g_v V_\mu + \frac{g_\rho}{2} \tau \cdot \mathbf{b}_\mu + \frac{e}{2} (1 + \tau_3) A_\mu \right) \gamma^\mu \right] \psi \\ & - \frac{\kappa}{3!} (g_s \phi)^3 - \frac{\lambda}{4!} (g_s \phi)^4 + \frac{\zeta}{4!} (g_v^2 V_\mu V^\mu)^2 \\ & + \Lambda_v (g_\rho^2 \mathbf{b}_\mu \cdot \mathbf{b}^\mu) (g_v^2 V_\mu V^\mu). \end{aligned} \quad (1)$$

The Lagrangian density includes Yukawa couplings of the nucleon field to various meson fields. It includes an isoscalar-scalar ϕ meson field and three vector fields: an isoscalar V^μ , an isovector \mathbf{b}^μ , and the photon A^μ . In addition to the Yukawa couplings, the Lagrangian is supplemented by four nonlinear meson interactions. The inclusion of isoscalar meson self-interactions (via κ , λ , and ζ) are used to soften the equation of state of symmetric nuclear matter, while the mixed isoscalar-isovector coupling (Λ_v) modifies the density dependence of the symmetry energy. While power counting suggests that other local meson terms may be equally important [17], their phenomenological impact has been documented to be small [17–19], so they will not be considered any further in this study.

Although in Refs. [18,19] it has been proven that the addition of the isoscalar-isovector coupling (Λ_v) is important for the softening of the symmetry energy, no attempt was made to optimize the various parameter sets. Following standard practices [5,14], we use binding energies and charge radii for a variety of magic nuclei—computed in a relativistic mean-field approximation—to produce an accurately calibrated set through a chi-square minimization procedure. We dubbed this set “FSUGold” and list the various mass parameters and coupling constants in Table I. Further details about the calibration procedure will be presented in a forthcoming publication. In Table II a comparison between the very successful NL3 parametrization [5], FSUGold, and, (when available) experimental data is provided. While the agreement with experiment (at the 1% level or better) is satisfactory—and this agreement extends all over the periodic table [20]—a question immediately arises: given the success of NL3, why the need for another effective interaction having two additional parameters? The answer to this question is provided below.

As alluded earlier, and argued in Refs. [12,13], the success of the NL3 set in reproducing the breathing mode in ^{208}Pb is accidental; it results from a combination of both a stiff equation of state for symmetric nuclear matter and a stiff symmetry energy. If true, this implies that NL3 should overestimate the location of the breathing mode in ^{90}Zr —a nucleus with a well-developed GMR strength but rather insensitive to the symmetry energy. Similarly, the energy of the IVGDR in ^{208}Pb , an observable sensitive to the density dependence of the symmetry energy, should be underestimated by NL3 (note that a stiff symmetry energy predicts a small symmetry energy at the low densities of relevance to the IVGDR). In Table III relativistic random phase approximation (RPA) results for the GMR (centroids) in ^{208}Pb and ^{90}Zr , and the IVGDR (peak energy) in ^{208}Pb are reported. These small-amplitude modes represent the linear response of the mean-field ground state to a variety of probes [6,21]. Note that the FSUGold (NL3) parameter set predicts a compression modulus for symmetric nuclear matter of $K = 230(271)$ MeV and a neutron skin in ^{208}Pb of $R_n - R_p = 0.21(0.28)$ fm. The good agreement between FSUGold and experiment is due to the addition of the

TABLE II. Experimental data for the binding energy per nucleon and the charge radii for the magic nuclei used in the least square fitting procedure. In addition, predictions are displayed for the neutron skin of these nuclei.

Nucleus	Observable	Experiment	NL3	FSUGold
^{40}Ca	B/A (MeV)	8.55	8.54	8.54
	R_{ch} (fm)	3.45	3.46	3.42
	$R_n - R_p$ (fm)	...	-0.05	-0.05
^{48}Ca	B/A (MeV)	8.67	8.64	8.58
	R_{ch} (fm)	3.45	3.46	3.45
	$R_n - R_p$ (fm)	...	0.23	0.20
^{90}Zr	B/A (MeV)	8.71	8.69	8.68
	R_{ch} (fm)	4.26	4.26	4.25
	$R_n - R_p$ (fm)	...	0.11	0.09
^{116}Sn	B/A (MeV)	8.52	8.48	8.50
	R_{ch} (fm)	4.63	4.60	4.60
	$R_n - R_p$ (fm)	...	0.17	0.13
^{132}Sn	B/A (MeV)	8.36	8.37	8.34
	R_{ch} (fm)	...	4.70	4.71
	$R_n - R_p$ (fm)	...	0.35	0.27
^{208}Pb	B/A (MeV)	7.87	7.88	7.89
	R_{ch} (fm)	5.50	5.51	5.52
	$R_n - R_p$ (fm)	...	0.28	0.21

TABLE III. Centroid energies for the breathing mode in ^{208}Pb and ^{90}Zr , and the peak energy for the IVGDR in ^{208}Pb . Experimental data are extracted from Refs. [6,21].

Nucleus	Observable	Experiment	NL3	FSUGold
^{208}Pb	GMR (MeV)	14.17 ± 0.28	14.32	14.04
^{90}Zr	GMR (MeV)	17.89 ± 0.20	18.62	17.98
^{208}Pb	IVGDR (MeV)	13.30 ± 0.10	12.70	13.07

two extra parameters (ζ to reduce the value of K and Λ_v to soften the symmetry energy). However, it seems that an additional softening of the symmetry energy could further improve the agreement with experiment. With the present parametrization this could not be achieved without compromising the quality of the fit. Thus, our prediction of $R_n - R_p = 0.21$ fm could be regarded as an upper bound. This smaller value for the neutron skin in ^{208}Pb , generated from the softer symmetry energy, is significant as it brings covariant meson-baryon models closer to nonrelativistic predictions based on Skyrme parametrizations [22]. We note that the Parity Radius Experiment (PREX) at the Jefferson Laboratory is scheduled to measure the neutron radius of ^{208}Pb accurately (to within 0.05 fm) and model independently via parity-violating electron scattering [23,24]. This experiment should provide a unique observational constraint on the density dependence of the symmetry energy.

Having constructed a new accurately calibrated parameter set, we now examine predictions for a few neutron-star properties. The structure of spherical neutron stars in hydrostatic equilibrium is solely determined by the EOS of neutron-rich matter in beta equilibrium. For the uniform liquid phase we assume an EOS for matter in beta equilibrium that is composed of neutrons, protons, electrons, and muons. Further, we assume that this description remains valid in the high-density interior of the star. Thus, transitions to exotic phases are not considered here.

However, at the lower densities of the inner crust the uniform system becomes unstable against density fluctuations. In this nonuniform region the system may consist of a variety of complex structures, collectively known as *nuclear pasta* [25,26]. While microscopic calculations of the nuclear pasta are becoming available [27–29], it is premature to incorporate them in our calculation. Hence, following the procedure adopted in Ref. [30], a simple polytropic equation of state is used to interpolate from the outer crust [31] to the uniform liquid.

Results for the transition density from uniform to non-uniform neutron-rich matter are displayed in Table IV. These results are consistent with the inverse correlation between the neutron-skin and the transition density found in Ref. [18]. This correlation suggests that models with a stiff equation of state (like NL3) predict a low transition density, as it is energetically unfavorable to separate nuclear matter into regions of high and low densities. We now present results for a few neutron-star observables that

TABLE IV. Predictions for a few neutron-star observables. The various quantities are as follows: ρ_c is the transition density from nonuniform to uniform neutron-rich matter, R is the radius of a 1.4 solar-mass neutron star, M_{\max} is the limiting mass, ρ_{Urca} is the threshold density for the direct Urca process, M_{Urca} is the minimum mass neutron star that may cool down by the direct Urca process, and ΔM_{Urca} is the mass fraction of a 1.4 solar-mass neutron star that supports enhanced cooling by the direct Urca process.

Observable	NL3	FSUGold
ρ_c (fm $^{-3}$)	0.052	0.076
R (km)	15.05	12.66
$M_{\max}(M_\odot)$	2.78	1.72
ρ_{Urca} (fm $^{-3}$)	0.21	0.47
$M_{\text{Urca}}(M_\odot)$	0.84	1.30
ΔM_{Urca}	0.38	0.06

depend critically on the equation of state [3,32], namely, masses, radii, and composition. Table IV includes predictions for the radius of a “canonical” 1.4 solar-mass neutron star alongside the maximum mass that the EOS can support against gravitational collapse; beyond this value the star collapses into a black hole. These results were obtained by numerically integrating the Tolman-Oppenheimer-Volkoff equations. The considerable smaller radius predicted by the FSUGold model originates in its softer symmetry energy. The stiffer symmetry energy of the NL3 set does not tolerate large central densities and produces stars with large radii. Note that the same physics that pushes neutrons out against surface tension in the nucleus of ^{208}Pb is also responsible for pushing neutrons out in a neutron star [18,19]. Further, while the sizable reduction in the limiting mass of FSUGold relative to NL3 is also due to the softening of the EOS, it is the softening induced by the (isoscalar) quartic vector-meson coupling ζ —rather than the softening of the symmetry energy controlled by Λ_v —that is responsible for this effect [17].

We conclude with a comment on the enhanced cooling of neutron stars. Recent observations by the Chandra and XMM-Newton observatories suggest that some neutron stars may cool rapidly, suggesting perhaps the need for some exotic component, such as condensates or color superconductors. Here we explore a more conservative alternative, namely, that of enhanced cooling of neutron stars by means of neutrino emission from nucleons in a mechanism known as the direct Urca process [32–35]. This mechanism is not exotic as it only relies on protons, neutrons, electrons, and muons—standard constituents of dense matter. However, it requires a large proton fraction Y_p for the momentum to be conserved in the above reactions. As a large proton fraction requires a stiff symmetry energy, it is interesting to determine if the newly proposed EOS is able to support such a large proton fraction. Note that in order for the direct Urca process to operate, the proton fraction must exceed $Y_p = 0.111$ for the low-density (muonless) case, and $Y_p = 0.148$ for the high-

density case (with equal number of electrons and muons). In Table IV we list the threshold density (ρ_{Urca}) and minimum mass (M_{Urca}) required for the onset of the direct Urca process. We note that in spite of its softer symmetry energy, FSUGold predicts that a 1.4 solar-mass neutron star may cool down by the direct Urca process. For completeness, the mass fraction that supports enhanced cooling in such a neutron star is listed as ΔM_{Urca} .

In conclusion, a new accurately calibrated relativistic model (FSUGold) has been fitted to the binding energies and charge radii of a variety of magic nuclei. Symmetric nuclear matter saturates at a Fermi momentum of $k_F = 1.30 \text{ fm}^{-1}$ with a binding energy per nucleon of $B/A = -16.30 \text{ MeV}$. Relative to the *NL3* set, used here as a successful paradigm, FSUGold contains two additional parameters whose main virtue is the softening of both the EOS of symmetric matter and the symmetry energy. These two parameters are essential for reproducing a few nuclear collective modes. Specifically, the breathing mode in ^{90}Zr is sensitive to the softening of symmetric matter, the isovector giant dipole resonance in ^{208}Pb to the softening of the symmetry energy, and the breathing mode in ^{208}Pb to both. Incorporating these constraints yields a nuclear-matter incompressibility of $K = 230 \text{ MeV}$ and a neutron skin thickness in ^{208}Pb of $R_n - R_p = 0.21 \text{ fm}$. While the description of the various collective modes imposes additional constraints on the EOS at densities around saturation density, the high-density component of the EOS remains largely unconstrained. We made no attempts to constrain the EOS at the supranuclear densities of relevance to neutron-star physics. Rather, we simply explored the consequences of the new parametrization on a variety of neutron star observables. In particular, we found a limiting mass of $M_{\text{max}} = 1.72M_\odot$, a radius of $R = 12.66 \text{ km}$ for a $M = 1.4M_\odot$ neutron star, and no direct Urca cooling in neutrons stars with masses below $M = 1.3M_\odot$. While the consequences of these results will be fully explored in a forthcoming publication, it is interesting to note that recent observations of pulsar-white dwarf binaries at the Arecibo observatory suggest a pulsar mass for PSRJ0751 + 1807 of $M = 2.1_{-0.5}^{+0.4}M_\odot$ at a 95% confidence level [36]. If this observation could be refined, not only would it rule out the high-density behavior of this (and many other) EOS, but it could provide us with a precious boost in our quest for the equation of state.

We acknowledge many useful discussions with C. J. Horowitz and D. Page. This work was supported in part by DOE Grant No. DE-FG05-92ER40750.

-
- [1] P. Danielewicz, R. Lacey, and W. G. Lynch, *Science* **298**, 1592 (2002).
 - [2] R. Buras, M. Rampp, H. T. Janka, and K. Kifonidis, *Phys. Rev. Lett.* **90**, 241101 (2003).
 - [3] J. M. Lattimer and M. Prakash, *Science* **304**, 536 (2004).

- [4] A. W. Steiner, M. Prakash, J. M. Lattimer, and P. J. Ellis, *Phys. Rep.* **411**, 325 (2005).
- [5] G. A. Lalazissis, J. Konig, and P. Ring, *Phys. Rev. C* **55**, 540 (1997).
- [6] D. H. Youngblood, H. L. Clark, and Y. W. Lui, *Phys. Rev. Lett.* **82**, 691 (1999).
- [7] G. Colò, P. F. Bortignon, N. Van Gai, A. Bracco, and R. A. Broglia, *Phys. Lett. B* **276**, 279 (1992).
- [8] J. P. Blaizot, J. F. Berger, J. Decharge, and M. Girod, *Nucl. Phys.* **A591**, 435 (1995).
- [9] I. Hamamoto, H. Sagawa, and X. Z. Zhang, *Phys. Rev. C* **56**, 3121 (1997).
- [10] D. Vretenar, A. Wandelt, and P. Ring, *Phys. Lett. B* **487**, 334 (2000).
- [11] D. Vretenar, T. Niksic, and P. Ring, *Phys. Rev. C* **68**, 024310 (2003).
- [12] J. Piekarewicz, *Phys. Rev. C* **66**, 034305 (2002).
- [13] J. Piekarewicz, *Phys. Rev. C* **69**, 041301 (2004).
- [14] B. K. Agrawal, S. Shlomo, and V. Kim Au, *Phys. Rev. C* **68**, 031304 (2003).
- [15] G. Colò and N. Van Gai, *nucl-th/0309002*.
- [16] D. Vretenar, P. Ring, G. A. Lalazissis, and N. Paar, *Nucl. Phys.* **A649**, 29 (1999).
- [17] H. Muller and B. D. Serot, *Nucl. Phys.* **A606**, 508 (1996).
- [18] C. J. Horowitz and J. Piekarewicz, *Phys. Rev. Lett.* **86**, 5647 (2001).
- [19] C. J. Horowitz and J. Piekarewicz, *Phys. Rev. C* **64**, 062802(R) (2001).
- [20] G. A. Lalazissis, S. Raman, and P. Ring, *At. Data Nucl. Data Tables* **71**, 1 (1999).
- [21] J. Ritman *et al.*, *Phys. Rev. Lett.* **70**, 533 (1993).
- [22] R. J. Furnstahl, *Nucl. Phys.* **A706**, 85 (2002).
- [23] C. J. Horowitz, S. J. Pollock, P. A. Souder, and R. Michaels, *Phys. Rev. C* **63**, 025501 (2001).
- [24] R. Michaels, P. A. Souder, and G. M. Urciuoli, Thomas Jefferson National Accelerator Facility Proposal E-00-003, 2002, http://www.jlab.org/exp_prog/generated/halla.html.
- [25] D. G. Ravenhall, C. J. Pethick, and J. R. Wilson, *Phys. Rev. Lett.* **50**, 2066 (1983).
- [26] M. Hashimoto, H. Seki, and M. Yamada, *Prog. Theor. Phys.* **71**, 320 (1984).
- [27] G. Watanabe and H. Sonoda, *cond-mat/0502515*, and references therein.
- [28] C. J. Horowitz, M. A. Perez-Garcia, and J. Piekarewicz, *Phys. Rev. C* **69**, 045804 (2004).
- [29] C. J. Horowitz, M. A. Perez-Garcia, J. Carriere, D. Berry, and J. Piekarewicz, *Phys. Rev. C* **70**, 065806 (2004).
- [30] J. Carriere, C. J. Horowitz, and J. Piekarewicz, *Astrophys. J.* **593**, 463 (2003).
- [31] G. Baym, C. Pethick, and P. Sutherland, *Astrophys. J.* **170**, 299 (1971).
- [32] J. M. Lattimer and M. Prakash, *Astrophys. J.* **550**, 426 (2001).
- [33] L. B. Leinson, *Nucl. Phys.* **A707**, 543 (2002).
- [34] D. Page, J. M. Lattimer, M. Prakash, and A. W. Steiner, *Astrophys. J.* **155**, 623 (2004).
- [35] D. G. Yakovlev and C. Pethick, *Annu. Rev. Astron. Astrophys.* **42**, 169 (2004).
- [36] D. J. Nice, E. M. Splaver, and I. H. Stairs, in *Proceedings of the 2004 IAU Symposium*, edited by F. Camilo and B. M. Gaensler, Vol. 218, p. 49, *astro-ph/0311296*.

This is the accepted manuscript made available via CHORUS. The article has been published as:

Building relativistic mean field models for finite nuclei and neutron stars

Wei-Chia Chen and J. Piekarewicz

Phys. Rev. C **90**, 044305 — Published 7 October 2014

DOI: [10.1103/PhysRevC.90.044305](https://doi.org/10.1103/PhysRevC.90.044305)

Building relativistic mean field models for finite nuclei and neutron stars

Wei-Chia Chen^{1,*} and J. Piekarewicz^{1,†}

¹*Department of Physics, Florida State University, Tallahassee, FL 32306*

(Dated: September 22, 2014)

Background: Theoretical approaches based on density functional theory provide the only tractable method to incorporate the wide range of densities and isospin asymmetries required to describe finite nuclei, infinite nuclear matter, and neutron stars.

Purpose: A relativistic energy density functional (EDF) is developed to address the complexity of such diverse nuclear systems. Moreover, a statistical perspective is adopted to describe the information content of various physical observables.

Methods: We implement the model optimization by minimizing a suitably constructed χ^2 objective function using various properties of finite nuclei and neutron stars. The minimization is then supplemented by a covariance analysis that includes both uncertainty estimates and correlation coefficients.

Results: A new model, “*FSUGold 2*”, is created that can well reproduce the ground-state properties of finite nuclei, their monopole response, and that accounts for the maximum neutron star mass observed up to date. In particular, the model predicts both a stiff symmetry energy and a soft equation of state for symmetric nuclear matter—suggesting a fairly large neutron-skin thickness in ^{208}Pb and a moderate value of the nuclear incompressibility.

Conclusions: We conclude that without any meaningful constraint on the isovector sector, relativistic EDFs will continue to predict significantly large neutron skins. However, the calibration scheme adopted here is flexible enough to create models with different assumptions on various observables. Such a scheme—properly supplemented by a covariance analysis—provides a powerful tool to identify the critical measurements required to place meaningful constraints on theoretical models.

PACS numbers: 21.60.Jz, 21.65.Cd, 21.65.Mn, 26.60-c

* wc09c@my.fsu.edu

† jpickarewicz@fsu.edu

I. INTRODUCTION

Finite nuclei, infinite nuclear matter, and neutron stars are complex, many-body systems governed largely by the strong nuclear force. Although Quantum Chromodynamics (QCD) is the fundamental theory of the strong interaction, enormous challenges have prevented us from solving the theory in the non-perturbative regime of relevance to nuclear systems. To date, these complex systems can be investigated only in the framework of an effective theory with appropriate degrees of freedom. Among the effective approaches, the one based on *density functional theory* (DFT) is most promising, as it is the only microscopic approach that may be applied to the entire nuclear landscape and to neutron stars. In the past decades numerous *energy density functionals* (EDFs) have been proposed which can be grouped into two main branches: non-relativistic and relativistic. Skyrme-type functionals are the most popular ones within the non-relativistic domain, where nucleons interact via density-dependent effective potentials. Using such a framework, the *Universal Nuclear Energy Density Functional* (UNEDF) Collaboration [1] aims to achieve a comprehensive understanding of finite nuclei and the reactions involving them [2–4]. On the other end, relativistic mean field (RMF) models, based on a quantum field theory having nucleons interacting via the exchange of various mesons, have been successfully used since the 1970’s and provide a covariant description of both infinite nuclear matter and finite nuclei [5–10].

In the traditional spirit of effective theories, both non-relativistic and relativistic EDFs are calibrated from nuclear experimental data that is obtained under normal laboratory conditions, namely, at or slightly below nuclear saturation density and with small to moderate isospin asymmetries. The lack of experimental data at both higher densities and with extreme isospin asymmetries leads to a large spread in the predictions of the models—even when they may all be calibrated to the same experimental data. Consequently, fundamental nuclear properties, such as the neutron density of medium-to-heavy nuclei [11–14], proton and neutron drip lines [15, 16], and a variety of neutron star properties [17–19], remain largely undetermined.

It has been a common practice for a long time to supplement experimental results with uncertainty estimates. Indeed, no experimental measurement could ever be published without properly estimated “error bars”. Often, the most difficult part of an experiment is a reliable quantification of systematic errors, and improving the precision of the measurement consists of painstaking efforts at reducing the sources of such uncertainties. On the contrary, theoretical predictions merely involve reporting a “central value” without any information on the uncertainties inherent in the formulation or the calculation. Thus, to determine whether a theory is successful or not, the only required criterion is to reproduce the experimental data. Although this approach has certain value—especially if the examined model reproduces a vast amount of experimental data—such a criterion is often neither helpful nor meaningful. And the situation becomes even worse if the predictions of an effective theory are extrapolated into unknown regions, such as the boundaries of the nuclear landscape and the interior of neutron stars. How can a model provide experimental or observational guidance without supplementing its predictions with theoretical errors? In recent years, “*the importance of including uncertainty estimates in papers involving theoretical calculations of physical quantities*” has been underscored [20]. This is particularly critical when theoretical models are used to extrapolate experimental data to uncharted regions of the observable landscape. Thus, theoretical uncertainty estimates are critical in assessing the reliability of the extrapolations. Moreover, if these theoretical errors are large, then one can perform a correlation analysis to uncover observables that can help reduce the size of the uncertainties. Several manuscripts highlighting the role of information and statistics in nuclear physics have been published recently [21–27]. Moreover, at the time of this writing, a focus issue devoted to “*Enhancing the interaction between nuclear experiment and theory through information and statistics*” was under development.

In this work we develop a modeling scheme within the framework of the RMF theory that consists of both the optimization of a theoretical model and the follow-up covariance analysis. However, unlike the UNEDF Collaboration, our goals are rather modest as we do not attempt to study all the facets of finite nuclei. Instead, we limit ourselves to a treatment of the ground-state properties of magic (or semi-magic) finite nuclei, centroid energies of monopole resonances, and properties of neutron stars. We would like to emphasize that all the data that we use in the optimization of the relativistic EDF consists of real physical observables without any reliance on bulk properties of infinite nuclear matter. This is now possible due to the remarkable advances in land- and space-based telescopes that have started to place meaningful constraints on the high-density component of the equation of state. In particular, observations made with the Green Bank Telescope have provided highly precise measurements of two massive (of about $2 M_{\odot}$) neutron stars [18, 19]. Further, an enormous effort is also being devoted to the extraction of stellar radii from x-ray observations [28–31]. Such astronomical observations will be instrumental in constraining the nuclear EDF in regions inaccessible to laboratory experiments. Note that apart from the recent work of Ref. [32], we are unaware of any other calibration procedure that includes both the properties of finite nuclei and neutron stars.

Not having to rely on the bulk properties of nuclear matter in the calibration procedure implies that these properties now become genuine model predictions—with associated theoretical errors—that may be compared against results from *ab initio* calculations or other microscopic approaches [33–37]. Although not directly measurable, a determination

of the bulk properties of infinite nuclear matter provides valuable constraints on the equation of state (EOS) of dense neutron-rich matter. Moreover, some of these critical parameters are known to be strongly correlated to observables that may be directly measured. This fact provides a powerful bridge between observation, experiment, and theory. However, until very recently most of these correlations were inferred by comparing a large set of EDFs; see Ref. [14] for a particularly illustrative example. Although such an analysis provides critical insights into the *systematic* errors associated with the biases and limitations of each model, it is essential that it be supplemented with a proper *statistical* analysis. Indeed, such a covariance analysis represents the least biased and most reliable approach to uncover correlations among physical observables [21–27].

The paper has been organized as follows. Following this introduction, we outline the theoretical framework in Sec. II. We follow closely the approach developed in Ref. [27] that starts from a gaussian approximation to a suitably defined likelihood function. To demonstrate the power of the approach, we construct in Sec. III a brand new functional (*FSUGold 2*) that is calibrated from the ground-state properties of finite nuclei, their isoscalar monopole response, and a maximum neutron star mass. Finally, we conclude with a summary and outlook in Sec. IV.

II. THEORETICAL FRAMEWORK

In this section we outline the theoretical framework required to accurately calibrate an energy density functional. The section itself is divided into three components. First, we introduce the RMF model that will be used to compute all required nuclear properties—from finite nuclei to neutron stars. Second, we develop, to our knowledge for the first time in the RMF context, a transformation that links the model parameters to “pseudo data” in the form of bulk properties of infinite nuclear matter. Such a transformation enables us to implement the optimization in the space of pseudo data, resulting in a both more intuitive and more efficient approach. Finally, in the third and last subsection we describe details of the optimization procedure followed by a covariance analysis that is used to estimate both theoretical uncertainties and correlations among observables.

A. Relativistic Mean Field Theory

In the framework of the RMF theory, the basic degrees of freedom include nucleons (protons and neutrons), three “mesons”, and the photon. The nucleons are the constituents of the nuclear many-body system, which interact via the transfer of the force carriers, with the various mesons conveying the strong force between the nucleons and the photons mediating the additional electromagnetic force between the protons. The interactions among the particles can be depicted by an effective Lagrangian density of the following form [5, 6, 38–40]:

$$\begin{aligned} \mathcal{L}_{\text{int}} = & \bar{\psi} \left[g_s \phi - \left(g_v V_\mu + \frac{g_\rho}{2} \boldsymbol{\tau} \cdot \mathbf{b}_\mu + \frac{e}{2} (1 + \tau_3) A_\mu \right) \gamma^\mu \right] \psi \\ & - \frac{\kappa}{3!} (g_s \phi)^3 - \frac{\lambda}{4!} (g_s \phi)^4 + \frac{\zeta}{4!} g_v^4 (V_\mu V^\mu)^2 + \Lambda_v \left(g_\rho^2 \mathbf{b}_\mu \cdot \mathbf{b}^\mu \right) \left(g_v^2 V_\nu V^\nu \right), \end{aligned} \quad (1)$$

where ψ is the isodoublet nucleon field, A_μ is the photon field, and ϕ , V_μ , and \mathbf{b}_μ represent the isoscalar-scalar σ -, isoscalar-vector ω -, and isovector-vector ρ -meson field, respectively. The first line of the above equation contains the conventional Yukawa couplings between the nucleons and the mesons, while the second line includes some nonlinear self and mixed interactions between the mesons. In the spirit of an effective field theory, one should incorporate all possible meson interactions that are allowed by symmetry considerations to a given order in a power-counting scheme. Moreover, once the dimensionful meson fields have been properly scaled using strong-interaction mass scales, the remaining dimensionless coefficients of the effective Lagrangian should all be “natural”, namely, of order one (i.e., neither too small nor too large) [41–45]. However, given the limited experimental database of nuclear observables, certain empirical coefficients—or linear combinations of them—may remain poorly constrained after the optimization procedure. This results in “unnatural” coefficients that deviate significantly from unity. Therefore, in an effort to avoid this problem only a subset of nonlinear meson interactions is retained in the formalism. For instance, in the interaction Lagrangian density depicted in Eq. (1), one only keeps the four meson interactions denoted by the coefficients: κ , λ , ζ , and Λ_v . In particular, these terms are found to have a clear physical connection to various properties of the nuclear equation of state. Two of the isoscalar parameters, κ and λ , were introduced by Boguta and Bodmer [46] to reduce the nuclear incompressibility coefficient of symmetric nuclear matter from an unreasonably large value in the original Walecka model [5, 6] to one that can be made consistent with measurements of giant monopole resonances in finite nuclei. In turn, ζ may be used to efficiently tune the maximum neutron star mass without sacrificing the agreement with other well reproduced observables [38]. Finally, Λ_v is highly sensitive to the density dependence of symmetry

energy—and in particular to its slope at saturation density—which has important implications in the structure and dynamics of neutron stars [40, 47–49].

With the Lagrangian density given in Eq.(1), one can derive the equation of motion for each of the constituent particles in the mean-field limit [50]. The nucleons satisfy a Dirac equation in the presence of mean-field potentials having Lorentz scalar and vector character. In turn, the various mesons satisfy nonlinear and inhomogeneous Klein-Gordon equations with the various nuclear densities acting as source terms. Lastly, the photon obeys the Poisson equation with the proton density being the relevant source term. Given that the nuclear densities act as sources for the meson fields and, in turn, the meson fields determine the mean-field potentials for the nucleons, the set of equations must be solved self-consistently. Once solved, these equations determine the ground-state properties of the nucleus of interest—such as its total binding energy, single-nucleon energies and wave functions, distribution of meson fields, and density profiles.

The solution of the mean-field equations is simplified significantly in the case of infinite nuclear matter, which we assume to be spatially uniform. For this uniform case, the meson fields are uniform (i.e., constant throughout space) and the nucleon orbitals are plane-wave Dirac spinors with medium-modified effective masses and energies. By forming the energy-momentum tensor in the mean-field approximation [6], one can readily infer (in the rest frame of the fluid) the energy density and pressure of the system as a function of the conserved baryon density $\rho = \rho_n + \rho_p$ and the neutron-proton asymmetry $\alpha \equiv (\rho_n - \rho_p)/(\rho_n + \rho_p)$. In particular, the energy per nucleon of the system may be expanded in even powers of α . That is,

$$\frac{E}{A}(\rho, \alpha) - M \equiv \mathcal{E}(\rho, \alpha) = \mathcal{E}_{\text{SNM}}(\rho) + \alpha^2 \mathcal{S}(\rho) + \mathcal{O}(\alpha^4), \quad (2)$$

where $\mathcal{E}_{\text{SNM}}(\rho) = \mathcal{E}(\rho, \alpha \equiv 0)$ is the energy per nucleon of symmetric nuclear matter (SNM) and the symmetry energy $\mathcal{S}(\rho)$ represents the first-order correction to the symmetric limit. Note that no odd powers of α appear as the nuclear force is assumed to be isospin symmetric and electromagnetic effects have been “turned off”. Also note that, although model dependent, to a very good approximation the symmetry energy has a very intuitive interpretation: it represents the energy cost required to convert symmetric nuclear matter into pure neutron matter (PNM):

$$\mathcal{S}(\rho) \approx \mathcal{E}(\rho, \alpha=1) - \mathcal{E}(\rho, \alpha=0). \quad (3)$$

It is also customary to characterize the behavior of both symmetric nuclear matter and the symmetry energy in terms of a few bulk parameters. To do so, we perform a Taylor series expansion around nuclear matter saturation density ρ_0 . That is [51],

$$\mathcal{E}_{\text{SNM}}(\rho) = \varepsilon_0 + \frac{1}{2} K x^2 + \dots, \quad (4a)$$

$$\mathcal{S}(\rho) = J + Lx + \frac{1}{2} K_{\text{sym}} x^2 + \dots, \quad (4b)$$

where $x = (\rho - \rho_0)/3\rho_0$ is a dimensionless parameter that quantifies the deviations of the density from its value at saturation. Here ε_0 and K represent the energy per nucleon and the incompressibility coefficient of SNM; J and K_{sym} are the corresponding quantities for the symmetry energy. However, unlike symmetric nuclear matter whose pressure vanishes at ρ_0 , the slope of the symmetry energy L does not vanish at saturation density. Indeed, assuming the validity of Eq.(3), L is directly proportional to the pressure of PNM (P_0) at saturation density, namely,

$$P_0 \approx \frac{1}{3} \rho_0 L. \quad (5)$$

Finally, one can go a step further and apply the above formalism to neutron star matter, which we assume to consist of neutrons, protons, electrons, and muons in β equilibrium. Note that no “exotic” degrees of freedom—such as hyperons, meson condensates, or quarks—are included in the formalism. At the densities at which neutron star matter is uniform, electrons and muons may be treated as relativistic Fermi gases that contribute to the total energy density and pressure of the system. In β equilibrium only the baryon density needs to be specified, as the neutron-proton asymmetry is adjusted to minimize the total energy density of the system. Given that uniform neutron-rich matter is unstable against cluster formation, we supplement our RMF predictions for the EOS with the standard parametrization for the outer crust by Baym, Pethick, and Sutherland [52]. Finally, we resort to a polytropic EOS to interpolate between the solid outer crust and the uniform liquid core [48, 53]. Given that the EOS is the only input required to solve the Tolman-Oppenheimer-Volkoff equation, one can predict a variety of neutron star properties that can then be compared against observation. Particularly relevant in this work will be the predictions for the maximum stellar mass and the radius of a “canonical” $1.4 M_\odot$ neutron star.

B. An Insightful Transformation

The main goal of the present work is the accurate calibration of a relativistic EDF by relying exclusively on measured properties of finite nuclei and neutron stars. The fitting protocol requires both the specification of a theoretical model and the selection of physical observables to constrain the fit. The conventional approach to the calibration of the EDF consists of first minimizing the objective function and then validating the model against observables not included in the fit. Traditionally, the optimization of the model is carried out in parameter space. That is, one searches for those model parameters (e.g., g_s, g_v, \dots) that minimize the objective function. Given that the connection between the model parameters and our physical intuition is tenuous at best, the searching algorithm often ends up wandering aimlessly in search of the minimum. A remarkable, but little known, fact in the framework of the RMF theory is that many of the model parameters can be expressed in terms of a few bulk properties of infinite nuclear matter [54]. Although relatively new, it appears that such a transformation between the model parameters and the bulk properties of infinite nuclear matter (or “pseudo data”) is better known in the case of the non-relativistic Skyrme interaction [2, 55, 56]. To avoid interrupting the flow of the narrative, we only summarize here the central points of the transformation. A detailed account of the transformation has been reserved to the appendix.

For the Lagrangian density given in Eq. (1), we identify five isoscalar ($g_s, g_v, \kappa, \lambda$, and ζ) and two isovector (g_ρ and Λ_v) parameters. Note that in a mean-field approximation, the properties of infinite nuclear matter are only sensitive to the combinations g_s^2/m_s^2 , g_v^2/m_v^2 , and g_ρ^2/m_ρ^2 . The transformation starts in the isoscalar sector and links the first four isoscalar parameters listed above with four bulk properties of symmetric nuclear matter; these are the density ρ_0 , the binding energy per nucleon ε_0 , the effective nucleon mass M^* , and the incompressibility coefficient K —all evaluated at saturation density. The fact that the pressure of SNM vanishes at saturation density implies, through the Hugenholtz-van Hove theorem, that the energy per nucleon must equal the nucleon Fermi energy. This fact, together with the classical equation of motion for the vector field, is sufficient to determine g_v^2/m_v^2 , for a given value of ζ . Note that ζ will remain as a model parameter throughout the optimization. To determine the three scalar parameters (g_s, κ, λ) one requires three pieces of information. These are (a) the binding energy per nucleon at saturation, (b) the classical equation of motion for the scalar field, and (c) the incompressibility coefficient. Although the algebraic manipulations are involved, they ultimately yield a system of three simultaneous linear equations [54]. That is, the solution is *unique*. Once the transformation has been completed in the isoscalar sector, one may proceed to determine the two remaining (isovector) parameters g_ρ^2/m_ρ^2 and Λ_v in terms of the value of symmetry energy J and its slope L at saturation density. This derivation—that to our knowledge has never been published in the literature—benefits greatly from the fact that the symmetry energy has a relatively simple analytic form [47]; for further details see the appendix.

In summary, we have carried out a transformation between the model parameters defining the Lagrangian density and various bulk parameters of infinite nuclear matter. Assuming that the nucleon mass as well as the masses of the two vector mesons in free space are fixed at their experimental value, i.e., $M = 939$ MeV, $m_v = 782.5$ MeV and $m_\rho = 763$ MeV, a point in an 8-dimensional Lagrangian parameter space may be written as follows: $\mathbf{q} = (m_s, g_s^2/m_s^2, g_v^2/m_v^2, g_\rho^2/m_\rho^2, \kappa, \lambda, \Lambda_v, \zeta)$. As already mentioned, in a mean-field approximation the bulk properties of infinite nuclear matter are only sensitive to the combination g_s^2/m_s^2 . Hence, the range of the intermediate-range attraction, expressed as the Compton wavelength of the scalar meson $r_s = \hbar c/m_s c^2$, can only be determined from the properties of finite nuclei, primarily from their charge radii. Moreover, given that most bulk properties of infinite nuclear matter at saturation density depend weakly on the value of ζ [38], the value of ζ must be determined from observables sensitive to the high-density component of the EOS, such as the maximum neutron star mass. In this way, the transformation enables one to write a point in the space of pseudo data as: $\mathbf{p} = (m_s, \rho_0, \varepsilon_0, M^*, K, J, L, \zeta)$. Note that the very existence of such transformation allows us to perform the model optimization in the space of pseudo data rather than in the Lagrangian parameter space.

There are several advantages to represent a point in parameter space in terms of \mathbf{p} rather than \mathbf{q} . First, that a unique algebraic solution exists for the Lagrangian parameters in terms of bulk properties of nuclear matter makes the theory well defined. Second, the parameters have evolved from abstract coupling constants to quantities with a precise physical meaning and with values narrowed down by experiment to a fairly small range. Thus, running the optimization in the space of pseudo data increases significantly the efficiency of the searching algorithm. Finally, given that the fitting protocol relies exclusively on experimental and observational data, the culmination of the optimization procedure provides bona-fide *theoretical predictions* for all bulk properties with meaningful error bars. These predictions may be compared against other theoretical approaches that could provide a bridge between *ab initio* calculations and phenomenological approaches.

C. Optimization and Covariance Analysis

The aim of the optimization procedure is to determine the set of model parameters that minimizes the objective function, or *goodness-of-fit parameter* χ^2 , that is defined as follows:

$$\chi^2(\mathbf{p}) \equiv \sum_{n=1}^N \frac{\left(\mathcal{O}_n^{(\text{th})}(\mathbf{p}) - \mathcal{O}_n^{(\text{exp})} \right)^2}{\Delta \mathcal{O}_n^2}, \quad (6)$$

where $\mathbf{p} = (p_1, \dots, p_F)$ is a point in the F -dimensional parameter space, $\mathcal{O}_n^{(\text{exp})}$ is the measured experimental value of the n -th observable (out of a total of N), and $\mathcal{O}_n^{(\text{th})}(\mathbf{p})$ the corresponding theoretical prediction. Although in principle the adopted error $\Delta \mathcal{O}_n$ is associated with the experimental uncertainty, in practice it must be supplemented by a “theoretical” contribution. The main reason for adding a theoretical error is that the objective function is weighted by the error associated with each observable: the smaller the error the larger the weight. Given that certain observables, such as nuclear binding energies, are known with enormous precision, the minimization of the objective function could be biased by such observables. However, it is important to recognize that no universal protocol exists for the selection of theoretical errors, although Ref. [26] provides a useful guiding principle. Most of the formalism required for the use of *information and statistics* in theoretical nuclear physics may be found in [21–23, 26, 27] and in references contained therein. In turn, most of the central ideas presented in those references are contained in the two excellent texts by Brandt [57] and Bevington [58]. However, in the interest of clarity we present a succinct summary of the main concepts.

A concept of great pedagogical significance and closely connected to the objective function is the *likelihood function*:

$$\mathcal{L}(\mathbf{p}) = e^{-\frac{1}{2}\chi^2(\mathbf{p})}. \quad (7)$$

Clearly, minimizing the objective function $\chi^2(\mathbf{p})$ is fully equivalent to maximizing the likelihood function $\mathcal{L}(\mathbf{p})$. However, the great merit of the likelihood function is that it may be regarded as a probability distribution. That is, given two arbitrary parameter sets (or “models”) \mathbf{p}_1 and \mathbf{p}_2 , the likelihood function provides the *relative* probability that the given models reproduce the given experimental data. In particular, the optimal (or most likely) parameter set is the one that maximizes the likelihood function. Using the probabilistic nature of the likelihood function one can efficiently sample the full parameter space via, for example, a standard Metropolis Monte Carlo algorithm. Averages, variances, and correlation coefficients can then be computed in a standard fashion. For example, if $\{\mathbf{p}_1, \mathbf{p}_2, \dots, \mathbf{p}_M\}$ represent the M models generated by the sampling algorithm, then the average of a generic observable A is simply given by

$$\langle A \rangle = \lim_{M \rightarrow \infty} \frac{1}{M} \sum_{m=1}^M A(\mathbf{p}_m). \quad (8)$$

Although the method of maximum likelihood along with a sampling algorithm is simple and insightful, generating a large set of model parameters, except in a few simple cases, is highly impractical. Indeed, certain observables adopted in the fit, such as giant monopole energies, are computationally expensive to evaluate. For such cases one must resort to other methods to minimize the objective function, so we rely on the well-known gaussian approximation where the parameter exploration is limited to the immediate vicinity of the χ^2 minimum. Denoting by \mathbf{p}_0 the *optimal* parameter set, the gaussian approximation consists of studying the small (quadratic) oscillations around the χ^2 minimum. That is,

$$\chi^2(\mathbf{p}) \approx \chi^2(\mathbf{p}_0) + \frac{1}{2} \sum_{i,j=1}^F (\mathbf{p} - \mathbf{p}_0)_i (\mathbf{p} - \mathbf{p}_0)_j \left(\frac{\partial^2 \chi^2}{\partial p_i \partial p_j} \right)_0 \equiv \chi_0^2 + \mathbf{x}^T \hat{\mathcal{M}}_0 \mathbf{x}, \quad (9)$$

where we have introduced the following dimensionless scaled variables:

$$x_i \equiv \frac{(\mathbf{p} - \mathbf{p}_0)_i}{(\mathbf{p}_0)_i}. \quad (10)$$

Note that the behavior of the χ^2 function around its minimum value is determined by the *curvature matrix* $\hat{\mathcal{M}}_0$, whose matrix elements are defined in terms of its second derivatives evaluated at the optimal point. That is,

$$(\hat{\mathcal{M}}_0)_{ij} \equiv \frac{1}{2} \left(\frac{\partial^2 \chi^2}{\partial x_i \partial x_j} \right)_0. \quad (11)$$

In this work we employ the *Levenberg-Marquardt* method [59] to minimize the objective function. Initially the algorithm uses the inverse Hessian method and then switches continuously to the method of steepest decent on its way toward the minimum. Furthermore, we take advantage of the fact that the objective function to be minimized is neither arbitrary nor totally unknown. Rather, it is defined directly in terms of the physical observables appearing in the definition of the objective function given in Eq. (6). This fact enables us to write the curvature matrix—which is essential for both the optimization and the covariance analysis—as follows:

$$\mathcal{M}_{ij} = \sum_{n=1}^N \frac{1}{\Delta \mathcal{O}_n^2} \left[\left(\frac{\partial \mathcal{O}_n^{(\text{th})}}{\partial x_i} \right) \left(\frac{\partial \mathcal{O}_n^{(\text{th})}}{\partial x_j} \right) + \left(\mathcal{O}_n^{(\text{th})} - \mathcal{O}_n^{(\text{exp})} \right) \left(\frac{\partial^2 \mathcal{O}_n^{(\text{th})}}{\partial x_i \partial x_j} \right) \right]. \quad (12)$$

Notice that $(\mathcal{O}_n^{(\text{th})} - \mathcal{O}_n^{(\text{exp})})$ in the above expression represents the difference between the experimental value and the theoretical prediction of a given observable. Assuming that the model is rich enough to reasonably describe the set of observables included in the fit, then this term should be small. Moreover, we may expect that such a deviation is not only small but also random in sign. Therefore, the contributions from all observables to the second term in Eq. (12) will tend to cancel each other and the curvature matrix may be computed without ever having to evaluate any second derivatives of $\mathcal{O}_n^{(\text{th})}$. That is, in the linear approximation one obtains [57, 58]

$$\mathcal{M}_{ij} \approx \sum_{n=1}^N \frac{1}{\Delta \mathcal{O}_n^2} \left(\frac{\partial \mathcal{O}_n^{(\text{th})}}{\partial x_i} \right) \left(\frac{\partial \mathcal{O}_n^{(\text{th})}}{\partial x_j} \right). \quad (13)$$

The Levenberg-Marquardt method along with this simplified expression for the curvature matrix has been shown to be very stable and efficient, and has become one of the standard routines for nonlinear optimization [59].

As mentioned earlier in the Introduction, the importance of including theoretical uncertainties in the prediction of physical quantities is gaining significant momentum. Knowledge of the curvature matrix is all that is needed to compute any statistical quantity, at least in the gaussian approximation. For example, the *covariance* between any two observables A and B is given by

$$\text{cov}(A, B) = \text{cov}(B, A) = \sum_{i,j=1}^F \left(\frac{\partial A}{\partial x_i} \right)_0 \Sigma_{ij} \left(\frac{\partial B}{\partial x_j} \right)_0, \quad (14)$$

where the *covariance matrix* $\hat{\Sigma} = \hat{\mathcal{M}}_0^{-1}$ is equal to the inverse of the curvature matrix evaluated at the optimal point. In the case in which $A = B$, this equation gives the *variance* of A which equals the square of its uncertainty. That is, $\text{cov}(A, A) \equiv \text{var}(A) = \sigma_A^2$. Note that the theoretical errors (σ_A) that will be reported in the next section have been computed in precisely this manner. Finally, given the covariance between A and B and their corresponding variances, the *Pearson product moment correlation coefficient* (or simply the correlation coefficient) is given by [57]

$$\rho(A, B) = \frac{\text{cov}(A, B)}{\sigma_A \sigma_B}. \quad (15)$$

In identifying a connection between two observables, the correlation coefficient provides a unique opportunity to infer the value of an observable that may not be accessible in either experiments or observations. Moreover, the correlation coefficient has an intuitive geometric interpretation. Suppose that a large number of M values for both A and B are generated according to the likelihood function \mathcal{L} . Then, by defining the following two unit vectors in M -dimensions

$$a_m = \frac{1}{\sqrt{M}} \left(\frac{A_m - \langle A \rangle}{\sigma_A} \right) \text{ and } b_m = \frac{1}{\sqrt{M}} \left(\frac{B_m - \langle B \rangle}{\sigma_B} \right), \quad (16)$$

the correlation coefficient becomes equal to the cosine of the angle between these two unit vectors. That is,

$$\rho(A, B) = \hat{a} \cdot \hat{b} \equiv \cos(\hat{a}, \hat{b}). \quad (17)$$

In particular, a value of $\rho(A, B) = \pm 1$ implies that the two observables are fully correlated/anti-correlated, whereas a value of $\rho(A, B) = 0$ means that the observables are totally uncorrelated. In the next section we will implement a covariance analysis to estimate theoretical uncertainties (i.e., “errors”) in the model parameters, the fitting observables, as well as a variety of observables that were not included in the calibration procedure. Moreover, we will examine correlations between: (i) observables, (ii) model parameters, and (iii) observables and model parameters. All three sets of correlations are insightful and provide complementary information on the strengths and weaknesses of the

model. In the first case, a strong correlation between two experimentally accessible observables prevents redundancy. However, if one of the observables is not accessible either experimentally or observationally, a strong correlation provides a clear path for its determination. In the case of correlations among model parameters the situation is vastly different. Indeed, rather than suggesting redundancy, a strong correlation between model parameters underscores the need for both. Finally, correlations between observables and model parameters reveal the sensitivity of the parameters to a particular kind of physics. Relying on such a covariance analysis makes possible to connect a variety of physical phenomena to the underlying microscopic theory and provides a unique and powerful tool for improving the quality of the models.

III. RESULTS

Having developed in the previous section most of the required formalism, we are now in a position to implement the calibration of a new relativistic energy density functional. We provide details that involve the optimization and the subsequent covariance analysis. Whenever appropriate, we supplement our results with properly estimated theoretical errors. Moreover, in a few instances, we provide correlation coefficients involving both observables and model parameters. The new relativistic EDF may be regarded as an improvement over the almost one-decade old FSUGold parametrization [10]. Accordingly, we name this newer version as *FSUGold 2*.

A. FSUGold 2: An accurately calibrated interaction for finite nuclei and neutron stars

Based on the relativistic Lagrangian density given in Eq. (1), there are a total of 11 model parameters: seven coupling constants, one nucleon mass, and three meson masses. The mass of the nucleon will be fixed at its free space value of $M = (M_p + M_n)/2 \approx 939$ MeV. Given the effective character of the theory, the three meson masses should in principle be treated as model parameters that should be determined by the fitting procedure. However, we have found—as many others have found before us—that with the exception of the scalar meson, the masses of the two vector mesons (m_v and m_ρ) may be fixed near their experimental values: $m_v \approx 782.5$ MeV and $m_\rho \approx 763$ MeV. Note that the mass of the scalar meson controls the range of the scalar attraction and is therefore critical for an accurate reproduction of charge radii [6]. As mentioned earlier, having fixed the masses of the vector mesons, the transformation between model parameters \mathbf{q} and pseudo data \mathbf{p} may be represented as follows: $\mathbf{q} = (m_s, g_s^2/m_s^2, g_v^2/m_v^2, g_\rho^2/m_\rho^2, \kappa, \lambda, \Lambda_v, \zeta) \leftrightarrow \mathbf{p} = (m_s, \rho_0, \varepsilon_0, M^*, K, J, L, \zeta)$. In essence, the objective function $\chi^2(\mathbf{p})$ is a function of the pseudo data, but the theoretical predictions depend on the model parameters \mathbf{q} . The transformation outlined in the appendix uniquely determines \mathbf{p} in terms of \mathbf{q} , and *vice versa*.

Having defined the parameters that must be optimized, we must now introduce the experimental and observational data that will be used to constrain the fit. The fitting observables that we use in the optimization include (a) binding energies, (b) charge radii, and (c) giant monopole resonance (GMR) of semi- and doubly-magic nuclei across the nuclear chart, and (d) the maximum neutron star mass observed up to date. Note that all these observables are genuine experimental or observational quantities; no properties of infinite nuclear matter are incorporated in the definition of the objective function. The ground-state properties and collective excitations of finite nuclei are effective in constraining the EOS of nuclear matter around saturation density with small to moderate values of the neutron-proton (i.e., isospin) asymmetry. On the other hand, neutron star properties—such as the maximum neutron star mass—may be used to constrain the high-density component of the EOS of neutron-rich matter. We believe that no laboratory experiment may constrain the EOS of cold, fully catalyzed, nuclear matter at high densities.

One of the greatest challenges involved in the definition of the χ^2 function introduced in Eq. (6) is the choice of errors $\Delta\mathcal{O}_n$ associated with each observable \mathcal{O}_n . Given the remarkable precision that has been achieved in measuring binding energies and charge radii, the χ^2 function would be dominated by the terms associated with these two sets of observables if we naively adopt their associated experimental errors. Although the optimization could still be carried out in such case, the overall quality of the EDF would be poor, as binding energies and charge radii would be well reproduced at the expense of all remaining observables. Therefore, in order to mitigate this deficiency one should manipulate the errors in such a way that the relative weights of all observables be commensurate with each other. By necessity, this implies some “trial and error” as there is no clear choice for the optimal protocol [26]. The choice of error for each observable adopted in the fit is discussed below.

Once the objective function has been properly defined by specifying a theoretical model and a set of observables with properly defined errors, the Levenberg-Marquardt method was used to obtain the optimal set of parameters $\mathbf{p} = (m_s, \rho_0, \varepsilon_0, M^*, K, J, L, \zeta)$. In turn, the model parameters \mathbf{q} may be obtained from the transformation outlined in the appendix. The resulting set of model parameters for the newly built functional FSUGold 2 (or “FSU2” for short) are displayed in Table I. Also shown for comparison are two canonical sets of parameters, NL3 [8] and FSUGold (or

“FSU” for short) [10]. Given that the EOS for symmetric nuclear matter and the symmetry energy are both stiff in the case of NL3 and both soft for FSU, such a comparison is very informative. However, when comparing these models, one should keep in mind that different models are calibrated using different sets of observables and associated errors. This introduces some inherent biases into the models that ultimately become an important source of systematic errors.

Model	m_s	m_v	m_ρ	g_s^2	g_v^2	g_ρ^2	κ	λ	ζ	Λ_v
NL3	508.194	782.501	763.000	104.3871	165.5854	79.6000	3.8599	-0.015905	0.0000	0.000000
FSU	491.500	782.500	763.000	112.1996	204.5469	138.4701	1.4203	+0.023762	0.0600	0.030000
FSU2	497.479	782.500	763.000	108.0943	183.7893	80.4656	3.0029	-0.000533	0.0256	0.000823

TABLE I. Model parameters for the newly optimized FSUGold 2 relativistic EDF along with two accurately calibrated RMF models: NL3 [8] and FSUGold [10]. The parameter κ and the meson masses m_s , m_v , and m_ρ are all given in MeV. The nucleon mass has been fixed at $M=939$ MeV in all the models.

B. Ground-State Properties

We start this section by displaying in Table II ground-state binding energies and charge radii for all the nuclei involved in the optimization. Experimental data for these observables were obtained from the latest atomic mass evaluation [60] and charge radii compilation [61], respectively. In turn, the errors assigned to the binding energies and charge radii are 0.1% and 0.2%, respectively. As mentioned earlier, these adopted errors are several orders of magnitude larger than the quoted experimental uncertainties [60, 61]. Only by doing so one can prevent the optimization from being dominated by these two ground-state observables. Also displayed in Table II are the theoretical predictions from all three models. Note that because the influence of pairing correlations in both the binding energies and charge radii are very small, we did not take pairing into consideration for the open-shell nuclei ^{116}Sn and ^{144}Sm . Also note that the theoretical errors predicted by FSU2 (of about one part in a thousand) are too small to be displayed in the table. Also note that the quoted theoretical value for the charge radius was obtained by adding to the extracted nuclear point proton radius the intrinsic charge radius of the proton $r=0.8783(86)$ fm [61]. That is, $R_{\text{ch}}=(R_p^2+r^2)^{1/2}$. We can see that both the binding energies and charge radii are very well reproduced by all the models. In the particular case of FSU2, with the exception of the charge radius of ^{16}O , the discrepancy relative to experiment is less than 0.5%. The slightly larger than 1% deviation in the case of ^{16}O should not come as a surprise, as with only 16 nucleons oxygen barely qualifies as a “mean-field” nucleus. It is important to stress that neither binding energies nor charge radii have a significant impact on the stiffness of the EOS. Indeed, NL3 and FSU predict significantly different stiffness for the EOS (see below) yet they both reproduce fairly accurately the experimental results for these two observables.

C. Giant Monopole Resonances

In optimizing the FSUGold 2 functional, we have also incorporated GMR energies for ^{90}Zr , ^{116}Sn , ^{144}Sm , and ^{208}Pb . In Table III we display *constrained* GMR energies $E_{\text{GMR}}=\sqrt{m_1/m_{-1}}$ extracted from measurements at the Texas A&M University (TAMU) cyclotron facility [62] and at the Research Center for Nuclear Physics (RCNP) in Osaka, Japan [63–67]. Here m_1 and m_{-1} are suitable moments of the strength distribution that represent the energy weighted and inverse energy weighted sums, respectively. The theoretical results listed on the table were obtained by following the constrained RMF formalism developed in Ref. [68]. Moreover, it was found in Ref. [69] that pairing correlations have a very minor impact on the GMR energies. Therefore, pairing was not included in the case of the open-shell nuclei ^{116}Sn and ^{144}Sm . The same information has been displayed in graphical form in Fig. 1. Note that the red solid line in the figure represents a fit to the FSU2 predictions of the form $E_{\text{fit}}=72.8A^{-0.31}$ MeV; this compares favorably against the macroscopic expectation of $E_{\text{GMR}}\approx 80A^{-1/3}$ MeV [70, 71]. We find both intriguing and unsettling that the TAMU and RCNP data—particularly for ^{208}Pb —are inconsistent with each other. Given the critical nature of this information, we trust that the discrepancy may be resolved in the near future. In the meantime, and to account for the experimental discrepancy, we have adopted slightly larger errors in the optimization of the functional, namely, 2% for ^{90}Zr and 1% for the rest.

Our results indicate that the predictions from FSU and FSU2 are compatible with each other. This is consistent with the notion that GMR energies probe the incompressibility coefficient of SNM, that is, K (see Table IV). Moreover, with the exception of ^{116}Sn , both FSU and FSU2 reproduce the experimental data, although they both favor the smaller

Nucleus	Observable	Experiment	NL3	FSU	FSU2
^{16}O	B/A	7.98	8.06	7.98	8.00
	R_{ch}	2.70	2.75	2.71	2.73
^{40}Ca	B/A	8.55	8.56	8.54	8.54
	R_{ch}	3.48	3.49	3.45	3.47
^{48}Ca	B/A	8.67	8.66	8.58	8.63
	R_{ch}	3.48	3.49	3.48	3.47
^{68}Ni	B/A	8.68	8.71	8.66	8.69
	R_{ch}	—	3.88	3.88	3.86
^{90}Zr	B/A	8.71	8.70	8.68	8.69
	R_{ch}	4.27	4.28	4.27	4.26
^{100}Sn	B/A	8.25	8.30	8.24	8.28
	R_{ch}	—	4.48	4.48	4.47
^{116}Sn	B/A	8.52	8.50	8.50	8.49
	R_{ch}	4.63	4.63	4.63	4.61
^{132}Sn	B/A	8.36	8.38	8.34	8.36
	R_{ch}	4.71	4.72	4.74	4.71
^{144}Sm	B/A	8.30	8.32	8.32	8.31
	R_{ch}	4.95	4.96	4.96	4.94
^{208}Pb	B/A	7.87	7.90	7.89	7.88
	R_{ch}	5.50	5.53	5.54	5.51

TABLE II. Experimental data for the binding energy per nucleon (in MeV) [60] and charge radii (in fm) [61] for all the nuclei involved in the optimization. Also displayed are the theoretical results obtained with NL3 [8], FSUGold [10], and FSUGold2.

RCNP measurement in the case of ^{208}Pb . Note that the answer to the question of *Why is Tin so soft?*” [51, 64, 65] continues to elude us to this day [69, 72–78]. By the same token NL3, with a significantly larger value of K than both FSU and FSU2, overestimates the experimental data—except in the case of the TAMU data for ^{208}Pb [79]. Although in principle GMR energies of neutron-rich nuclei probe the incompressibility coefficient of *neutron-rich matter* [51], in practice the neutron-proton asymmetry for these nuclei is simply too small to provide any meaningful constraint on the density dependence of the symmetry energy. This is the main reason behind the agreement between FSU and FSU2, even though they predict radically different values for the slope of the symmetry energy L (see Table IV).

Nucleus	TAMU	RCNP	NL3	FSU	FSU2
^{90}Zr	17.81 ± 0.35	—	18.76	17.86	17.93 ± 0.09
^{116}Sn	15.90 ± 0.07	15.70 ± 0.10	17.19	16.39	16.47 ± 0.08
^{144}Sm	15.25 ± 0.11	15.77 ± 0.17	16.29	15.55	15.59 ± 0.09
^{208}Pb	14.18 ± 0.11	13.50 ± 0.10	14.32	13.72	13.76 ± 0.08

TABLE III. Constrained energies $E_{\text{GMR}} = \sqrt{m_1/m_{-1}}$ (in MeV) for the giant monopole resonance in ^{90}Zr , ^{116}Sn , ^{144}Sm , and ^{208}Pb obtained from experiments at TAMU [62] and RCNP [63–67]. Theoretical results were obtained by following the constrained RMF formalism developed in Ref. [68].

D. Neutron Star Structure

The last observable that was included in the calibration of the new FSU2 functional was the maximum neutron star mass. Displayed in Fig. 2 with horizontal bars are the two most massive, and accurately measured, neutron stars [18, 19]. Clearly, those observations place stringent constraints on the high-density component of the EOS, as models that predict limiting masses below $2 M_{\odot}$ —such as FSUGold—must be stiffened accordingly. Therefore, for the optimization of the FSU2 functional, we have adopted a value of $M_{\text{max}} = 2.10 M_{\odot}$ with a relatively small 1% error. If required by future observations, this input can be easily modified by a suitable tuning of the quartic vector coupling constant ζ .

Also displayed in Fig. 2 are theoretical predictions for the mass-vs-radius (M-R) relations for the three models considered in the text. As alluded earlier, with a stiff EOS NL3 predicts large stellar radii and a maximum neutron star mass of almost $3 M_{\odot}$. In contrast, FSUGold with a relatively soft EOS predicts smaller values for both. The new FSUGold 2 functional displays a M-R relation that appears intermediate between NL3 and FSUGold. In particular,

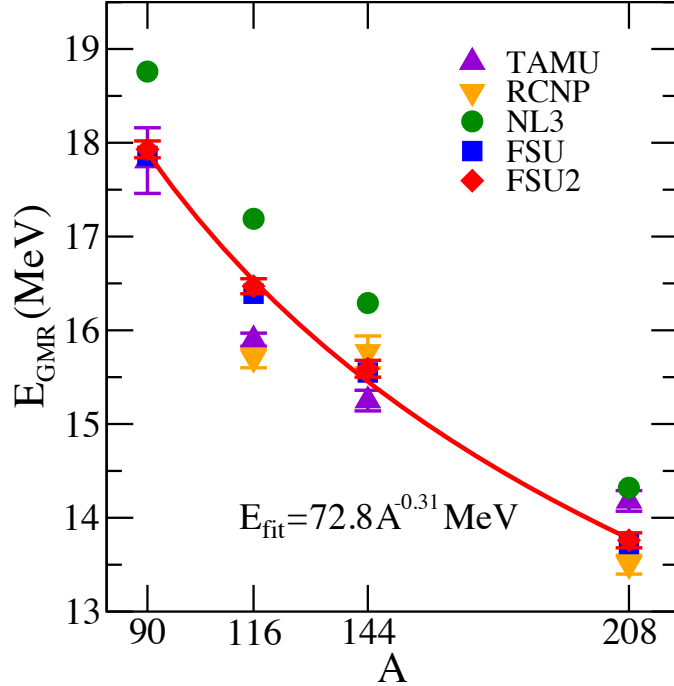


FIG. 1. (Color online) Constrained giant monopole energies for ^{90}Zr , ^{116}Sn , ^{144}Sm , and ^{208}Pb . Experimental data were obtained from experiments carried out at TAMU [62] and RCNP [63–67]. Theoretical predictions are presented for NL3 [8], FSUGold [10], and FSUGold 2 supplemented with theoretical errors. The red solid line represents a best fit to the FSUGold 2 predictions of the form $E_{\text{fit}} = 72.8A^{-0.31} \text{ MeV}$.

after the optimization we obtain a maximum stellar mass of $M_{\text{max}} = (2.07 \pm 0.02) M_{\odot}$, safely within the bounds set by observation. Given the large impact that the quartic vector coupling constant ζ has on the EOS at high densities, these results are totally consistent with our expectations (see Table I). On the other hand, stellar radii seem to be controlled by the density dependence of the symmetry energy in the immediate vicinity of saturation density [80]. Thus models with large values of L tend to predict neutron stars with large radii [47]. This is the main reason behind the relatively uniform “shift” between FSU and FSU2 (see Table IV.) It is important to realize that no observable highly sensitive to the density dependence of the symmetry energy, such as the neutron-skin thickness of ^{208}Pb or stellar radii, was used in the calibration of FSU2. Such a choice was deliberate, as at present there are no stringent experimental or observational constraints on the isovector sector of the nuclear density functional. Although the Lead Radius Experiment (“PREX”) at the Jefferson Laboratory has provided the first model-independent evidence on the existence of a neutron-rich skin in ^{208}Pb [81, 82], the determination came with an error that is too large to impose any significant constraint. That is,

$$R_{\text{skin}}^{208} = 0.33^{+0.16}_{-0.18} \text{ fm}. \quad (18)$$

In the case of stellar radii, the present situation is highly unsatisfactory as further illustrated in Fig. 2. First, an initial attempt by Özel and collaborators to determine simultaneously the mass and radius of three x-ray bursters resulted in predictions for stellar radii between 8 and 10 km [28]. Shortly after, Steiner et al. supplemented Özel’s study with three additional neutron stars and concluded that systematic uncertainties make the most probable radii lie in the 11–12 km region [29]. However, even this more conservative estimate has been put into question by Suleimanov and collaborators, who suggested a *lower limit* on the stellar radius of 14 km on neutron stars with masses below $2.3 M_{\odot}$ [30]. That is, three different analyses of (mostly) the same sources seem to differ in their conclusions by more than 5 km in the radius of a typical neutron star. Recognizing this unacceptable situation and the many challenges posed by the study of x-ray bursters, Guillot and collaborators concentrated on the determination of stellar radii by studying five quiescent low mass x-ray binaries (qLMXB) in globular clusters. By clearly and explicitly stating all their assumptions, some of them apparently not without controversy [83], Guillot et al. were able to determine a rather small neutron star radius of [31]:

$$R_0 = 9.1^{+1.3}_{-1.5} \text{ km}. \quad (19)$$

Note that this value represents the “common” radius of all neutron stars, a critical assumption in the analysis of

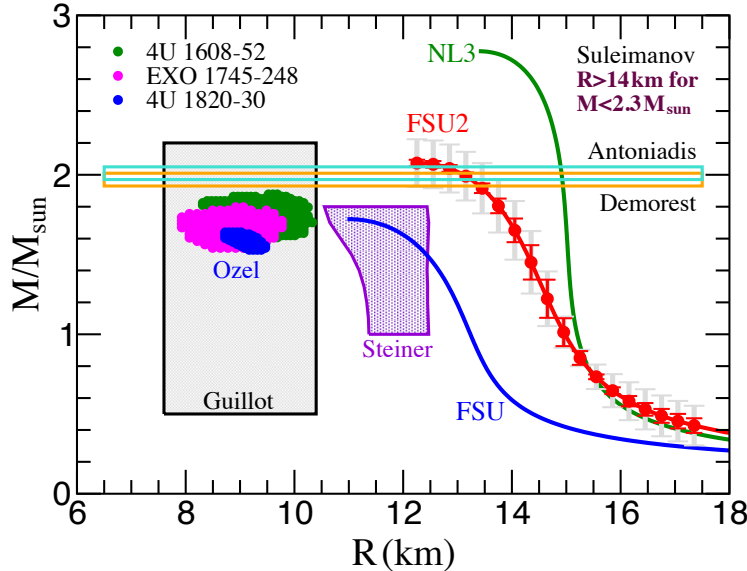


FIG. 2. (Color online) Mass-vs-radius relation predicted by the three models considered in the text: NL3 [8], FSUGold [10], and FSUGold 2. Also shown are recent observational constraints on neutron star masses [18, 19] and radii [28–31]. The FSUGold 2 results are supplemented with two sets of theoretical errors: one (red) in which the maximum neutron star mass was included in the calibration of the functional and the other (grey) estimated also using FSUGold 2, but with the impact of the maximum neutron star mass being removed from the curvature matrix, as explained in the text.

Ref. [31]. Given such an unfortunate state of affairs concerning stellar radii, we have then decided against including such information into the calibration of FSUGold 2. This, of course, does not prevent us from offering FSU2 predictions for stellar radii, as displayed in Fig. 2. In particular, we find the radius of a “canonical” $1.4 M_{\odot}$ neutron star to be $R_{1.4} = (14.42 \pm 0.26)$ km. Note that the large stellar radii predicted by FSU2 satisfy the constraint set by Suleimanov et al., but only for neutron stars with masses below $\simeq 1.8 M_{\odot}$. Moreover, we should mention that although no assumptions on either the neutron-skin thickness of ^{208}Pb or stellar radii were incorporated into the calibration of FSUGold 2, a manuscript that contemplates various possible scenarios is in preparation.

Finally, we close this section by exploring the impact of the maximum neutron star mass M_{\max} on the estimation of errors. Recall that M_{\max} is the only observable included in the calibration that is sensitive to the high-density component of the EOS. Although we preserve the same optimal set of parameters as FSUGold 2, we assess the impact of M_{\max} by removing its contribution to the curvature matrix. This invariably results in some flattening of certain directions in parameter space. In particular, the additional set of theoretical errors displayed (in grey) in Fig. 2 were estimated in precisely this manner. As expected, the (grey) theoretical “error band” becomes significantly thicker when the maximum neutron star mass is removed from consideration. Particularly, the uncertainty in M_{\max} is increased significantly from 0.02 to $0.15 M_{\odot}$ and the error in the radius of a $1.4 M_{\odot}$ neutron star becomes almost three times as large. It is clear that the inclusion of M_{\max} in the calibration of the functional is essential to constrain the high-density component of the EOS. Indeed, we believe that no terrestrial experiment can reliably constrain the EOS of neutron star matter.

E. Predictions and Correlations

With the exception of stellar radii, up till now we have concentrated on physical observables that were included in the calibration of the density functional. In the present section we shift our attention to genuine theoretical predictions of a variety of observables that were not incorporated into the fit. We start by displaying in Table IV a few bulk properties of nuclear matter at saturation density. These properties are of critical importance in constraining the EOS of neutron-rich matter and the covariance analysis developed here serves to determine whether the physical observables incorporated into the fit impose meaningful constraints on these properties. We note that the four isoscalar properties that characterize the EOS of SNM (i.e., ρ_0 , ε_0 , M^*/M , and K) are all accurately determined (to about 1%). In particular, we attribute the small theoretical error associated with the incompressibility coefficient ($K = 238.0 \pm 2.8$ MeV) to the inclusion of GMR energies into the calibration of FSUGold 2. Moreover, we find good agreement with the isoscalar predictions from both NL3 and FSU except in the case of K for NL3.

Model	$\rho_0(\text{fm}^{-3})$	ε_0 (MeV)	M^*/M	K (MeV)	J (MeV)	L (MeV)
NL3	0.1481	-16.24	0.595	271.5	37.28	118.2
FSU	0.1484	-16.30	0.610	230.0	32.59	60.5
FSU2	0.1505 ± 0.0007	-16.28 ± 0.02	0.593 ± 0.004	238.0 ± 2.8	37.62 ± 1.11	112.8 ± 16.1

TABLE IV. Bulk properties of nuclear matter predicted by the models: NL3 [8], FSUGold [10], and FSUGold2. The results from FSUGold2 are supplemented with their theoretical errors.

However, the situation is radically different in the isovector sector. Although the ground-state properties of neutron-rich nuclei, such as ^{48}Ca , ^{132}Sn , ^{208}Pb , are able to constrain the value of the symmetry energy J to about 3%, its slope L remains poorly constrained (to about 15%). We attribute this situation to the lack of well measured isovector observables, such as the neutron skin of heavy nuclei. We reiterate that when relativistic models of the kind given in Eq. (1) do not incorporate strong isovector constraints, they tend to generate a fairly stiff symmetry energy. Note that although the density dependence of the symmetry energy remains rather uncertain, all three models considered in the table are consistent at a sub-saturation density of $\tilde{\rho}_0 \approx 0.10 \text{ fm}^{-3} \approx 2\rho_0/3$. Indeed, according to Eq. (4b) one obtains

$$\tilde{J} \equiv \mathcal{S}(\tilde{\rho}_0) \approx J + L \frac{(\tilde{\rho}_0 - \rho_0)}{3\rho_0} \approx \left(J - \frac{L}{9} \right) \approx (25-26) \text{ MeV}. \quad (20)$$

This point has been emphasized repeatedly in various references [11, 12, 40, 85–88]. That is, the above correlation between J and L that emerges from the masses of neutron-rich nuclei determines rather accurately the value of the symmetry energy at an average between the central nuclear density ρ_0 and some characteristic density at the surface. Clearly, more information is required to determine both J and L .

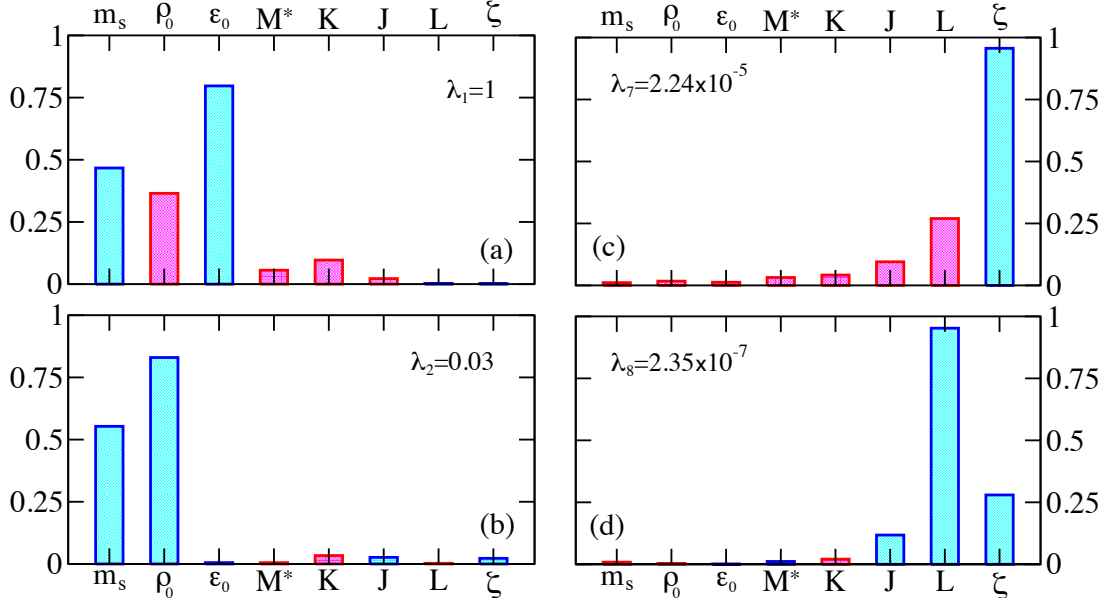


FIG. 3. (Color online) Amplitude decomposition of the eigenvectors of the curvature matrix corresponding to the two largest [(a) and (b)] and the two smallest [(c) and (d)] eigenvalues, with the largest eigenvalue normalized to one. The two different colors (blue and red) indicate that the amplitudes contribute with opposite signs.

The large theoretical error attached to the prediction of L suggests that relatively large changes in L from its average value only produce a mild deterioration in the quality of the fit. This indicates that there are directions in the model space that are relatively “soft” or “flat”. An equivalent and highly intuitive way to illustrate this effect is to diagonalize the 8×8 curvature matrix $\hat{\mathcal{M}}$ defined in Eq. (13). This then becomes effectively a *small-oscillations* problem. In particular, each eigenvalue λ_i of $\hat{\mathcal{M}}$ controls the deterioration in the quality of the fit as one moves along a direction defined by its corresponding eigenvector [22]. A “flat” direction, characterized by a small eigenvalue λ_i , involves a particular linear combination of parameters that is poorly constrained by the choice of observables included

in the calibration of the functional. To illustrate such a behavior we have plotted in Fig. 3 the components of four out of the eight eigenvectors along the original directions in the pseudo-parameter space. Note that we have considered only those eigenvectors having the two largest and two smallest eigenvalues, with the largest eigenvalue being normalized arbitrarily to one. The blue and red rectangles serve to indicate component having opposite signs. The eigenvectors associated with the two largest eigenvalues determine the two stiffest directions in parameter space. Small departures from the minimum along those two eigenvectors result in a rapid deterioration of the quality of the fit. Perhaps not surprisingly given the importance of ground-state energies and charge radii (see Table II), the scalar-meson mass, the saturation density, and the binding energy per nucleon are the most accurately determined parameters. Note that the scalar mass was determined with a small 0.3% theoretical error: $m_s = (497.479 \pm 1.492)$ MeV. In stark contrast, the eigenvalues associated with the two softest directions are down by five to seven orders of magnitude. These two directions are represented by almost “pure” eigenvectors with amplitudes in excess of 0.95 along the original ζ and L directions, respectively. The reason for L to remain poorly constrained has already been discussed earlier. However, the reason for ζ to remain largely undetermined is slightly more subtle. From the work of Müller and Serot it is already known that the value of ζ is insensitive to ground-state properties of finite nuclei that probe densities near nuclear matter saturation [38]. On the other hand, Müller and Serot showed that the value of ζ may be efficiently tuned to control the high-density component of the EOS, and ultimately the maximum neutron star mass M_{\max} . Naively then, one would have expected a better constraint on ζ from the inclusion of M_{\max} in the calibration of the functional. We believe that the poor determination of ζ may be attributed to the large value of L suggested by FSUGold 2 (see Table IV). Indeed, when L is small as in the case of FSUGold, the high-density component of the EOS needs to be stiffened to account for the existence of massive stars. And this can be efficiently done by only tuning ζ , as was done in Ref. [89]. However, if the symmetry energy is already stiff and no isovector constraints are available, then it appears that only a linear combination of L and ζ can be constrained. This analysis reinforces the urgent need for well measured isovector observables.

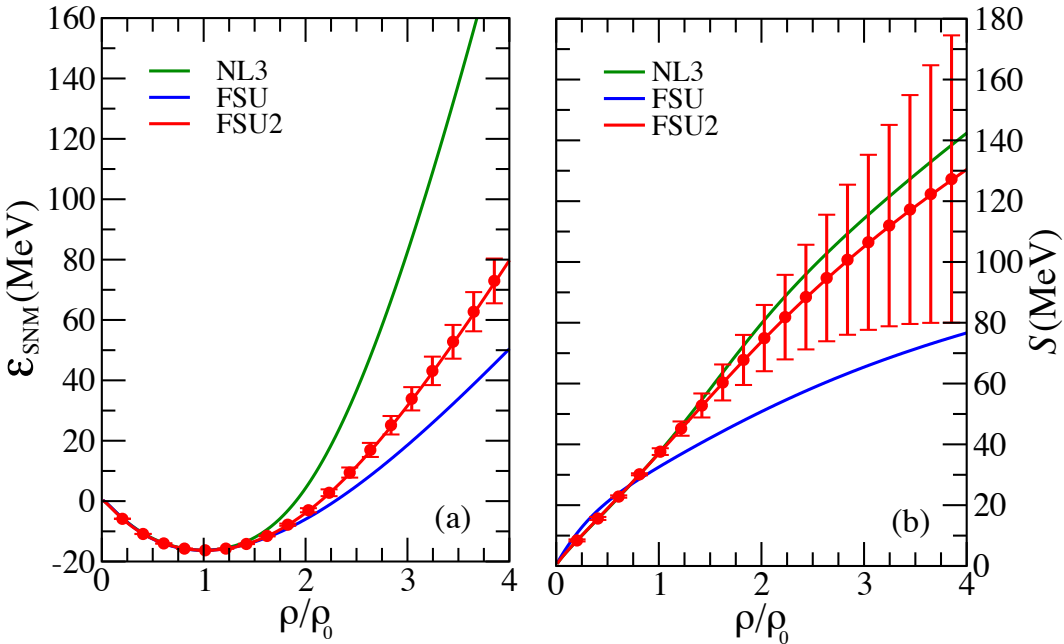


FIG. 4. (Color online) (a) Binding energy per nucleon of symmetric nuclear matter and (b) symmetry energy as a function of density in units of nuclear matter saturation density $\rho_0 = 0.148 \text{ fm}^{-3}$. Predictions are included from the three models discussed in the text: NL3 [8], FSUGold [10], and FSUGold 2 supplemented with theoretical errors.

A more comprehensive view of the behavior of infinite nuclear matter is given in Fig. 4 where predictions for the EOS of SNM (left panel) and the symmetry energy (right panel) are displayed for the three RMF models considered in this work. Due to the inclusion of GMR energies into the calibration of FSUGold 2, the incompressibility coefficient was fairly accurately determined (see Table IV) and this, in turn, generates small theoretical errors on the EOS up to 2-3 times saturation density. The larger theoretical uncertainty with increasing density is a reflection of the inability of ground-state properties and GMR energies to constrain the high-density behavior of the EOS. In principle, the inclusion of a maximum neutron star mass M_{\max} into the fit should have served to constrain the EOS at high density. However, given that the symmetry energy is stiff (see right-hand panel) one can satisfy the M_{\max} constraint without imposing stringent limits on the EOS of SNM at high densities. However, the situation is radically different in the

case of the symmetry energy, as the model has lost its predictability at densities only slightly above saturation density. Although we expect to mitigate this situation once strong isovector observables, such as neutron skins and stellar radii, are incorporated into the calibration of the density functional, our results underscore the importance of including theoretical uncertainties. Whereas the symmetry energy predicted by FSUGold 2 is stiff at saturation density, it is consistent at the 1σ level with a symmetry energy almost as soft as FSUGold and as stiff as (or even stiffer than) NL3 at high densities. The impact of a stiff symmetry energy on the neutron-skin thickness of all the nuclei used in the calibration procedure is displayed in Table V. These results help to reinforce the recent claim that at present there is no compelling reason to rule out models with large neutron skins [84]. We close this part of the discussion with a brief comment on the EOS of pure neutron matter. Given that the EOS of PNM may be approximated as that of SNM plus the symmetry energy, the EOS of PNM at low densities for FSUGold 2 strongly resembles the one for NL3. Although PNM is not experimentally accessible, there are important theoretical constraints that have emerged from the universal behavior of dilute Fermi gases in the unitary limit [33]. As already mentioned earlier, without additional isovector constraints the symmetry energy predicted by RMF models tends to be fairly stiff. Therefore, whereas FSUGold is consistent with most theoretical constraints [33–35, 90], both FSUGold 2 and NL3 are not.

Nucleus	NL3	FSU	FSU 2
^{16}O	−0.028	−0.029	-0.028 ± 0.005
^{40}Ca	−0.049	−0.051	-0.050 ± 0.004
^{48}Ca	0.226	0.197	0.232 ± 0.008
^{68}Ni	0.261	0.211	0.268 ± 0.010
^{90}Zr	0.114	0.088	0.117 ± 0.008
^{100}Sn	−0.076	−0.080	-0.077 ± 0.008
^{116}Sn	0.167	0.122	0.172 ± 0.011
^{132}Sn	0.346	0.271	0.354 ± 0.019
^{144}Sm	0.145	0.103	0.149 ± 0.011
^{208}Pb	0.278	0.207	0.287 ± 0.020

TABLE V. Predictions for the neutron skins, $R_{\text{skin}} \equiv R_n - R_p$, (in fm) of all the nuclei included in the calibration procedure for NL3 [8], FSUGold [10], and FSUGold 2 supplemented with theoretical error bars.

So far we have discussed the results from the optimization and the theoretical errors associated to a large number of physical quantities. We now turn the discussion to the important topic of correlations based on Eqs. (14) and (15). We start in Fig. 5 by displaying correlation coefficients in graphical form for various physical quantities. From these, only GMR energies and the maximum neutron star mass were included in the calibration procedure. As anticipated, we find a strong correlation of the GMR energies to the nuclear incompressibility coefficient K , verifying the age-old idea of extracting a fundamental parameter of the EOS from laboratory measurements of the breathing mode. To our knowledge, this is the first time that GMR energies are directly incorporated into the calibration of a relativistic EDF. In the case of the two fundamental parameters of the symmetry energy J and L , we observe a strong correlation with “size” parameters, specifically with the neutron radius of ^{48}Ca and ^{208}Pb , as well as with the radius of “canonical” $1.4 M_\odot$ neutron star. The sensitivity of the size parameters to L has a clear physical underpinning. In the particular case of a nucleus, surface tension favors the formation of a spherical drop of uniform equilibrium density. However, if the nucleus has a significant neutron excess, it may be energetically advantageous to move some of these neutrons from the center of the nucleus to the dilute surface where the symmetry energy is reduced. In particular, if the slope L is large, then this reduction is significant so it becomes favorable to move most of the excess neutrons to the surface, thereby creating a thick neutron skin [88]. And given that the same pressure that pushes against surface tension in a nucleus pushes against gravity in a neutron star, the larger the value of L the larger the stellar radius [40, 47]. However, whereas the neutron skin is sensitive to the pressure around the saturation density, the neutron star radius also depends on the pressure at higher densities. This weakens slightly the correlation between the stellar radius and the neutron radius of the nucleus. Nevertheless, that a correlation between systems that differ by 18 orders of magnitude in size exists is remarkable indeed. Moreover, the correlation between the neutron-skin thickness of ^{208}Pb and the radius of low mass neutron stars is even stronger [23, 48]. This suggests how a laboratory measurement may place a significant constraint on an astronomical object, and *vice versa*. This example clearly illustrates the power of the covariance analysis.

We now proceed to display in Fig. 6 correlation coefficients between the Lagrangian model parameters. The prevalence of “dark patches” suggests a strong correlation among several model parameters. A large correlation coefficient of $|\rho(A, B)| \simeq 1$ between two observables may indicate “redundancy”, in the sense that there may be little to gain by including both observables in the calibration procedure. This could alleviate the need for performing a complex

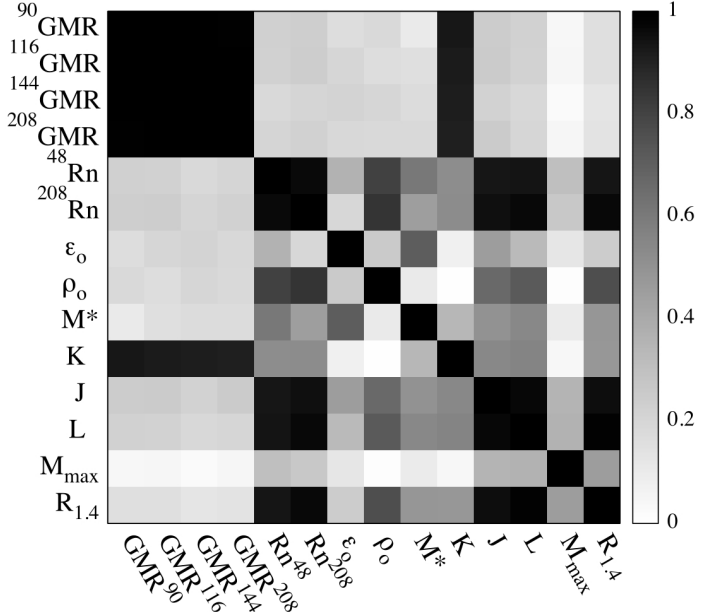


FIG. 5. Correlation coefficients (in absolute value) depicted in graphical form for a representative set of observables. The set includes four GMR energies (for ${}^{90}\text{Zr}$, ${}^{116}\text{Sn}$, ${}^{144}\text{Sm}$, and ${}^{208}\text{Pb}$), two neutron radii (for ${}^{48}\text{Ca}$ and ${}^{208}\text{Pb}$), several bulk properties of nuclear matter (ϵ_0 , ρ_0 , M^* , K , J , and L), and two neutron star observables (the maximum mass M_{\max} and the radius of a $1.4 M_\odot$ neutron star $R_{1.4}$).

experiment. Alternatively, a strong correlation may suggest an experiment that could constrain the value of an inaccessible quantity. However, in the case of the model parameters, a strong correlation does not imply redundancy, but quite the opposite. For example, a strong correlation between two well determined model parameters, such as $g_s^2 = 108.0943 \pm 1.8376$ and $g_v^2 = 183.7893 \pm 4.9623$ implies a strong interdependence. That is, if g_s^2 is fixed at a certain value, then g_v^2 must attain the precise value suggested by their correlation; otherwise the quality of the fit will deteriorate significantly.

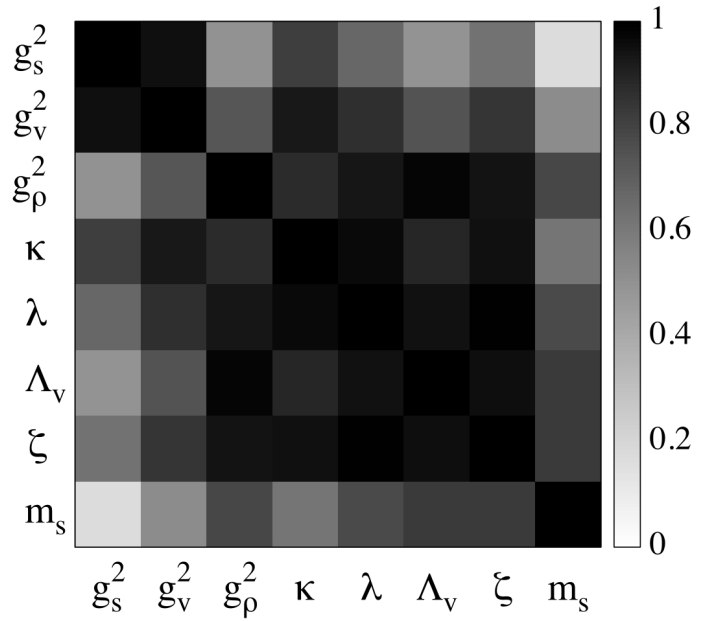


FIG. 6. Correlation coefficients (absolute values) between Lagrangian model parameters depicted in graphical form.

We conclude by displaying in Fig. 7 correlation coefficients between the Lagrangian model parameters and a representative set of physical observables. Contrary to expectations, the strong correlation between ζ and the maximum neutron star mass is missing. As already explained, a large maximum neutron star mass may be generated by having either a stiff EOS for SNM or a stiff symmetry energy. If the symmetry energy is soft, as in the case of FSUGold, then one must stiffen the EOS of SNM, which may be efficiently done by tuning ζ . However, given that the symmetry energy predicted by FSUGold 2 is stiff (see Fig. 4) the correlation between ζ and M_{\max} weakens. Indeed, M_{\max} displays the strongest correlation with the two isovector parameters g_ρ^2 and Λ_v —although the correlation appears fairly weak. This suggests that the maximum mass constraint results from a competition between ζ and the slope of symmetry energy L . For instance, if ζ increases, thereby softening the EOS of SNM, then M_{\max} is reduced. Thus, in order to maintain M_{\max} at its specified value, the symmetry energy must stiffen accordingly. This implies a strong and positive correlation between ζ and L , as precisely indicated in Fig. 7. An important lesson learned from the present discussion is that one must exercise caution in examining correlations among parameters and observables. For example, it appears that certain bulk parameters of SNM, such as the binding energy per nucleon ε_0 , the effective nucleon mass M^* , and the incompressibility coefficient K are uncorrelated to the four isoscalar parameters g_s^2 , g_v^2 , κ , and λ . Such lack of correlation may come as a surprise in view that ε_0 , M^* , K , and the saturation density ρ_0 uniquely determine the value of the four isoscalar parameters (see appendix). The solution to this apparent contradiction lies in the fact that in generating the distribution of Lagrangian model parameters all four isoscalar parameters become inextricably linked. In order to isolate the proper correlation between a given observables (say ε_0) and a given model parameter (say g_s^2) one should monitor the response of the observable to changes to only that one parameter. That is, if one could provide suitable selection cuts to maintain the other parameters (say g_v^2 , κ , and λ) fixed, then the strong correlation between ε_0 and g_s^2 will become manifest [27].

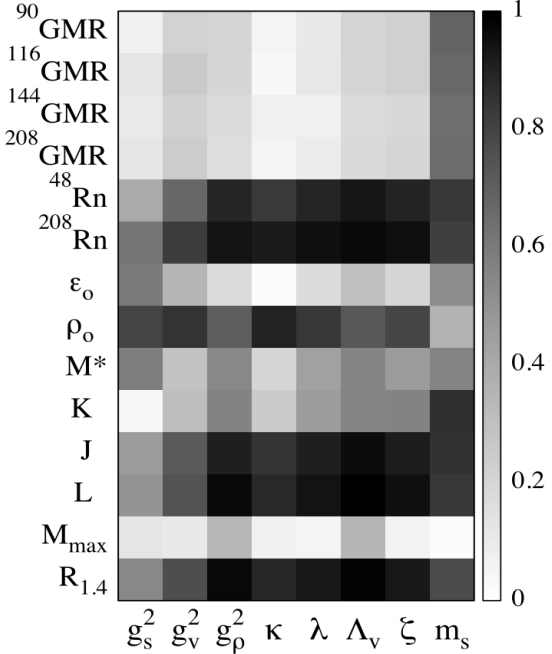


FIG. 7. Correlation coefficients (absolute values) between Lagrangian model parameters and a representative set of physical observables. The set of observables are the same as those considered in Fig. 5.

IV. SUMMARY AND OUTLOOK

Finite nuclei, infinite nuclear matter, and neutron stars are strongly interacting, nuclear many-body systems that span an enormous range of densities and isospin asymmetries. Lacking the tools to solve QCD in these regimes, DFT-based approaches, such as Skyrme and RMF models, provide the most powerful alternative for investigating such complex systems within a single unified framework. For the systematic study of such diverse nuclear systems, we have developed a new RMF model, *FSUGold 2*, to describe the physics of both finite nuclei and neutron stars; objects that differ in size by 18 orders of magnitude.

The philosophy behind our calibration procedure adheres to two important principles. First, the calibration relies exclusively on genuine physical observables that can be either measured in the laboratory or extracted from observation. Second, the optimization of the functional was implemented in the space of “pseudo data”, consisting mostly of bulk properties of infinite nuclear matter. This has the enormous advantage that, unlike the Lagrangian model parameters, the pseudo data have both a clear physical interpretation and acceptable values that range over a fairly small interval. To our knowledge, this is the first time that such a transformation between model parameters and pseudo data is implemented in the relativistic domain. We should note that in an effort to limit the input to only accurately measured physical observables, neither neutron skins of neutron-rich nuclei nor radii of neutron stars were included in the optimization. Hence, values for these observables become bona-fide model predictions.

In addition to neutron skins and stellar radii, we provide predictions for a variety of bulk properties of both symmetric nuclear matter and the symmetry energy. Isoscalar properties, such as the density, binding energy per nucleon, and incompressibility coefficient of SNM at saturation are all determined with small theoretical errors and in close agreement with their conventionally accepted values. In particular, the incompressibility coefficient was determined with a theoretical uncertainty of only 1%. Such a small theoretical error was obtained because of the inclusion of GMR energies into the calibration of FSUGold 2. This too, we believe, has been done here for the first time. The theoretical errors attached to the predictions of ρ_0 and ε_0 are even smaller, indicating that the isoscalar sector is well constrained by the binding energies, charge radii, and GMR energies of finite nuclei.

The lack of well measured isovector observables in the calibration of the functional has radically different consequences on the determination of the bulk parameters of the symmetry energy, especially in the case of its slope L . First, without stringent isovector constraints, RMF models of the type used here tend to favor a stiff symmetry energy. We obtained a value for the slope of the symmetry energy of $L = (112.8 \pm 16.1)$ MeV. In turn, this large slope yields values of $R_{\text{skin}}^{208} = (0.287 \pm 0.020)$ fm and $R_{1.4} = (14.42 \pm 0.26)$ km for the neutron-skin thickness of ^{208}Pb and the radius of a $1.4 M_\odot$ neutron star, respectively. Although both large, we underscore that at present there is no conclusive experimental result nor astrophysical observation that can rule out large neutron skins [84] or large stellar radii. Thus, there is urgent need for the accurate measurement of strong isovector indicators.

Following the optimization of the density functional one proceeds to explore the richness of the covariance analysis. This we did in two stages. First, we provided predictions for a variety of observables with properly estimated theoretical errors. This is particularly critical when models are extrapolated to unknown regions. Second, we explored correlations between both observables and model parameters. A correlation analysis can reveal interdependences that may be of great value. For example, a strong correlation between two observables may eliminate the need to measure both. Further, if from these two observables, e.g., L and R_{skin}^{208} , one of these is of critical importance but inaccessible in the laboratory (e.g., L) one could measure the latter to determine the former. Although there are ambitious plans to experimentally constrain the isovector sector by improving and expanding on previous measurements of both neutron skins and electric dipole polarizabilities, we will use some of the insights developed here to anticipate several different outcomes. We are planning to exploit the power and flexibility of the covariance analysis to constrain the poorly determined isovector parameters g_ρ^2 and Λ_v by assuming a variety of scenarios involving neutron skins of neutron-rich nuclei. For example, how precisely does one have to measure the neutron radius of ^{208}Pb in order to constrain L to a given acceptable range? Is this precision attainable with PREX-II? If not, what other neutron-rich nuclei should be used? Or, is it better to measure the weak form factor of ^{208}Pb at another momentum transfer? In this manner the development of an efficient modeling scheme is invaluable for the simulation of various scenarios. Research along these lines is in progress and its results will be presented in a forthcoming publication.

ACKNOWLEDGMENTS

We are grateful to Dr. F. J. Fattoyev for calling to our attention the transformation employed in the model building which greatly facilitates the optimization. This material is based upon work supported by the U.S. Department of Energy Office of Science, Office of Nuclear Physics under Award Number DE-FD05-92ER40750.

Appendix

In this appendix we describe the connection between the coupling constants appearing in the Lagrangian density depicted in Eq. (1) and various bulk parameters of infinite nuclear matter. This connection has proved to be extremely useful. Indeed, expressing the objective function in terms of physically intuitive parameters provides important insights on the quest for the optimal parametrization. For example, based on the large experimental database of accurately measured nuclear masses, both the saturation density and the energy per nucleon at saturation are fairly well known. In turn, limiting the searches to a fairly well known region of parameter space increases significantly the efficiency of

the Levenberg-Marquardt algorithm. We start by connecting the isoscalar sector of the Lagrangian density with a few bulk parameters of symmetric nuclear matter [54]. We then proceed to determine the two isovector parameters of the Lagrangian density (g_ρ^2 and Λ_v) from the value of the symmetry energy J and its slope L at saturation density. To our knowledge, we are the first ones to establish such a connection in the isovector sector.

1. Isoscalar sector

Given the Lagrangian density of Eq. (1), the energy density ($\mathcal{E}=E/V$) of infinite nuclear matter may be computed directly from the corresponding energy-momentum tensor in the mean-field approximation. Note that only the zero-temperature limit will be addressed. Restricting ourselves to the isoscalar sector, the energy density of symmetric nuclear matter is given by the following expression [6]:

$$\begin{aligned}\mathcal{E}(\rho) &= \gamma \int_0^{k_F} \frac{d^3 k}{(2\pi)^3} E_k^{(+)} + \left(\frac{1}{2} \frac{m_s^2}{g_s^2} \Phi_0^2 + \frac{\kappa}{6} \Phi_0^3 + \frac{\lambda}{24} \Phi_0^4 \right) - \left(\frac{1}{2} \frac{m_v^2}{g_v^2} W_0^2 + \frac{\zeta}{24} W_0^4 \right) \\ &= \frac{M^{*4}}{4\pi^2} \left[\frac{k_F E_F^* (k_F^2 + E_F^{*2})}{M^{*4}} - \ln \left(\frac{k_F + E_F^*}{M^*} \right) \right] + \left(\frac{1}{2} \frac{m_s^2}{g_s^2} \Phi_0^2 + \frac{\kappa}{6} \Phi_0^3 + \frac{\lambda}{24} \Phi_0^4 \right) + \left(\rho_v W_0 - \frac{1}{2} \frac{m_v^2}{g_v^2} W_0^2 - \frac{\zeta}{24} W_0^4 \right).\end{aligned}\quad (\text{A.1})$$

where $\gamma=4$ is the spin-isospin degeneracy, $\rho_v \equiv \rho = (2k_F^3)/(3\pi^2)$ is the conserved baryon density, $\Phi_0 = g_s \phi_0$, $W_0 = g_v V_0$, $M^* = M - \Phi_0$ is the effective nucleon mass, and $E_k^{(+)} = E_k^* + W_0 = \sqrt{k^2 + M^{*2}} + W_0$ is the single-nucleon energy. Note that the classical equations of motion for the meson fields may be obtained directly from the Lagrangian density or equivalently, by demanding that the derivatives of $\mathcal{E}(\rho)$ with respect to Φ_0 and W_0 both vanish. That is,

$$\frac{\partial \mathcal{E}}{\partial \Phi_0} = \frac{m_s^2}{g_s^2} \Phi_0 + \frac{\kappa}{2} \Phi_0^2 + \frac{\lambda}{6} \Phi_0^3 - \rho_s = 0, \quad (\text{A.2a})$$

$$\frac{\partial \mathcal{E}}{\partial W_0} = \frac{m_v^2}{g_v^2} W_0 + \frac{\zeta}{6} W_0^3 - \rho_v = 0. \quad (\text{A.2b})$$

Here ρ_s is the scalar density that is defined as follows:

$$\rho_s(M^*) = \gamma \int_0^{k_F} \frac{d^3 k}{(2\pi)^3} \frac{M^*}{E_k^*} = \frac{M^{*3}}{\pi^2} \left[\frac{k_F E_F^*}{M^{*2}} - \ln \left(\frac{k_F + E_F^*}{M^*} \right) \right]. \quad (\text{A.3})$$

Note that the scalar density is not conserved and must be self-consistently determined from the equations of motion.

At zero temperature the pressure of the system may be calculated from its thermodynamic definition, i.e.,

$$P = - \left(\frac{\partial E}{\partial V} \right)_N = \rho \frac{\partial \mathcal{E}}{\partial \rho} - \mathcal{E} = \rho \left(E_F^{(+)} - \frac{E}{A} \right), \quad (\text{A.4})$$

where the last line follows from using $\partial \mathcal{E}/\partial \rho = E_F^{(+)}$, an identity that should hold in any thermodynamically consistent many-body theory. Moreover, note that at saturation density, the pressure vanishes and one obtains—in accordance with the Hugenholtz-van Hove theorem—that the energy per nucleon becomes equal to the Fermi energy. That is,

$$E_F^{(+)} = \sqrt{k_F^2 + M^{*2}} + W_0 = \frac{E}{A}. \quad (\text{A.5})$$

To make further progress, we now obtain an analytic expression for the incompressibility coefficient of symmetric nuclear matter K . As defined in Eq. (4a), it is given by

$$K = 9\rho_0^2 \left[\frac{d^2(E/A)}{d\rho^2} \right]_0 = 9\rho_0^2 \left[\frac{d}{d\rho} \left(\frac{P}{\rho^2} \right) \right]_0 = 9\rho_0 \left(\frac{dE_F^{(+)}}{d\rho} \right)_0. \quad (\text{A.6})$$

Given that the Fermi energy depends in a complicated way on the density, i.e., both explicitly and implicitly through M^* and W_0 , there are three terms that need to be evaluated. That is,

$$\begin{aligned}\frac{K}{9\rho_0} &= \left(\frac{\partial E_F^{(+)}}{\partial \rho} \right)_0 + \left(\frac{\partial E_F^{(+)}}{\partial W_0} \right)_0 \left(\frac{\partial W_0}{\partial \rho} \right)_0 + \left(\frac{\partial E_F^{(+)}}{\partial M^*} \right)_0 \left(\frac{\partial M^*}{\partial \rho} \right)_0 \\ &= \left(\frac{\partial E_F^{(+)}}{\partial \rho} \right)_0 + \left(\frac{\partial W_0}{\partial \rho} \right)_0 + \left(\frac{M^*}{E_F^*} \right)_0 \left(\frac{\partial M^*}{\partial \rho} \right)_0.\end{aligned}\quad (\text{A.7})$$

We now proceed to evaluate each of the three terms. The first one is the simplest and yields:

$$\left(\frac{\partial E_F^{(+)}}{\partial \rho} \right)_0 = \left(\frac{\pi^2}{2k_F E_F^*} \right)_0. \quad (\text{A.8})$$

We continue with the second term and make use of the equation of motion for W_0 [Eq. (A.2b)] to write:

$$\left(\frac{\partial W_0}{\partial \rho} \right)_0 = \left(\frac{g_v^2}{m_v^{*2}} \right)_0, \quad \text{with } m_v^{*2} \equiv m_v^2 + \frac{\zeta}{2} g_v^2 W_0^2. \quad (\text{A.9})$$

Using the previous two results we can rewrite Eq. (A.7) as follows:

$$\left(\frac{\partial M^*}{\partial \rho} \right)_0 = \left[\frac{E_F^*}{M^*} \left(\frac{K}{9\rho} - \frac{\pi^2}{2k_F E_F^*} - \frac{g_v^2}{m_v^{*2}} \right) \right]_0. \quad (\text{A.10})$$

The left-hand side of the equation may be computed by invoking the scalar equation of motion [Eq. (A.2a)] and depends on the three isoscalar coupling constants. We obtain,

$$\left(\frac{\partial M^*}{\partial \rho} \right)_0 = - \left[\frac{M^*}{E_F^*} \left(\frac{m_s^{*2}}{g_s^2} + \rho'_s(M^*) \right)^{-1} \right]_0, \quad \text{with } \frac{m_s^{*2}}{g_s^2} \equiv \frac{m_s^2}{g_s^2} + \kappa \Phi_0 + \frac{\lambda}{2} \Phi_0^2. \quad (\text{A.11})$$

Note that we have defined the derivative of the scalar density [Eq. (A.3)] with respect to M^* as follows:

$$\rho'_s(M^*) = \left(\frac{\partial \rho_s}{\partial M^*} \right) = \frac{1}{\pi^2} \left[\frac{k_F}{E_F^*} (E_F^{*2} + 2M^{*2}) - 3M^{*2} \ln \left(\frac{k_F + E_F^*}{M^*} \right) \right]. \quad (\text{A.12})$$

This is all the formalism that is needed to establish the connection between the isoscalar parameters appearing in the Lagrangian and a few bulk parameters of infinite nuclear matter. In the isoscalar sector the four bulk parameters of infinite nuclear matter that we consider here are as follows: (i) the density ρ , (ii) the binding energy per nucleon E/A , (iii) the incompressibility coefficient K , and (iv) the effective nucleon mass M^* —all of them evaluated at saturation density. Specification of these four bulk parameters enables one to determine four out of the five isoscalar coupling constants, namely, g_v^2/m_v^2 , g_s^2/m_s^2 , κ , and λ . The sole remaining coupling constant ζ is left intact as it is fairly insensitive to the properties of symmetric nuclear matter. Indeed, ζ is sensitive to the high-density component of the EOS and can be easily tuned by specifying the maximum neutron star mass. Note that in the mean-field approximation the Yukawa meson couplings always appear in combination with the corresponding meson mass.

The vector coupling may be readily determined from the vanishing of the pressure at saturation density. Indeed, from Eq. (A.5) one obtains the value of the vector field W_0 at saturation density. In turn, substituting this value in Eq. (A.2b) determines (for a given ζ) g_v^2/m_v^2 . Given that the vector mass has been fixed at its experimental value of $m_v = 782.5$ MeV, this provides a determination of g_v^2 .

The specification of the three isoscalar parameters is significantly more involved and depends critically on knowledge of the effective nucleon mass M^* at saturation density. Further, it requires three independent pieces of information for their determination. Perhaps surprisingly, such information is provided in the form of three *simultaneous linear equations*. That is, the solution is unique. The first equation to be used involves the energy density of symmetric nuclear matter depicted in Eq. (A.1). Given that at saturation density $\mathcal{E}(\rho_0) = \rho_0(E/A)_0$, every term in such expression is known—with the exception of m_s^2/g_s^2 , κ , and λ . The classical equation of motion for the scalar field Eq. (A.2a) provides the second linear equation in these three parameters, since the scalar density is fully specified in terms of the density and effective nucleon mass at saturation. Finally, knowledge of the incompressibility coefficient K at saturation density supplies the third and last linear equation. Indeed, a comparison between Eq. (A.10) and Eq. (A.11) indicates that the only unknown is the quantity m_s^{*2}/g_s^2 , which again contains the three scalar parameters of interest. Given that these equations provide a system of three simultaneous linear equations, the solution may be obtained by elementary means.

2. Isovector sector

In the previous section we concentrated on connecting the isoscalar parameters of the Lagrangian density to a few bulk parameters of symmetric nuclear matter. We now shift our focus to the isovector sector and show that the two isovector parameters g_ρ^2/m_ρ^2 and Λ_v may be determined from knowledge of two quantities of central importance,

namely, the symmetry energy J and its slope at saturation density L . To our knowledge, this connection is established here for the first time.

For the Lagrangian density given in Eq.(1), an analytic expression for the density dependence of the symmetry energy was derived in Ref.[47]. One obtains,

$$S(\rho) = \frac{k_F^2}{6E_F^*} + \frac{g_\rho^2 \rho}{8m_\rho^{*2}}, \quad \text{with } \frac{m_\rho^{*2}}{g_\rho^2} \equiv \frac{m_\rho^2}{g_\rho^2} + 2\Lambda_v W_0^2. \quad (\text{A.13})$$

We note that the density dependence of the symmetry energy given above consists of a purely “isoscalar” term and a largely “isovector” term. That is, we define

$$S_0(\rho) = \frac{k_F^2}{6E_F^*} \quad \text{and} \quad S_1(\rho) = \frac{g_\rho^2 \rho}{8m_\rho^{*2}}. \quad (\text{A.14})$$

In particular, given that the isoscalar sector has already been fixed, $S_0(\rho)$ along with all its derivatives are known. In contrast, $S_1(\rho)$ depends on both g_ρ^2/m_ρ^2 and Λ_v which are unknown. As already mentioned, critical to the determination of these two isovector parameters are the symmetry energy and its slope at saturation density, which according to Eq.(4b) are given as follows:

$$J = S(\rho_0) \quad \text{and} \quad L = 3\rho_0 \left(\frac{dS}{d\rho} \right)_0. \quad (\text{A.15})$$

The determination of the quantity m_ρ^{*2}/g_ρ^2 , which still depends on both isovector parameters, is fairly simple:

$$J_1 \equiv \left(\frac{g_\rho^2 \rho}{8m_\rho^{*2}} \right)_0 = (J - J_0) = J - \left(\frac{k_F^2}{6E_F^*} \right)_0. \quad (\text{A.16})$$

In contrast, the determination of each individual isovector parameters is considerably more difficult and involves several of the same manipulations carried out in the isoscalar sector. In analogy with the above equation we write:

$$L_1 = 3\rho_0 \left(\frac{dS_1}{d\rho} \right)_0 = (L - L_0) = L - 3\rho_0 \left(\frac{dS_0}{d\rho} \right)_0. \quad (\text{A.17})$$

We start by computing the contribution to the slope from the isoscalar term. That is,

$$\begin{aligned} L_0 &= 3\rho_0 \left(\frac{dS_0}{d\rho} \right)_0 = 3\rho_0 \left[\left(\frac{\partial S_0}{\partial \rho} \right) + \left(\frac{\partial S_0}{\partial M^*} \right) \left(\frac{\partial M^*}{\partial \rho} \right) \right]_0 \\ &= J_0 \left(1 + \frac{M^{*2}}{E_F^{*2}} \left[1 - \frac{3\rho}{M^*} \left(\frac{\partial M^*}{\partial \rho} \right) \right] \right)_0. \end{aligned} \quad (\text{A.18})$$

Note that this expression is given exclusively in terms of isoscalar parameters, so it is completely known. Also note that the answer has been left in terms of $(\partial M^*/\partial \rho)_0$ which has already been calculated in the previous section. We now proceed to compute the isovector contribution to the slope of the symmetry energy. Following similar steps as before, we obtain

$$\begin{aligned} L_1 &= 3\rho_0 \left(\frac{dS_1}{d\rho} \right)_0 = 3\rho_0 \left[\left(\frac{\partial S_1}{\partial \rho} \right) + \left(\frac{\partial S_1}{\partial W_0} \right) \left(\frac{\partial W_0}{\partial \rho} \right) \right]_0 \\ &= 3J_1 \left[1 - 32 \left(\frac{g_v^2}{m_v^{*2}} \right) W_0 \Lambda_v J_1 \right]_0 = (L - L_0). \end{aligned} \quad (\text{A.19})$$

This is all that is needed to achieve the desired goal of expressing g_ρ^2/m_ρ^2 and Λ_v in terms of J and L . Indeed, given that L is provided, and J_1 and L_0 have been determined from Eqs.(A.16) and (A.18), respectively, the only unknown in the previous equation is Λ_v . Finally, using the definition of the effective ρ -meson mass given in Eq.(A.13), we can solve for g_ρ^2/m_ρ^2 . That is,

$$\frac{m_\rho^2}{g_\rho^2} = \frac{m_\rho^{*2}}{g_\rho^2} - 2\Lambda_v W_0^2 = \frac{\rho_0}{8J_1} - 2\Lambda_v W_0^2. \quad (\text{A.20})$$

[1] “Building a universal nuclear energy density functional,” (UNEDF Collaboration).

- [2] M. Kortelainen, T. Lesinski, J. More, W. Nazarewicz, J. Sarich, N. Schunck, M. V. Stoitsov, and S. Wild, Phys. Rev. C **82**, 024313 (2010).
- [3] M. Kortelainen, J. McDonnell, W. Nazarewicz, P.-G. Reinhard, J. Sarich, N. Schunck, M. V. Stoitsov, and S. M. Wild, Phys. Rev. C **85**, 024304 (2012).
- [4] M. Kortelainen, J. McDonnell, W. Nazarewicz, E. Olsen, P.-G. Reinhard, J. Sarich, N. Schunck, S. M. Wild, D. Davesne, and A. Pastore, Phys. Rev. C **89**, 054314 (2013).
- [5] J. D. Walecka, Ann. Phys. (NY) **83**, 491 (1974).
- [6] B. D. Serot and J. D. Walecka, Adv. Nucl. Phys. **16**, 1 (1986).
- [7] C. J. Horowitz and B. D. Serot, Nucl. Phys. A **368**, 503 (1981).
- [8] G. A. Lalazissis, J. Konig, and P. Ring, Phys. Rev. C **55**, 540 (1997).
- [9] G. A. Lalazissis, S. Raman, and P. Ring, At. Data Nucl. Data Tables **71**, 1 (1999).
- [10] B. G. Todd-Rutel and J. Piekarewicz, Phys. Rev. Lett. **95**, 122501 (2005).
- [11] B. A. Brown, Phys. Rev. Lett. **85**, 5296 (2000).
- [12] R. J. Furnstahl, Nucl. Phys. A **706**, 85 (2002).
- [13] M. Centelles, X. Roca-Maza, X. Viñas, and M. Warda, Phys. Rev. Lett. **102**, 122502 (2009).
- [14] X. Roca-Maza, M. Centelles, X. Vinas, and M. Warda, Phys. Rev. Lett. **106**, 252501 (2011).
- [15] J. Erler, N. Birge, M. Kortelainen, W. Nazarewicz, E. Olsen, A. M. Perhac, and M. Stoitsov, Nature **486**, 509 (2012).
- [16] A. V. Afanasjev, S. E. Agbemava, D. Ray, and P. Ring, Phys. Lett. B **726**, 680 (2013).
- [17] J. M. Lattimer and M. Prakash, Science **304**, 536 (2004).
- [18] P. Demorest, T. Pennucci, S. Ransom, M. Roberts, and J. Hessels, Nature **467**, 1081 (2010).
- [19] J. Antoniadis, P. C. Freire, N. Wex, T. M. Tauris, R. S. Lynch, *et al.*, Science **340**, 6131 (2013).
- [20] Editors, Phys. Rev. A **83**, 040001 (2011).
- [21] P.-G. Reinhard and W. Nazarewicz, Phys. Rev. C **81**, 051303 (2010).
- [22] F. J. Fattoyev and J. Piekarewicz, Phys. Rev. C **84**, 064302 (2011).
- [23] F. J. Fattoyev and J. Piekarewicz, Phys. Rev. C **88**, 015802 (2012).
- [24] P.-G. Reinhard and W. Nazarewicz, Phys. Rev. C **87**, 014324 (2013).
- [25] P.-G. Reinhard, J. Piekarewicz, W. Nazarewicz, B. Agrawal, N. Paar, *et al.*, Phys. Rev. C **88**, 034325 (2013).
- [26] J. Dobaczewski, W. Nazarewicz, and P.-G. Reinhard, J. Phys. G **41**, 074001 (2014).
- [27] J. Piekarewicz, W.-C. Chen, and F. J. Fattoyev, arXiv:1407.0911 (2014).
- [28] F. Ozel, G. Baym, and T. Guver, Phys. Rev. D **82**, 101301 (2010).
- [29] A. W. Steiner, J. M. Lattimer, and E. F. Brown, Astrophys. J. **722**, 33 (2010).
- [30] V. Suleimanov, J. Poutanen, M. Revnivtsev, and K. Werner, Astrophys. J. **742**, 122 (2011).
- [31] S. Guillot, M. Servillat, N. A. Webb, and R. E. Rutledge, Astrophys. J. **772**, 7 (2013).
- [32] J. Erler, C. J. Horowitz, W. Nazarewicz, M. Rafalski, and P.-G. Reinhard, Phys. Rev. C **87**, 044320 (2013).
- [33] A. Schwenk and C. J. Pethick, Phys. Rev. Lett. **95**, 160401 (2005).
- [34] A. Gezerlis and J. Carlson, Phys. Rev. C **81**, 025803 (2010).
- [35] I. Vidana, C. Providencia, A. Polls, and A. Rios, Phys. Rev. C **80**, 045806 (2009).
- [36] K. Hebeler, J. Lattimer, C. Pethick, and A. Schwenk, Phys. Rev. Lett. **105**, 161102 (2010).
- [37] K. Hebeler, J. Lattimer, C. Pethick, and A. Schwenk, Astrophys. J. **773**, 11 (2013).
- [38] H. Mueller and B. D. Serot, Nucl. Phys. A **606**, 508 (1996).
- [39] B. D. Serot and J. D. Walecka, Int. J. Mod. Phys. E **6**, 515 (1997).
- [40] C. J. Horowitz and J. Piekarewicz, Phys. Rev. Lett. **86**, 5647 (2001).
- [41] R. J. Furnstahl, B. D. Serot, and H.-B. Tang, Nucl. Phys. A **615**, 441 (1997).
- [42] R. J. Furnstahl, B. D. Serot, and H.-B. Tang, Nucl. Phys. A **618**, 446 (1997).
- [43] J. J. Rusnak and R. J. Furnstahl, Nucl. Phys. A **627**, 495 (1997).
- [44] R. J. Furnstahl and J. C. Hackworth, Phys. Rev. C **56**, 2875 (1997).
- [45] M. Kortelainen, R. J. Furnstahl, W. Nazarewicz, and M. Stoitsov, Phys. Rev. C **82**, 011304 (2010).
- [46] J. Boguta and A. R. Bodmer, Nucl. Phys. A **292**, 413 (1977).
- [47] C. J. Horowitz and J. Piekarewicz, Phys. Rev. C **64**, 062802 (2001).
- [48] J. Carriere, C. J. Horowitz, and J. Piekarewicz, Astrophys. J. **593**, 463 (2003).
- [49] C. J. Horowitz, M. A. Perez-Garcia, and J. Piekarewicz, Phys. Rev. C **69**, 045804 (2004).
- [50] B. G. Todd and J. Piekarewicz, Phys. Rev. C **67**, 044317 (2003).
- [51] J. Piekarewicz and M. Centelles, Phys. Rev. C **79**, 054311 (2009).
- [52] G. Baym, C. Pethick, and P. Sutherland, Astrophys. J. **170**, 299 (1971).
- [53] B. Link, R. I. Epstein, and J. M. Lattimer, Phys. Rev. Lett. **83**, 3362 (1999).
- [54] N. K. Glendenning, “Compact stars,” (Springer-Verlag New York, 2000).
- [55] B. K. Agrawal, S. Shlomo, and V. K. Au, Phys. Rev. C **72**, 0143310 (2005).
- [56] L.-W. Chen, C. M. Ko, B.-A. Li, and J. Xu, Phys. Rev. C **82**, 024321 (2010).
- [57] S. Brandt, “Data analysis: Statistical and computational methods for scientists and engineers,” (Springer, New York, 1999) 3rd ed.
- [58] P. Bevington and D. Robinson, “Data reduction and error analysis,” (McGraw Hill, New York, 2003) 3rd ed.
- [59] W. H. Press, B. P. Flannery, S. A. Teukolsky, and W. T. Vetterling, “Numerical recipes: The art of scientific computing,” (Cambridge University Press, 1989).
- [60] M. Wang, G. Audi, A. H. Wapstra, F. G. Kondev, M. MacCormick, X. Xu, and B. Pfeiffer, Chin. Phys. C **36**, 1603 (2012).

- [61] I. Angeli and K. Marinova, At. Data Nucl. Data Tables **99**, 69 (2013).
- [62] D. H. Youngblood, H. L. Clark, and Y.-W. Lui, Phys. Rev. Lett. **82**, 691 (1999).
- [63] M. Uchida, H. Sakaguchi, M. Itoh, M. Yosoi, T. Kawabata, *et al.*, Phys. Rev. C **69**, 051301 (2004).
- [64] T. Li *et al.*, Phys. Rev. Lett. **99**, 162503 (2007).
- [65] T. Li *et al.*, Phys. Rev. C **81**, 034309 (2010).
- [66] D. Patel, U. Garg, M. Fujiwara, T. Adachi, H. Akimune, *et al.*, Phys. Lett. B **726**, 178 (2013).
- [67] D. Patel and U. Garg, private communication.
- [68] W.-C. Chen, J. Piekarewicz, and M. Centelles, Phys. Rev. C **88**, 024319 (2013).
- [69] W.-C. Chen, J. Piekarewicz, and A. Volya, Phys. Rev. C **89**, 014321 (2014).
- [70] P. Ring and P. Schuck, “The nuclear many-body problem,” (Springer, New York, 2004).
- [71] M. N. Harakeh and A. van der Woude, “Giant resonances-fundamental high-frequency modes of nuclear excitation,” (Clarendon, Oxford, 2001).
- [72] J. Piekarewicz, Phys. Rev. C **76**, 031301 (2007).
- [73] H. Sagawa, S. Yoshida, G.-M. Zeng, J.-Z. Gu, and X.-Z. Zhang, Phys. Rev. C **76**, 034327 (2007).
- [74] A. Avdeenkov, F. Grummer, S. Kamerdzhev, S. Krewald, E. Litvinova, *et al.*, Phys. Rev. C **79**, 034309 (2009).
- [75] J. Piekarewicz, J. Phys. G **37**, 064038 (2010).
- [76] L.-G. Cao, H. Sagawa, and G. Colo, arXiv:1206.6552 (2012).
- [77] P. Vesely, J. Toivanen, B. Carlsson, J. Dobaczewski, N. Michel, *et al.*, Phys. Rev. C **86**, 024303 (2012).
- [78] J. Piekarewicz, Eur. Phys. J. A **50**, 25 (2013).
- [79] J. Piekarewicz, Phys. Rev. C **69**, 041301 (2004).
- [80] J. M. Lattimer and M. Prakash, Phys. Rept. **442**, 109 (2007).
- [81] S. Abrahanyan, Z. Ahmed, H. Albataineh, K. Aniol, D. Armstrong, *et al.*, Phys. Rev. Lett. **108**, 112502 (2012).
- [82] C. J. Horowitz, Z. Ahmed, C. Jen, A. Rakhman, P. Souder, *et al.*, Phys. Rev. C **85**, 032501 (2012).
- [83] J. M. Lattimer and A. W. Steiner, arXiv:1305.3242 (2013).
- [84] F. J. Fattoyev and J. Piekarewicz, Phys. Rev. Lett. **111**, 162501 (2013).
- [85] M. Farine, J. Pearson, and B. Rouben, Nucl. Phys. A **304**, 317 (1978).
- [86] Z. Zhang and L.-W. Chen, Phys. Lett. B **726**, 234 (2013).
- [87] B. A. Brown, Phys. Rev. Lett. **111**, 232502 (2013).
- [88] C. J. Horowitz, E. Brown, Y. Kim, W. Lynch, R. Michaels, *et al.*, J. Phys. G **41**, 093001 (2014).
- [89] F. J. Fattoyev, C. J. Horowitz, J. Piekarewicz, and G. Shen, Phys. Rev. C **82**, 055803 (2010).
- [90] A. Gezerlis and J. Carlson, Phys. Rev. C **77**, 032801 (2008).



EQUATION OF STATE FOR NUCLEONIC AND HYPERONIC NEUTRON STARS WITH MASS AND RADIUS CONSTRAINTS

LAURA TOLOS^{1,2}, MARIO CENTELLES³, AND ANGELS RAMOS³

¹ Institute of Space Sciences (CSIC-IEEC), Campus Universitat Autònoma de Barcelona, Carrer de Can Magrans, s/n, E-08193 Cerdanyola del Vallès, Spain

² Frankfurt Institute for Advanced Studies, Goethe University Frankfurt, Ruth-Moufang-Str. 1, D-60438 Frankfurt am Main, Germany

³ Departament de Física Quàntica i Astrofísica and Institut de Ciències del Cosmos (ICCUB), Universitat de Barcelona, Martí i Franquès 1, E-08028 Barcelona, Spain

Received 2016 October 4; revised 2016 November 9; accepted 2016 November 11; published 2016 December 22

ABSTRACT

We obtain a new equation of state for the nucleonic and hyperonic inner core of neutron stars that fulfills the $2 M_{\odot}$ observations as well as the recent determinations of stellar radii below 13 km. The nucleonic equation of state is obtained from a new parameterization of the FSU2 relativistic mean-field functional that satisfies these latest astrophysical constraints and, at the same time, reproduces the properties of nuclear matter and finite nuclei while fulfilling the restrictions on high-density matter deduced from heavy-ion collisions. On the one hand, the equation of state of neutron star matter is softened around saturation density, which increases the compactness of canonical neutron stars leading to stellar radii below 13 km. On the other hand, the equation of state is stiff enough at higher densities to fulfil the $2 M_{\odot}$ limit. By a slight modification of the parameterization, we also find that the constraints of $2 M_{\odot}$ neutron stars with radii around 13 km are satisfied when hyperons are considered. The inclusion of the high magnetic fields present in magnetars further stiffens the equation of state. Hyperonic magnetars with magnetic fields in the surface of $\sim 10^{15}$ G and with values of $\sim 10^{18}$ G in the interior can reach maximum masses of $2 M_{\odot}$ with radii in the 12–13 km range.

Key words: dense matter – equation of state – magnetic fields – stars: magnetars – stars: neutron

1. INTRODUCTION

Neutron stars are the most compact known objects without event horizons. They are formed in the aftermath of core-collapse supernovae and are usually observed as pulsars. Their features, such as the mass and radius, strongly depend on the properties of their dense interior. Thus, neutron stars serve as a unique laboratory for dense matter physics.

With more than 2000 pulsars known up to date, one of the best determined pulsar masses is that of the Hulse–Taylor pulsar of $1.4 M_{\odot}$ (Hulse & Taylor 1975). Until very recently, the most precise measurements of neutron star masses clustered around this canonical value. Higher masses in neutron star binary systems have been measured in recent years with very high precision, using post-Keplerian parameters. This is the case of the binary millisecond pulsar PSR J1614-2230 of $M = 1.97 \pm 0.04 M_{\odot}$ (Demorest et al. 2010) and the PSR J0348+0432 of $M = 2.01 \pm 0.04 M_{\odot}$ (Antoniadis et al. 2013).

While the measurement of neutron star masses is accurate, the observational determination of their radii is more difficult and, as a consequence, comparably accurate values of radii do not yet exist. The radius of a neutron star can be extracted from the analysis of X-ray spectra emitted by the neutron star atmosphere. The modeling of the X-ray emission strongly depends on the distance to the source, its magnetic field and the composition of its atmosphere, thus making the determination of the radius a difficult task. As a result, different values for the stellar radii have been derived (Verbiest et al. 2008; Ozel et al. 2010, 2016; Suleimanov et al. 2011; Bogdanov 2013; Guillot et al. 2013; Guver & Ozel 2013; Lattimer & Lim 2013; Steiner et al. 2013; Guillot & Rutledge 2014; Heinke et al. 2014; Lattimer & Steiner 2014; Poutanen et al. 2014; Ozel & Psaltis 2015; Lattimer & Prakash 2016; Ozel & Freire 2016). In general, the extractions based on the spectral analysis of X-ray emission from quiescent X-ray transients in low-mass binaries (QLMXBs) favor small stellar radii in the 9–12 km

range, whereas the determinations from neutron stars with recurring powerful bursts may lead to larger radii, of up to 16 km, although they are subject to larger uncertainties and controversy (see the discussion in the analysis of Fortin et al. 2015). The very recent work of Lattimer & Prakash (2016) indicates that the realistic range for radii of canonical neutron stars should be 10.7 km to 13.1 km. This analysis is based on observations of pulsar masses and estimates of symmetry properties derived from neutron matter studies and nuclear experiments. It is expected that robust observational upper bounds on stellar radii will be within reach in the near future. With space missions such as NICER (Neutron star Interior Composition ExploreR; Arzoumanian et al. 2014), high-precision X-ray astronomy will be able to offer precise measurements of masses and radii (Watts et al. 2016), while gravitational-wave signals from neutron star mergers hold promise to determine neutron star radii with a precision of 1 km (Bauswein & Janka 2012; Lackey & Wade 2015).

In anticipation that these upcoming astrophysical determinations could confirm small neutron star sizes, it is important and timely to explore the smallest radii that can be delivered by the theoretical models of compressed matter that are able to fulfil the $2 M_{\odot}$ maximum mass constraint, while reproducing at the same time the phenomenology of atomic nuclei. The masses and radii of neutron stars are linked to the physics of their interior, that is, the equation of state (EoS) of dense matter (Lattimer & Prakash 2004, 2007; Oertel et al. 2016). Many of the current nuclear models for the EoS are able to satisfy the $2 M_{\odot}$ constraint required by the discovery of massive neutron stars (Demorest et al. 2010; Antoniadis et al. 2013). However, the possible existence of neutron stars with small radii suggested by recent astrophysical analyses (Guillot et al. 2013; Guver & Ozel 2013; Guillot & Rutledge 2014; Heinke et al. 2014; Lattimer & Steiner 2014; Lattimer & Prakash 2016; Ozel & Freire 2016; Ozel et al. 2016) poses a

difficult challenge to most of the nuclear models (Chen & Piekarewicz 2015a; Dexheimer et al. 2015; Jiang et al. 2015; Ozel & Freire 2016).

A small neutron star radius for a canonical neutron star requires a certain softening of the pressure of neutron matter, and hence of the nuclear symmetry energy, around 1–2 times saturation density n_0 ($n_0 \approx 0.16 \text{ fm}^{-3}$) (Lattimer & Prakash 2007; Tsang et al. 2012; Ozel & Freire 2016). The star radius could also be reduced by decreasing the pressure of the isospin-symmetric part of the EoS in the intermediate-density region, but this is only possible with severe limitations due to the saturation properties of nuclear matter and the constraints on the EoS of dense nuclear matter extracted from nuclear collective flow (Danielewicz et al. 2002) and kaon production (Fuchs et al. 2001; Lynch et al. 2009) in high-energy heavy-ion collisions (HICs). Moreover, the requirement of maximum masses of $2 M_\odot$ does not allow a significant reduction of the total pressure. Indeed, very few models seem to exist that can meet both constraints (small radius and large mass) simultaneously, and fewer such models can in addition render accurate descriptions of the finite nuclei properties (Horowitz & Piekarewicz 2001a, 2001b; Chen & Piekarewicz 2015a; Jiang et al. 2015; Sharma et al. 2015).

It has also been long known that the transition from nuclear to hyperonic matter is energetically favored as the density increases inside neutron stars (Ambartsumyan & Saakyan 1960). The opening of hyperon degrees of freedom leads to a considerable softening of the EoS (Glendenning 1982). As a consequence, the maximum neutron star masses obtained are usually smaller than the $2 M_\odot$ observations (Demorest et al. 2010; Antoniadis et al. 2013). The solution of this so-called “hyperon puzzle” is not easy, and requires a mechanism that could provide additional repulsion to make the EoS stiffer. Possible mechanisms could be: (1) stiffer hyperon–nucleon and/or hyperon–hyperon interactions (see the recent works by Bednarek et al. 2012; Weissenborn et al. 2012; Maslov et al. 2015; Oertel et al. 2015); (2) the inclusion of three-body forces with one or more hyperons (see Vidana et al. 2011; Yamamoto et al. 2014; Lonardoni et al. 2015 for recent studies); (3) the appearance of other hadronic degrees of freedom such as the Δ isobar (Drago et al. 2014) or meson condensates that push the onset of hyperons to higher densities; and (4) the appearance of a phase transition to deconfined quark matter at densities below the hyperon threshold (Alford et al. 2007; Klahn et al. 2013; Zdunik & Haensel 2013). For a detailed review on the “hyperon puzzle,” we refer the reader to Chatterjee & Vidana (2016) and references therein.

The presence of strong magnetic fields inside neutron stars is another possible source for a stiffer EoS that could sustain masses of $2 M_\odot$. Anomalous X-ray pulsars and soft γ -ray repeaters are identified with highly magnetized neutron stars with a surface magnetic field of $\sim 10^{14}\text{--}10^{15} \text{ G}$ (Vasishth & Gotthelf 1997; Kouveliotou et al. 1998; Woods et al. 1999). This class of compact objects has been named “magnetars,” i.e., neutron stars with magnetic fields several orders of magnitude larger than the canonical surface dipole magnetic fields $B \sim 10^{12}\text{--}10^{13} \text{ G}$ of the bulk of the pulsar population (Mereghetti 2008; Rea & Esposito 2011; Turolla et al. 2015). It has been shown that magnetic fields larger than $B/B_c^e = 10^5$, with $B_c^e = 4.414 \times 10^{13} \text{ G}$ being the critical magnetic field at which the electron cyclotron energy is equal to the electron mass, will affect the EoS of dense nuclear matter (Chakrabarty

et al. 1997; Bandyopadhyay et al. 1998; Broderick et al. 2000; Suh & Mathews 2001; Harding & Lai 2006; Chen et al. 2007; Rabhi et al. 2008; Dexheimer et al. 2012; Strickland et al. 2012). The study of the effects upon the EoS of hyperonic matter of very strong magnetic fields ($B \sim 10^{18}\text{--}10^{19} \text{ G}$ in the star center) was initiated by Broderick et al. (2002) and has been recently addressed (Rabhi & Providencia 2010; Lopes & Menezes 2012; Sinha et al. 2013; Gomes et al. 2014).

In the present paper we reconcile the $2 M_\odot$ mass observations with the recent analyses of radii below 13 km for neutron stars, while fulfilling the constraints from the properties of nuclear matter, nuclei, and HICs at high energy. This is accomplished for neutron stars with nucleonic and hyperonic cores. The formalism is based on the covariant field-theoretical approach to hadronic matter (see for example Serot & Walecka 1986, 1997, and chapter 4 of Glendenning 2000, and references therein). The nucleonic EoS is obtained as a new parameterization of the nonlinear realization of the relativistic mean-field (RMF) model (Serot & Walecka 1986, 1997; Glendenning 2000; Chen & Piekarewicz 2014). Starting from the recent RMF parameter set FSU2 (Chen & Piekarewicz 2014), we find that by softening the pressure of neutron star matter in the neighborhood of saturation one can accommodate smaller stellar radii, while the properties of nuclear matter and finite nuclei are still fulfilled. Moreover, we are able to keep the pressure at high densities in agreement with HIC data and sufficiently stiff such that it can sustain neutron stars of $\sim 2 M_\odot$. We denote the new parameterization by FSU2R. Next we introduce hyperons in our calculation and fit the hyperon couplings to the value of the hyperon–nucleon and hyperon–hyperon optical potentials extracted from the available data on hypernuclei. Whereas the radius of the neutron stars is insensitive to the appearance of the hyperons, we find a reduction of the maximum mass of the neutron stars due to the expected softening of the EoS. However, we find that the $2 M_\odot$ constraint is still fulfilled when hyperons are considered by means of a slight modification of the parameters of the model, denoted as FSU2H, compatible with astrophysical observations and empirical data. We also analyze the effect of strong magnetic fields in the mass and radius of neutron stars. The origin of the intense magnetic fields in magnetars is still open to debate and the strength of the inner values is still unknown (Thompson & Duncan 1993; Ardeljan et al. 2005; Vink & Kuiper 2006). Nevertheless, it is worth exploring the modification on the EoS and on the neutron star properties induced by magnetic fields that are as large as the upper limit imposed by the scalar virial theorem (Chandrasekhar & Fermi 1953; Shapiro & Teukolsky 1983), which is of the order of $B \sim 2 \times 10^8 (M/M_\odot)(R/R_\odot)^{-2}$. For a star of $R \sim 10 \text{ km}$ and $M \sim 2 M_\odot$ the magnetic field could then reach around $2 \times 10^{18} \text{ G}$. In our study we have magnetic fields close to this value only at the very center of the star and assume a magnetic field profile toward a value of 10^{15} G at the surface, hence fulfilling the stability constraint. From the calculations with the proposed EoS we conclude that nucleonic and hyperonic magnetars with a surface magnetic field of $\sim 10^{15} \text{ G}$ and with magnetic fields values of $\sim 10^{18} \text{ G}$ in the interior can reach maximum masses of $2 M_\odot$ with radii in the 12–13 km range.

The paper is organized as follows. In Section 2 we present the RMF model and the inclusion of magnetic fields for the

determination of the EoS in beta-equilibrated matter. In Section 3 we show how we calibrate the nucleonic model FSU2R by fulfilling the constraints of $2 M_{\odot}$ mass observations and small neutron star radii, as well as the properties of nuclear matter, nuclei, and HICs at high energy. Then, in Section 4 we introduce hyperons and magnetic fields and provide a slightly changed parameterization, FSU2H, that also fulfills the observational and experimental requirements while allowing for maximum masses of $2 M_{\odot}$. We finally summarize our results in Section 5.

2. FORMALISM

Our starting point is the RMF model of matter, where baryons interact through the exchange of mesons and which provides a covariant description of the EoS and nuclear systems. The Lagrangian density of the theory can be written as (Serot & Walecka 1986, 1997; Glendenning 2000; Chen & Piekarewicz 2014)

$$\mathcal{L} = \sum_b \mathcal{L}_b + \mathcal{L}_m + \sum_{l=e,\mu} \mathcal{L}_l, \quad (1)$$

with the baryon (b), lepton ($l = e, \mu$), and meson ($m = \sigma, \omega, \rho, \phi$) Lagrangians given by

$$\begin{aligned} \mathcal{L}_b &= \bar{\Psi}_b (i\gamma_{\mu} \partial^{\mu} - q_b \gamma_{\mu} A^{\mu} - m_b \\ &\quad + g_{\sigma b} \sigma - g_{\omega b} \gamma_{\mu} \omega^{\mu} - g_{\phi b} \gamma_{\mu} \phi^{\mu} - g_{\rho b} \gamma_{\mu} \mathbf{I}_b \cdot \boldsymbol{\rho}^{\mu}) \Psi_b, \\ \mathcal{L}_l &= \bar{\psi}_l (i\gamma_{\mu} \partial^{\mu} - q_l \gamma_{\mu} A^{\mu} - m_l) \psi_l, \\ \mathcal{L}_m &= \frac{1}{2} \partial_{\mu} \sigma \partial^{\mu} \sigma - \frac{1}{2} m_{\sigma}^2 \sigma^2 - \frac{\kappa}{3!} (g_{\sigma N} \sigma)^3 - \frac{\lambda}{4!} (g_{\sigma N} \sigma)^4 \\ &\quad - \frac{1}{4} \Omega^{\mu\nu} \Omega_{\mu\nu} + \frac{1}{2} m_{\omega}^2 \omega_{\mu} \omega^{\mu} + \frac{\zeta}{4!} (g_{\omega N} \omega_{\mu} \omega^{\mu})^4 \\ &\quad - \frac{1}{4} \mathbf{R}^{\mu\nu} \mathbf{R}_{\mu\nu} + \frac{1}{2} m_{\rho}^2 \boldsymbol{\rho}_{\mu} \boldsymbol{\rho}^{\mu} + \Lambda_{\omega} g_{\rho N}^2 \boldsymbol{\rho}_{\mu} \boldsymbol{\rho}^{\mu} g_{\omega N}^2 \omega_{\mu} \omega^{\mu} \\ &\quad - \frac{1}{4} P^{\mu\nu} P_{\mu\nu} + \frac{1}{2} m_{\phi}^2 \phi_{\mu} \phi^{\mu} - \frac{1}{4} F^{\mu\nu} F_{\mu\nu}, \end{aligned} \quad (2)$$

where Ψ_b and ψ_l are the baryon and lepton Dirac fields, respectively. The mesonic and electromagnetic field strength tensors are $\Omega_{\mu\nu} = \partial_{\mu} \omega_{\nu} - \partial_{\nu} \omega_{\mu}$, $\mathbf{R}_{\mu\nu} = \partial_{\mu} \boldsymbol{\rho}_{\nu} - \partial_{\nu} \boldsymbol{\rho}_{\mu}$, $P_{\mu\nu} = \partial_{\mu} \phi_{\nu} - \partial_{\nu} \phi_{\mu}$, and $F_{\mu\nu} = \partial_{\mu} A_{\nu} - \partial_{\nu} A_{\mu}$. The electromagnetic field is assumed to be externally generated and, as we will discuss below, we do not consider the coupling of the particles to the electromagnetic field tensor via the baryon anomalous magnetic moments. The strong interaction couplings of a meson to a certain baryon are denoted by g (with N indicating nucleon), the electromagnetic couplings by q and the baryon, meson, and lepton masses by m . The vector \mathbf{I}_b stands for the isospin operator.

The Lagrangian density (2) incorporates scalar and vector meson self-interactions as well as a mixed quartic vector meson interaction. The nonlinear meson interactions are important for a quantitative description of nuclear matter and finite nuclei, as they lead to additional density dependence that represents in an effective way the medium dependence induced by many-body correlations. The scalar self-interactions with coupling constants κ and λ , introduced by Boguta & Bodmer (1977), are responsible for softening the EoS of symmetric nuclear matter (SNM) around saturation density and allow one to obtain a

realistic value for the compression modulus of nuclear matter (Boguta & Bodmer 1977; Boguta & Stoecker 1983). The quartic isoscalar–vector self-interaction (with coupling ζ) softens the EoS at high densities (Mueller & Serot 1996), while the mixed quartic isovector–vector interaction (with coupling Λ_{ω}) is introduced (Horowitz & Piekarewicz 2001a, 2001b) to modify the density dependence of the nuclear symmetry energy, which measures the energy cost involved in changing the protons into neutrons in nuclear matter.

The Dirac equations for baryons and leptons are given by

$$(i\gamma_{\mu} \partial^{\mu} - q_b \gamma_{\mu} A^{\mu} - m_b^* - g_{\omega b} \gamma_0 \omega^0 - g_{\phi b} \gamma_0 \phi^0 - g_{\rho b} I_{3b} \gamma_0 \rho_3^0) \Psi_b = 0, \quad (3)$$

$$(i\gamma_{\mu} \partial^{\mu} - q_l \gamma_{\mu} A^{\mu} - m_l) \psi_l = 0, \quad (4)$$

where the effective baryon masses are defined as

$$m_b^* = m_b - g_{\sigma b} \sigma. \quad (5)$$

The field equations of motion follow from the Euler–Lagrange equations. In the mean-field approximation, the meson fields are replaced by their respective mean-field expectation values, which are given in uniform matter as $\bar{\sigma} = \langle \sigma \rangle$, $\bar{\rho} = \langle \rho_3^0 \rangle$, $\bar{\omega} = \langle \omega^0 \rangle$, and $\bar{\phi} = \langle \phi^0 \rangle$. Thus, the equations of motion for the meson fields in the mean-field approximation for the uniform medium are

$$m_{\sigma}^2 \bar{\sigma} + \frac{\kappa}{2} g_{\sigma N}^3 \bar{\sigma}^2 + \frac{\lambda}{3!} g_{\sigma N}^4 \bar{\sigma}^3 = \sum_b g_{\sigma b} n_b^s, \quad (6)$$

$$m_{\omega}^2 \bar{\omega} + \frac{\zeta}{3!} g_{\omega N}^4 \bar{\omega}^3 + 2\Lambda_{\omega} g_{\rho N}^2 g_{\omega N}^2 \bar{\rho}^2 \bar{\omega} = \sum_b g_{\omega b} n_b, \quad (7)$$

$$m_{\rho}^2 \bar{\rho} + 2\Lambda_{\omega} g_{\rho N}^2 g_{\omega N}^2 \bar{\omega}^2 \bar{\rho} = \sum_b g_{\rho b} I_{3b} n_b, \quad (8)$$

$$m_{\phi}^2 \bar{\phi} = \sum_b g_{\phi b} n_b, \quad (9)$$

where I_{3b} represents the third component of isospin of baryon b , with the convention $I_{3p} = 1/2$. The quantities $n_b^s = \langle \bar{\Psi}_b \Psi_b \rangle$ and $n_b = \langle \bar{\Psi}_b \gamma^0 \Psi_b \rangle$ are the scalar and baryon density for a given baryon, respectively.

In the presence of a magnetic field, the single-particle energy of the charged baryons and leptons is quantized in the perpendicular direction to the magnetic field. Taking the magnetic field in the z -direction, $\mathbf{B} = B z \hat{z}$, the single particle energies of all baryons and leptons are given by (Broderick et al. 2000)

$$\begin{aligned} E_{\nu}^{cb} &= \sqrt{k_z^2 + m_{cb}^{*2} + 2\nu|q_{cb}|B} \\ &\quad + g_{\omega cb} \bar{\omega} + g_{\rho cb} I_{3b} \bar{\rho} + g_{\phi cb} \bar{\phi}, \end{aligned} \quad (10)$$

$$\begin{aligned} E_{\nu}^{ub} &= \sqrt{k^2 + m_{ub}^{*2}} \\ &\quad + g_{\omega ub} \bar{\omega} + g_{\rho ub} I_{3b} \bar{\rho} + g_{\phi ub} \bar{\phi}, \end{aligned} \quad (11)$$

$$E_{\nu}^l = \sqrt{k_z^2 + m_l^2 + 2\nu|q_l|B}, \quad (12)$$

with cb denoting charged baryons and ub uncharged baryons. The quantity $\nu = \left(n + \frac{1}{2} - \frac{1}{2} \frac{q}{|q|} \sigma_z \right) = 0, 1, 2, \dots$, with n being the principal quantum number and σ_z the Pauli matrix,

indicates the Landau levels of the fermions with electric charge q .

As mentioned above, we have omitted the coupling of the baryons to the electromagnetic field tensor via their anomalous magnetic moments. The interaction of the baryon anomalous magnetic moments with the field strength has been found to partly compensate for the effects on the EoS associated with Landau quantization (Broderick et al. 2000). However, to see some appreciable changes in the EoS and the neutron star composition, intense fields of the order of 5×10^{18} G are needed. Moreover, those effects are mostly concentrated at low densities ($\lesssim 2n_0$) for such a field strength (Broderick et al. 2000; Rabhi et al. 2008). Therefore, neglecting the effects associated to the anomalous magnetic moments is a reasonable approximation in the present work since we consider neutron stars with magnetic fields at the core of at most 2×10^{18} G and magnetic field profiles that do not reach 5×10^{17} G in the region $\lesssim 2n_0$.

The Fermi momenta of the charged baryons, $k_{F,\nu}^{cb}$, uncharged baryons, k_F^{ub} , and leptons, $k_{F,\nu}^l$, are related to the Fermi energies E_F^{cb} , E_F^{ub} and E_F^l as

$$\begin{aligned} k_{F,\nu}^{cb} &= \sqrt{(E_F^{cb})^2 - (m_{cb}^{*2} + 2\nu|q_{cb}|B)}, \\ k_F^{ub} &= \sqrt{(E_F^{ub})^2 - m_{ub}^{*2}}, \\ k_{F,\nu}^l &= \sqrt{(E_F^l)^2 - (m_l^2 + 2\nu|q_l|B)}, \end{aligned} \quad (13)$$

while the chemical potentials of baryons and leptons are defined as

$$\mu_b = E_F^b + g_{\omega b} \bar{\omega} + g_{pb} I_{3b} \bar{\rho} + g_{\phi b} \bar{\phi}, \quad (14)$$

$$\mu_l = E_F^l. \quad (15)$$

The largest value of ν is obtained by imposing that the square of the Fermi momentum of the particle is still positive, i.e., by taking the closest integer from below defined by the ratio

$$\begin{aligned} \nu_{\max} &= \left[\frac{(E_F^l)^2 - m_l^2}{2|q_l|B} \right], \quad \text{leptons} \\ \nu_{\max} &= \left[\frac{(E_F^{cb})^2 - m_{cb}^{*2}}{2|q_{cb}|B} \right], \quad \text{charged baryons}. \end{aligned}$$

With all these ingredients, the scalar and vector densities for baryons and leptons are given by (Broderick et al. 2000)

$$\begin{aligned} n_{cb}^s &= \frac{|q_{cb}|B m_{cb}^*}{2\pi^2} \sum_{\nu=0}^{\nu_{\max}} r_\nu \ln \frac{k_{F,\nu}^{cb} + E_F^{cb}}{\sqrt{m_{cb}^{*2} + 2\nu|q_{cb}|B}}, \\ n_{ub}^s &= \frac{m_{ub}^*}{2\pi^2} \left[E_F^{ub} k_F^{ub} - m_{ub}^{*2} \ln \frac{k_F^{ub} + E_F^{ub}}{m_{ub}^*} \right], \\ n_{cb} &= \frac{|q_{cb}|B}{2\pi^2} \sum_{\nu=0}^{\nu_{\max}} r_\nu k_{F,\nu}^{cb}, \\ n_{ub} &= \frac{(k_F^{ub})^3}{3\pi^2}, \\ n_l &= \frac{|q_l|B}{2\pi^2} \sum_{\nu=0}^{\nu_{\max}} r_\nu k_{F,\nu}^l, \end{aligned} \quad (16)$$

where r_ν is the degeneracy of the ν Landau level, which is 1 for $\nu = 0$ and 2 for $\nu \neq 0$.

We can now obtain the energy density ε and pressure P of the system. The energy density of matter, $\varepsilon_{\text{matt}}$, is given by

$$\begin{aligned} \varepsilon_{\text{matt}} &= \sum_b \varepsilon_b + \sum_l \varepsilon_l \\ &+ \frac{1}{2} m_\sigma^2 \bar{\sigma}^2 + \frac{1}{2} m_\omega^2 \bar{\omega}^2 + \frac{1}{2} m_\rho^2 \bar{\rho}^2 + \frac{1}{2} m_\phi^2 \bar{\phi}^2 \\ &+ \frac{\kappa}{3!} (g_\sigma \bar{\sigma})^3 + \frac{\lambda}{4!} (g_\sigma \bar{\sigma})^4 \\ &+ \frac{\zeta}{8} (g_\omega \bar{\omega})^4 + 3\Lambda_\omega (g_\rho g_\omega \bar{\rho} \bar{\omega})^2, \end{aligned} \quad (17)$$

where the energy densities of baryons and leptons have the following expressions

$$\begin{aligned} \varepsilon_{cb} &= \frac{|q_{cb}|B}{4\pi^2} \sum_{\nu=0}^{\nu_{\max}} r_\nu \\ &\times \left[k_{F,\nu}^{cb} E_F^{cb} + (m_{cb}^{*2} + 2\nu|q_{cb}|B) \ln \frac{k_{F,\nu}^{cb} + E_F^{cb}}{\sqrt{m_{cb}^{*2} + 2\nu|q_{cb}|B}} \right], \\ \varepsilon_{ub} &= \frac{1}{8\pi^2} \left[k_F^{ub} (E_F^{ub})^3 + (k_F^{ub})^3 E_F^{ub} - m_{ub}^{*4} \ln \frac{k_F^{ub} + E_F^{ub}}{m_{ub}^*} \right], \\ \varepsilon_l &= \frac{|q_l|B}{4\pi^2} \sum_{\nu=0}^{\nu_{\max}} r_\nu \\ &\times \left[k_{F,\nu}^l E_F^l + (m_l^2 + 2\nu|q_l|B) \ln \frac{k_{F,\nu}^l + E_F^l}{\sqrt{m_l^2 + 2\nu|q_l|B}} \right]. \end{aligned} \quad (18)$$

The pressure of matter, P_{matt} , is obtained using the thermodynamic relation

$$P_{\text{matt}} = \sum_i \mu_i n_i - \varepsilon_{\text{matt}}. \quad (19)$$

While the contribution from the electromagnetic field to the energy density is $B^2/8\pi$, we use the so-called “chaotic field” prescription for the calculation of the pressure of the system (Menezes & Lopes 2016), so that we have

$$\varepsilon = \varepsilon_{\text{matt}} + \frac{B^2}{8\pi}, \quad (20)$$

$$P = P_{\text{matt}} + \frac{B^2}{24\pi}. \quad (21)$$

2.1. Neutron Star Matter in β -equilibrium

In order to determine the structure of neutron stars one needs to obtain the EoS over a wide range of densities. For the inner and outer crust of the star we employ the EoS of Sharma et al. (2015), which has been obtained from microscopic calculations. In the core of neutron stars, we find β -equilibrated globally neutral, charged matter. Consequently, the chemical

potentials, μ_i , and particle densities, n_i , satisfy the conditions

$$\begin{aligned}\mu_i &= b_i \mu_n - q_i \mu_e, \\ 0 &= \sum_{cb,l} q_i n_i, \\ n &= \sum_{cb,ub} n_i,\end{aligned}\quad (22)$$

with b_i the baryon number and q_i the charge of the particle i . These relations together with Equations (3), (4) and the field Equations (6)–(9) for σ , ω , ρ and ϕ have to be solved self-consistently for total baryon density n in the presence of a magnetic field. In this way, we obtain the chemical potential and the corresponding density of each species for a given n , so that we can determine the energy density and pressure of the neutron star matter at each density.

Once the EoS is known, the mass M and the corresponding radius R of the neutron star are obtained from solving the Tolman–Oppenheimer–Volkoff (TOV) equations (Oppenheimer & Volkoff 1939)

$$\begin{aligned}\frac{dP(r)}{dr} &= -\frac{G}{r^2} [\varepsilon(r) + P(r)] \\ &\times [M(r) + 4\pi r^3 P(r)] \left[1 - \frac{2GM(r)}{r} \right]^{-1}, \\ \frac{dM(r)}{dr} &= 4\pi \varepsilon(r) r^2,\end{aligned}\quad (23)$$

where r is the radial coordinate. To solve these equations one needs to specify the initial conditions, namely the enclosed mass and the pressure at the center of the star, $M(r = 0) = 0$ and $P(r = 0) = P_c$, while the energy density is taken from the assumed EoS. The integration of the TOV equations over the radial coordinate ends when $P(r = R) = 0$.

3. CALIBRATION OF THE NUCLEONIC MODEL

3.1. Equation of State, Stellar Masses, and Stellar Radii

We start our analysis by defining the baseline model for nuclear matter to compute masses and radii of neutron stars. Nuclear models that perform similarly well in the description of finite nuclei often extrapolate very differently at high densities, as usually no information on the high-density sector of the EoS has been incorporated in the fitting of the model. In this work we are interested in a model that gives neutron star radii as small as possible and massive enough neutron stars, in order to reconcile in a unified formalism the new astrophysical indications of small stellar radii and the existence of stars of $2 M_\odot$ masses, while still meeting the constraints from the nuclear data of terrestrial laboratories.

For the nuclear model we start from the Lagrangian density of Equations (1), (2) by only considering nucleons and mesons. As mentioned in Section 2, the ζ self-coupling of the ω meson (see Equation (2)) is efficient in softening the EoS at supranormal densities while the Λ_ω cross-coupling of the ω and ρ mesons (Equation (2)) regulates the density dependence of the symmetry energy. In order to show the effect of these nonlinear contributions to the EoS, in Figure 1 we plot for selected interactions the pressures of SNM in the upper panel and of pure neutron matter (PNM) in the lower panel. The two shaded areas in the SNM panel depict the regions that are compatible with the data on collective flow (Danielewicz

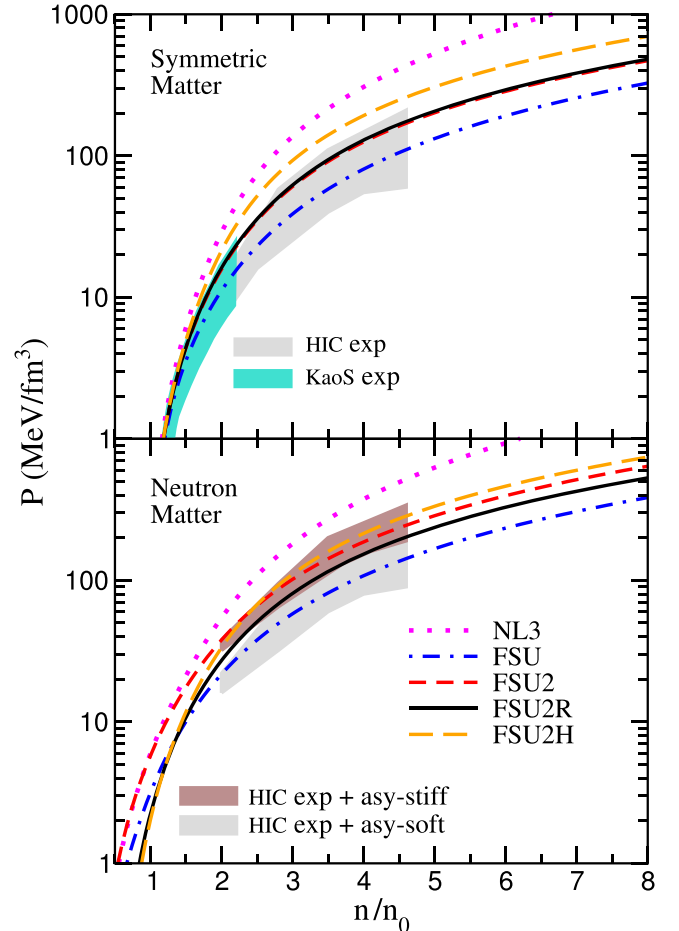


Figure 1. Pressure vs. baryon density for SNM (upper panel) and PNM (lower panel) for the different models presented in the text: NL3 (Lalazissis et al. 1997), FSU (Todd-Rutel & Piekarewicz 2005), FSU2 (Chen & Piekarewicz 2014), FSU2R (this work), and FSU2H (this work, Section 4). The regions compatible with the experimental data on collective flow (Danielewicz et al. 2002) and on kaon production (Fuchs et al. 2001; Lynch et al. 2009) in HICs are depicted in gray and turquoise, respectively, in the upper panel. The shaded areas in the panel of PNM correspond to the constraints from the flow data supplemented by a soft (gray area) or a stiff (brown area) symmetry energy (Danielewicz et al. 2002).

et al. 2002) (gray area) and on kaon production (Fuchs et al. 2001; Lynch et al. 2009) (turquoise region) according to the modeling of energetic HICs. The shaded areas in the PNM panel correspond to the constraints from the flow data supplemented by a symmetry energy with weak (gray area) or strong (brown area) density dependence (Danielewicz et al. 2002).

We first consider the well-known parameter sets NL3 (Lalazissis et al. 1997) and FSU (also called FSUGold) (Todd-Rutel & Piekarewicz 2005). NL3 has $\zeta = \Lambda_\omega = 0$ while FSU has $\zeta = 0.06$ and $\Lambda_\omega = 0.03$ (the full set of parameters of the models can be found in Table 1). Both NL3 and FSU reproduce quite well a variety of properties of atomic nuclei. However, they render two EoSs in SNM with different behavior at supranormal densities due to the different ζ value (we recall that the Λ_ω coupling does not contribute in SNM). We can see in Figure 1 (upper panel) that above density $n \sim 1.5-2n_0$ the FSU model with $\zeta = 0.06$ (dot-dashed blue line) yields a much softer SNM pressure than the NL3 model with $\zeta = 0$ (dotted magenta line). In PNM, the isovector coupling Λ_ω tunes the change with density of the EoS, as it

Table 1
 Parameters for the Models NL3 (Lalazissis et al. 1997), FSU (Todd-Rutel & Piekarewicz 2005), FSU2 (Chen & Piekarewicz 2014), FSU2R (This Work), and FSU2H (This Work, Section 4)

Models	NL3	FSU	FSU2	FSU2R	FSU2H
m_σ [MeV]	508.194	491.500	497.479	497.479	497.479
m_ω [MeV]	782.501	782.500	782.500	782.500	782.500
m_p [MeV]	763.000	763.000	763.000	763.000	763.000
$g_{\sigma N}^2$	104.3871	112.1996	108.0943	107.5751	102.7200
$g_{\omega N}^2$	165.5854	204.5469	183.7893	182.3949	169.5315
g_{pN}^2	79.6000	138.4701	80.4656	247.3409	247.3409
κ	3.8599	1.4203	3.0029	3.0911	4.0014
λ	-0.015905	0.023762	-0.000533	-0.001680	-0.013298
ζ	0.00	0.06	0.0256	0.024	0.008
Λ_ω	0.00	0.03	0.000823	0.05	0.05
n_0 [fm $^{-3}$]	0.1481	0.1484	0.1505	0.1505	0.1505
E/A [MeV]	-16.24	-16.30	-16.28	-16.28	-16.28
K [MeV]	271.5	230.0	238.0	238.0	238.0
m_N^*/m_N	0.595	0.610	0.593	0.593	0.593
$E_{\text{sym}}(n_0)$ [MeV]	37.3	32.6	37.6	30.2	30.2
L [MeV]	118.2	60.5	112.8	44.3	41.0
$P(n_0)$ [MeV fm $^{-3}$]	5.99	3.18	5.81	2.27	2.06

Note. The mass of the nucleon is set to 939 MeV. Also shown are the corresponding energy per particle (E/A), compression modulus (K), and effective nucleon mass m_N^*/m_N at saturation density n_0 , as well as the symmetry energy (E_{sym}), slope of the symmetry energy (L) and PNM pressure (P) at n_0 .

softens the symmetry energy. Indeed, if we compare the same models FSU and NL3 in PNM (see Figure 1(lower panel)), FSU ($\Lambda_\omega = 0.03$) has its pressure strongly further reduced with respect to NL3 ($\Lambda_\omega = 0$) in the density window from around saturation density n_0 up to $n \sim 1.5\text{--}2n_0$. For densities above $2n_0$ the softening effect from Λ_ω is less prominent and the PNM pressures of FSU and NL3 show comparable differences with the case of SNM. We therefore note, consistently with the systematics in earlier works (Horowitz & Piekarewicz 2001a, 2001b; Carriere et al. 2003; Chen & Piekarewicz 2014), that the Λ_ω and ζ couplings have a complementary impact on the EoS by each one influencing almost separate density sectors. This will be important for our goals for stellar radii and masses as we shall see below.

Next, we obtain the mass–radius (M–R) relation of neutron stars for a given EoS by solving the TOV equations (Oppenheimer & Volkoff 1939). As mentioned in Section 2, for the crust region of the star we have employed the EoS recently derived in Sharma et al. (2015).⁴ In this section we focus on neutron stars with cores of purely nucleonic matter; hence, we compute the EoS of the core assuming a β -equilibrated and charge neutral uniform liquid of neutrons, protons, and leptons (electrons and muons). As expected from its stiff EoS, the NL3 set predicts a large maximum mass ($M_{\text{max}} \approx 2.8 M_\odot$) and large stellar radii (≈ 13 km for M_{max} and ≈ 15 km for a typical neutron star of $1.5 M_\odot$); see the M–R relations plotted in Figure 2 and the values in Table 2. In comparison, the soft EoS of the FSU model brings in a dramatic reduction of the stellar masses and radii. The two shaded bands in Figure 1 portray the observed masses of the heaviest neutron stars known, i.e., $M = 1.97 \pm 0.04 M_\odot$ in the pulsar PSR J1614–2230 (Demorest et al. 2010) and $M = 2.01 \pm 0.04 M_\odot$ in the pulsar PSR J0348+0432

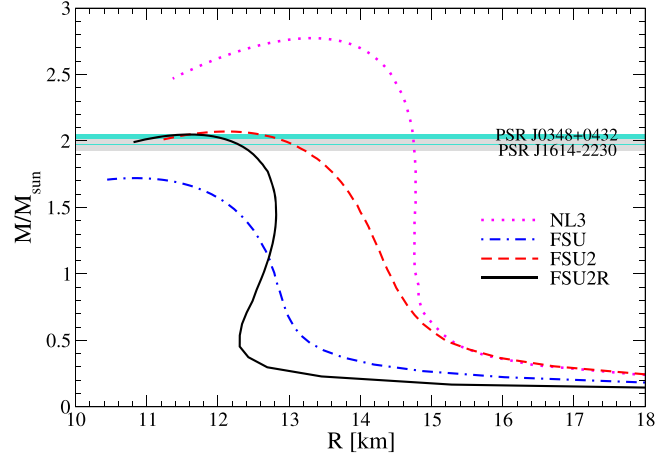


Figure 2. Mass vs. radius for neutron stars for the models NL3 (Lalazissis et al. 1997), FSU (Todd-Rutel & Piekarewicz 2005), FSU2 (Chen & Piekarewicz 2014), and FSU2R (this work). The two shaded bands portray the masses $M = 1.97 \pm 0.04 M_\odot$ in the pulsar PSR J1614–2230 (gray band) (Demorest et al. 2010) and $M = 2.01 \pm 0.04 M_\odot$ in the pulsar PSR J0348 +0432 (turquoise band) (Antoniadis et al. 2013).

(Antoniadis et al. 2013). These two astrophysical measurements are arguably the most accurate constraints available so far to validate or defeat the model predictions for the high-density EoS. The recently formulated relativistic parameter set FSU2 (Chen & Piekarewicz 2014)—based on the same Lagrangian we are discussing—is one of the first best-fit models to take into account the condition of a limiting stellar mass of $2 M_\odot$ in the calibration of the parameters (also see Erler et al. 2013; Chen & Piekarewicz 2015b). The FSU2 model has been optimized to accurately reproduce the experimental data on a pool of properties of finite nuclei with the maximum neutron star mass observable included in the fit (Chen & Piekarewicz 2014). The resulting FSU2 set has $\zeta = 0.0256$ and $\Lambda_\omega = 0.0008$, see Table 1. In consonance with these values, we can appreciate in Figure 1 that FSU2 predicts an intermediate

⁴ We did not find sizable changes in our results when we repeated some of the M–R calculations using the crustal EoS from the Baym–Pethick–Sutherland model (Baym et al. 1971).

Table 2
Neutron Star Properties Obtained for the Different Nuclear Models Discussed in This Work

Composition	Models	M_{\max}/M_{\odot}	$R(M_{\max})$ (km)	$n_c(M_{\max})/n_0$	$R(1.5 M_{\odot})$ (km)	$Y \text{ onset}$ (n/n_0)
$pne\mu$	NL3	2.77	13.3	4.5	14.8	...
	FSU	1.72	10.8	7.8	12.2	...
	FSU2	2.07	12.1	5.9	14.0	...
	FSU2R	2.05	11.6	6.3	12.8	...
	FSU2H	2.38	12.3	5.3	13.2	...
$pnYe\mu$	NL3	2.27	12.9	5.3	14.8	1.9
	FSU2	1.76	12.1	6.3	13.9	2.1
	FSU2R	1.77	11.6	6.5	12.8	2.4
	FSU2H	2.03	12.0	5.8	13.2	2.2
$pne\mu$ ($B_c = 2 \times 10^{18} \text{ G}$)	FSU2R	2.11	11.6	6.1	12.8	
	FSU2H	2.42	12.3	5.2	13.2	
$pnYe\mu$ ($B_c = 2 \times 10^{18} \text{ G}$)	FSU2R	1.88	11.6	6.3	12.8	2.4
	FSU2H	2.15	12.3	5.3	13.2	2.2

Note. Results are shown for nucleonic-only ($pne\mu$) or hyperonic ($pnYe\mu$) stars, and including or not a magnetic field having the profile of the solid line in Figure 6 (Section 4). The quantity $n_c(M_{\max})/n_0$ denotes the central baryonic density at the maximum mass, M_{\max} , normalized to the corresponding saturation density, n_0 , whereas Y onset is the onset of appearance of hyperons normalized to n_0 .

EoS between the stiff EoS of the NL3 set ($\zeta = \Lambda_{\omega} = 0$) and the soft EoS of the FSU set ($\zeta = 0.06$, $\Lambda_{\omega} = 0.03$). Accordingly, FSU2 produces a neutron star M–R relation located in between the curves of NL3 and FSU in Figure 2. FSU2 yields a heaviest stellar mass $M_{\max} = 2.07 M_{\odot}$ with a radius of 12.1 km, and predicts $1.5 M_{\odot}$ stars with a radius of 14 km, see Table 2.

While the limiting stellar mass is governed by the stiffness of the EoS above several times the saturation density n_0 (see column $n_c(M_{\max})/n_0$ in Table 2), the radius of a canonical neutron star is dominated by the density dependence of the EoS of PNM at 1–2 times n_0 (Lattimer & Prakash 2007; Ozel & Freire 2016). Thus, observational information on masses and radii of neutron stars has the potential to uniquely pin down the nuclear EoS in a vast density region. As mentioned in the Introduction, several of the recent astrophysical analyses for radii (Guillot et al. 2013; Guver & Ozel 2013; Guillot & Rutledge 2014; Heinke et al. 2014; Lattimer & Steiner 2014; Ozel & Freire 2016; Ozel et al. 2016) are converging in the 9–12 km range (also see Fortin et al. 2015 for a detailed discussion). The review study of Lattimer & Prakash (2016) indicates a similar range around 11–13 km for the radii of canonical neutron stars. The possibility that neutron stars have these small radii is as exciting as it is deeply challenging for nuclear theory. Note that small radii demand a sufficiently soft EoS below twice the saturation density, while the observed large masses require that the same EoS must be able to evolve into a stiff EoS at high densities. It is therefore timely to explore whether such small radii can be obtained by the EoS of the covariant field-theoretical Lagrangian (1), (2), while fulfilling at the same time the maximum mass constraint of $2 M_{\odot}$ and the phenomenology of the atomic nucleus.

To construct the new EoS we start from the FSU2 model and increase the Λ_{ω} coupling. This softens the PNM pressure especially up to densities of $1.5\text{--}2n_0$. For a given stellar mass there is less pressure to balance gravity, thereby leading to a more compact object of smaller radius. The increase of Λ_{ω} also produces a certain reduction of the PNM pressure in the high-density sector. This may spoil the $2 M_{\odot}$ maximum mass but can be counteracted by a decrease of the strength of the ζ coupling.

During the change of the $(\Lambda_{\omega}, \zeta)$ couplings, we refit the remaining couplings $g_{\sigma N}$, $g_{\omega N}$, $g_{\rho N}$, κ , and λ of the nucleon–meson Lagrangian (1), (2) by invoking the same saturation properties of FSU2 in SNM (i.e., same saturation density n_0 , energy per particle E/A , compression modulus K , and effective nucleon mass m_N^*) and a symmetry energy $E_{\text{sym}} = 25.7 \text{ MeV}$ at subsaturation density $n = 0.10 \text{ fm}^{-3}$. The last condition arises from the fact that the binding energies of atomic nuclei constrain the symmetry energy at an average density of nuclei of $\sim 0.10 \text{ fm}^{-3}$ better than the symmetry energy at normal density n_0 (Horowitz & Piekarewicz 2001a; Centelles et al. 2009). We found that under this protocol a noteworthy decrease of neutron star radii is achieved with $\Lambda_{\omega} = 0.05$ and $\zeta = 0.024$. We refer to the resulting model as FSU2R. The coupling constants and several bulk properties of FSU2R are collected in Table 1.

We observe in Figure 1 that the EoS of the new FSU2R model is within the boundaries deduced in the studies of energetic HICs (Fuchs et al. 2001; Danielewicz et al. 2002; Lynch et al. 2009). It is worth noting that FSU2R features a *soft* PNM EoS at $n \lesssim 1.5\text{--}2n_0$ and a *stiff* PNM EoS at $n \gtrsim 2n_0$ —apparently a necessary condition to satisfy small radii and heavy limiting neutron star masses. The reduction of the stellar radii in FSU2R compared with the other parameterizations of the Lagrangian (1), (2) is very clear from Figure 2, also see Table 2. The maximum mass of $2.05 M_{\odot}$ calculated with FSU2R is compatible with the heaviest neutron stars (Demorest et al. 2010; Antoniadis et al. 2013) and is characterized by a radius of 11.6 km. For canonical neutron stars of 1.4–1.5 solar masses, FSU2R predicts radii of $\approx 12.8 \text{ km}$, which are more compact than in the other EoSs, see Table 2. Hence, the smaller radii reproduced by the new model point toward the reconciliation between the nuclear EoS, the largest neutron star masses (Demorest et al. 2010; Antoniadis et al. 2013), and the recent extractions of small neutron star sizes from the astrophysical observations of quiescent low-mass X-ray binaries (Guillot & Rutledge 2014) and X-ray bursters (Guver & Ozel 2013) (also see Guillot et al. 2013; Heinke et al. 2014; Lattimer & Steiner 2014; Lattimer & Prakash 2016; Ozel &

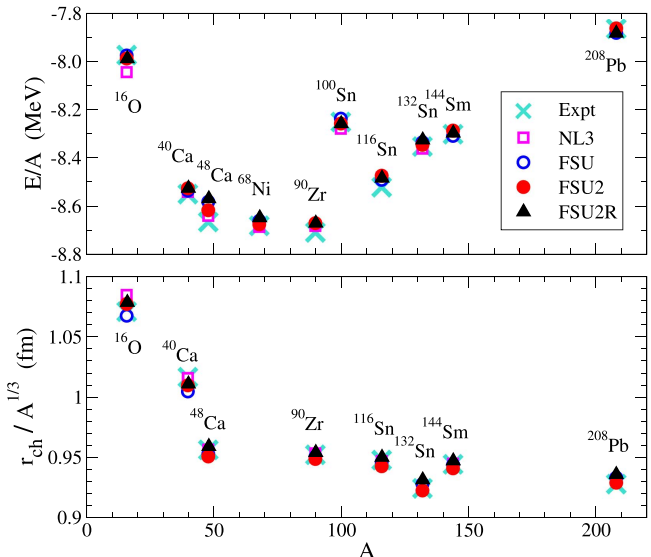


Figure 3. Energy per nucleon E/A and charge radius r_{ch} over $A^{1/3}$, where A is the mass number, of several nuclei with magic proton and/or neutron numbers. The values calculated with the models discussed in the text are compared with experiment. The experimental data are from Wang et al. (2012) for the energies and from Angeli & Marinova (2013) for the charge radii.

Freire 2016; Ozel et al. 2016). We are only aware of similar models RMF012 and RMF016 (also called FSUGarnet) introduced in a recent work (Chen & Piekarewicz 2015b). The RMF012 and RMF016 models were fitted with the same procedure of the FSU2 model of Chen & Piekarewicz (2014) but requiring values for the neutron skin thickness of the ^{208}Pb nucleus of, respectively, 0.12 fm and 0.16 fm. As reported in Chen & Piekarewicz (2015a, 2015b), the RMF016 model supports $2 M_{\odot}$ neutron stars and leads to a radius of 13 km for a $1.4 M_{\odot}$ star, similarly to the predictions we obtain with our FSU2R model.

3.2. Implications for Finite Nuclei: Symmetry Energy, Slope of the Symmetry Energy, and Neutron Skin Thickness

Once the new EoS has been calibrated for neutron stars, it is important to review its implications for the physics regime of atomic nuclei since this regime is accessible in laboratory experiments. We first verify that the new model FSU2R is able to provide a satisfactory description of the best known properties of nuclei, i.e., nuclear ground-state energies and sizes of the nuclear charge distributions. We display in Figure 3 our results for the energies and charge radii of a set of representative nuclei ranging from the light ^{16}O to the heavy ^{208}Pb . The experimental data of these same nuclei were used in the fit of the FSU2 model in Chen & Piekarewicz (2014). In Figure 3, we show the predictions of our FSU2R model alongside the experimental values and the results from the parameter sets NL3, FSU, and FSU2. It can be seen that the four models successfully reproduce the energies and charge radii across the mass table. The agreement of FSU2R with experiment is overall comparable to the other models. We find that the differences between FSU2R and the experimental energies and radii are at the level of 1% or smaller. We mention that we have not drawn error bars of the experimental data in Figure 3, because the nuclear masses and charge radii are measured so precisely (Wang et al. 2012; Angeli &

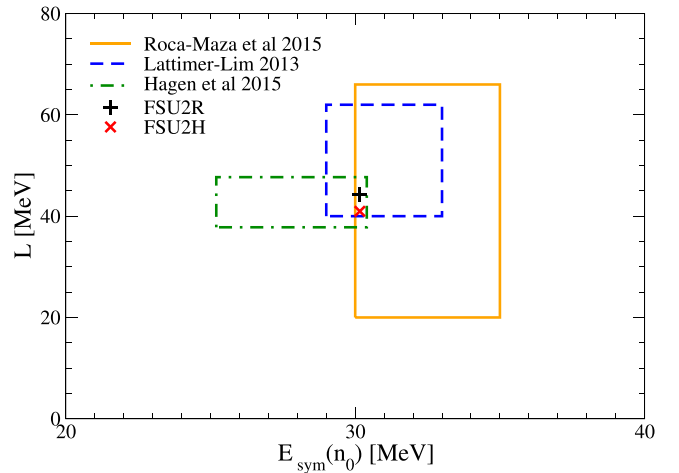


Figure 4. Slope of the symmetry energy (L) vs. symmetry energy ($E_{\text{sym}}(n_0)$) at saturation for the models FSU2R discussed in this section, and FSU2H discussed in Section 4. The rectangular areas are the determinations from Lattimer & Lim (2013) Hagen et al. (2015), and Roca-Maza et al. (2015).

Marinova 2013) that the experimental uncertainties cannot be resolved in the plot.

For our purposes, of special relevance is the fact that the neutron density distributions and other isospin-sensitive observables of atomic nuclei are closely related to the density dependence of the symmetry energy, which in FSU2R has been tailored to supply small stellar radii. The stiffness of the symmetry energy with density is conventionally characterized by its density slope L at the saturation point: $L = 3n_0 \left(\frac{\partial E_{\text{sym}}(n)}{\partial n} \right)_{n_0}$. The L parameter and the pressure $P(n_0)$ of PNM at saturation density are related as $P(n_0) = \frac{1}{3}n_0 L$ (Lynch et al. 2009; Lattimer & Prakash 2016). The new FSU2R EoS yields $E_{\text{sym}}(n_0) = 30.2$ MeV for the symmetry energy at saturation and a slope parameter $L = 44.3$ MeV, which corresponds to a mildly soft nuclear symmetry energy. The PNM pressure at saturation is $P(n_0) = 2.27$ MeV fm $^{-3}$. We have collected these values in Table 1 along with the results for $E_{\text{sym}}(n_0)$, L , and $P(n_0)$ from the other discussed EoSs; now, large differences can be appreciated among the models.

Despite the fact that a precise knowledge of the density dependence of the symmetry energy remains elusive, the windows of values for $E_{\text{sym}}(n_0)$ and the slope parameter L have been continuously narrowed down as the empirical and theoretical constraints have improved over recent years (see, e.g., Li et al. 2014 for a topical review). Remarkably, the values of 30.2 MeV for $E_{\text{sym}}(n_0)$ and 44.3 MeV for L that we find after constraining the EoS to reflect small neutron star radii turn out to be very consistent with the newest determinations of the symmetry energy and its slope at saturation, see Figure 4. Indeed, the quoted FSU2R values overlap with the ranges $30 \lesssim E_{\text{sym}}(n_0) \lesssim 35$ MeV and $20 \lesssim L \lesssim 66$ MeV extracted in Roca-Maza et al. (2015) from the recent high-resolution measurements at RCNP and GSI of the electric dipole polarizability α_D in the nuclei ^{208}Pb (Tamii et al. 2011), ^{120}Sn (Hashimoto et al. 2015), and ^{68}Ni (Rossi et al. 2013). We note that the dipole polarizability α_D , related to the response of nuclei to an external electric field, has been identified as one of the strongest isovector indicators (Reinhard & Nazarewicz 2010). Also note that, compared to hadronic experiments used to probe the symmetry energy, the electromagnetic reactions

involved in the measurements of the α_D observable (Tamii et al. 2011; Rossi et al. 2013; Hashimoto et al. 2015) are particularly suited because they are not hindered by large or uncontrolled uncertainties. The FSU2R predictions for $E_{\text{sym}}(n_0)$ and L also fit within the windows $29 \lesssim E_{\text{sym}}(n_0) \lesssim 33$ MeV and $40 \lesssim L \lesssim 62$ MeV obtained in Lattimer & Lim (2013) from the combined analysis of a variety of empirical nuclear constraints and astrophysical information, which are in line with similar windows obtained in other recent studies (Tsang et al. 2012; Li et al. 2014; Lattimer & Prakash 2016). It also deserves to be mentioned that the $E_{\text{sym}}(n_0)$ and L values of the FSU2R EoS are quite compatible with the theoretical ranges $25.2 \lesssim E_{\text{sym}}(n_0) \lesssim 30.4$ MeV and $37.8 \lesssim L \lesssim 47.7$ MeV that have been derived from the latest progress in ab initio calculations of nuclear systems with chiral forces (Hagen et al. 2015).

The neutron skin thickness $\Delta r_{np} = r_n - r_p$ (difference between the neutron and proton matter radii) of a heavy nucleus such as ^{208}Pb , also provides strong sensitivity to the symmetry energy and the pressure of neutron-rich matter near saturation (Alex Brown 2000; Horowitz & Piekarwicz 2001a, 2001b; Centelles et al. 2009). Basically, the same nuclear pressure that is responsible for determining the radius of a canonical neutron star determines how far neutrons extend out further than protons in a nucleus. By the same token, models that produce smaller stellar radii are expected to predict thinner neutron skins. We find that the FSU2R model, constrained to small neutron star radii, predicts $\Delta r_{np} = 0.133$ fm in ^{208}Pb . Unfortunately, neutron skins are difficult to extract from experiments in a model-independent fashion. The new experiments to measure neutron skins are being designed with electroweak and electromagnetic probes where, unlike hadronic experiments, the interactions with the nucleus (Abrahamyan et al. 2012), or at least the initial state interactions (Tarbert et al. 2014), are not complicated by the strong force. The challenging, purely electroweak (nearly model-independent) measurement of the neutron skin of ^{208}Pb by parity violating electron scattering at JLab (Abrahamyan et al. 2012; Horowitz et al. 2012) has been able to provide $\Delta r_{np} = 0.302 \pm 0.177$ fm for this isotope (Horowitz et al. 2012), although the data are not conclusive due to the large error bars (a follow-up measurement at JLab with better statistics has been proposed). The recent measurement of the neutron skin of ^{208}Pb at the MAMI facility from coherent pion production by photons (Tarbert et al. 2014) has obtained $\Delta r_{np} = 0.15 \pm 0.03$ fm. A similar range $0.13 \lesssim \Delta r_{np} \lesssim 0.19$ fm for ^{208}Pb is extracted (Roca-Maza et al. 2015) by comparing theory with the accurately measured electric dipole polarizability in ^{208}Pb (Tamii et al. 2011), ^{120}Sn (Hashimoto et al. 2015), and ^{68}Ni (Rossi et al. 2013). Thus, the FSU2R prediction of a neutron skin of 0.133 fm in ^{208}Pb turns out to be fairly compatible within error bars with the recent determinations of this isospin-sensitive observable.

In summary, when the nuclear EoS has been constrained to encode the recent astrophysical indications of small neutron star radii, yet without compromising massive stars, a high degree of consistency has emerged between the predictions of the model and the latest terrestrial information on the symmetry energy, its density dependence, and neutron skins, as well as with the constraints inferred from state-of-the-art ab initio microscopic calculations (Hagen et al. 2015). All in all, we believe that the present findings make a compelling case in

favor of the prospect that neutron stars may have small, or moderate-to-small, radii.

4. HYPERONS AND MAGNETIC FIELD

Having calibrated the nuclear model to produce small neutron star radii and fulfil maximum masses of $2 M_\odot$, while at the same time reproducing the phenomenology of atomic nuclei and the empirical constraints from collective flow and kaon production in HICs, we explore in this section the effect on the EoS and neutron stars of including hyperons and magnetic fields.

We should first determine the value of the hyperon couplings in our RMF model. Those couplings are calculated by fitting the experimental data available for hypernuclei, in particular, the value of the optical potential of hyperons extracted from these data. In our model, the contribution to the potential of a hyperon i in j -particle matter is given by

$$U_i^{(j)}(n_j) = -g_{\sigma i} \bar{\sigma}^{(j)} + g_{\omega i} \bar{\omega}^{(j)} + g_{\rho i} I_{3i} \bar{\rho}^{(j)} + g_{\phi i} \bar{\phi}^{(j)}, \quad (24)$$

where $\bar{\sigma}^{(j)}$, $\bar{\omega}^{(j)}$, $\bar{\rho}^{(j)}$ and $\bar{\phi}^{(j)}$ are the values of the meson fields in the j -particle matter and I_{3i} stands for the third component of the isospin operator.

The couplings of the hyperons to the vector mesons are related to the nucleon couplings, $g_{\omega N}$ and $g_{\rho N}$, by assuming SU(3)-flavor symmetry, the vector dominance model and ideal mixing for the physical ω and ϕ mesons, as e.g., employed in many recent works (Schaffner & Mishustin 1996; Weissenborn et al. 2012; Colucci & Sedrakian 2013; Miyatsu et al. 2013; Banik et al. 2014). This amounts to assuming the following relative coupling strengths:

$$\begin{aligned} g_{\omega\Lambda} : g_{\omega\Sigma} : g_{\omega\Xi} : g_{\omega N} &= \frac{2}{3} : \frac{2}{3} : \frac{1}{3} : 1 \\ g_{\rho\Lambda} : g_{\rho\Sigma} : g_{\rho\Xi} : g_{\rho N} &= 0 : 1 : 1 : 1 \\ g_{\phi\Lambda} : g_{\phi\Sigma} : g_{\phi\Xi} : g_{\phi N} &= -\frac{\sqrt{2}}{3} : -\frac{\sqrt{2}}{3} : -\frac{2\sqrt{2}}{3} : 1, \end{aligned} \quad (25)$$

and $g_{\phi N} = 0$. Note that the isospin operator I_{3i} appearing in the definition of the potentials in Equation (24) implements the relative factor of 2 missing in the 1:1 relation between $g_{\rho\Sigma}$ and $g_{\rho N}$ displayed in Equation (25), so that the effective coupling of the ρ meson to the Σ hyperon ($I_3 = -1, 0, +1$) is twice that to the nucleon ($I_3 = -1/2, +1/2$), as required by the symmetries assumed.

The coupling of each hyperon to the σ field is adjusted to reproduce the hyperon potential in SNM derived from hyper-nuclear observables (see, e.g., Hashimoto & Tamura 2006; Gal et al. 2016). The Λ binding energy of Λ -hypernuclei is well reproduced by an attractive Woods-Saxon potential of depth $U_\Lambda^{(N)}(n_0) \sim -28$ MeV (Millener et al. 1988). The analyses of the (π^-, K^+) reaction data on medium to heavy nuclei (Noumi et al. 2002) performed in Harada & Hirabayashi (2006) and Kohno et al. (2006) revealed a moderately repulsive Σ -nuclear potential in the nuclear interior of around 10–40 MeV, while the fits to Σ^- atomic data (Friedman & Gal 2007) indicate a clear transition from an attractive Σ potential in the surface, to a repulsive one in the interior, although the size of the repulsion cannot be precisely determined. As for the strangeness -2 systems, the Nagara event (Takahashi et al. 2001) and other experiments providing consistency checks established the size of the $\Lambda\Lambda$ interaction to be mildly attractive,

$\Delta B_{\Lambda\Lambda}^{(6)}(\Lambda\Lambda\text{He}) = 0.67 \pm 0.17$ MeV (Ahn et al. 2013), while the knowledge obtained for the Ξ - N interaction is more uncertain. Analyses of old emulsion data indicate a sizable attractive Ξ -nucleus potential of $U_{\Xi}^{(N)}(n_0) = -24 \pm 4$ MeV (Dover & Gal 1983), while the missing-mass spectra of the (K^- , K^+) reaction on a ^{12}C target suggest a milder attraction of $\gtrsim -20$ MeV (Fukuda et al. 1998) or $\sim -14 \pm 2$ MeV (Khaustov et al. 2000). These values are compatible with the recent analysis of the nuclear emulsion event KISO, claiming to have observed a nuclear bound state of the Ξ^- - ^{14}N system with a binding energy of 4.38 ± 0.25 MeV (Nakazawa et al. 2015). From the above considerations, we fix the hyperon potentials in SNM to the following values:

$$\begin{aligned} U_{\Lambda}^{(N)}(n_0) &= -28 \text{ MeV} \\ U_{\Sigma}^{(N)}(n_0) &= +30 \text{ MeV} \\ U_{\Xi}^{(N)}(n_0) &= -18 \text{ MeV}, \end{aligned} \quad (26)$$

which allow us to determine the couplings $g_{\sigma\Lambda}$, $g_{\sigma\Sigma}$ and $g_{\sigma\Xi}$, from Equation (24). We finally note that the coupling of the ϕ meson to the Λ baryon is reduced by 20% with respect to its SU(3) value in order to obtain a $\Lambda\Lambda$ bond energy in Λ matter at a density $n_{\Lambda} \simeq n_0/5$ of $\Delta B_{\Lambda\Lambda}(n_0/5) = 0.67$ MeV, thereby reproducing the Nagara event (Ahn et al. 2013).

Let us comment on the fact that the presence of hyperons in the neutron star interior and their influence on the EoS suffer from uncertainties tied to our lack of knowledge of the hyperon-nucleon and hyperon-hyperon interactions around the hyperon onset density of $\sim 2n_0$ and beyond. This freedom has been exploited by different groups to build up RMF models that ensure the existence of neutron stars with masses larger than $2 M_{\odot}$ even with the presence of hyperons (see for example Bednarek et al. 2012; Weissenborn et al. 2012; van Dalen et al. 2014; Oertel et al. 2015). While the radii of neutron stars are essentially determined by the nucleonic part of the EoS, the uncertainties in the hyperon interactions reflect on maximum masses that are scattered within a $0.3 M_{\odot}$ band, as can be seen from the thorough analysis of various models done by Fortin et al. (2015), which is consistent with admitting a deviation by at most 30% of the symmetries assumed to determine the hyperon coupling constants (Weissenborn et al. 2012). These results provide an estimate of the uncertainties that one must admit in the hyperonic sector until data on the hyperon interactions at higher densities, coming for instance from HIC experiments (Morita et al. 2015), become available. As explained in the preceding paragraph, in this work we have simply made a minimal adjustment of the hyperon parameters away from the symmetry constraints imposed by Equation (25) in order to reproduce the known hypernuclear properties.

In Figure 5 we show how the presence of hyperons affects the M-R relationship for some representative nuclear EoSs selected from the previous section: the highly stiff EoS of the NL3 model and the FSU2 and FSU2R EoSs. These models differ essentially on the lower density ($n \lesssim 2n_0$) and/or the higher density ($n \gtrsim 2n_0$) stiffness of the EoS. As already noted (see Horowitz & Piekarewicz 2001b; Chen & Piekarewicz 2014, 2015a) and also discussed in the previous section, models with a larger value of the Λ_{ω} coupling produce a softer symmetry energy and, in consequence, become more compressible leading to stars with higher central densities and smaller radii. The presence of hyperons softens the EoS by essentially releasing Fermi pressure. Thereby, the stars get

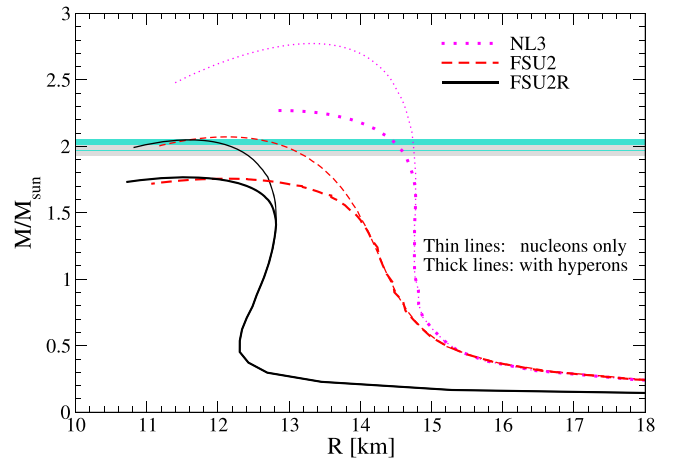


Figure 5. Mass vs. radius for neutron stars for the models NL3 (Lalazissis et al. 1997), FSU2 (Chen & Piekarewicz 2014), and FSU2R (this work) with hyperons (thick lines) and without hyperons (thin lines). The two shaded bands portray the masses $M = 1.97 \pm 0.04 M_{\odot}$ in the pulsar PSR J1614–2230 (gray band) (Demorest et al. 2010) and $M = 2.01 \pm 0.04 M_{\odot}$ in the pulsar PSR J0348+0432 (turquoise band) (Antoniadis et al. 2013).

further compressed than their nucleonic counterparts, and the maximum masses get reduced by about 15%, as seen by the thick lines in Figure 5. It is also seen from this figure that the occurrence of hyperons leaves the stellar radii almost unaffected.

Except for the NL3 model, which has shown to be exceedingly stiff at supranormal densities, the maximum masses of hyperonic stars attained by the other two models are too low, of about $M_{\max} = 1.8 M_{\odot}$, to reproduce the $2 M_{\odot}$ limit. The specific values of the maximum masses of hyperonic stars for all these models can be seen in Table 2 in the “pneYμ” section. We observe a weak sensitivity to the slope of the symmetry energy, as FSU2 and FSU2R produce essentially the same maximum masses. This was already noted in the context of nucleonic-only EoSs in Horowitz & Piekarewicz (2001b). As the symmetry energy softens, the star simply becomes more compressed and attains a larger central density, but reaches a similar maximum mass value. This phenomenology remains when hyperons are present, as was also found in Providencia & Rabhi (2013), the only difference being that the hyperonic stars attain a lower maximum mass and have a higher central density than their nucleonic-only counterparts, as expected for a softer EoS. This can be seen upon comparing the values shown in the “pneμ” and “pneYμ” sections of Table 2.

Since the hyperonic EoS based on the FSU2R model does not produce $M_{\max} > 2 M_{\odot}$, we tense the parameters of this nuclear model a little further so as to make it stiffer. We essentially reduce the value of ζ from 0.024 to 0.008, which stiffens the EoS at densities larger than twice the saturation density, i.e., around the region where hyperons start appearing (see the hyperon onset density for the different models in Table 2). The remaining parameters of the model are refitted so as to reproduce the SNM saturation properties of the FSU2 model and a symmetry energy $E_{\text{sym}} = 26.2$ MeV at density $n = 0.10 \text{ fm}^{-3}$. The values of the parameters of this new interaction, named FSU2H, are listed in Table 1, together with the predicted E_{sym} value at saturation density and its slope L , which fall comfortably within the newest empirical and theoretical constraints of these quantities, as can be seen in Figure 4. The couplings of the hyperons to the different vector

mesons can be readily obtained from Equation (25), and those to the σ meson, determined from fixing the hyperon potentials in SNM, are $g_{\sigma\Lambda} = 0.6113$, $g_{\sigma\Sigma} = 0.4665$ and $g_{\sigma\Xi} = 0.3157$.

We note that the FSU2H interaction produces a certain overpressure in SNM at $n \gtrsim 2n_0$, since the pressure falls above the allowed region obtained from the modeling of collective flow in HICs, as seen by the long dashed line in the upper part of Figure 1. Nevertheless, the EoS for PNM, seen in the lower panel of this figure, falls within the PNM extrapolated band compatible with collective flow. Since neutron-star matter in beta equilibrium is highly asymmetric we consider this model to be sufficiently realistic to describe neutron stars, whose properties are presented in Table 2. We observe that the maximum mass of $2.38 M_\odot$ obtained for a “*pneμ*” neutron star with the FSU2H model gets reduced to $2.03 M_\odot$, with a radius of 12 km, when hyperons are present. We also observe that the radius of a canonical star of $\sim 1.5 M_\odot$ gets slightly enhanced from 12.8 km for FSU2R to 13.2 km for FSU2H, which is the price one pays for having stiffened the EoS.

On comparing the “*pneμ*” with the “*pneYμ*” parts of Table 2 we essentially see, as in Figure 5, a reduction of about 15% on the maximum mass when hyperons are allowed to appear in the neutron star cores. Since the hyperonic EoSs become more compressible, the “*pneYμ*” stars attain higher central densities, but the radii of the maximum-mass stars stay rather similar to their nucleonic-only counterparts.

We note that the FSU2H parameterization, which produces $M_{\max} > 2 M_\odot$ even in the presence of hyperons, fulfills the pressure constraint in neutron star matter at saturation density n_0 :

$$1.7 \text{ MeV fm}^{-3} < P(n_0) < 2.8 \text{ MeV fm}^{-3}, \quad (27)$$

estimated in Fortin et al. (2015) from the results shown in Hebeler et al. (2013), which were obtained from microscopic calculations of PNM based on chiral two-nucleon and three-nucleon interactions, and which are in remarkable agreement with the quantum Monte Carlo results of Gandolfi et al. (2012), obtained from the phenomenological Argonne v18 NN potential plus three-nucleon forces. It is argued in Fortin et al. (2015) that nearly all hyperonic EoS models that are able to sustain $M_{\max} > 2 M_\odot$ produce large PNM pressures of about 5 MeV fm⁻³ at saturation density, leading to an overpressure of the nucleonic (pre-hyperon) segment and resulting in large radii of around 14 km or more for neutron stars in the range $1 < M/M_\odot < 1.6$. Our FSU2H model does not encounter this problem, since it gives a PNM pressure of ~ 2 MeV fm⁻³ at n_0 (see Table 1), well within the constraint of Equation (27), and as a consequence is able to reach a smaller radius of 13 km. We note that the symmetry energy slope parameter L of the hyperonic models analyzed in Fortin et al. (2015) lies in the range of values 67–118 MeV, which deviate considerably from the recent constraints displayed in Figure 4.

We now discuss the effect of including a magnetic field in our nucleonic and hyperonic stars. We consider a density-dependent magnetic field with a profile of the type

$$B(n) = B_s + B_c \{1 - \exp[-\beta(n/n_0)^\gamma]\}, \quad (28)$$

introduced in Chakrabarty et al. (1997) and employed in several other works (Rabhi & Providencia 2010; Lopes & Menezes 2012; Sinha et al. 2013). We take a surface magnetic field value of $B_s = 10^{15}$ G, consistent with the surface

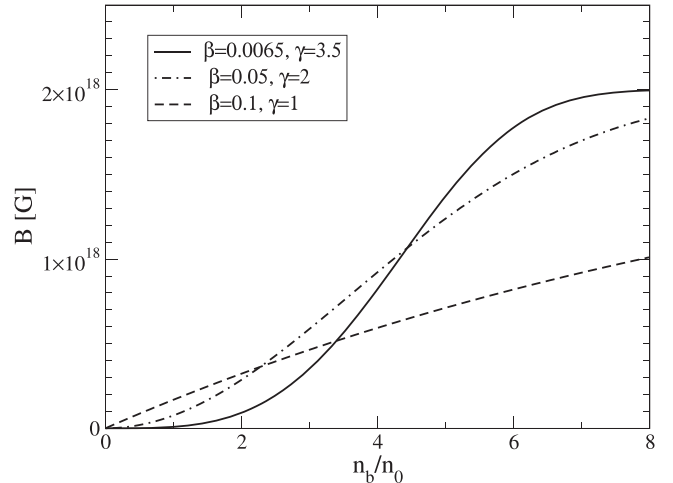


Figure 6. Magnetic field vs. baryonic density for a function of the type of Equation (28), taking $B_s = 10^{15}$ G and $B_c = 2 \times 10^{18}$ G, for $(\beta, \gamma) = (0.0065, 3.5)$ (solid line), $(\beta, \gamma) = (0.05, 2)$ (dashed-dotted line), and $(\beta, \gamma) = (0.1, 1)$ (dashed line).

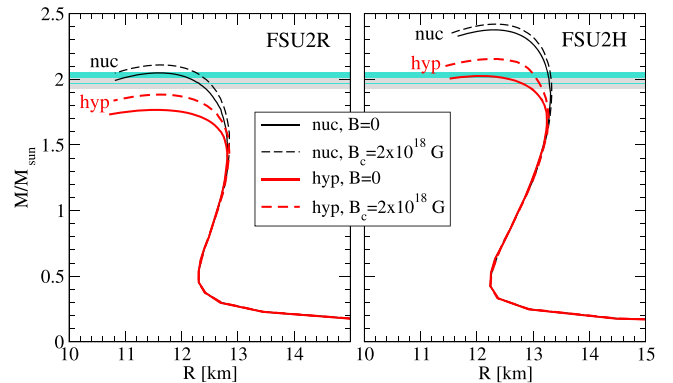


Figure 7. Mass vs. radius of neutron stars for FSU2R (left panel) and FSU2H (right panel) models, with (thick lines) or without (thin lines) hyperons, and without (solid lines) or with (dashed lines) a magnetic field with the profile of Figure 6, for $\beta = 0.0065$ and $\gamma = 3.5$. The two shaded bands portray the masses $M = 1.97 \pm 0.04 M_\odot$ in the pulsar PSR J1614–2230 (gray band) (Demorest et al. 2010) and $M = 2.01 \pm 0.04 M_\odot$ in the pulsar PSR J0348+0432 (turquoise band) (Antoniadis et al. 2013).

magnetic fields of observed magnetars (Vasisht & Gotthelf 1997; Kouveliotou et al. 1998; Woods et al. 1999) and a core magnetic field value of $B_c = 2 \times 10^{18}$ G, which is sufficiently strong to produce distinguishable effects on the properties of neutron stars. The parameters β and γ control the density where the magnetic field saturates and the steepness of the transition from the surface to the core field, respectively. We take $\beta = 0.0065$ and $\gamma = 3.5$ which ensure that the magnetic field has practically saturated to its maximum value at around 5–6 n_0 , a range that covers the typical central densities of the maximum mass neutron stars explored in this work. Moreover, the indicated β and γ values produce moderate field values below saturation density, as can be seen by the solid line in Figure 6. We note that this field profile does not incur on instabilities of the parallel component of the pressure $P_{||}$ associated to rapidly rising magnetic field toward relatively strong central values (Sinha et al. 2013).

The effect of this magnetic field on the M–R relationship is displayed in Figure 7. On the left (right) panel we show the

results obtained for the EoS employing the FSU2R (FSU2H) model. The solid lines correspond to vanishing magnetic field, while the dashed lines include the effects of the magnetic field with the density profile discussed above. The thin black lines show the results for nucleonic neutron stars and the thick red lines correspond to the hyperonic stars. As observed in earlier works (Lopes & Menezes 2012), including the magnetic field produces stars with larger maximum masses. This is essentially a consequence of the increase in the total pressure which, apart from the matter pressure P_{matt} , also includes the extra average field pressure component, as seen in Equation (21). The size of this enhancement is larger for the hyperonic than for the nucleonic stars, which is essentially due, as we will show below, to the additional effect of de-hyperonization that takes place in the presence of a magnetic field. The reduction of hyperons is responsible for enhancing the value of the matter pressure P_{matt} , since the Fermi contributions of the other species are larger than in the $B = 0$ case. Nevertheless, the increase in the maximum mass induced by magnetic field effects is not enough to produce hyperonic star masses of the order of $2 M_{\odot}$ in the case of the FSU2R model, as the dashed red line on the left panel does not reach the observational bands. The effects of the magnetic field on the M–R relationships obtained with the FSU2H EoS (right panel) are similar to those for the FSU2R EoS, the only difference being that the constraint $M_{\text{max}} > 2 M_{\odot}$ is now amply fulfilled, since the FSU2H model served this purpose even in the absence of a magnetic field.

We now explore the effect of employing different magnetic field profiles having the same surface and central values, $B_s = 10^{15}$ G and $B_c = 2 \times 10^{18}$ G, but different β and γ parameters. To this end, we consider, in addition to the profile obtained with the parameters $(\beta, \gamma) = (0.0065, 3.5)$ chosen in this work, the profiles with $(\beta, \gamma) = (0.05, 2)$ (Rabhi & Providencia 2010) and $(\beta, \gamma) = (0.1, 1)$ (Sinha et al. 2013), which are represented, respectively, by the dashed-dotted and dashed lines in Figure 6. We observe that our parameterization produces a substantially lower magnetic field in the $n < 2n_0$ region and reaches 90% of the saturation value around $5n_0$, while the dashed-dotted parameterization does it right after $6n_0$. The parameterization of the dashed line does not even reach the value $B = 10^{18}$ G within the densities of interest ($n \lesssim 6n_0$).

In Figure 8 we display the M–R relationships obtained with these profiles, together with the zero magnetic field case, represented by a thin solid line. A noticeable dependence of the M–R relationship on the magnetic field profile is observed. The results for the $(\beta, \gamma) = (0.05, 2)$ case (thick dashed-dotted line) are similar to those obtained with our $(\beta, \gamma) = (0.0065, 3.5)$ parameterization (thick solid line), but the stars are produced with a somewhat larger radius since the magnetic field and, hence, the total pressure are larger in the pre-hyperon region. This is even more evident for the M–R relationship obtained with the $(\beta, \gamma) = (0.1, 1)$ profile (thick dashed line), which produces stars that are ~ 0.5 km wider than the other two cases and deviates from the 13 km maximum radius constraint. The reason is that this profile clearly gives larger magnetic fields in the $n \lesssim n_0$ region, hence producing a larger total pressure and making the star less compressible.

The particle fractions for beta-stable neutron star matter obtained using the FSU2H EoS are shown in Figure 9 as functions of the baryonic density. The upper panel displays the fractions in the absence of magnetic field, while the other

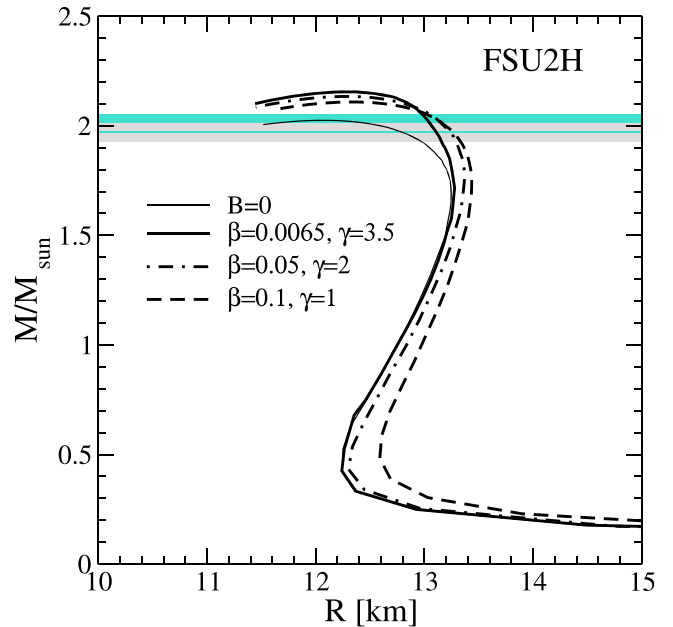


Figure 8. Mass vs. radius of hyperonic neutron stars obtained with the FSU2H model and including a magnetic field with the different profiles displayed in Figure 6. The field-free case is shown by the thin solid line. The two shaded bands portray the masses $M = 1.97 \pm 0.04 M_{\odot}$ in the pulsar PSR J1614–2230 (gray band) (Demorest et al. 2010) and $M = 2.01 \pm 0.04 M_{\odot}$ in the pulsar PSR J0348+0432 (turquoise band) (Antoniadis et al. 2013).

panels implement the magnetic field with the three different profiles shown in Figure 6. Landau oscillations are seen in the charged particle fractions when a magnetic field is applied, reflecting the successive filling of the Landau levels as the quantity $(E_F^2 - m^{\ast 2})/2|q|B$ reaches integer values. For a fixed density, smaller magnetic fields accommodate more Landau levels and, correspondingly, more oscillations are observed, as seen for instance when comparing the three $B \neq 0$ panels in the $n < 2n_0$ density region, where the smallest field corresponds to the $(\beta, \gamma) = (0.0065, 3.5)$ case. As density increases, so does the magnetic field in all the considered profiles, eventually needing only one Landau level to accommodate the population of the charged particles. The oscillations then tend to smooth out and disappear with increasing density. As is evident, the magnetic field mostly affects the charged particles, which in general increases their population with respect the $B = 0$ case. At low and intermediate densities up to $n \sim 4n_0$, we clearly observe an increase in the occupation of negatively charged electrons and muons. This delays the appearance of the negatively charged hyperons, an effect that is especially visible for the Σ^- baryon, whose onset moves to $n \gtrsim 4n_0$ for all the considered magnetic field profiles.

According to the results shown in the second panel of Figure 9, in the case of a magnetized hyperonic star having a mass of about $2 M_{\odot}$ with a maximum density of about $5n_0$ (see Table 2), the baryon fractions at the center would be 38% for n, 28% for Λ , 26% for p, 6% for Ξ^- and 2% for Σ^- . In the $B = 0$ case (upper panel), these fractions would be 45% for n, 31% for Λ , 13% for p, 6% for Ξ^- and 5% for Σ^- . We then see that the proton abundance can be twice as large in a magnetar as it is in a field-free star. Our results are qualitatively consistent with those obtained by other works in the literature studying the effect of magnetic fields in hyperonic stars (Broderick et al. 2002; Yue et al. 2009; Rabhi & Providencia 2010; Lopes & Menezes 2012; Sinha et al. 2013). We can conclude that, in

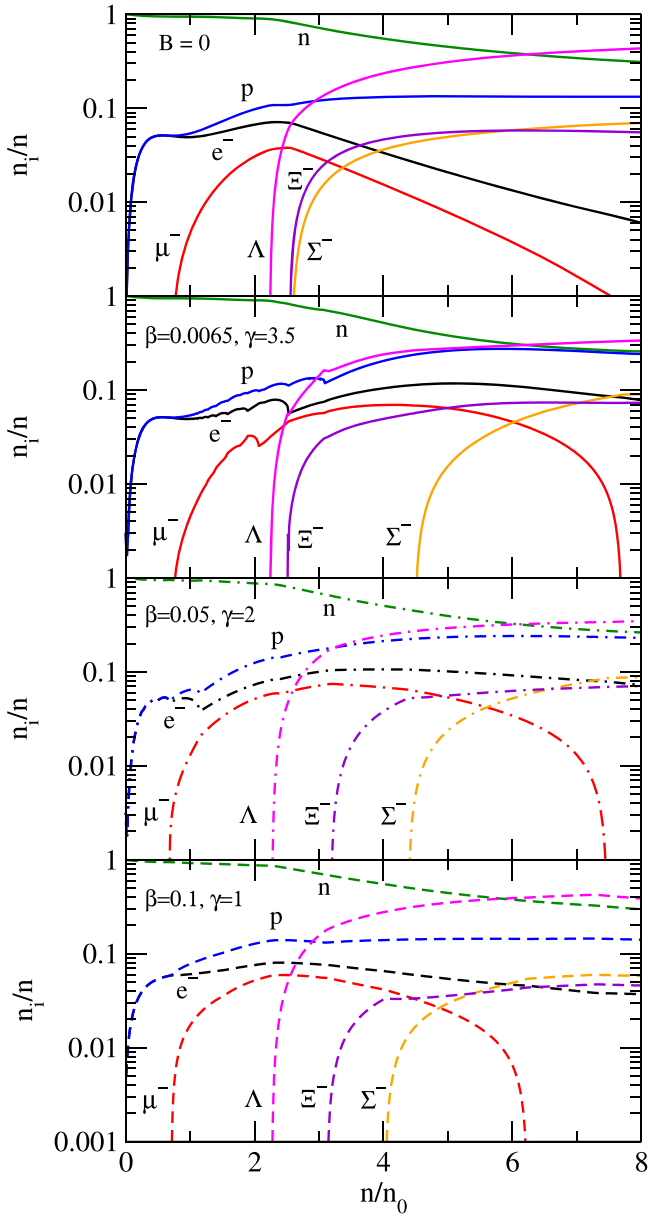


Figure 9. Particle fractions as functions of the baryonic density for the FSU2H model without magnetic field (first panel) and including the magnetic field profile of Equation (28), taking $B_s = 10^{15}$ G and $B_c = 2 \times 10^{18}$ G and for $(\beta, \gamma) = (0.0065, 3.5)$ (second panel), $(\beta, \gamma) = (0.05, 2)$ (third panel), and $(\beta, \gamma) = (0.1, 1)$ (fourth panel).

general, hyperonic magnetars re-leptonize and de-hyperonize with respect to zero-field stars, while the proton abundance increases substantially. This might facilitate direct Urca processes, drastically altering the cooling evolution of the star.

5. SUMMARY

We have obtained a new EoS for the nucleonic inner core of neutron stars that fulfills the constraints coming from recent astrophysical observations of maximum masses and determinations of radii, as well as the requirements from experimental nuclear data known from terrestrial laboratories. This EoS results from a new parameterization of the FSU2 force (Chen & Piekarewicz 2014), the so-called FSU2R model, that reproduces: (i) the $2 M_\odot$ observations (Demorest et al. 2010; Antoniadis et al. 2013), (ii) the recent determinations of radii

below 13 km region (Guillot et al. 2013; Guillot & Rutledge 2014; Heinke et al. 2014; Lattimer & Steiner 2014; Lattimer & Prakash 2016; Ozel et al. 2016), (iii) the saturation properties of nuclear matter and finite nuclei (Tsang et al. 2012; Chen & Piekarewicz 2014) and (iv) the constraints extracted from nuclear collective flow (Danielewicz et al. 2002) and kaon production (Fuchs et al. 2001; Lynch et al. 2009) in HICs.

The FSU2R model is obtained by modifying the Λ_ω and ζ couplings of the Lagrangian simultaneously, while recalculating the couplings $g_{\sigma N}$, $g_{\omega N}$, $g_{\rho N}$, κ , and λ to grant the same saturation properties of FSU2 in SNM and a symmetry energy of 25.7 MeV at $n = 0.10 \text{ fm}^{-3}$. On the one hand, radii of 12–13 km are obtained, owing to the fact that we softened the symmetry energy and, consequently, the pressure of PNM at densities $\sim 1.5\text{--}2n_0$, while reproducing the properties of nuclear matter and nuclei. Indeed, we obtain $E_{\text{sym}} = 30 \text{ MeV}$ and $L = 44 \text{ MeV}$, which lie within the limits of recent determinations (see Lattimer & Lim 2013; Hagen et al. 2015; Roca-Maza et al. 2015). Moreover, the FSU2R model predicts a neutron skin thickness of 0.133 fm for the ^{208}Pb nucleus, which is compatible with recent experimental results (Abrahamyan et al. 2012; Horowitz et al. 2012; Tarbert et al. 2014; Roca-Maza et al. 2015). On the other hand, we have stiffened the EoS above twice the saturation density, which satisfies the constraints of HICs (Fuchs et al. 2001; Danielewicz et al. 2002; Lynch et al. 2009) and allows for maximum masses of $2 M_\odot$ (Demorest et al. 2010; Antoniadis et al. 2013). All in all, the FSU2R parameterization allows for a compromise between small stellar sizes and large masses, a task that seemed difficult to achieve in up-to-date RMF models.

We also analyze the consequences of the appearance of hyperons inside the core of neutron stars. The values of the hyperon couplings are determined from the available experimental information on hypernuclei, in particular by fitting to the optical potential of hyperons extracted from the data. On the one hand, we find that the radii of the neutron stars are rather insensitive to the appearance of the hyperons and, thus, still respect the observations of radii < 13 km. On the other hand, we obtain a reduction of the maximum mass below $2 M_\odot$ once hyperons appear due to the expected softening of the EoS. However, by refitting the parameters of the FSU2R model slightly, the new parameterization FSU2H fulfills the $2 M_\odot$ limit while still reproducing the properties of nuclear matter and nuclei. The price to pay is a stiffer EoS in SNM as compared to the constraint derived from the modeling of HICs. Nonetheless, the HICs estimate in PNM is still satisfied by the FSU2H parameterization (Danielewicz et al. 2002).

We finally study the effect of high magnetic fields on the nucleonic and hyperonic EoSs. This is of particular interest for understanding the behavior of highly magnetized neutron stars, the so-called magnetars. Employing magnetic fields with crustal and interior values of $\sim 10^{15}$ G and $\sim 10^{18}$ G, respectively, we find EoSs that are stiffer and produce larger maximum-mass stars, while keeping radii in the 12–13 km range, both for nucleonic and hyperonic magnetars, as long as the magnetic field does not reach values larger than about 10^{17} G at saturation density. The particle fractions in the interior of the stars depend on the specific profile of the magnetic field, but the general trend with respect to zero-field stars is that hyperonic magnetars re-leptonize and de-hyperonize, while the amount of protons may double, a fact

that may trigger direct Urca processes affecting the cooling and other transport properties of the star.

We are most grateful to J. Piekarewicz for a careful reading of the manuscript and for valuable comments. L.T. acknowledges support from the Ramón y Cajal research programme, FPA2013-43425-P Grant from Ministerio de Economía y Competitividad (MINECO) and NewCompstar COST Action MP1304. M.C. and A.R. acknowledge support from Grant No. FIS2014-54672-P from MINECO, Grant No. 2014SGR-401 from Generalitat de Catalunya, and the project MDM-2014-0369 of ICCUB (Unidad de Excelencia María de Maeztu) from MINECO. L.T. and A.R. acknowledge support from the Spanish Excellence Network on Hadronic Physics FIS2014-57026-REDT from MINECO.

REFERENCES

- Abrahamyan, S., Ahmed, Z., Albataineh, H., et al. 2012, *PhRvL*, **108**, 112502
 Ahn, J. K., Akikawa, H., Aoki, S., et al. 2013, *PhRvC*, **88**, 014003
 Alex Brown, B. 2000, *PhRvL*, **85**, 5296
 Alford, M., Blaschke, D., Drago, A., et al. 2007, *Natur*, **445**, E7
 Ambartsumyan, V. A., & Saakyan, G. S. 1960, *SvA*, **4**, 187
 Angeli, I., & Marinova, K. 2013, *ADNDT*, **99**, 69
 Antoniadis, J., Freire, P. C. C., Wex, N., et al. 2013, *Sci*, **340**, 6131
 Ardeljan, N. V., Bisnovatyi-Kogan, G. S., & Moiseenko, S. G. 2005, *MNRAS*, **359**, 333
 Arzoumanian, Z., Gendreau, K. C., Baker, C. L., et al. 2014, Proc. SPIE, 9144, 914420
 Bandyopadhyay, D., Chakrabarty, S., Dey, P., & Pal, S. 1998, *PhRvD*, **58**, 121301
 Banik, S., Hempel, M., & Bandyopadhyay, D. 2014, *ApJS*, **214**, 22
 Bauswein, A., & Janka, H. T. 2012, *PhRvL*, **108**, 011101
 Baym, G., Pethick, C., & Sutherland, P. 1971, *ApJ*, **170**, 299
 Bednarek, I., Haensel, P., Zdunik, J. L., Bejger, M., & Manka, R. 2012, *A&A*, **543**, A157
 Bogdanov, S. 2013, *ApJ*, **762**, 96
 Boguta, J., & Bodmer, A. R. 1977, *NuPhA*, **292**, 413
 Boguta, J., & Stoecker, H. 1983, *PhLB*, **120**, 289
 Broderick, A., Prakash, M., & Lattimer, J. M. 2000, *ApJ*, **537**, 351
 Broderick, A. E., Prakash, M., & Lattimer, J. M. 2002, *PhLB*, **531**, 167
 Carriere, J., Horowitz, C. J., & Piekarewicz, J. 2003, *ApJ*, **593**, 463
 Centelles, M., Roca-Maza, X., Viñas, X., & Warda, M. 2009, *PhRvL*, **102**, 122502
 Chakrabarty, S., Bandyopadhyay, D., & Pal, S. 1997, *PhRvL*, **78**, 2898
 Chandrasekhar, S., & Fermi, E. 1953, *ApJ*, **118**, 116 (Erratum: 1955, *ApJ* 122, 208)
 Chatterjee, D., & Vidana, I. 2016, *EPJA*, **A52**, 29
 Chen, W., Zhang, P.-Q., & Liu, L.-G. 2007, *MPLA*, **A22**, 623
 Chen, W.-C., & Piekarewicz, J. 2014, *PhRvC*, **90**, 044305
 Chen, W.-C., & Piekarewicz, J. 2015a, *PhRvL*, **115**, 161101
 Chen, W.-C., & Piekarewicz, J. 2015b, *PhLB*, **748**, 284
 Colucci, G., & Sedrakian, A. 2013, *PhRvC*, **87**, 055806
 Danielewicz, P., Lacey, R., & Lynch, W. G. 2002, *Sci*, **298**, 1592
 Demorest, P., Pennucci, T., Ransom, S., Roberts, M., & Hessels, J. 2010, *Natur*, **467**, 1081
 Dexheimer, V., Negreiros, R., & Schramm, S. 2012, *EPJA*, **A48**, 189
 Dexheimer, V., Negreiros, R., & Schramm, S. 2015, *PhRvC*, **92**, 012801
 Dover, C. B., & Gal, A. 1983, *AnPhy*, **146**, 309
 Drago, A., Lavagno, A., Pagliara, G., & Pigato, D. 2014, *PhRvC*, **90**, 065809
 Erler, J., Horowitz, C. J., Nazarewicz, W., Rafalski, M., & Reinhard, P. G. 2013, *PhRvC*, **87**, 044320
 Fortin, M., Zdunik, J. L., Haensel, P., & Bejger, M. 2015, *A&A*, **576**, A68
 Friedman, E., & Gal, A. 2007, *PhR*, **452**, 89
 Fuchs, C., Faessler, A., Zabrodin, E., & Zheng, Y.-M. 2001, *PhRvL*, **86**, 1974
 Fukuda, T., Higashi, A., Matsuyama, Y., et al. 1998, *PhRvC*, **58**, 1306
 Gal, A., Hungerford, E. V., & Millener, D. J. 2016, *RvMP*, **88**, 035004
 Gandolfi, S., Carlson, J., & Reddy, S. 2012, *PhRvC*, **85**, 032801
 Glendenning, N. K. 1982, *PhLB*, **114**, 392
 Glendenning, N. K. 2000, *Compact Stars: Nuclear Physics, Particle Physics, and General Relativity* (2nd ed.; New York: Springer)
 Gomes, R. O., Dexheimer, V., & Vasconcellos, C. A. Z. 2014, *AN*, **335**, 666
 Guillot, S., & Rutledge, R. E. 2014, *ApJL*, **796**, L3
 Guillot, S., Servillat, M., Webb, N. A., & Rutledge, R. E. 2013, *ApJ*, **772**, 7
 Guver, T., & Ozel, F. 2013, *ApJL*, **765**, L1
 Hagen, G., Ekstrom, A., Forssen, C., et al. 2015, *NatPh*, **12**, 186
 Harada, T., & Hirabayashi, Y. 2006, *NuPhA*, **767**, 206
 Harding, A. K., & Lai, D. 2006, *RPPh*, **69**, 2631
 Hashimoto, O., & Tamura, H. 2006, *PrPNP*, **57**, 564
 Hashimoto, T., Krumbholz, A. M., Reinhard, P.-G., et al. 2015, *PhRvC*, **92**, 031305
 Hebeler, K., Lattimer, J. M., Pethick, C. J., & Schwenk, A. 2013, *ApJ*, **773**, 11
 Heinicke, C. O., Cohn, H. N., Lugger, P. M., et al. 2014, *MNRAS*, **444**, 443
 Horowitz, C. J., Ahmed, Z., Jen, C.-M., et al. 2012, *PhRvC*, **85**, 032501
 Horowitz, C. J., & Piekarewicz, J. 2001a, *PhRvL*, **86**, 5647
 Horowitz, C. J., & Piekarewicz, J. 2001b, *PhRvC*, **64**, 062802
 Hulse, R. A., & Taylor, J. H. 1975, *ApJL*, **195**, L51
 Jiang, W.-Z., Li, B.-A., & Fattoyev, F. J. 2015, *EPJA*, **A51**, 119
 Khaustov, P., Alburger, D. E., Barnes, P. D., et al. 2000, *PhRvC*, **61**, 054603
 Klahn, T., Aastowiecki, R., & Blaschke, D. B. 2013, *PhRvD*, **88**, 085001
 Kohno, M., Fujiwara, Y., Watanabe, Y., Ogata, K., & Kawai, M. 2006, *PhRvC*, **74**, 064613
 Kouveliotou, C., Dieters, S., Strohmayer, T., et al. 1998, *Natur*, **393**, 235
 Lackey, B. D., & Wade, L. 2015, *PhRvD*, **91**, 043002
 Lalazissis, G. A., Konig, J., & Ring, P. 1997, *PhRvC*, **55**, 540
 Lattimer, J. M., & Lim, Y. 2013, *ApJ*, **771**, 51
 Lattimer, J. M., & Prakash, M. 2004, *Sci*, **304**, 536
 Lattimer, J. M., & Prakash, M. 2007, *PhR*, **442**, 109
 Lattimer, J. M., & Prakash, M. 2016, *PhR*, **621**, 127
 Lattimer, J. M., & Steiner, A. W. 2014, *ApJ*, **784**, 123
 Li, B.-A., Ramos, A., Verde, G., & Vidana, I. 2014, *EPJA*, **A50**, 9
 Lonardoni, D., Lovato, A., Gandolfi, S., & Pederiva, F. 2015, *PhRvL*, **114**, 092301
 Lopes, L. L., & Menezes, D. P. 2012, *BrJPh*, **42**, 428
 Lynch, W. G., Tsang, M. B., Zhang, Y., et al. 2009, *PrPNP*, **62**, 427
 Maslov, K. A., Kolomeitsev, E. E., & Voskresensky, D. N. 2015, *PhLB*, **748**, 369
 Menezes, D. P., & Lopes, L. L. 2016, *EPJA*, **A52**, 17
 Mereghetti, S. 2008, *A&ARv*, **15**, 225
 Millener, D. J., Dover, C. B., & Gal, A. 1988, *PhRvC*, **38**, 2700
 Miyatsu, T., Yamamoto, S., & Nakazato, K. 2013, *ApJ*, **777**, 4
 Morita, K., Furumoto, T., & Ohnishi, A. 2015, *PhRvC*, **91**, 024916
 Mueller, H., & Serot, B. D. 1996, *NuPhA*, **606**, 508
 Nakazawa, K., Endo, Y., Fukunaga, S., et al. 2015, *PTEP*, **033D02**, <http://ptep.oxfordjournals.org/content/2015/3/033D02>
 Noumi, H., Saha, P. K., Abe, D., et al. 2002, *PhRvL*, **89**, 072301 (Erratum: 2003, *PhRvL* 90, 049902)
 Oertel, M., Hempel, M., Klahn, T., & Typel, S. 2016, arXiv:1610.03361
 Oertel, M., Providencia, C., Gulminelli, F., & Raduta, A. R. 2015, *JPhG*, **42**, 075202
 Oppenheimer, J. R., & Volkoff, G. M. 1939, *PhRv*, **55**, 374
 Ozel, F., Baym, G., & Guver, T. 2010, *PhRvD*, **82**, 101301
 Ozel, F., & Freire, P. 2016, *ARA&A*, **54**, 401
 Ozel, F., & Psaltis, D. 2015, *ApJ*, **810**, 135
 Ozel, F., Psaltis, D., Guver, T., et al. 2016, *ApJ*, **820**, 28
 Poutanen, J., Nattila, J., Kajava, J. J. E., et al. 2014, *MNRAS*, **442**, 3777
 Providencia, C., & Rabhi, A. 2013, *PhRvC*, **87**, 055801
 Rabhi, A., & Providencia, C. 2010, *JPhG*, **37**, 075102
 Rabhi, A., Providencia, C., & Da Providencia, J. 2008, *JPhG*, **35**, 125201
 Rea, N., & Esposito, P. 2011, in Proc. 1st Session of the Sant Cugat Forum on Astrophysics: High-Energy Emission from Pulsars and their Systems, ed. D. F. Torres & N. Rea (Berlin: Springer), 247
 Reinhard, P.-G., & Nazarewicz, W. 2010, *PhRvC*, **81**, 051303
 Roca-Maza, X., Viñas, X., Centelles, M., et al. 2015, *PhRvC*, **92**, 064304
 Rossi, D. M., Adrich, P., Aksouh, F., et al. 2013, *PhRvL*, **111**, 242503
 Schaffner, J., & Mishustin, I. N. 1996, *PhRvC*, **53**, 1416
 Serot, B. D., & Walecka, J. D. 1986, *AdNuP*, **16**, 1
 Serot, B. D., & Walecka, J. D. 1997, *IJMPE*, **6**, 515
 Shapiro, S. L., & Teukolsky, S. A. 1983, *Black Holes, White Dwarfs, and Neutron Stars: The Physics of Compact Objects* (New York: Wiley)
 Sharma, B. K., Centelles, M., Viñas, X., Baldo, M., & Burgio, G. F. 2015, *A&A*, **584**, A103
 Sinha, M., Mukhopadhyay, B., & Sedrakian, A. 2013, *NuPhA*, **898**, 43
 Steiner, A. W., Lattimer, J. M., & Brown, E. F. 2013, *ApJL*, **765**, L5
 Strickland, M., Dexheimer, V., & Menezes, D. P. 2012, *PhRvD*, **86**, 125032
 Suh, I.-S., & Mathews, G. J. 2001, *ApJ*, **546**, 1126
 Suleimanov, V., Poutanen, J., Revnivtsev, M., & Werner, K. 2011, *ApJ*, **742**, 122
 Takahashi, H., Ahn, J. K., Akikawa, H., et al. 2001, *PhRvL*, **87**, 212502

- Tamii, A., Poltoratska, I., von Neumann-Cosel, P., et al. 2011, *PhRvL*, **107**, 062502
- Tarbert, C. M., Watts, D. P., Glazier, D. I., et al. 2014, *PhRvL*, **112**, 242502
- Thompson, C., & Duncan, R. C. 1993, *ApJ*, **408**, 194
- Todd-Rutel, B. G., & Piekarewicz, J. 2005, *PhRvL*, **95**, 122501
- Tsang, M. B., Stone, J. R., Camera, F., et al. 2012, *PhRvC*, **86**, 015803
- Turolla, R., Zane, S., & Watts, A. 2015, *RPPh*, **78**, 116901
- van Dalen, E. N. E., Colucci, G., & Sedrakian, A. 2014, *PhLB*, **734**, 383
- Vasisht, G., & Gotthelf, E. V. 1997, *ApJL*, **486**, L129
- Verbiest, J. P. W., Bailes, M., van Straten, W., et al. 2008, *ApJ*, **679**, 675
- Vidana, I., Logoteta, D., Providencia, C., Polls, A., & Bombaci, I. 2011, *EL*, **94**, 11002
- Vink, J., & Kuiper, L. 2006, *MNRAS*, **370**, L14
- Wang, M., Audi, G., Wapstra, A., et al. 2012, *ChPhC*, **36**, 1603
- Watts, A. L., Andersson, N., Chakrabarty, D., et al. 2016, *RvMP*, **88**, 021001
- Weissenborn, S., Chatterjee, D., & Schaffner-Bielich, J. 2012, *PhRvC*, **85**, 065802 (Erratum: 2014, *PhRvC* 90, 019904)
- Woods, P. M., Kouveliotou, C., van Paradijs, J., et al. 1999, *ApJL*, **519**, L139
- Yamamoto, Y., Furumoto, T., Yasutake, N., & Rijken, T. A. 2014, *PhRvC*, **90**, 045805
- Yue, P., Yang, F., & Shen, H. 2009, *PhRvC*, **79**, 025803
- Zdunik, J. L., & Haensel, P. 2013, *A&A*, **551**, A61

The Equation of State for the Nucleonic and Hyperonic Core of Neutron Stars

Laura Tolos^{1,2}, Mario Centelles³ and Angels Ramos³

¹Institute of Space Sciences (CSIC-IEEC), Campus Universitat Autònoma de Barcelona, Carrer de Can Magrans, s/n, 08193 Cerdanyola del Vallès, Spain

²Frankfurt Institute for Advanced Studies, Goethe University Frankfurt, Ruth-Moufang-Str. 1, 60438 Frankfurt am Main, Germany

³Departament de Física Quàntica i Astrofísica and Institut de Ciències del Cosmos (ICCUB), Universitat de Barcelona, Martí i Franquès 1, 08028 Barcelona, Spain

Abstract

We reexamine the equation of state for the nucleonic and hyperonic inner core of neutron stars that satisfies the $2M_{\odot}$ observations as well as the recent determinations of stellar radii below 13 km, while fulfilling the saturation properties of nuclear matter and finite nuclei together with the constraints on the high-density nuclear pressure coming from heavy-ion collisions. The recent nucleonic FSU2R and hyperonic FSU2H models are updated in order to improve the behavior of pure neutron matter at subsaturation densities. The corresponding nuclear matter properties at saturation, the symmetry energy and its slope turn out to be compatible with recent experimental and theoretical determinations. We obtain the mass, radius and composition of neutron stars for the two updated models and study the impact on these properties of the uncertainties in the hyperon-nucleon couplings estimated from hypernuclear data. We find that the onset of appearance of each hyperon strongly depends on the hyperon-nuclear uncertainties, whereas the maximum masses for neutron stars differ by at most $0.1 M_{\odot}$, although a larger deviation should be expected tied to the lack of knowledge of the hyperon potentials at the high densities present in the center of $2M_{\odot}$ stars. For easier use, we provide tables with the results from the FSU2R and FSU2H models for the equation of state and the neutron star mass-radius relation.

Keywords: equation of state – neutron stars – mass-radius constraints – hyperons

1 INTRODUCTION

The equation of state (EoS) of matter inside neutron stars has received a lot of attention over the last decades (Lattimer & Prakash, 2004, 2007; Oertel et al., 2017). Besides black holes, neutron stars (usually observed as pulsars) are the most compact known objects in the universe. Their bulk features, such as mass and radius, strongly depend on the properties of matter in their interior and, hence, on the EoS.

With regards to mass determinations, the most precise measurements of masses are clustered around the Hulse-Taylor pulsar of $1.4M_{\odot}$ (Hulse & Taylor, 1975). However, accurate values of approximately $2M_{\odot}$ have been determined very recently. This is the case of the PSR J1614-2230 of $M = 1.97 \pm 0.04M_{\odot}$ (Demorest et al., 2010) and the PSR J0348+0432 of $M = 2.01 \pm 0.04M_{\odot}$ (Antoniadis et al., 2013).

As for radii, precise determinations do not yet exist due to the difficulties in modeling the X-ray spectra emitted by the atmosphere of a neutron star (Verbiest

et al., 2008; Ozel et al., 2010; Suleimanov et al., 2011; Lattimer & Lim, 2013; Steiner et al., 2013; Bogdanov, 2013; Guver & Ozel, 2013; Guillot et al., 2013; Lattimer & Steiner, 2014a; Poutanen et al., 2014; Heinke et al., 2014; Guillot & Rutledge, 2014; Ozel et al., 2016; Ozel & Psaltis, 2015; Ozel & Freire, 2016; Lattimer & Prakash, 2016). Nevertheless, most of these analysis seem to favor small radii below 13 km (Fortin et al., 2015). High-precision X-ray space missions, such as the on-going NICER (Neutron star Interior Composition ExploreR) (Arzoumanian et al., 2014), will shed some light by offering simultaneous measurements of masses and radii (Watts et al., 2016), whereas neutron-star radii are expected to be measured with a precision of 1 km by means of gravitational-wave signals coming from neutron-star mergers (Bauswein & Janka, 2012; Lackey & Wade, 2015).

In view of these findings and future observations, it is opportune to analyze whether theoretical models for the EoS of dense matter can satisfy both the $2M_{\odot}$ max-

imum mass constraint and radii below 13 km. Moreover, these models should fulfill the saturation properties¹ of nuclear matter and finite nuclei (or atomic nuclei). On the one hand, in order to obtain small neutron star radii, a softening of the pressure of neutron matter, and hence of the nuclear symmetry energy, around 1-2 times saturation density n_0 ($n_0 \approx 0.16 \text{ fm}^{-3}$) is required (Latimer & Prakash, 2007; Tsang et al., 2012; Ozel & Freire, 2016). On the other hand, the total pressure should be stiff enough in order to sustain $2M_\odot$ neutron stars. Very few models can reconcile simultaneously both constraints (small radius and large masses) and, at the same time, produce a precise description of finite nuclei (Jiang et al., 2015; Horowitz & Piekarewicz, 2001a,b; Chen & Piekarewicz, 2015a; Sharma et al., 2015).

Furthermore, as density increases inside neutron stars, the transition from nuclear to hyperonic matter would be favoured energetically (Ambartsumyan & Saakyan, 1960). Thus, the EoS softens as new degrees of freedom, hyperons, appear (Glendenning, 1982) leading to smaller neutron stars masses, below the $2M_\odot$ observations. This is known as the “hyperon puzzle”, whose solution requires a new mechanism to stiffen the EoS: stiffer hyperon-nucleon and/or hyperon-hyperon interactions, repulsive three-body forces with hyperons, new hadronic degrees of freedom that push the onset of appearance of hyperons to higher densities or the phase transition to quark matter below the hyperon onset (see Ref. (Chatterjee & Vidana, 2016) and references herein).

In a recent paper (Tolos et al., 2017) we have obtained the EoS for the nucleonic and hyperonic inner core of neutron stars by reconciling the $2M_\odot$ mass observations with the recent analyses of radii below 13 km for neutron stars. Moreover, we have fulfilled the saturation properties of nuclear matter and finite nuclei (Tsang et al., 2012; Chen & Piekarewicz, 2014) as well as the recent constraints extracted from nuclear collective flow (Danielewicz et al., 2002) and kaon production (Fuchs et al., 2001; Lynch et al., 2009) in heavy-ion collisions (HICs). The study was performed in the relativistic mean-field (RMF) theory for describing both the nucleon and hyperon interactions and the EoS of the neutron star core. Two models were formulated, denoted as FSU2R (with nucleons) and FSU2H (with nucleons and hyperons), based on the nucleonic FSU2 model of (Chen & Piekarewicz, 2014).

In the present paper, we update the parameters of our two models in order to improve the behaviour of the EoS of pure neutron matter (PNM) at subsaturation densities by avoiding possible instabilities in the low-density region. We determine the properties at saturation of the modified interactions and we compare our results for the symmetry energy and the slope of the

¹Saturation properties refer to the physical characteristics of infinite symmetric nuclear matter at the density ρ_0 , where the energy per particle, E/A , presents a minimum.

symmetry energy to recent experimental and theoretical determinations, while providing predictions for the neutron skin thickness of the ^{208}Pb and ^{48}Ca nuclei. Finally, we reinvestigate the mass-radius relationships for the two models, and estimate the impact on the neutron star masses, radii and composition of the uncertainties in the hyperon-nucleon couplings.

The paper is organized as follows. In Sec. 2 we present the RMF model for the determination of the EoS in beta-equilibrated matter. In Sec. 3 we show the newly calibrated nucleonic FSU2R and hyperonic FSU2H models. Then, in Sec. 4 we display the results for the mass-radius relationship for neutron stars and in Sec. 5 we estimate the impact on the stellar properties of the uncertainties in the hyperon-nucleon couplings. We finally summarize our results in Sec. 6. Tables with numerical data of the EoSs are provided in the Appendix.

2 THEORETICAL FRAMEWORK

In the covariant field theory of hadronic matter, the baryons are treated as Dirac particles that interact through the exchange of mesons (Serot & Walecka, 1986). The formalism has been in wide use over the last four decades for describing the properties of the nuclear EoS and of finite nuclei in a relativistic quantum framework. A contemporary formulation of the Lagrangian density of the theory (Serot & Walecka, 1986, 1997; Glendenning, 2000; Chen & Piekarewicz, 2014) may be written in terms of the contributions from the baryons (b), leptons ($l=e, \mu$), and mesons ($m=\sigma, \omega, \rho$, and ϕ) as

$$\begin{aligned} \mathcal{L} &= \sum_b \mathcal{L}_b + \mathcal{L}_m + \sum_l \mathcal{L}_l, \\ \mathcal{L}_b &= \bar{\Psi}_b (i\gamma_\mu \partial^\mu - q_b \gamma_\mu A^\mu - m_b \\ &\quad + g_{\sigma b} \sigma - g_{\omega b} \gamma_\mu \omega^\mu - g_{\phi b} \gamma_\mu \phi^\mu - g_{\rho b} \gamma_\mu \vec{I}_b \vec{\rho}^\mu) \Psi_b, \\ \mathcal{L}_l &= \bar{\psi}_l (i\gamma_\mu \partial^\mu - q_l \gamma_\mu A^\mu - m_l) \psi_l, \\ \mathcal{L}_m &= \frac{1}{2} \partial_\mu \sigma \partial^\mu \sigma - \frac{1}{2} m_\sigma^2 \sigma^2 - \frac{\kappa}{3!} (g_{\sigma N} \sigma)^3 - \frac{\lambda}{4!} (g_{\sigma N} \sigma)^4 \\ &\quad - \frac{1}{4} \Omega^{\mu\nu} \Omega_{\mu\nu} + \frac{1}{2} m_\omega^2 \omega_\mu \omega^\mu + \frac{\zeta}{4!} (g_{\omega N} \omega_\mu \omega^\mu)^4 \\ &\quad - \frac{1}{4} \vec{R}^{\mu\nu} \vec{R}_{\mu\nu} + \frac{1}{2} m_\rho^2 \vec{\rho}_\mu \vec{\rho}^\mu + \Lambda_\omega g_{\rho N}^2 \vec{\rho}_\mu \vec{\rho}^\mu g_{\omega N}^2 \omega_\mu \omega^\mu \\ &\quad - \frac{1}{4} P^{\mu\nu} P_{\mu\nu} + \frac{1}{2} m_\phi^2 \phi_\mu \phi^\mu - \frac{1}{4} F^{\mu\nu} F_{\mu\nu}, \end{aligned} \quad (1)$$

where Ψ_b and ψ_l stand for the baryonic and leptonic Dirac fields, respectively. The mesonic and electromagnetic field strength tensors are $\Omega_{\mu\nu} = \partial_\mu \omega_\nu - \partial_\nu \omega_\mu$, $\vec{R}_{\mu\nu} = \partial_\mu \vec{\rho}_\nu - \partial_\nu \vec{\rho}_\mu$, $P_{\mu\nu} = \partial_\mu \phi_\nu - \partial_\nu \phi_\mu$ and $F_{\mu\nu} = \partial_\mu A_\nu - \partial_\nu A_\mu$. The isospin operator is represented by the vector \vec{I}_b . The strong interaction coupling of a meson to a certain baryon is denoted by g (with N indicating nucleon) and the electromagnetic couplings by q , while the

masses of the baryons, mesons, and leptons are denoted by m .

The coupling constants of the above Lagrangian encode in an approximate way the complicated nuclear many-body dynamics. The $g_{\sigma N}$ and $g_{\omega N}$ couplings of the isoscalar σ and ω mesons to the nucleon determine the energy per particle and density of the nuclear matter saturation point, and, thus, are instrumental for the ground-state properties of finite nuclei. The $g_{\rho N}$ coupling of the isovector ρ meson to the nucleon is key for the nuclear symmetry energy. Essentially, the symmetry energy measures the energy cost involved in changing all the protons into neutrons in nuclear matter (Li et al., 2014). Therefore, the $g_{\rho N}$ coupling impacts on the properties of heavy neutron-rich nuclei and of neutron stars. The Lagrangian density (I), moreover, incorporates self-interactions of the meson fields. The σ -meson self-interactions, with the κ and λ couplings, were introduced by (Boguta & Bodmer, 1977) and allowed for the first quantitatively successful descriptions of nuclear matter and finite nuclei within the relativistic theory. These couplings soften the EoS at moderate densities and allow one to obtain a realistic compressibility of nuclear matter (Boguta & Bodmer, 1977; Boguta & Stoecker, 1983) in agreement with the values extracted from experiments on nuclear giant resonances and heavy ion collisions.² The quartic self-coupling ζ of the vector ω meson was introduced by (Bodmer, 1991). The ζ coupling must be nonnegative to prevent abnormal solutions of the vector field equation of motion (Bodmer, 1991; Mueller & Serot, 1996). It then implies an attractive nonlinear interaction that softens the EoS for high densities (Bodmer, 1991), thereby directly affecting the structure and maximum mass of neutron stars (Mueller & Serot, 1996). Finally, a mixed interaction between the ω and ρ mesons, with the coupling Λ_ω , modulates the density dependence of the nuclear symmetry energy—which is related to the pressure of neutron matter—and influences the neutron radius of heavy nuclei and the radii of neutron stars (Horowitz & Piekarewicz, 2001a,b).

The Dirac equations for the different baryons and leptons are obtained from the Lagrangian density (I) as

$$\begin{aligned} (i\gamma_\mu \partial^\mu - q_b \gamma_0 A^0 - m_b^* \\ - g_{\omega b} \gamma_0 \omega^0 - g_{\phi b} \gamma_0 \phi^0 - g_{\rho b} I_{3b} \gamma_0 \rho_3^0) \Psi_b = 0, \\ (i\gamma_\mu \partial^\mu - q_l \gamma_0 A^0 - m_l) \psi_l = 0, \end{aligned} \quad (2)$$

where the quantities

$$m_b^* = m_b - g_{\sigma b} \sigma \quad (3)$$

denote the effective masses of the baryons. Let us mention that only the time-like component of the vector

²Note that it has been suggested that the nuclear compressibility could be also inferred from gravitational wave observations of pulsar glitch recoveries (Bennett et al., 2010)

fields and the third component of isospin have been written in Eq. (2) due to the assumption of rotational invariance and charge conservation. The field equations of motion of the mesons follow from the respective Euler–Lagrange equations, see for example (Serot & Walecka, 1986). Altogether, the theory leads to a set of coupled nonlinear field equations that involve strong couplings. The exact solution of these equations is extremely complicated if one attempts to quantize both the baryon fields and the meson fields. Physically, the baryons are the constituents of the nuclear medium, whereas the mesons are the carriers of the interaction between baryons. Thus, in order to be able to solve the equations of the theory, it is meaningful to replace the meson field operators by their expectation values, which then act as classical fields in which the baryons move. This approach is known as the relativistic mean-field theory (Serot & Walecka, 1986). Denoting the meson mean fields in uniform matter as $\bar{\sigma} = \langle \sigma \rangle$, $\bar{\omega} = \langle \omega^0 \rangle$, $\bar{\rho} = \langle \rho_3^0 \rangle$, and $\bar{\phi} = \langle \phi^0 \rangle$, the mesonic equations of motion in the mean-field approximation for the uniform medium are

$$\begin{aligned} m_\sigma^2 \bar{\sigma} + \frac{\kappa}{2} g_{\sigma N}^3 \bar{\sigma}^2 + \frac{\lambda}{3!} g_{\sigma N}^4 \bar{\sigma}^3 &= \sum_b g_{\sigma b} n_b^s, \\ m_\omega^2 \bar{\omega} + \frac{\zeta}{3!} g_{\omega N}^4 \bar{\omega}^3 + 2\Lambda_\omega g_{\rho N}^2 g_{\omega N}^2 \bar{\rho}^2 \bar{\omega} &= \sum_b g_{\omega b} n_b, \\ m_\rho^2 \bar{\rho} + 2\Lambda_\omega g_{\rho N}^2 g_{\omega N}^2 \bar{\omega}^2 \bar{\rho} &= \sum_b g_{\rho b} I_{3b} n_b, \\ m_\phi^2 \bar{\phi} &= \sum_b g_{\phi b} n_b, \end{aligned} \quad (4)$$

where I_{3b} is the third component of the isospin of a given baryon, and we use the convention that for protons $I_{3p} = +1/2$. The quantities

$$\begin{aligned} n_b^s &= \langle \bar{\Psi}_b \Psi_b \rangle, \\ n_b &= \langle \bar{\Psi}_b \gamma^0 \Psi_b \rangle, \end{aligned} \quad (5)$$

are, respectively, the scalar and vector densities for the b baryon. In terms of the baryonic and leptonic Fermi momenta, k_{Fb} and k_{Fl} , and of the respective Fermi energies

$$\begin{aligned} E_{Fb} &= \sqrt{k_{Fb}^2 + m_b^{*2}}, \\ E_{Fl} &= \sqrt{k_{Fl}^2 + m_l^2}, \end{aligned} \quad (6)$$

the scalar and vector densities for the baryons and the vector densities for the leptons are expressed as

$$\begin{aligned} n_b^s &= \frac{m_b^*}{2\pi^2} \left[E_{Fb} k_{Fb} - m_b^{*2} \ln \frac{k_{Fb} + E_{Fb}}{m_b^*} \right], \\ n_b &= \frac{k_{Fb}^3}{3\pi^2}, \\ n_l &= \frac{k_{Fl}^3}{3\pi^2}. \end{aligned} \quad (7)$$

With the above ingredients, one can compute the energy density and the pressure of the system. The energy density is given by

$$\begin{aligned} \varepsilon &= \sum_b \varepsilon_b + \sum_l \varepsilon_l \\ &+ \frac{1}{2} m_\sigma^2 \bar{\sigma}^2 + \frac{1}{2} m_\omega^2 \bar{\omega}^2 + \frac{1}{2} m_\rho^2 \bar{\rho}^2 + \frac{1}{2} m_\phi^2 \bar{\phi}^2 \\ &+ \frac{\kappa}{3!} (g_\sigma \bar{\sigma})^3 + \frac{\lambda}{4!} (g_\sigma \bar{\sigma})^4 \\ &+ \frac{\zeta}{8} (g_\omega \bar{\omega})^4 + 3\Lambda_\omega (g_\rho g_\omega \bar{\rho} \bar{\omega})^2, \end{aligned} \quad (8)$$

where the energy densities of baryons and leptons take the expressions

$$\begin{aligned} \varepsilon_b &= \frac{1}{8\pi^2} \left[k_{Fb} E_{Fb}^3 + k_{Fb}^3 E_{Fb} - m_b^{*4} \ln \frac{k_{Fb} + E_{Fb}}{m_b^*} \right], \\ \varepsilon_l &= \frac{1}{8\pi^2} \left[k_{Fl} E_{Fl}^3 + k_{Fl}^3 E_{Fl} - m_l^4 \ln \frac{k_{Fl} + E_{Fl}}{m_l} \right]. \end{aligned} \quad (9)$$

We note that in obtaining Eq. (8) for the energy density, the equations of motion (4) were used to rewrite the contribution to ε of $\sum_b (g_{\omega b} \bar{\omega} n_b + g_{\rho b} \bar{\rho} I_{3b} n_b + g_{\phi b} \bar{\phi} n_b)$. Finally, the pressure can be computed using the thermodynamic relation

$$P = \sum_i \mu_i n_i - \varepsilon, \quad (10)$$

where the baryonic and leptonic chemical potentials are given by

$$\begin{aligned} \mu_b &= E_{Fb} + g_{\omega b} \bar{\omega} + g_{\rho b} I_{3b} \bar{\rho} + g_{\phi b} \bar{\phi}, \\ \mu_l &= E_{Fl}. \end{aligned} \quad (11)$$

The cores of neutron stars harbor globally neutral matter that is in β -equilibrium. Therefore, the chemical potentials and the number densities of the different particles in a neutron star core are related by the conditions

$$\begin{aligned} \mu_i &= b_i \mu_n - q_i \mu_e, \\ 0 &= \sum_{b,l} q_i n_i, \\ n &= \sum_b n_i, \end{aligned} \quad (12)$$

where b_i and q_i denote, respectively, the baryon number and the charge of the particle i . These relations, the Dirac equations (2) for the baryons and leptons, and the field equations (4) for the mesonic fields σ , ω , ρ and ϕ , are to be solved self-consistently for a given total baryon density n . Once the chemical potential and the density of each species have been obtained at the given n , one can determine the energy density and pressure of the neutron star matter for each density.

3 MODELS FOR THE EQUATION OF STATE

From the Lagrangian (1), in (Tolos et al., 2017) we formulated the models FSU2R (with nucleons) and FSU2H (with nucleons and hyperons), with a motivation for accomodating massive enough stars and the new astrophysical measurements of small stellar radii within a self-consistent microscopic theory of the EoS for the core of neutron stars. Note that this type of approach is different from—but complementary to—the methods where the astrophysical and nuclear observables are mapped onto the EoS through piecewise parametrizations of the EoS (Raithel et al., 2016; Lattimer & Prakash, 2016; Ozel & Freire, 2016). To build our models we started from the nucleonic FSU2 model of (Chen & Piekarewicz, 2014) that reproduces heavy neutron star masses but was not constrained to radii. The condition of small stellar radii imposed a soft nuclear symmetry energy in the theory. We showed that the resulting FSU2R and FSU2H models, besides the mentioned astrophysical constraints, can successfully describe the properties of finite nuclei and conform to the constraints on the nuclear EoS from kaon production and collective flow in HICs (Fuchs et al., 2001; Lynch et al., 2009; Danielewicz et al., 2002).

In the present work we start by introducing a modification of the parameters of our models FSU2R and FSU2H of (Tolos et al., 2017) in order to refine the behavior of the EoS of pure neutron matter (PNM) in the region of subsaturation densities. We report the new version of the parameters in Table 1 (it should be mentioned that the form of the equations of motion remains the same irrespective of the specific values of the coupling constants). We have changed the value of the quartic isovector-vector coupling Λ_ω of FSU2R and FSU2H from 0.05 in (Tolos et al., 2017) to 0.045. This has been done because it results in a symmetry energy that is a little stiffer than before and avoids a previous instability in the EoS of PNM for low subsaturation densities. As Λ_ω has been changed, we have refitted accordingly the value of the coupling $g_{\rho N}^2$ between the ρ -meson and the nucleons to obtain the same good reproduction of binding energies and charge radii of finite nuclei as in (Tolos et al., 2017). The values of the other parameters of FSU2R and FSU2H are the same of (Tolos et al., 2017). Owing to the fact the Λ_ω and $g_{\rho N}^2$ couplings only contribute in neutron-rich matter, the EoS of symmetric nuclear matter (SNM), composed of the same number of protons and neutrons, is identical to that of our models FSU2R and FSU2H in (Tolos et al., 2017).

We collect in Table 2 a few characteristic isoscalar and isovector properties at the nuclear matter saturation density n_0 for the present version of our models. In the work (Fortin et al., 2015), the authors derived the constraint $1.7 \lesssim P(n_0) \lesssim 2.8 \text{ MeV fm}^{-3}$ for the pressure of neutron star matter at saturation density.

Table 1 Parameters of the models FSU2R and FSU2H of this work. The mass of the nucleon is $m_N = 939$ MeV.

Model	m_σ (MeV)	m_ω (MeV)	m_ρ (MeV)	$g_{\sigma N}^2$	$g_{\omega N}^2$	$g_{\rho N}^2$	κ	λ	ζ	Λ_ω
FSU2R	497.479	782.500	763.000	107.5751	182.3949	206.4260	3.0911	-0.001680	0.024	0.045
FSU2H	497.479	782.500	763.000	102.7200	169.5315	197.2692	4.0014	-0.013298	0.008	0.045

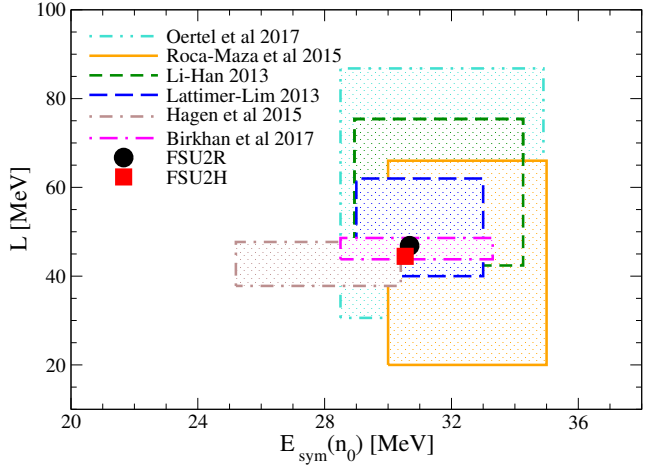
Table 2 Properties at saturation of the models FSU2R and FSU2H of this work. We show the saturation density (n_0), energy per particle (E/A), compressibility (K), and effective nucleon mass (m_N^*/m_N) in symmetric nuclear matter, as well as the symmetry energy (E_{sym}), slope of the symmetry energy (L), curvature of the symmetry energy (K_{sym}), and pressure of pure neutron matter (P_{PNM}) at n_0 .

Model	n_0 (fm $^{-3}$)	E/A (MeV)	K (MeV)	m_N^*/m_N	$E_{\text{sym}}(n_0)$ (MeV)	L (MeV)	K_{sym} (MeV)	$P_{\text{PNM}}(n_0)$ (MeV fm $^{-3}$)
FSU2R	0.1505	-16.28	238.0	0.593	30.7	46.9	55.7	2.44
FSU2H	0.1505	-16.28	238.0	0.593	30.5	44.5	86.7	2.30

They deduced this constraint from the results of the microscopic calculations of PNM performed by (Hebeler et al., 2013) using chiral two-nucleon and three-nucleon interactions, which are in good agreement with the results by (Gandolfi et al., 2012) from Quantum Monte Carlo calculations with the Argonne v_{18} nucleon-nucleon potential plus three-nucleon forces. A narrower range $2.3 \lesssim P(n_0) \lesssim 2.6$ MeV fm $^{-3}$ was estimated more recently by (Hagen et al., 2015) from ab initio calculations of nuclear systems with chiral interactions. While our models FSU2R and FSU2H of (Tolos et al., 2017), with PNM pressures at saturation of 2.27 and 2.06 MeV fm $^{-3}$, fulfill the constraint of (Fortin et al., 2015), they are somewhat below the constraint of (Hagen et al., 2015). Now, with the new parametrization of our models, we are able to obtain PNM pressures at saturation density of 2.44 MeV fm $^{-3}$ in FSU2R and of 2.30 MeV fm $^{-3}$ in FSU2H (see Table 2) that are consistent with both the predictions from chiral forces derived by (Fortin et al., 2015) and (Hagen et al., 2015).

The EoS of PNM of the present FSU2R and FSU2H models differs from the results we showed in (Tolos et al., 2017) almost only for densities in the low-density region $n \lesssim n_0$, where the pressure of PNM is a little higher now. However, above saturation density, the pressures of our current parameters and those of (Tolos et al., 2017) are very similar. Consequently, compared with (Tolos et al., 2017), one may anticipate that the predictions for masses and radii of neutron stars will not be drastically affected.

The slope parameter L of the symmetry energy, i.e., $L = 3n_0 \left(\frac{\partial E_{\text{sym}}(n)}{\partial n} \right)_{n_0}$, has become a standard reference in the literature for characterizing the stiffness of the change of the nuclear symmetry energy $E_{\text{sym}}(n)$ with density. In our original version of the FSU2R and FSU2H models shown in (Tolos et al., 2017), the value of the symmetry energy at saturation density

**Figure 1.** Slope of the symmetry energy (L) versus symmetry energy ($E_{\text{sym}}(n_0)$) at the nuclear matter saturation density for the models FSU2R and FSU2H discussed in text. The shaded regions depict the determinations from (Li & Han, 2013; Lattimer & Lim, 2013; Roca-Maza et al., 2015; Hagen et al., 2015; Oertel et al., 2017; Birkhan et al., 2017).

was $E_{\text{sym}}(n_0) = 30.2$ MeV in both models, while the slope parameter was $L = 44.3$ MeV in FSU2R and $L = 41$ MeV in FSU2H. In the updated version of FSU2R and FSU2H of the present work, these properties become $E_{\text{sym}}(n_0) = 30.7$ MeV and $L = 46.9$ MeV in FSU2R and $E_{\text{sym}}(n_0) = 30.5$ MeV and $L = 44.5$ MeV in FSU2H (see Table 2). These values suggest a relatively soft nuclear symmetry energy. We have plotted in Fig. 1 the ranges for $E_{\text{sym}}(n_0)$ and L that have been estimated in several recent works through the analysis of a variety of nuclear data from terrestrial experiments, astrophysical observations, and theoretical calculations (Li & Han, 2013; Lattimer & Lim, 2013; Roca-Maza et al., 2015; Hagen et al., 2015; Oertel et al., 2017; Birkhan et al., 2017). It can be seen that the predictions of FSU2R

and FSU2H have an overlap with the majority of these ranges. We would like to remark that this is an *a posteriori* result, because the predicted values of $E_{\text{sym}}(n_0)$ and L are the consequence (Tolos et al., 2017) of having adjusted the FSU2R and FSU2H parameter sets to reproduce neutron star radii of about 13 km, without sacrificing maximum masses of $2M_\odot$ nor the description of binding energies and charge radii of atomic nuclei. Hence, we interpret the reasonable agreement of our results with the multiple constraints in Fig. 1 as hinting at the plausibility of the existence of neutron stars with relatively small radii.

The neutron matter EoS is also strongly related with the neutron distribution in atomic nuclei. Models with softer symmetry energies produce a thinner neutron skin Δr_{np} (difference between the rms radii of the neutron and proton density distributions) in nuclei (Alex Brown, 2000; Horowitz & Piekarewicz, 2001a). Unfortunately, neutron densities and neutron radii are poorly known to date because the distribution of neutrons in a nucleus is hard to measure. Our present FSU2R and FSU2H models predict a neutron skin thickness of 0.15 fm in the neutron-rich nucleus ^{208}Pb . This prediction is compatible with the range $0.13 \lesssim \Delta r_{np} \lesssim 0.19$ fm for ^{208}Pb extracted in (Roca-Maza et al., 2015) from measurements of the electric dipole polarizability of nuclei, the value $\Delta r_{np} = 0.15 \pm 0.03$ fm determined from coherent pion photoproduction in ^{208}Pb at the MAMI facility (Tarbert et al., 2014), and the value $\Delta r_{np} = 0.302 \pm 0.177$ fm from parity violating electron scattering on ^{208}Pb performed at JLab (Abrahamyan et al., 2012; Horowitz et al., 2012).³ In the case of the lighter nucleus ^{48}Ca , we find a neutron radius of 3.55 fm with FSU2R and of 3.57 fm with FSU2H, and a neutron skin of 0.166 fm with both models. The prediction is in good accord with the ranges 3.47–3.60 fm for the neutron radius and 0.12–0.15 fm for the neutron skin of ^{48}Ca obtained in (Hagen et al., 2015) through ab initio calculations of the neutron distribution of ^{48}Ca using nuclear interactions derived from chiral effective field theory; it also is in accord with the neutron skin of 0.14–0.20 fm for ^{48}Ca found from the new measurement of the electric dipole polarizability in ^{48}Ca (Birkhan et al., 2017). Altogether, it appears that the properties of the symmetry energy of the proposed models for the EoS, which are motivated by reproducing small neutron star radii (see next section), are compatible within uncertainties with different empirical and theoretical extractions of these properties.

³We note that while experimental data are always provided with the associated error bars, theoretical models like ours, after the values of the coupling constants have been specified, make “exact” predictions with no error bars. In the future, it will be worth estimating error bars on our theoretical results, following recent initiatives to assess statistical errors and error propagation in nuclear functionals (Dobaczewski et al., 2014; Chen & Piekarewicz, 2014).

4 STELLAR PROPERTIES

Having access to the pressure and energy density of matter, we can compute the properties of neutron stars by solving the Tolman-Oppenheimer-Volkoff (TOV) equations (Oppenheimer & Volkoff, 1939). For static and spherically-symmetric stars, the TOV equations read as

$$\begin{aligned} \frac{dP}{dr} &= -\frac{G}{r^2}(\varepsilon + P)(m + 4\pi r^3 P) \left(1 - \frac{2Gm}{r}\right)^{-1}, \\ \frac{dm}{dr} &= 4\pi r^2 \varepsilon, \end{aligned} \quad (13)$$

where r is the radial coordinate, m is the mass enclosed by a radius r , and G is the gravitational constant. For a given central density, the integration of these equations provides the corresponding mass and radius of the star. By repeating the calculation for different central densities, the mass-radius (M-R) relation of neutron stars can be obtained.

Indeed, to solve the TOV equations for a neutron star we need the EoS of matter over a wide range of densities from the center to the surface of the star. The structure of a neutron star is such that the heavy liquid core is surrounded by a thin solid crust (Shapiro & Teukolsky, 1983; Haensel et al., 2006). The transition from the core to the crust occurs when the density of matter becomes lower than approximately 1.5×10^{14} g/cm³. Below this density, matter ceases to exist in a homogeneous liquid phase because it is favorable that the protons concentrate with neutrons in nuclear clusters, which arrange themselves in a crystal lattice in order to minimize the Coulomb repulsion among them (Baym et al., 1971b;a; Shapiro & Teukolsky, 1983; Haensel et al., 2006). In the inner layers of the crust, the nuclear clusters are beyond the neutron drip point and the lattice is permeated by a gas of free neutrons in addition to the electron gas, whereas in the outer crust the nuclear clusters are neutron-rich nuclei below the neutron drip point, embedded in the electron gas. We have solved the TOV equations using the FSU2R and FSU2H models for the EoS of the uniform matter of the liquid core of the star for densities above 0.09 fm⁻³ ($\approx 1.5 \times 10^{14}$ g/cm³), under the conditions of β -equilibrium and global charge neutrality expressed in Eq. (12) of Sec. 2. At the densities of the crust, in the absence of calculations with our models of the complex structures that can populate this region of the star, we have used the EoS for the crust of neutron stars that has recently been derived from calculations based on the Brueckner theory in (Sharma et al., 2015).

The FSU2R model applies to nucleonic cores of neutron stars, i.e., when the whole stellar core is assumed to consist of neutrons, protons, electrons, and muons (‘*npeμ*’ matter). In the dense inner region of a neutron star core, however, the chemical potential may become so high that matter will be able to undergo a transition

to other states of the low-lying octet of baryons, with hyperons appearing in the composition (' $npY\mu$ ' matter). Thus, we have devised the FSU2H model to allow for the presence of hyperons in the star interior (Tolos et al., 2017). In consequence, in the case of the FSU2H EoS, besides the nucleon and meson couplings shown in Table 1, we have considered the complete octet of baryons in the Lagrangian density (1). We have fixed the corresponding hyperon couplings from SU(3) flavor symmetry and from information on hyperon optical potentials in hypernuclei. We leave for the next section the discussion of the determination of the hyperon couplings and the analysis of the influence of the uncertainties associated with these couplings. Here, we focus on the results for the masses and sizes of neutron stars from the FSU2R nucleonic EoS and from the FSU2H hyperonic EoS with our baseline values for the hyperon couplings (given in Sec. 5).

We display the results for the relation between mass and radius of neutron stars in Fig. 2. A few data on the maximum mass configuration and the $1.5M_{\odot}$ configuration from FSU2R and FSU2H are presented in Table 3. For completeness, in Fig. 2 besides the curves of FSU2R and FSU2H, we also plot the M-R relations of two popular EoSs widely used in astrophysical calculations. They correspond to the Shen et al. EoS based on the relativistic TM1 nuclear mean field model (Shen et al., 1998) and to the Lattimer–Swesty EoS based on a non-relativistic Skyrme nuclear force (in its Ska version) (Lattimer & Swesty, 1991). Also shown is the result of the recent EoS from the Brueckner theory with the Argonne v_{18} potential plus three-body forces computed with the Urbana model (Sharma et al., 2015). These additional EoSs are all non-hyperonic. We have included in the same Fig. 2 a few recent astrophysical determinations of neutron star mass-radius limits.

The M-R curve from each EoS exhibits a maximum mass, beyond which the star would become unstable against collapse into a black hole. The heaviest known masses of neutron stars are $M = 1.97 \pm 0.04M_{\odot}$ in the PSR J1614–2230 pulsar (Demorest et al., 2010) and $M = 2.01 \pm 0.04M_{\odot}$ in the PSR J0348+0432 pulsar (Antoniadis et al., 2013). We depict them by the horizontal bands in Fig. 2. Both the nucleonic FSU2R EoS and the hyperonic FSU2H EoS are able to provide maximum masses fulfilling the $\approx 2M_{\odot}$ observational limit, as well as the other EoSs shown in the same figure. We note that FSU2R reaches the maximum mass with a fairly compact stellar radius of 11.6 km (see Table 3). For canonical neutron stars with masses of $1.4M_{\odot}$ – $1.5M_{\odot}$, FSU2R predicts a radius of 12.8 km. The recent astrophysical determinations of neutron star radii from quiescent low-mass X-ray binaries in globular clusters and X-ray bursters seem to point in this direction (Guillot et al., 2013; Guillot & Rutledge, 2014; Guver & Ozel, 2013; Heine et al., 2014; Lattimer & Steiner, 2014a,b;

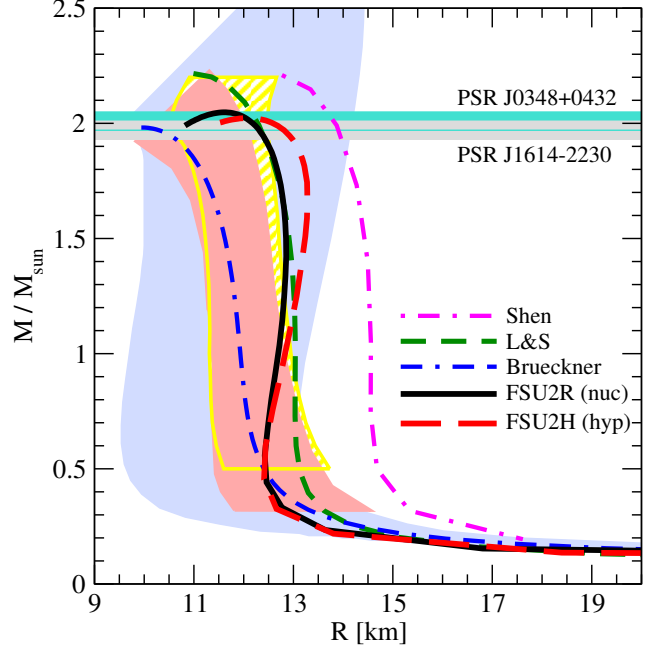


Figure 2. Mass versus radius for neutron stars from the models FSU2R and FSU2H of this work and from some models from the literature (Shen: (Shen et al., 1998), L&S: (Lattimer & Swesty, 1991), Brueckner: (Sharma et al., 2015)). The thin horizontal bands indicate the heaviest observed masses $M = 1.97 \pm 0.04M_{\odot}$ (Demorest et al., 2010) and $M = 2.01 \pm 0.04M_{\odot}$ (Antoniadis et al., 2013). The vertical blue band at the back depicts the M-R region constrained in (Hebeler et al., 2013) from chiral nuclear interactions up to $n = 1.1n_0$ and the conditions of $M_{\max} > 1.97M_{\odot}$ and causality. The vertical red band at the front shows the M-R region derived from five quiescent low-mass X-ray binaries and five photospheric radius expansion X-ray bursters after a Bayesian analysis (Lattimer & Steiner, 2014b). The vertical striped yellow band is the M-R constraint derived from the cooling tails of type-I X-ray bursts in three low-mass X-ray binaries and a Bayesian analysis in (Näyttälä et al., 2016) (model A of the paper).

Ozel et al., 2016). Although these determinations are indirect and depend on stellar atmosphere models, they overall converge in favoring small neutron star radii in the range of about 9–13 km (Lattimer & Prakash, 2016; Ozel & Freire, 2016). An accurate radius measurement by new observatories such as NICER (Arzoumanian et al., 2014), which has begun operating aboard the International Space Station in June 2017, would represent a major step forward to corroborate or modify these expectations.

The compromise between having large maximum masses and small radii for canonical neutron stars is a challenging constraint that rules out a large number of theoretical EoSs (Lattimer & Prakash, 2016; Ozel & Freire, 2016; Oertel et al., 2017). This follows from the fact that the pressure of the high-density EoS must be hard enough to sustain massive stars, whereas the pressure at 1–2 times the nuclear saturation density n_0 must be, in contrast, effectively soft in order to pro-

Table 3 Properties of the maximum mass and $1.5M_{\odot}$ configurations for nucleonic ($npe\mu$) neutron stars calculated with the FSU2R EoS and for hyperonic ($npYe\mu$) neutron stars calculated with the FSU2H EoS. From top to bottom, mass, radius, compactness parameter GM/Rc^2 , surface gravitational red shift $z_{\text{surf}} = (1 - 2GM/Rc^2)^{-1/2} - 1$, and the values of the number density, pressure, and mass-energy density at the center of the star.

	M_{max} configuration		$1.5M_{\odot}$ configuration	
	FSU2R (nuc)	FSU2H (hyp)	FSU2R (nuc)	FSU2H (hyp)
M/M_{\odot}	2.05	2.02	1.50	1.50
R (km)	11.6	12.1	12.8	13.2
GM/Rc^2	0.26	0.25	0.17	0.17
z_{surf}	0.45	0.40	0.24	0.23
n_c/n_0	6.3	5.8	2.7	2.3
P_c (10^{15} g cm $^{-3}$)	0.62	0.46	0.11	0.09
ε_c (10^{15} g cm $^{-3}$)	2.08	1.80	0.75	0.63

duce small radii for canonical mass stars. Given that the pressure of neutron star matter in the vicinity of n_0 is basically governed by the nuclear symmetry energy, the challenge is particularly acute in relativistic field theoretical models because the relativistic models usually have stiff symmetry energies. As we have demonstrated with FSU2R, it is possible to obtain parametrizations of the considered relativistic Lagrangian that meet both large stellar masses and—on condition of a soft symmetry energy—radii smaller than ~ 13 km for $M \gtrsim 1.4M_{\odot}$, and that still provide an excellent reproduction of the binding energies and charge radii of finite nuclei (Tolos et al., 2017). There are some other parametrizations in the frame of the relativistic field theory that support these findings, such as the recent RMF012 and RMF016 models of (Chen & Piekarewicz, 2015b,a). Indeed, the accurately calibrated RMF016 model produces neutron stars of $2M_{\odot}$ and gives radii of 13 km for stars of $1.4M_{\odot}$ (Chen & Piekarewicz, 2015b,a), in keeping with the predictions of our FSU2R EoS.

When we allow for the appearance of hyperons in the neutron star core with the FSU2R model, the maximum mass of the star experiences a reduction of the order of 15%, due to the expected softening of the EoS, and then, with a maximum mass of $1.77M_{\odot}$, it falls short of the $2M_{\odot}$ limit. In an effort to shed some light on the question whether with exotic degrees of freedom in the core, the star can satisfy the targets of $2M_{\odot}$ maximum mass and small radius at canonical mass, we have developed the hyperonic model FSU2H. In FSU2H, we essentially have stiffened further the nucleonic pressure above twice the saturation density, i.e., around the onset of appearance of hyperons. This comes at the price of a certain overpressure in symmetric nuclear matter for densities $n \gtrsim 2n_0$ when we compare it with the constraints deduced from the modeling of collective flow in HICs (Danielewicz et al., 2002), cf. Fig. 1 of (Tolos et al., 2017). Yet the pressure of FSU2H in pure neutron matter, shown also in Fig. 1 of (Tolos et al., 2017), fits

within the projected region from the collective flow studies. Given that the β -equilibrated neutron-star matter is highly asymmetric, we consider this model as sufficiently realistic for describing neutron stars. The determination of narrower constraints on the EoS of PNM at several times n_0 from HIC experiments (Russotto et al., 2016) in the future should be of great help in this regard.

It can be observed in Fig. 2 that the FSU2H model with hyperons produces a comparable M-R relation to FSU2R and satisfies, as mentioned, the observational limit of $2M_{\odot}$. With respect to FSU2R, in FSU2H the size of the radii has increased by 0.2–0.5 km for neutron stars heavier than $1M_{\odot}$, expectedly, from the stiffer pressure of the nucleonic sector above twice the saturation density. The onset of hyperons occurs at a baryon density of 0.33 fm $^{-3}$, or $2.2n_0$. The maximum mass of $2.02M_{\odot}$ calculated with FSU2H is characterized by a radius of 12.1 km (see Table 3). For $1.5M_{\odot}$ stars, the hyperonic FSU2H EoS predicts radii of 13.2 km, which, although on the upper edge, are still compatible with the recent astrophysical indications of neutron star radii of about 9–13 km (Lattimer & Prakash, 2016; Ozel & Freire, 2016). The numerical results for the EoS and M-R relation of the FSU2R and FSU2H models are tabulated in the Appendix.

In closing this section, we ought to mention that the results for stellar radii of our EoSs have been possible while obtaining, within the same models, a realistic reproduction of the properties of atomic nuclei and of several other constraints. It seems unlikely that one may be able to account for significantly smaller neutron star radii in the theory considered here without abandoning the physical region of parameters. Hence, a discovery of even smaller stellar radii could provide evidence in favor of a phase transition to other degrees of freedom in neutron star interiors (Dexheimer et al., 2015).

5 IMPACT OF UNCERTAINTIES IN THE HYPERON COUPLINGS

We next discuss the determination of the values of the hyperon couplings in our FSU2H EoS and estimate the influence that the uncertainties in these couplings may have on the predictions for neutron star masses and radii.

We recall that the potential felt by a hyperon i in j -particle matter is given by

$$U_i^{(j)}(n_j) = -g_{\sigma i} \bar{\sigma}^{(j)} + g_{\omega i} \bar{\omega}^{(j)} + g_{\rho i} I_{3i} \bar{\rho}^{(j)} + g_{\phi i} \bar{\phi}^{(j)}, \quad (14)$$

in our model, where $\bar{\sigma}^{(j)}$, $\bar{\omega}^{(j)}$, $\bar{\rho}^{(j)}$ and $\bar{\phi}^{(j)}$ are the meson field values in j -particle matter while I_{3i} denotes the third component of the isospin operator. Flavor SU(3) symmetry, the vector dominance model and ideal mixing for the physical ω and ϕ mesons, permit relating the couplings between the hyperons and the vector mesons to the nucleon couplings $g_{\omega N}$ and $g_{\rho N}$ (Schaffner & Mishustin, 1996; Banik et al., 2014; Miyatsu et al., 2013; Weissenborn et al., 2012; Colucci & Sedrakian, 2013; Tolos et al., 2017), according to the ratios

$$\begin{aligned} g_{\omega \Lambda} : g_{\omega \Sigma} : g_{\omega N} &= \frac{2}{3} : \frac{2}{3} : \frac{1}{3} : 1 \\ g_{\rho \Lambda} : g_{\rho \Sigma} : g_{\rho \Xi} : g_{\rho N} &= 0 : 1 : 1 : 1 \\ g_{\phi \Lambda} : g_{\phi \Sigma} : g_{\phi \Xi} : g_{\phi N} &= -\frac{\sqrt{2}}{3} : -\frac{\sqrt{2}}{3} : -\frac{2\sqrt{2}}{3} : 1, \end{aligned} \quad (15)$$

and noting that $g_{\phi N} = 0$. We reduce by 20% the coupling of the Λ hyperon to the ϕ meson in order to obtain a $\Lambda\Lambda$ bond energy in Λ matter at a density $n_\Lambda \simeq n_0/5$ of $\Delta B_{\Lambda\Lambda}(n_0/5) = 0.67$ MeV, thereby reproducing the value extracted from the $^6_{\Lambda\Lambda}\text{He}$ double Λ hypernucleus, also known as the Nagara event (Takahashi et al., 2001; Ahn et al., 2013).

The coupling of each hyperon to the scalar σ meson field is left as a free parameter to be adjusted to reproduce the hyperon potential in SNM, derived from hypernuclear data. It is well known that a Woods-Saxon type potential of depth $U_\Lambda^{(N)}(n_0) \sim -28$ MeV reproduces the bulk of Λ hypernuclei binding energies (Millener et al., 1988). As for the Σ hyperon, a moderate repulsive potential could be extracted from analyses of (π^-, K^+) reactions off nuclei (Noumi et al., 2002) done in (Harada & Hirabayashi, 2006; Kohno et al., 2006). Fits to Σ^- atomic data (Friedman & Gal, 2007) also point towards a transition from an attractive Σ -nucleus potential at the surface to a repulsive one inside the nucleus, the size of the repulsion not being well determined. The potential felt by a Ξ hyperon in SNM is also quite uncertain. Old emulsion data indicate sizable attractive values of around $U_\Xi^{(N)}(n_0) = -24 \pm 4$ MeV (Dover & Gal, 1983), while the analyses of the (K^-, K^+) reaction on a ^{12}C target suggest a milder attraction (Fukuda et al., 1998;

Khaustov et al., 2000). Taking these experimental uncertainties into account, we allow the hyperon potentials in SNM to take the following range of values:

$$\begin{aligned} U_\Lambda^{(N)}(n_0) &= -28 \text{ MeV} \\ U_\Sigma^{(N)}(n_0) &= 0 \text{ to } 30 \text{ MeV} \\ U_\Xi^{(N)}(n_0) &= -18 \text{ to } 0 \text{ MeV}, \end{aligned} \quad (16)$$

Note that we only consider uncertainties for the Σ and Ξ potentials, given the consensus on the Λ potential at saturation. The range of values for the hyperon potentials in SNM give rise to the following range for the hyperon- σ couplings:

$$\begin{aligned} g_{\sigma \Lambda}/g_{\sigma N} &= 0.611 \\ g_{\sigma \Sigma}/g_{\sigma N} &= 0.467 - 0.541 \\ g_{\sigma \Xi}/g_{\sigma N} &= 0.271 - 0.316, \end{aligned} \quad (17)$$

where the lower values correspond to the most repulsive situation ($U_\Sigma^{(N)}(n_0) = 30$ MeV, $U_\Xi^{(N)}(n_0) = 0$ MeV) and the upper ones to the most attractive one ($U_\Sigma^{(N)}(n_0) = 0$ MeV, $U_\Xi^{(N)}(n_0) = -18$ MeV). In our baseline FSU2H model used in the calculations of Sec. 4 we have adopted the values $U_\Lambda^{(N)}(n_0) = -28$ MeV, $U_\Sigma^{(N)}(n_0) = 30$ MeV and $U_\Xi^{(N)}(n_0) = -18$ MeV, which lead to the couplings $g_{\sigma \Lambda} = 0.611 g_{\sigma N}$, $g_{\sigma \Sigma} = 0.467 g_{\sigma N}$ and $g_{\sigma \Xi} = 0.316 g_{\sigma N}$.

The hyperon potentials are shown, as functions of the nuclear density, in Fig. 3. The left panel shows the potentials for isospin SNM, while the right panel corresponds to PNM, which is closer to the conditions of beta stable neutron star matter, where differences between the potentials for the different members of the same isospin multiplet can be seen. In order not to overcrowd the figure we have omitted the potentials of the positively charged hyperons, as they do not appear in the beta stable neutron star matter configurations appropriate for the present study. The coloured bands enclose the dispersion of results obtained employing the hyperon- σ coupling ranges displayed in Eq. (17). The range of couplings has been determined from the uncertainties of the hypernuclear data and, strictly speaking, corresponds to normal nuclear matter density, n_0 . However, the coupling constants are density independent in our model and we can then obtain a range of values for the potential at any density. Specially important are the potentials around $2n_0$ and beyond, which is the region of densities where hyperons are present in the models explored here (Tolos et al., 2017). As can be seen from the figure, the range of values for the hyperon potentials at $2n_0$ in PNM are the following: $U_\Lambda^{(N)}(2n_0) = 4$ MeV, $U_\Sigma^{(N)}(2n_0) = 84$ to 130 MeV, $U_{\Sigma^0}^{(N)}(2n_0) = 47$ to 93 MeV, $U_{\Xi^-}^{(N)}(2n_0) = 14$ to 42 MeV and $U_{\Xi^0}^{(N)}(2n_0) = -22$ to 5 MeV. We note that this range of values will strongly affect the composition of the neutron star, as we will show at the end of this section.

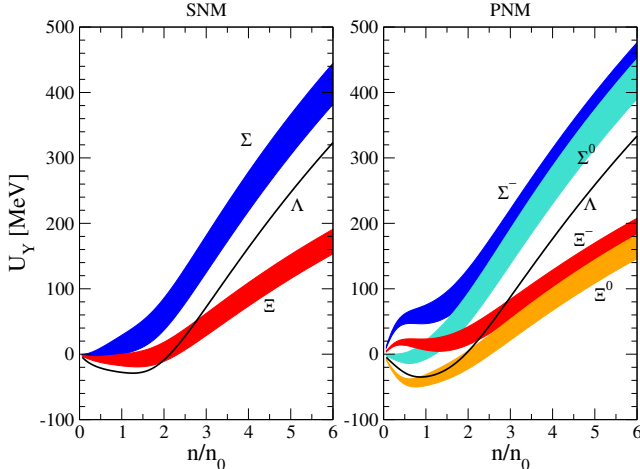


Figure 3. Hyperon single-particle potentials of our RMF models, as functions of the nuclear density, in the case of isospin SNM (left panel) and PNM (right panel). The bands result from varying the hyperon- σ couplings within the values given in Eq. (17) to account for the experimental uncertainties of the hyperon potentials derived from hypernuclear data.

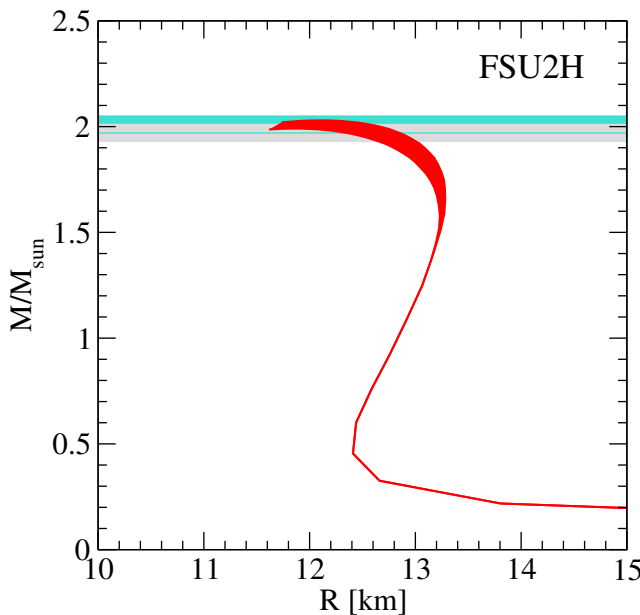


Figure 4. Mass versus radius for neutron stars from the FSU2H model. The band results from varying the hyperon- σ couplings within the values given in Eq. (17) to account for the experimental uncertainties of the hyperon potentials derived from hypernuclear data.

In Fig. 4 we show the mass-radius relation for neutron stars obtained with the FSU2H model. The band collects the results obtained varying the hyperon couplings to the σ meson within the ranges in Eq. (17), which produce maximum masses that differ by at most $0.1M_\odot$. This is a small effect, as it is obvious that the hyperon potentials at nuclear densities of around $6n_0$ in

the center of $2M_\odot$ stars (see Table 3) suffer a much larger uncertainty than the one we extrapolated from the normal nuclear densities characteristic of hypernuclear data. Indeed, the uncertainties tied to our lack of knowledge of the hyperon-nucleon and hyperon-hyperon interactions around the hyperon onset density of $\sim 2n_0$ and beyond have often been exploited to build up RMF models that produce hyperonic neutron stars with maximum masses larger than $2M_\odot$ (Weissenborn et al., 2012; Bednarek et al., 2012; van Dalen et al., 2014; Oertel et al., 2015; Fortin et al., 2017). As can be seen in the extensive analyses of various models in (Fortin et al., 2015), the maximum masses turn out to be within a $0.3M_\odot$ band. It is therefore clear that determining the hyperon interactions at higher densities, as could be done from the analysis of HIC experiments (Morita et al., 2015), would help constraining the models in the appropriate regimes found in neutron stars.

Let us finish this section by showing, in Fig. 5, the particle fractions as functions of the baryonic density, for the FSU2H model (lower panel), where the coloured bands are obtained for the range of hyperon- σ couplings employed in this work. For completeness, we also show the particle fractions for the nucleonic FSU2R model in the upper panel, where we can see that the absence of negatively charged hyperons maintains a constant population of electrons and muons, and hence of protons and neutrons, already from slightly above $2n_0$. As for the FSU2H model, we note that all the particle fractions are affected by the hypernuclear data uncertainties, even if these are encoded only in the Σ and Ξ couplings to the σ meson. Upon inspecting the range of densities where hyperons may be present, we see that, although one can generally conclude that hyperons appear around $2n_0$, the order of appearance of each species is not determined, owing to the uncertainties derived from hypernuclear data. The first hyperon to appear can be either a Λ or a Σ^- , the latter case only in the less repulsive situation allowed by data, namely when $U_\Sigma^{(N)}(n_0) \simeq 0$ MeV. In fact, when the Σ feels its most repulsive potential value, it can even appear after the Ξ^- hyperon. This happens when the Ξ potential value is on the most attractive side of the allowed region, namely $U_\Xi^{(N)}(n_0) = -18$ MeV. However, if one decreases the amount of attraction, as data permits, the Ξ^- onset density is rapidly pushed towards larger values, even beyond the maximum density of $6n_0$ represented in the figure, which stands as a representative central density of hyperonic stars. Summarizing, although hyperons are present in the interior of neutron stars modeled by the FSU2H interaction, the lack of precise knowledge on the hyperon-nuclear interactions prevents one from establishing the specific hyperonic composition in the interior of the star.

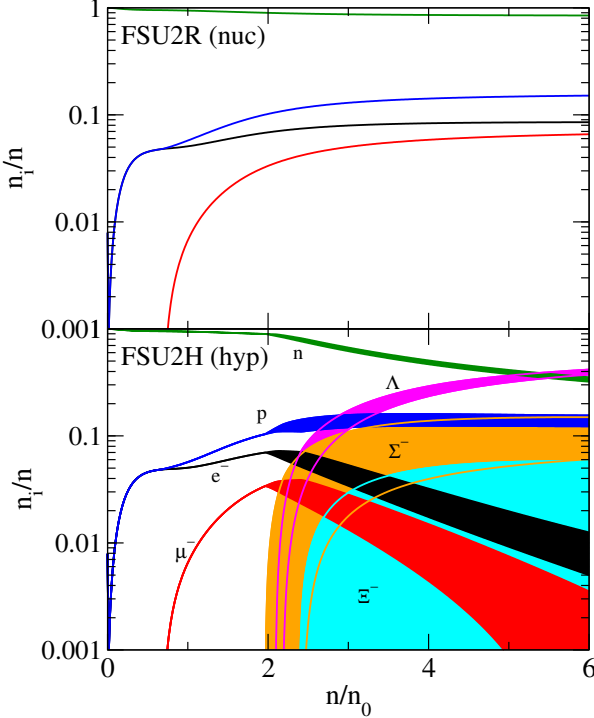


Figure 5. Particle fractions as functions of the baryonic density for the nucleonic FSU2R model (upper panel) and the hyperonic FSU2H model (lower panel). The bands in the lower panel result from varying the hyperon- σ couplings within the values given in Eq. (17) to account for the experimental uncertainties of the hyperon potentials derived from hypernuclear data. The coloured lines guide the eye to help distinguishing each case properly in the regions of overlapping bands.

6 SUMMARY

We have reinvestigated our previous results on the equation of state for the nucleonic and hyperonic inner core of neutron stars (Tolos et al., 2017), that fullfill the $2M_\odot$ observations (Demorest et al., 2010; Antoniadis et al., 2013) and the recent determinations of radii below 13 km region (Guillot et al., 2013; Lattimer & Steiner, 2014a; Heinke et al., 2014; Guillot & Rutledge, 2014; Ozel et al., 2016; Lattimer & Prakash, 2016), as well as the saturation properties of nuclear matter and finite nuclei (Tsang et al., 2012; Chen & Piekarewicz, 2014) and the constraints extracted from HICs (Danielewicz et al., 2002; Fuchs et al., 2001; Lynch et al., 2009). The two models formulated in (Tolos et al., 2017), the FSU2R (with nucleons) and FSU2H (with nucleons and hyperons) models, have been updated by improving the behavior of PNM at subsaturation densities. Above saturation density, the updated models and those of (Tolos et al., 2017) are very similar.

Using these updated interactions, we have obtained values for the PNM pressure at saturation density of 2.44 MeV fm $^{-3}$ in FSU2R and of 2.30 MeV fm $^{-3}$ in FSU2H, that are consistent with the estimates from

chiral forces (Fortin et al., 2015; Hagen et al., 2015). The symmetry energy and its slope at saturation become $E_{\text{sym}}(n_0) = 30.7$ MeV and $L = 46.9$ MeV in FSU2R and $E_{\text{sym}}(n_0) = 30.5$ MeV and $L = 44.5$ MeV in FSU2H, thus being in good agreement with several recent estimates based on terrestrial experiments, different astrophysical observations, and theoretical calculations (Li & Han, 2013; Lattimer & Lim, 2013; Roca-Maza et al., 2015; Hagen et al., 2015; Oertel et al., 2017; Birkhan et al., 2017). Furthermore, the reviewed FSU2R and FSU2H models predict a neutron skin thickness of 0.15 fm in ^{208}Pb and of 0.166 fm in ^{48}Ca , which turn out to be compatible with previous experimental and theoretical determinations (Roca-Maza et al., 2015; Tarbert et al., 2014; Abrahamyan et al., 2012; Horowitz et al., 2012; Hagen et al., 2015; Birkhan et al., 2017).

With regards to the mass and radius of neutron stars, radii below 13 km can be achieved because of the softening of the symmetry energy around saturation density whereas, at the same time, $2M_\odot$ stars can be obtained as the pressure of the high-density EoS is hard enough. These results are not drastically changed when using the updated FSU2R and FSU2H interactions as compared to the previous versions in Ref. (Tolos et al., 2017), because of the similar EoSs produced above saturation density. The numerical tabulations of the EoS and of the M-R relation from the models FSU2R ($npe\mu$ matter) and FSU2H ($npYe\mu$ matter) as a function of the number density n/n_0 are shown in Tables 4 and 5 for completeness.

However, the mass and composition of neutron stars might be strongly affected due to the uncertainties of the hyperon-nucleon couplings. The values of the hyperon couplings are determined from SU(3) flavor symmetry and from the available experimental information on hypernuclei, in particular by fitting to the optical potential of hyperons extracted from the data. The coupling of each hyperon to the σ meson field is left as a free parameter to be adjusted to reproduce the hyperon potential in SNM within the experimental uncertainties. As a result, we have found that the onset of appearance of the different hyperons strongly depends on the hyperon-nuclear uncertainties, whereas the maximum masses differ by at most $0.1 M_\odot$, thus being less sensitive to the changes on the hyperon-nucleon couplings. This latter conclusion has to be taken with care, though, since the hyperon potentials at densities in the center of $2M_\odot$ stars suffer much larger uncertainties than the ones we have extrapolated from hypernuclear data at saturation. Hence, a greater dispersion of values for the maximum mass might be expected. The progress in the characterization of hyperon-nucleon interactions in dense matter derived from chiral effective forces (Haidenbauer et al., 2017), on the theoretical front, and from studies of HICs (Morita et al., 2015), on the experimental front, should contribute greatly to narrow down these uncertainties.

7 ACKNOWLEDGEMENTS

L.T. acknowledges support from the Ramón y Cajal research programme, FPA2013-43425-P and FPA2016-81114-P Grants from Ministerio de Economía y Competitividad (MINECO) and NewCompstar COST Action MP1304. M.C. and A.R. acknowledge support from Grant No. FIS2014-54672-P from MINECO, Grant No. 2014SGR-401 from Generalitat de Catalunya, and the project MDM-2014-0369 of ICCUB (Unidad de Excelencia María de Maeztu) from MINECO. L.T. and A.R. acknowledge support from the Spanish Excellence Network on Hadronic Physics FIS2014-57026-REDT from MINECO.

REFERENCES

- Abrahamyan *et al.* S., 2012, *Phys. Rev. Lett.*, 108, 112502
- Ahn J. K., et al., 2013, *Phys. Rev.* C88, 014003
- Alex Brown B., 2000, *Phys. Rev. Lett.*, 85, 5296
- Ambartsumyan V. A., Saakyan G. S., 1960, Sov. Astron., 4, 187
- Antoniadis J., et al., 2013, *Science*, 340, 6131
- Arzoumanian Z., et al., 2014, in Space Telescopes and Instrumentation 2014: Ultraviolet to Gamma Ray. p. 914420, doi:10.1117/12.2056811
- Banik S., Hempel M., Bandyopadhyay D., 2014, *Astrophys. J. Suppl.*, 214, 22
- Bauswein A., Janka H. T., 2012, *Phys. Rev. Lett.*, 108, 011101
- Baym G., Pethick C., Sutherland P., 1971a, *Astrophys. J.*, 170, 299
- Baym G., Bethe H. A., Pethick C., 1971b, *Nucl. Phys.* A175, 225
- Bednarek I., Haensel P., Zdunik J. L., Bejger M., Manka R., 2012, *Astron. Astrophys.*, 543, A157
- Bennett M. F., van Eysden C. A., Melatos A., 2010, *Mon. Not. Roy. Astron. Soc.*, 409, 1705
- Birkhan J., et al., 2017, *Phys. Rev. Lett.*, 118, 252501
- Bodmer A. R., 1991, *Nucl. Phys.* A526, 703
- Bogdanov S., 2013, *Astrophys. J.*, 762, 96
- Boguta J., Bodmer A. R., 1977, *Nucl. Phys.* A292, 413
- Boguta J., Stoecker H., 1983, *Phys. Lett.*, B120, 289
- Chatterjee D., Vidana I., 2016, *Eur. Phys. J.* A52, 29
- Chen W.-C., Piekarewicz J., 2014, *Phys. Rev.* C90, 044305
- Chen W.-C., Piekarewicz J., 2015a, *Phys. Rev. Lett.*, 115, 161101
- Chen W.-C., Piekarewicz J., 2015b, *Phys. Lett.*, B748, 284
- Colucci G., Sedrakian A., 2013, *Phys. Rev.* C87, 055806
- Danielewicz P., Lacey R., Lynch W. G., 2002, *Science*, 298, 1592
- Demorest P., Pennucci T., Ransom S., Roberts M., Hessels J., 2010, *Nature*, 467, 1081
- Dexheimer V., Negreiros R., Schramm S., 2015, *Phys. Rev.* C92, 012801
- Dobaczewski J., Nazarewicz W., Reinhard P. G., 2014, *J. Phys.* G41, 074001
- Dover C. B., Gal A., 1983, *Annals Phys.*, 146, 309
- Fortin M., Zdunik J. L., Haensel P., Bejger M., 2015, *Astron. Astrophys.*, 576, A68
- Fortin M., Avancini S. S., Providênciâ C., Vidaña I., 2017, *Phys. Rev.* C95, 065803
- Friedman E., Gal A., 2007, *Phys. Rept.*, 452, 89
- Fuchs C., Faessler A., Zabrodin E., Zheng Y.-M., 2001, *Phys. Rev. Lett.*, 86, 1974
- Fukuda T., et al., 1998, *Phys. Rev.* C58, 1306
- Gandolfi S., Carlson J., Reddy S., 2012, *Phys. Rev.* C85, 032801
- Glendenning N. K., 1982, *Phys. Lett.*, B114, 392
- Glendenning N. K., 2000, Compact stars: Nuclear physics, particle physics, and general relativity, 2 edn. Springer, New York
- Guillot S., Rutledge R. E., 2014, *Astrophys. J.*, 796, L3
- Guillot S., Servillat M., Webb N. A., Rutledge R. E., 2013, *Astrophys. J.*, 772, 7
- Guver T., Ozel F., 2013, *Astrophys. J.*, 765, L1
- Haensel P., Potekhin A. Y., Yakovlev D. G., 2006, Neutron Stars 1: Equation of State and Structure. Springer, New York
- Hagen G., et al., 2015, *Nature Phys.*, 12, 186
- Haidenbauer J., Meißner U. G., Kaiser N., Weise W., 2017, *Eur. Phys. J.*, A53, 121
- Harada T., Hirabayashi Y., 2006, *Nucl. Phys.* A767, 206
- Hebeler K., Lattimer J. M., Pethick C. J., Schwenk A., 2013, *Astrophys. J.*, 773, 11
- Heinke C. O., et al., 2014, *Mon. Not. Roy. Astron. Soc.*, 444, 443
- Horowitz C. J., Piekarewicz J., 2001a, *Phys. Rev. Lett.*, 86, 5647
- Horowitz C. J., Piekarewicz J., 2001b, *Phys. Rev.* C64, 062802
- Horowitz C. J., et al., 2012, *Phys. Rev.* C85, 032501
- Hulse R. A., Taylor J. H., 1975, *Astrophys. J.*, 195, L51
- Jiang W.-Z., Li B.-A., Fattoyev F. J., 2015, *Eur. Phys. J.* A51, 119
- Khaustov P., et al., 2000, *Phys. Rev.* C61, 054603
- Kohno M., Fujiwara Y., Watanabe Y., Ogata K., Kawai M., 2006, *Phys. Rev.* C74, 064613
- Lackey B. D., Wade L., 2015, *Phys. Rev.* D91, 043002
- Lattimer J. M., Lim Y., 2013, *Astrophys. J.*, 771, 51
- Lattimer J. M., Prakash M., 2004, *Science*, 304, 536
- Lattimer J. M., Prakash M., 2007, *Phys. Rept.*, 442, 109
- Lattimer J. M., Prakash M., 2016, *Phys. Rept.*, 621, 127
- Lattimer J. M., Steiner A. W., 2014a, *Astrophys. J.*, 784, 123
- Lattimer J. M., Steiner A. W., 2014b, *Eur. Phys. J.*

- A50, 40
- Lattimer J. M., Swesty D. F., 1991, *Nuclear Physics A*, 535, 331
- Li B.-A., Han X., 2013, *Phys. Lett.*, B727, 276
- Li B.-A., Ramos A., Verde G., Vidana I., 2014, *Eur. Phys. J.*, A50, 9
- Lynch W. G., Tsang M. B., Zhang Y., Danielewicz P., Famiano M., Li Z., Steiner A. W., 2009, *Prog. Part. Nucl. Phys.*, 62, 427
- Millener D. J., Dover C. B., Gal A., 1988, *Phys. Rev.*, C38, 2700
- Miyatsu T., Yamamoto S., Nakazato K., 2013, *Astrophys. J.*, 777, 4
- Morita K., Furumoto T., Ohnishi A., 2015, *Phys. Rev.*, C91, 024916
- Mueller H., Serot B. D., 1996, *Nucl. Phys.*, A606, 508
- Nätilä J., Steiner A. W., Kajava J. J. E., Suleimanov V. F., Poutanen J., 2016, *Astron. Astrophys.*, 591, A25
- Noumi H., et al., 2002, *Phys. Rev. Lett.*, 89, 072301
- Oertel M., Providencia C., Gulminelli F., Raduta A. R., 2015, *J. Phys.*, G42, 075202
- Oertel M., Hempel M., Klähn T., Typel S., 2017, *Rev. Mod. Phys.*, 89, 015007
- Oppenheimer J. R., Volkoff G. M., 1939, *Phys. Rev.*, 55, 374
- Ozel F., Freire P., 2016, *Annu. Rev. Astron. Astrophys.*, 54, 401
- Ozel F., Psaltis D., 2015, *Astrophys. J.*, 810, 135
- Ozel F., Baym G., Guver T., 2010, *Phys. Rev.*, D82, 101301
- Ozel F., Psaltis D., Guver T., Baym G., Heinke C., Guillot S., 2016, *Astrophys. J.*, 820, 28
- Poutanen J., Nattila J., Kajava J. J. E., Latvala O.-M., Galloway D., Kuulkers E., Suleimanov V., 2014, *Mon. Not. Roy. Astron. Soc.*, 442, 3777
- Raihel C. A., Ozel F., Psaltis D., 2016, *Astrophys. J.*, 831, 44
- Roca-Maza X., Viñas X., Centelles M., Agrawal B. K., Colo' G., Paar N., Piekarewicz J., Vretenar D., 2015, *Phys. Rev.*, C92, 064304
- Russotto P., et al., 2016, *Phys. Rev.*, C94, 034608
- Schaffner J., Mishustin I. N., 1996, *Phys. Rev.*, C53, 1416
- Serot B. D., Walecka J. D., 1986, *Adv. Nucl. Phys.*, 16, 1
- Serot B. D., Walecka J. D., 1997, *Int. J. Mod. Phys.*, E6, 515
- Shapiro S. L., Teukolsky S. A., 1983, Black holes, white dwarfs, and neutron stars: The physics of compact objects. Wiley-Interscience, New York
- Sharma B. K., Centelles M., Viñas X., Baldo M., Burgio G. F., 2015, *Astron. Astrophys.*, 584, A103
- Shen H., Toki H., Oyamatsu K., Sumiyoshi K., 1998, *Nucl. Phys.*, A637, 435
- Steiner A. W., Lattimer J. M., Brown E. F., 2013, *Astrophys. J.*, 765, L5
- Suleimanov V., Poutanen J., Revnivtsev M., Werner K., 2011, *Astrophys. J.*, 742, 122
- Takahashi H., et al., 2001, *Phys. Rev. Lett.*, 87, 212502
- Tarbert C. M., et al., 2014, *Phys. Rev. Lett.*, 112, 242502
- Tolos L., Centelles M., Ramos A., 2017, *Astrophys. J.*, 834, 3
- Tsang M. B., et al., 2012, *Phys. Rev.*, C86, 015803
- Verbiest J. P. W., et al., 2008, *Astrophys. J.*, 679, 675
- Watts A. L., et al., 2016, *Rev. Mod. Phys.*, 88, 021001
- Weissenborn S., Chatterjee D., Schaffner-Bielich J., 2012, *Phys. Rev.*, C85, 065802
- van Dalen E. N. E., Colucci G., Sedrakian A., 2014, *Phys. Lett.*, B734, 383

APPENDIX

For ease of use, in this appendix we provide in tabular form the results for the EoS and the M-R relation calculated with the FSU2R and FSU2H models discussed in the text.

Table 4 Numerical data of the EoS for the core of neutron stars and of the M-R relation from the models FSU2R ($npe\mu$ matter) and FSU2H ($npYe\mu$ matter), as a function of the number density n/n_0 (with $n_0 = 0.1505 \text{ fm}^{-3}$, cf. Table 2). The pressure P and mass-energy density ε are in MeV fm $^{-3}$, while the neutron star radius R and mass M are in km and M_\odot units, respectively.

n/n_0	FSU2R model (nucleonic)				FSU2H model (hyperonic)			
	P	ε	R	M	P	ε	R	M
0.9	1.3737	128.98	28.701	0.10	1.2675	128.98	36.393	0.09
1.0	2.1255	143.50	17.229	0.15	2.0182	143.49	18.143	0.14
1.1	3.0982	158.11	14.256	0.21	3.0319	158.08	14.317	0.20
1.2	4.3089	172.82	13.129	0.27	4.3426	172.79	13.015	0.27
1.3	5.7741	187.63	12.660	0.35	5.9878	187.61	12.541	0.36
1.4	7.5095	202.58	12.482	0.43	8.0082	202.58	12.400	0.46
1.5	9.5289	217.65	12.428	0.52	10.445	217.70	12.416	0.57
1.6	11.844	232.87	12.440	0.61	13.340	233.00	12.509	0.68
1.7	14.462	248.24	12.498	0.70	16.725	248.50	12.638	0.81
1.8	17.389	263.78	12.553	0.79	20.626	264.21	12.764	0.93
1.9	20.626	279.49	12.618	0.88	25.058	280.16	12.885	1.06
2.0	24.171	295.37	12.680	0.97	30.022	296.35	13.004	1.18
2.1	28.019	311.44	12.739	1.06	35.510	312.80	13.099	1.30
2.2	32.162	327.70	12.774	1.14	41.504	329.52	13.175	1.41
2.3	36.592	344.16	12.813	1.22	46.755	346.51	13.233	1.49
2.4	41.297	360.81	12.829	1.29	51.366	363.71	13.255	1.56
2.5	46.266	377.67	12.844	1.36	55.951	381.10	13.274	1.61
2.6	51.487	394.73	12.851	1.42	60.285	398.67	13.282	1.66
2.7	56.947	411.99	12.854	1.48	64.452	416.40	13.284	1.69
2.8	62.634	429.47	12.843	1.53	68.763	434.29	13.272	1.73
2.9	68.536	447.14	12.830	1.58	73.242	452.33	13.269	1.76
3.0	74.642	465.03	12.816	1.63	77.898	470.53	13.239	1.78
3.1	80.941	483.12	12.792	1.67	82.732	488.89	13.224	1.81
3.2	87.421	501.42	12.763	1.71	87.745	507.41	13.194	1.83
3.3	94.075	519.92	12.734	1.74	92.934	526.09	13.161	1.85
3.4	100.89	538.63	12.702	1.77	98.299	544.93	13.134	1.87
3.5	107.87	557.54	12.669	1.80	103.84	563.93	13.093	1.89
3.6	114.99	576.66	12.633	1.83	109.55	583.09	13.058	1.90
3.7	122.25	595.97	12.603	1.85	115.42	602.41	13.016	1.92
3.8	129.64	615.48	12.566	1.87	121.46	621.89	12.982	1.93
3.9	137.16	635.18	12.521	1.89	127.66	641.53	12.935	1.94

Table 5 Continuation of Table 4.

n/n_0	FSU2R model (nucleonic)				FSU2H model (hyperonic)			
	P	ε	R	M	P	ε	R	M
4.0	144.80	655.08	12.479	1.91	134.02	661.33	12.886	1.95
4.1	152.56	675.18	12.442	1.93	140.53	681.30	12.842	1.96
4.2	160.44	695.46	12.400	1.94	147.19	701.42	12.804	1.97
4.3	168.41	715.93	12.359	1.96	154.00	721.71	12.756	1.98
4.4	176.49	736.59	12.323	1.97	160.96	742.15	12.703	1.99
4.5	184.67	757.44	12.280	1.98	168.06	762.76	12.662	1.99
4.6	192.95	778.46	12.235	1.99	175.30	783.52	12.613	2.00
4.7	201.32	799.67	12.196	2.00	182.67	804.45	12.571	2.00
4.8	209.77	821.06	12.155	2.01	190.18	825.53	12.523	2.01
4.9	218.31	842.62	12.124	2.01	197.81	846.77	12.476	2.01
5.0	226.94	864.36	12.074	2.02	205.58	868.16	12.427	2.01
5.1	235.64	886.27	12.035	2.02	213.47	889.72	12.383	2.02
5.2	244.43	908.36	11.996	2.03	221.48	911.42	12.339	2.02
5.3	253.28	930.61	11.963	2.03	229.62	933.29	12.293	2.02
5.4	262.22	953.03	11.921	2.04	237.87	955.31	12.252	2.02
5.5	271.22	975.62	11.886	2.04	246.24	977.48	12.208	2.02
5.6	280.30	998.37	11.852	2.04	254.72	999.81	12.166	2.02
5.7	289.44	1021.3	11.808	2.04	263.31	1022.3	12.120	2.02
5.8	298.65	1044.4	11.775	2.04	272.01	1044.9	12.078	2.02
5.9	307.93	1067.6	11.743	2.05	280.82	1067.7	12.038	2.02
6.0	317.26	1091.0	11.704	2.05	289.74	1090.6	11.997	2.02
6.1	326.67	1114.5	11.670	2.05	298.76	1113.7	11.952	2.02
6.2	336.13	1138.2	11.639	2.05	307.88	1136.9	11.920	2.02
6.3	345.65	1162.1	11.604	2.05	317.10	1160.3	11.872	2.02
6.4	355.23	1186.1	11.573	2.05	326.42	1183.8	11.833	2.02
6.5	364.87	1210.3	11.538	2.05	335.83	1207.5	11.793	2.02

Relativistic mean-field hadronic models under nuclear matter constraints

M. Dutra

Departamento de Física e Matemática-ICT, Universidade Federal Fluminense, 28895-532 Rio das Ostras, Rio de Janeiro, Brazil

O. Lourenço

Departamento de Ciências da Natureza, Matemática e Educação, CCA, Universidade Federal de São Carlos, 13600-970 Araras, São Paulo, Brazil

S. S. Avancini

Depto de Física-CFM-Universidade Federal de Santa Catarina, CP 476, 88040-900 Florianópolis, Santa Catarina, Brazil

B. V. Carlson

Departamento de Física, Instituto Tecnológico de Aeronáutica, CTA, 12228-900 São José dos Campos, São Paulo, Brazil

A. Delfino

Departamento de Física-Universidade Federal Fluminense, Avenida Litorânea s/n, 24210-150 Boa Viagem, Niterói, Rio de Janeiro, Brazil

D. P. Menezes

Depto de Física-Universidade Federal de Santa Catarina, CP 476, 88040-900 Florianópolis, Santa Catarina, Brazil

and Departamento de Física Aplicada, Universidad de Alicante, Apartado Correus 99, E-03080 Alicante, Spain

C. Providênci

Centro de Física Computacional, Department of Physics, University of Coimbra, P-3004-516 Coimbra, Portugal

S. Typel

GSI Helmholtzzentrum für Schwerionenforschung GmbH, Theorie, Planckstrasse 1, D-64291 Darmstadt, Germany

J. R. Stone

Oxford Physics, University of Oxford, OX1 3PU Oxford, United Kingdom

and Department of Physics and Astronomy, University of Tennessee, Knoxville, Tennessee 37996, USA

(Received 14 May 2014; revised manuscript received 26 September 2014; published 10 November 2014)

Background: The microscopic composition and properties of infinite hadronic matter at a wide range of densities and temperatures have been subjects of intense investigation for decades. The equation of state (EoS) relating pressure, energy density, and temperature at a given particle number density is essential for modeling compact astrophysical objects such as neutron stars, core-collapse supernovae, and related phenomena, including the creation of chemical elements in the universe. The EoS depends not only on the particles present in the matter, but, more importantly, also on the forces acting among them. Because a realistic and quantitative description of infinite hadronic matter and nuclei from first principles is not available at present, a large variety of phenomenological models has been developed in the past several decades, but the scarcity of experimental and observational data does not allow a unique determination of the adjustable parameters.

Purpose: It is essential for further development of the field to determine the most realistic parameter sets and to use them consistently. Recently, a set of constraints on properties of nuclear matter was formed and the performance of 240 nonrelativistic Skyrme parametrizations was assessed [M. Dutra *et al.*, Phys. Rev. C **85**, 035201 (2012)] in describing nuclear matter up to about three times nuclear saturation density. In the present work we examine 263 relativistic-mean-field (RMF) models in a comparable approach. These models have been widely used because of several important aspects not always present in nonrelativistic models, such as intrinsic Lorentz covariance, automatic inclusion of spin, appropriate saturation mechanism for nuclear matter, causality, and, therefore, no problems related to superluminal speed of sound in medium.

Method: Three different sets of constraints related to symmetric nuclear matter, pure neutron matter, symmetry energy, and its derivatives were used. The first set (SET1) was the same as used in assessing the Skyrme parametrizations. The second and third sets (SET2a and SET2b) were more suitable for analysis of RMF and included, up-to-date theoretical, experimental and empirical information.

Results: The sets of updated constraints (SET2a and SET2b) differed somewhat in the level of restriction but still yielded only 4 and 3 approved RMF models, respectively. A similarly small number of approved Skyrme parametrizations were found in the previous study with Skyrme models. An interesting feature of our analysis

has been that the results change dramatically if the constraint on the volume part of the isospin incompressibility ($K_{\tau,v}$) is eliminated. In this case, we have 35 approved models in SET2a and 30 in SET2b.

Conclusions: Our work provides a new insight into application of RMF models to properties of nuclear matter and brings into focus their problematic proliferation. The assessment performed in this work should be used in future applications of RMF models. Moreover, the most extensive set of refined constraints (including nuclear matter and finite-nuclei-related properties) should be used in future determinations of new parameter sets to provide models that can be used with more confidence in a wide range of applications. Pointing to reasons for the many failures, even of the frequently used models, should lead to their improvement and to the identification of possible missing physics not included in present energy density functionals.

DOI: [10.1103/PhysRevC.90.055203](https://doi.org/10.1103/PhysRevC.90.055203)

PACS number(s): 21.30.Fe, 21.65.Cd, 21.65.Ef, 26.60.Kp

I. INTRODUCTION

The theoretical description of infinite nuclear matter and finite nuclear properties has been relying on models since the primordial developments of nuclear physics. Unfortunately, so far there are neither a specific nuclear physics theory nor enough adequate solutions for QCD, which is still in the early stages of lattice calculations. Many models have been developed since the beginning of the past century, from the famous semiempirical Bethe-Weizsäcker mass formula proposed in 1935 [1], to nonrelativistic Skyrme models [2,3] that first appeared around 1950, to relativistic quantum hadrodynamics (QHD) models [4] developed after 1974, to which we devote our attention in the present work.

All relativistic models are written in terms of parameters that are fitted to reproduce either bulk nuclear matter or finite nuclei properties. This means that most models behave approximately the same as far as equations of state are concerned around saturation density and at zero temperature. Nevertheless, these very same models have been used to describe physics taking place at subsaturation densities, such as liquid-gas phase transitions, and also at very high densities, such as neutron-star matter. As a consequence, models that describe similar physics at saturation density yield very different results when used in the low- or high-density limits. The same holds true if finite systems are investigated. We devote the next section to the mean field-approximation usually employed when relativistic models are considered and to seven different types of parametrizations of QHD *Walecka-type* models. In these models, the baryons interact among each other by exchanging scalar-isoscalar (σ) and vector-isoscalar (ω) mesons. For our analyses of nuclear matter properties, only nucleons are necessary as hadronic degrees of freedom. When the models are extended to describe stellar matter, hyperons are generally also included. More sophisticated versions include vector-isovector (ρ) and vector-isoscalar (δ) mesons. The seven variations we treat next are (1) the original linear Walecka model, (2) the nonlinear Walecka model with σ self-interacting mesons, (3) the nonlinear Walecka model with σ and ω self-interacting mesons, (4) the nonlinear Walecka model with σ and ω self-interacting mesons and possible mesonic cross terms, (5) models in which the parameters that couple the baryons with the mesons are density dependent, (6) point-coupling models, in which the baryons only interact with each other through effective pointlike interactions, without exchanging mesons, and (7) models with the inclusion of δ

mesons. Details about the Lagrangian density, equations of motion, and equations of state for each of the seven model types are given in the next section.

In a previous work [5], 240 different Skyrme model parametrizations were confronted with experimentally and empirically derived constraints and only 16 of them were shown to satisfy all of the constraints. The authors argue that the production of new parameter sets with a limited range of application should not be encouraged. In the present work our aim is to obtain the physical properties related to the same derived constraints used in Ref. [5] with 263 relativistic models belonging to one of the seven classes mentioned above and check whether they satisfy these constraints.

A few words on our choice of constraints are now in order. We start with the isospin symmetric nuclear matter incompressibility (or compression modulus) K_0 , the one most used to constrain mean-field models. The incompressibility values have been inferred from experiment and from theory. Experimentally, results coming from giant resonances, mainly isoscalar giant monopole resonance (GMR) [6] and isovector giant dipole resonance (GDR) [7] have been used as an important source of information. Theoretically, efforts to obtain values for the incompressibility started with the use of the Hartree-Fock plus random-phase approximation (RPA) [8] and continued to other calculations involving even more sophisticated treatments. The developments of these calculations can be tracked from many papers, but we mention specifically Refs. [9,10]. In the present paper, we follow the suggestions given in Refs. [11,12] for the value of $K_0 = 230 \pm 40$ MeV.

Our second and third most important constraints are the symmetry energy (J) and its slope (L_0) at the saturation density. The density dependence of the symmetry energy carries information about the isospin dependence of nuclear forces and gives interesting hints on both finite nuclei and neutron-star properties. Experimental data for the symmetry energy come from various sources, namely heavy-ion collisions [13], pygmy dipole resonances [14,15], and isobaric analog states [16], besides GMR and GDR. In Ref. [17], the authors have shown that a direct correlation between the neutron skin thickness (controlled by the density dependence of the symmetry energy) and the neutron-star radii exists, such that models that yield smaller neutron skins in heavy nuclei generate smaller neutron-star radii. Recent reviews on this subject can be found in Refs. [18,19] and a comprehensive study of the imprint of the symmetry energy on the crust

and strangeness content of neutron star can be seen in Ref. [20]. Moreover, in Refs. [21,22], a correlation between the values of the incompressibility and the symmetry energy was proposed based on the fact that the isoscalar giant monopole resonance (ISGMR) and isovector giant dipole resonance (IVGDR) of ^{208}Pb were sensitive to both the incompressibility and the symmetry energy owing to its isospin asymmetry. Therefore, the author claims that the ISGMR data from a nucleus with a well-developed breathing mode but a small neutron-proton asymmetry such as ^{90}Zr should be used to fix the incompressibility at saturation instead of a nucleus with a non-negligible isospin asymmetry like ^{208}Pb . Once the incompressibility at saturation is fixed, the IVGDR ^{208}Pb may be used to constrain the symmetry energy. Although not conclusive, there seems to exist a correlation among the values of J , L_0 , and the curvature (K_{sym}^0) of the symmetry energy at the saturation density [23–25], and we tackle this point later.

Another constraint that we intend to use is the volume part of the isospin incompressibility, known as $K_{\tau,v}$, which depends on several liquid drop model quantities. When it is extracted from a simple fitting to GMR data, it includes not only volume, but also surface contributions. According to isospin diffusion calculations [26], it should be $K_{\tau} = -500 \pm 50$ MeV. According to neutron skin thickness [27], $K_{\tau} = -500^{+125}_{-100}$ MeV, and according to GMR measured in Sn isotopes [28], $K_{\tau} = -550 \pm 100$ MeV. To take into account all these uncertainties, we have chosen $K_{\tau} = -550 \pm 150$ MeV.

The other constraints are obtained directly from the equation of state or are related to the constraints mentioned above and we add more comments after they are defined.

We note that we consider here only systems made of nucleons at zero temperature. Relativistic models are also used to describe systems at higher densities, including heavy baryons (hyperons) (see, e.g., [29]), and at finite temperatures, important in modeling of high-density matter in protoneutron stars and core-collapse supernovae, which we examine in a separate study.

Our paper is organized as follows. In Sec. II we present the basic equations that define the relativistic mean-field models we have chosen to analyze, such as the Lagrangian densities and their related equations of state. Our results and discussions, including the sets of constraints with which the models are confronted, are shown in Sec. III and we draw the conclusions in Sec. IV.

II. RELATIVISTIC MEAN-FIELD MODELS AT ZERO TEMPERATURE

Relativistic mean-field (RMF) models have been widely used to describe infinite nuclear matter (INM), finite nuclei, and stellar matter properties. The main representative of such kinds of models, the Walecka model, QHD, or linear Walecka model, as it is also known, proposed in 1974 [4], treats protons and neutrons as fundamental particles interacting with each other through the exchange of scalar and vector mesons. The σ and ω fields represent, respectively, these mesons and mimic the attractive and repulsive parts of the nuclear interaction.

The two free parameters of the Walecka model, i.e., the couplings between the fields and the nucleons, are fitted to

reproduce well-established properties of INM, namely, the binding energy ($E_0 \sim 16$ MeV) and the saturation density ($\rho_0 \sim 0.15 \text{ fm}^{-3}$). However, it does not give reasonable values for the incompressibility (K_0), and nucleon effective mass (M^*), both related to symmetric nuclear matter (SNM). This problem was circumvented by Boguta and Bodmer [30], who added to the Walecka model cubic and quartic self-interactions in the scalar field σ , introducing, consequently, two more free parameters, which are fitted so as to fix the values of K_0 and M^* . In the same way, more terms can be added to the Boguta-Bodmer model to make it compatible with other observables, such as those related to finite nuclei. Actually, many RMF models and parametrizations have been constructed following this method. In our work, we take into account a more general nonlinear finite-range RMF model, by considering it to be represented by the Lagrangian density,

$$\mathcal{L}_{\text{NL}} = \mathcal{L}_{\text{nm}} + \mathcal{L}_{\sigma} + \mathcal{L}_{\omega} + \mathcal{L}_{\rho} + \mathcal{L}_{\delta} + \mathcal{L}_{\sigma\omega\rho} \quad (1)$$

where

$$\mathcal{L}_{\text{nm}} = \bar{\psi}(i\gamma^{\mu}\partial_{\mu} - M)\psi + g_{\sigma}\sigma\bar{\psi}\psi - g_{\omega}\bar{\psi}\gamma^{\mu}\omega_{\mu}\psi - \frac{g_{\rho}}{2}\bar{\psi}\gamma^{\mu}\vec{\rho}_{\mu}\vec{\tau}\psi + g_{\delta}\bar{\psi}\vec{\delta}\vec{\tau}\psi, \quad (2)$$

$$\mathcal{L}_{\sigma} = \frac{1}{2}(\partial^{\mu}\sigma\partial_{\mu}\sigma - m_{\sigma}^2\sigma^2) - \frac{A}{3}\sigma^3 - \frac{B}{4}\sigma^4, \quad (3)$$

$$\mathcal{L}_{\omega} = -\frac{1}{4}F^{\mu\nu}F_{\mu\nu} + \frac{1}{2}m_{\omega}^2\omega_{\mu}\omega^{\mu} + \frac{C}{4}(g_{\omega}^2\omega_{\mu}\omega^{\mu})^2, \quad (4)$$

$$\mathcal{L}_{\rho} = -\frac{1}{4}\vec{B}^{\mu\nu}\vec{B}_{\mu\nu} + \frac{1}{2}m_{\rho}^2\vec{\rho}_{\mu}\vec{\rho}^{\mu}, \quad (5)$$

$$\mathcal{L}_{\delta} = \frac{1}{2}(\partial^{\mu}\vec{\delta}\partial_{\mu}\vec{\delta} - m_{\delta}^2\vec{\delta}^2), \quad (6)$$

and

$$\begin{aligned} \mathcal{L}_{\sigma\omega\rho} = & g_{\sigma}g_{\omega}^2\sigma\omega_{\mu}\omega^{\mu}(\alpha_1 + \frac{1}{2}\alpha'_1g_{\sigma}\sigma) \\ & + g_{\sigma}g_{\rho}^2\sigma\vec{\rho}_{\mu}\vec{\rho}^{\mu}(\alpha_2 + \frac{1}{2}\alpha'_2g_{\sigma}\sigma) \\ & + \frac{1}{2}\alpha'_3g_{\omega}^2g_{\rho}^2\omega_{\mu}\omega^{\mu}\vec{\rho}_{\mu}\vec{\rho}^{\mu}. \end{aligned} \quad (7)$$

In this Lagrangian density, \mathcal{L}_{nm} stands for the kinetic part of the nucleons added to the terms representing the interaction between the nucleons and mesons σ , δ , ω , and ρ . The term \mathcal{L}_j represents the free and self-interacting terms of the meson j , for $j = \sigma, \delta, \omega$, and ρ . The last term, $\mathcal{L}_{\sigma\omega\rho}$, takes into account crossed interactions between the meson fields. The antisymmetric field tensors $F_{\mu\nu}$ and $\vec{B}_{\mu\nu}$ are given by $F_{\mu\nu} = \partial_{\mu}\omega_{\nu} - \partial_{\nu}\omega_{\mu}$ and $\vec{B}_{\mu\nu} = \partial_{\nu}\vec{\rho}_{\mu} - \partial_{\mu}\vec{\rho}_{\nu} - g_{\rho}(\vec{\rho}_{\mu} \times \vec{\rho}_{\nu})$. The nucleon mass is M and the meson masses are m_j .

The use of the mean-field approximation, in which the meson fields are treated as classical fields as

$$\begin{aligned} \sigma & \rightarrow \langle\sigma \equiv \sigma, \quad \omega_{\mu} \rightarrow \langle\omega_{\mu}\rangle \equiv \omega_0, \\ \vec{\rho}_{\mu} & \rightarrow \langle\vec{\rho}_{\mu}\rangle \equiv \vec{\rho}_{0(3)}, \quad \text{and} \quad \vec{\delta} \rightarrow \langle\vec{\delta}\rangle \equiv \delta_{(3)}, \end{aligned} \quad (8)$$

together with the Euler-Lagrange equations, leads to the following field equations:

$$\begin{aligned} m_{\sigma}^2\sigma & = g_{\sigma}\rho_s - A\sigma^2 - B\sigma^3 + g_{\sigma}g_{\omega}^2\omega_0^2(\alpha_1 + \alpha'_1g_{\sigma}\sigma) \\ & + g_{\sigma}g_{\rho}^2\vec{\rho}_{0(3)}^2(\alpha_2 + \alpha'_2g_{\sigma}\sigma), \end{aligned} \quad (9)$$

$$\begin{aligned} m_\omega^2 \omega_0 &= g_\omega \rho - C g_\omega (g_\omega \omega_0)^3 - g_\sigma g_\omega^2 \sigma \omega_0 (2\alpha_1 + \alpha'_1 g_\sigma \sigma) \\ &\quad - \alpha'_1 g_\omega^2 g_\rho^2 \bar{\rho}_{0(3)}^2 \omega_0, \end{aligned} \quad (10)$$

$$\begin{aligned} m_\rho^2 \bar{\rho}_{0(3)} &= \frac{g_\rho}{2} \rho_3 - g_\sigma g_\rho^2 \sigma \bar{\rho}_{0(3)} (2\alpha_2 + \alpha'_2 g_\sigma \sigma) \\ &\quad - \alpha'_3 g_\omega^2 g_\rho^2 \bar{\rho}_{0(3)} \omega_0^2, \end{aligned} \quad (11)$$

$$m_\delta^2 \delta_{(3)} = g_\delta \rho_{s3}, \quad (12)$$

$$[\gamma^\mu (i\partial_\mu - V_\tau) - (M + S_\tau)]\psi = 0. \quad (13)$$

Owing to the translational invariance and rotational symmetry of INM, only the zero components of the four-vector fields are nonvanishing. Also considering rotational invariance around the third axis in isospin space, we only deal with the third components of the isospin space vectors $\vec{\rho}_\mu$ and $\vec{\delta}$.

The scalar and vector densities are given by

$$\begin{aligned} \rho_s &= \langle \bar{\psi} \psi \rangle = \rho_{sp} + \rho_{sn}, \\ \rho_{s3} &= \langle \bar{\psi} \tau_3 \psi \rangle = \rho_{sp} - \rho_{sn}, \end{aligned} \quad (14)$$

$$\begin{aligned} \rho &= \langle \bar{\psi} \gamma^0 \psi \rangle = \rho_p + \rho_n, \\ \rho_3 &= \langle \bar{\psi} \gamma^0 \tau_3 \psi \rangle = \rho_p - \rho_n = (2y - 1)\rho, \end{aligned} \quad (15)$$

with

$$\begin{aligned} \rho_{s,p,n} &= \frac{\gamma M_{p,n}^*}{2\pi^2} \int_0^{k_{F,p,n}} \frac{k^2 dk}{\sqrt{k^2 + M_{p,n}^{*2}}} \\ &= \frac{\gamma (M_{p,n}^*)^3 q^2}{2\pi^2} \int_0^1 \frac{\xi^2 d\xi}{\sqrt{\xi^2 + 1/q^2}} \\ &= \frac{\gamma (M_{p,n}^*)^3}{4\pi^2} [q \sqrt{1 + q^2} - \ln(q + \sqrt{1 + q^2})], \end{aligned} \quad (16)$$

and

$$\rho_{p,n} = \frac{\gamma}{2\pi^2} \int_0^{k_{F,p,n}} k^2 dk = \frac{\gamma}{6\pi^2} k_{F,p,n}^3, \quad (17)$$

for $\xi = k/k_{F,p,n}$ and $q = k_{F,p,n}/M_{p,n}^*$ with the indices p,n standing for protons and neutrons, respectively. The degeneracy factor is $\gamma = 2$ for asymmetric matter, and the proton fraction is defined as $y = \rho_p/\rho$. The quantity $k_{F,p,n}$ is the Fermi momentum in the units in which $\hbar = c = 1$.

From the Dirac equation (13), we recognize the vector and scalar potentials written as

$$V_\tau \text{NL} = g_\omega \omega_0 + \frac{g_\rho}{2} \bar{\rho}_{0(3)} \tau_3 \quad \text{and} \quad (18)$$

$$S_\tau \text{NL} = -g_\sigma \sigma - g_\delta \delta_{(3)} \tau_3, \quad (19)$$

with $\tau_3 = 1$ and -1 for protons and neutrons, respectively. We can also define the effective nucleon mass as $M_\tau^* = M + S_\tau \text{NL}$, leading to

$$\begin{aligned} M_p^* &= M - g_\sigma \sigma - g_\delta \delta_{(3)} \quad \text{and} \\ M_n^* &= M - g_\sigma \sigma + g_\delta \delta_{(3)}. \end{aligned} \quad (20)$$

Note the effect of the meson δ , which splits the effective masses M_p^* and M_n^* . For SNM $\delta_{(3)}$ vanishes, because $\rho_{sp} = \rho_{sn}$, and consequently, $M_p^* = M_n^* = M^* = M - g_\sigma \sigma$.

From the energy-momentum tensor $T^{\mu\nu}$, calculated through the Lagrangian density in Eq. (1), it is possible to obtain the energy density and the pressure of the asymmetric system, because $\mathcal{E} = \langle T_{00} \rangle$ and $P = \langle T_{ii} \rangle / 3$. These quantities are given as

$$\begin{aligned} \mathcal{E}_{\text{NL}} &= \frac{1}{2} m_\sigma^2 \sigma^2 + \frac{A}{3} \sigma^3 + \frac{B}{4} \sigma^4 - \frac{1}{2} m_\omega^2 \omega_0^2 - \frac{C}{4} (g_\omega^2 \omega_0^2)^2 - \frac{1}{2} m_\rho^2 \bar{\rho}_{0(3)}^2 + g_\omega \omega_0 \rho + \frac{g_\rho}{2} \bar{\rho}_{0(3)} \rho_3 + \frac{1}{2} m_\delta^2 \delta_{(3)}^2 \\ &\quad - g_\sigma g_\omega^2 \sigma \omega_0^2 \left(\alpha_1 + \frac{1}{2} \alpha'_1 g_\sigma \sigma \right) - g_\sigma g_\rho^2 \sigma \bar{\rho}_{0(3)}^2 \left(\alpha_2 + \frac{1}{2} \alpha'_2 g_\sigma \sigma \right) - \frac{1}{2} \alpha'_3 g_\omega^2 g_\rho^2 \omega_0^2 \bar{\rho}_{0(3)}^2 + \mathcal{E}_{\text{kin}}^p + \mathcal{E}_{\text{kin}}^n, \end{aligned} \quad (21)$$

where

$$\begin{aligned} \mathcal{E}_{\text{kin}}^p &= \frac{\gamma}{2\pi^2} \int_0^{k_{F,p,n}} k^2 (k^2 + M_{p,n}^{*2})^{1/2} dk = \frac{\gamma k_{F,p,n}^4}{2\pi^2} \int_0^1 \xi^2 (\xi^2 + z^2)^{1/2} d\xi \\ &= \frac{\gamma k_{F,p,n}^4}{2\pi^2} \left[\left(1 + \frac{z^2}{2} \right) \frac{\sqrt{1+z^2}}{4} - \frac{z^4}{8} \ln \left(\frac{1+\sqrt{1+z^2}}{z} \right) \right] = \frac{3}{4} E_{F,p,n} \rho_{p,n} + \frac{1}{4} M_{p,n}^* \rho_{s,p,n}, \end{aligned} \quad (22)$$

and

$$\begin{aligned} P_{\text{NL}} &= -\frac{1}{2} m_\sigma^2 \sigma^2 - \frac{A}{3} \sigma^3 - \frac{B}{4} \sigma^4 + \frac{1}{2} m_\omega^2 \omega_0^2 + \frac{C}{4} (g_\omega^2 \omega_0^2)^2 + \frac{1}{2} m_\rho^2 \bar{\rho}_{0(3)}^2 + \frac{1}{2} \alpha'_3 g_\omega^2 g_\rho^2 \omega_0^2 \bar{\rho}_{0(3)}^2 \\ &\quad - \frac{1}{2} m_\delta^2 \delta_{(3)}^2 + g_\sigma g_\omega^2 \sigma \omega_0^2 \left(\alpha_1 + \frac{1}{2} \alpha'_1 g_\sigma \sigma \right) + g_\sigma g_\rho^2 \sigma \bar{\rho}_{0(3)}^2 \left(\alpha_2 + \frac{1}{2} \alpha'_2 g_\sigma \sigma \right) + P_{\text{kin}}^p + P_{\text{kin}}^n, \end{aligned} \quad (23)$$

with

$$\begin{aligned} P_{\text{kin}}^p &= \frac{\gamma}{6\pi^2} \int_0^{k_{F,p,n}} \frac{k^4 dk}{(k^2 + M_{p,n}^{*2})^{1/2}} = \frac{\gamma k_{F,p,n}^4}{6\pi^2} \int_0^1 \frac{\xi^4 d\xi}{(\xi^2 + z^2)^{1/2}} \\ &= \frac{\gamma k_{F,p,n}^4}{6\pi^2} \left[\left(1 - \frac{3z^2}{2} \right) \frac{\sqrt{1+z^2}}{4} + \frac{3z^4}{8} \ln \left(\frac{1+\sqrt{1+z^2}}{z} \right) \right] = \frac{1}{4} E_{F,p,n} \rho_{p,n} - \frac{1}{4} M_{p,n}^* \rho_{s,p,n}, \end{aligned} \quad (24)$$

and

$$E_{F,p,n} = \sqrt{k_{F,p,n}^2 + (M_{p,n}^*)^2}. \quad (25)$$

In the above equations, the parameter z is defined as $z = M_{p,n}^*/k_{F,p,n}$.

To better identify the parametrizations related to the model described in Eq. (1), we define here four different types of parametrizations.

- (i) *Type 1 (linear finite range models)*: Models in which $A = B = C = \alpha_1 = \alpha_2 = \alpha'_1 = \alpha'_2 = \alpha'_3 = g_\delta = 0$. This is the case of the linear Walecka model. Different parametrizations correspond to different values of the pair (ρ_0, E_0) .
- (ii) *Type 2 ($\sigma^3 + \sigma^4$ models)*: Models in which $C = \alpha_1 = \alpha_2 = \alpha'_1 = \alpha'_2 = \alpha'_3 = g_\delta = 0$. This type corresponds to parametrizations related to the Boguta-Bodmer model.
- (iii) *Type 3 ($\sigma^3 + \sigma^4 + \omega_0^4$ models)*: Models in which $\alpha_1 = \alpha_2 = \alpha'_1 = \alpha'_2 = \alpha'_3 = g_\delta = 0$. These parametrizations include a quartic self-interaction in the ω field.
- (iv) *Type 4 ($\sigma^3 + \sigma^4 + \omega_0^4 + \text{cross terms}$ models)*: Models in which $g_\delta = 0$ and at least one of the coupling constants, $\alpha_1, \alpha_2, \alpha'_1, \alpha'_2$, or α'_3 is different from zero.

Another widely used approach in QHD is that in which the couplings between nucleons and mesons are sensitive to the nuclear medium. Specifically, the RMF model proposed in Ref. [31] allows density dependence in the aforementioned couplings by making

$$g_\sigma \rightarrow \Gamma_\sigma(\rho), \quad g_\omega \rightarrow \Gamma_\omega(\rho), \quad g_\rho \rightarrow \Gamma_\rho(\rho), \quad \text{and} \quad g_\delta \rightarrow \Gamma_\delta(\rho). \quad (26)$$

Its Lagrangian density is given by

$$\begin{aligned} \mathcal{L}_{DD} = & \bar{\psi}(i\gamma^\mu \partial_\mu - M)\psi + \Gamma_\sigma(\rho)\sigma\bar{\psi}\psi - \Gamma_\omega(\rho)\bar{\psi}\gamma^\mu\omega_\mu\psi - \frac{\Gamma_\rho(\rho)}{2}\bar{\psi}\gamma^\mu\vec{\rho}_\mu\vec{\tau}\psi + \Gamma_\delta(\rho)\bar{\psi}\vec{\delta}\vec{\tau}\psi \\ & + \frac{1}{2}(\partial^\mu\sigma\partial_\mu\sigma - m_\sigma^2\sigma^2) - \frac{1}{4}F^{\mu\nu}F_{\mu\nu} + \frac{1}{2}m_\omega^2\omega_\mu\omega^\mu - \frac{1}{4}\vec{B}^{\mu\nu}\vec{B}_{\mu\nu} + \frac{1}{2}m_\rho^2\vec{\rho}_\mu\vec{\rho}^\mu + \frac{1}{2}(\partial^\mu\vec{\delta}\partial_\mu\vec{\delta} - m_\delta^2\vec{\delta}^2), \end{aligned} \quad (27)$$

where

$$\begin{aligned} \Gamma_i(\rho) &= \Gamma_i(\rho_0)f_i(x), \quad \text{with} \\ f_i(x) &= a_i \frac{1 + b_i(x + d_i)^2}{1 + c_i(x + d_i)^2}, \end{aligned} \quad (28)$$

for $i = \sigma, \omega$, and

$$\Gamma_\rho(\rho) = \Gamma_\rho(\rho_0)e^{-a(x-1)}, \quad \text{with} \quad x = \rho/\rho_0. \quad (29)$$

Some density-dependent parametrizations have couplings different from those of the above equations. In particular, the GDFM model [32] presents a form for its couplings,

$$\Gamma_i(\rho) = a_i + (b_i + d_i x^3)e^{-c_i x}, \quad (30)$$

for $i = \sigma, \omega, \rho, \delta$. A correction to the coupling parameter for the meson ω is also taken into account:

$$\Gamma_{\text{cor}}(\rho) = \Gamma_\omega(\rho) - a_{\text{cor}}e^{-(\frac{\rho-\rho_0}{b_{\text{cor}}})^2}. \quad (31)$$

The DDH δ parametrization has the same coupling parameters as in Eq. (28) for the mesons σ and ω , but functions $f_i(x)$ given by [33]

$$f_i(x) = a_i e^{-b_i(x-1)} - c_i(x - d_i), \quad (32)$$

for $i = \rho, \delta$.

By applying the mean-field approximation and the Euler-Lagrange equations, we find the same field equations as in Eqs. (9)–(13), taking into account Eq. (26) and $A = B = C = \alpha_1 = \alpha_2 = \alpha'_1 = \alpha'_2 = \alpha'_3 = 0$. The scalar and vector densities are defined as in the previous nonlinear RMF model. The proton and neutron effective masses, M_p^* and M_n^* , and the scalar potential are also defined as in Eqs. (20) and (19),

respectively, observing the generalizations in Eq. (26). The same does not occur for the vector potential that now reads

$$V_\tau \text{DD} = \Gamma_\omega(\rho)\omega_0 + \frac{\Gamma_\rho(\rho)}{2}\bar{\rho}_{0(3)}\tau_3 + \Sigma_R(\rho), \quad (33)$$

with

$$\Sigma_R(\rho) = \frac{\partial \Gamma_\omega}{\partial \rho}\omega_0\rho + \frac{1}{2}\frac{\partial \Gamma_\rho}{\partial \rho}\bar{\rho}_{0(3)}\rho_3 - \frac{\partial \Gamma_\sigma}{\partial \rho}\sigma\rho_s - \frac{\partial \Gamma_\delta}{\partial \rho}\delta_{(3)}\rho_{s3} \quad (34)$$

being the rearrangement term.

The energy density and pressure are given, respectively, by

$$\begin{aligned} \mathcal{E}_{DD} = & \frac{1}{2}m_\sigma^2\sigma^2 - \frac{1}{2}m_\omega^2\omega_0^2 - \frac{1}{2}m_\rho^2\bar{\rho}_{0(3)}^2 + \frac{1}{2}m_\delta^2\delta_{(3)}^2 \\ & + \Gamma_\omega(\rho)\omega_0\rho + \frac{\Gamma_\rho(\rho)}{2}\bar{\rho}_{0(3)}\rho_3 + \mathcal{E}_{\text{kin}}^p + \mathcal{E}_{\text{kin}}^n, \quad \text{and} \end{aligned} \quad (35)$$

$$\begin{aligned} P_{DD} = & \rho\Sigma_R(\rho) - \frac{1}{2}m_\sigma^2\sigma^2 + \frac{1}{2}m_\omega^2\omega_0^2 + \frac{1}{2}m_\rho^2\bar{\rho}_{0(3)}^2 \\ & - \frac{1}{2}m_\delta^2\delta_{(3)}^2 + P_{\text{kin}}^p + P_{\text{kin}}^n. \end{aligned} \quad (36)$$

We also define here the fifth type of parametrization analyzed in our work.

- (v) *Type 5 (density-dependent models)*: Parametrizations obtained from Eq. (27) in which $\Gamma_\delta = 0$.

Another class of RMF models is the nonlinear point-coupling (NLPC) model [34]. In this theory, nucleons interact with each other only through effective pointlike interactions, without exchanging mesons. It can be easily proved that the

linear version of the PC model results in the same equations of state as the linear Walecka model [35]. The same does not hold for NLPC models with cubic and quartic interactions and finite-range RMF models of type 2; besides, both versions can describe equally well INM [36]. Here, we treat a general type of NLPC model, described by the following Lagrangian density:

$$\begin{aligned} \mathcal{L}_{\text{NLPC}} = & \bar{\psi}(i\gamma^\mu\partial_\mu - M)\psi - \frac{\alpha_s}{2}(\bar{\psi}\psi)^2 - \frac{\beta_s}{3}(\bar{\psi}\psi)^3 \\ & - \frac{\gamma_s}{4}(\bar{\psi}\psi)^4 - \frac{\alpha_V}{2}(\bar{\psi}\gamma^\mu\psi)^2 - \frac{\gamma_V}{4}(\bar{\psi}\gamma^\mu\psi)^4 \\ & - \frac{\alpha_{\text{TV}}}{2}(\bar{\psi}\gamma^\mu\vec{\tau}\psi)^2 - \frac{\gamma_{\text{TV}}}{4}(\bar{\psi}\gamma^\mu\vec{\tau}\psi)^4 - \frac{\alpha_{\text{TS}}}{2}(\bar{\psi}\vec{\tau}\psi)^2 \\ & + [\eta_1 + \eta_2(\bar{\psi}\psi)](\bar{\psi}\psi)(\bar{\psi}\gamma^\mu\psi)^2 \\ & - \eta_3(\bar{\psi}\psi)(\bar{\psi}\gamma^\mu\vec{\tau}\psi)^2. \end{aligned} \quad (37)$$

The mean-field approximation gives rise to the Dirac equation given in Eq. (13), with the vector and scalar potentials modified, respectively, as

$$\begin{aligned} V_\tau^{\text{NLPC}} = & \alpha_V\rho + \alpha_{\text{TV}}\rho_3\tau_3 + \gamma_V\rho_3^3 + \gamma_{\text{TV}}\rho_3^3\tau_3 \\ & + 2(\eta_1 + \eta_2\rho_s)\rho_s\rho + 2\eta_3\rho_s\rho_3\tau_3, \end{aligned} \quad (38)$$

$$\begin{aligned} S_\tau^{\text{NLPC}} = & \alpha_s\rho_s + \beta_s\rho_s^2 + \gamma_s\rho_s^3 + \eta_1\rho^2 + 2\eta_2\rho_s\rho^2 \\ & + \eta_3\rho_3^2 + \alpha_{\text{TS}}\rho_s\tau_3, \end{aligned} \quad (39)$$

with ρ_s , ρ_{s3} , ρ , and ρ_3 defined as in Eqs. (14)–(17). The proton and neutron effective masses read

$$\begin{aligned} M_p^* = & M + \alpha_s\rho_s + \beta_s\rho_s^2 + \gamma_s\rho_s^3 + \eta_1\rho^2 + 2\eta_2\rho_s\rho^2 \\ & + \eta_3\rho_3^2 + \alpha_{\text{TS}}\rho_{s3}, \end{aligned} \quad (40)$$

$$\begin{aligned} M_n^* = & M + \alpha_s\rho_s + \beta_s\rho_s^2 + \gamma_s\rho_s^3 + \eta_1\rho^2 + 2\eta_2\rho_s\rho^2 \\ & + \eta_3\rho_3^2 - \alpha_{\text{TS}}\rho_{s3}. \end{aligned} \quad (41)$$

Notice that the interaction whose magnitude is given by α_{TS} plays the same role as the meson δ in the finite-range RMF models, namely, the splitting of proton and neutron effective masses.

Finally, we obtain the energy density and the pressure for the NLPC model as

$$\begin{aligned} \mathcal{E}_{\text{NLPC}} = & \frac{1}{2}\alpha_V\rho^2 + \frac{1}{2}\alpha_{\text{TV}}\rho_3^2 + \frac{1}{4}\gamma_V\rho^4 + \frac{1}{4}\gamma_{\text{TV}}\rho_3^4 \\ & - \eta_2\rho_s^2\rho^2 - \frac{1}{2}\alpha_s\rho_s^2 - \frac{2}{3}\beta_s\rho_s^3 - \frac{3}{4}\gamma_s\rho_s^4 \\ & - \frac{1}{2}\alpha_{\text{TS}}\rho_{s3}^2 + \mathcal{E}_{\text{kin}}^p + \mathcal{E}_{\text{kin}}^n, \quad \text{and} \end{aligned} \quad (42)$$

$$\begin{aligned} P_{\text{NLPC}} = & \frac{1}{2}\alpha_V\rho^2 + \frac{1}{2}\alpha_{\text{TV}}\rho_3^2 + \frac{3}{4}\gamma_V\rho^4 + \frac{3}{4}\gamma_{\text{TV}}\rho_3^4 \\ & + 2\eta_1\rho_s^2 + 3\eta_2\rho_s^2\rho^2 + 2\eta_3\rho_s\rho_3^2 + \frac{1}{2}\alpha_s\rho_s^2 \\ & + \frac{2}{3}\beta_s\rho_s^3 + \frac{3}{4}\gamma_s\rho_s^4 + \frac{1}{2}\alpha_{\text{TS}}\rho_{s3}^2 + P_{\text{kin}}^p + P_{\text{kin}}^n, \end{aligned} \quad (43)$$

respectively. We now define the sixth type of the analyzed parametrizations as follows.

(vi) *Type 6 (point-coupling models):* Parametrizations of the model described by Eq. (37) in which $\alpha_{\text{TS}} = 0$.

For the sake of completeness, we still define a last type of parametrization.

(vii) *Type 7 (δ meson models):* Parametrizations of finite-range models presenting the meson δ , i.e., models in which $g_\delta \neq 0$ in the respective Lagrangian density and equations of state.

We still calculate the symmetry energy, $\mathcal{S}(\rho)$, for the RMF model shown here from the general definition,

$$\mathcal{S}(\rho) = \frac{1}{8} \left. \frac{\partial^2(\mathcal{E}/\rho)}{\partial y^2} \right|_{\rho,y=1/2}. \quad (44)$$

The expressions are

$$\begin{aligned} \mathcal{S}_{\text{NL}}(\rho) = & \frac{k_F^2}{6E_F^*} + \frac{g_\rho^2}{8m_\rho^{*2}}\rho \\ & - \left(\frac{g_\delta}{m_\delta} \right)^2 \frac{M^{*2}\rho}{2E_F^{*2}[1 + (g_\delta/m_\delta)^2 A(k_F, M^*)]}, \end{aligned} \quad (45)$$

$$\begin{aligned} \mathcal{S}_{\text{DD}}(\rho) = & \frac{k_F^2}{6E_F^*} + \frac{\Gamma_\rho^2}{8m_\rho^{*2}}\rho \\ & - \left(\frac{\Gamma_\delta}{m_\delta} \right)^2 \frac{M^{*2}\rho}{2E_F^{*2}[1 + (\Gamma_\delta/m_\delta)^2 A(k_F, M^*)]}, \end{aligned} \quad (46)$$

$$\begin{aligned} \mathcal{S}_{\text{NLPC}}(\rho) = & \frac{k_F^2}{6E_F^*} + \frac{1}{2}\alpha_{\text{TV}}\rho + \eta_3\rho_s\rho \\ & + \frac{1}{2}\alpha_{\text{TS}}\frac{M^{*2}\rho}{2E_F^{*2}[1 - \alpha_{\text{TS}}A(k_F, M^*)]}, \end{aligned} \quad (47)$$

with

$$E_F^* = (k_F^2 + M^{*2})^{1/2}, \quad (48)$$

$$A(k_F, M^*) = \frac{2}{\pi^2} \int_0^{k_F} \frac{k^4 dk}{(k^2 + M^{*2})^{3/2}}, \quad \text{and} \quad (49)$$

$$m_\rho^{*2} = m_\rho^2 + g_\sigma g_\rho^2 \sigma (2\alpha_2 + \alpha'_2 g_\sigma \sigma) + \alpha'_3 g_\omega^2 g_\rho^2 \omega_0^2. \quad (50)$$

All quantities chosen as constraints that are presented in the next section are directly calculated from P , \mathcal{E} , and \mathcal{S} , as can be seen from the definitions

$$K_0 = 9 \left. \left(\frac{\partial P}{\partial \rho} \right) \right|_{\rho=\rho_0, y=1/2} \quad (\text{incompressibility}), \quad (51)$$

$$Q_0 = 27\rho_0^3 \left. \left(\frac{\partial^3(\mathcal{E}/\rho)}{\partial \rho^3} \right) \right|_{\rho=\rho_0, y=1/2} \quad (\text{skewness coefficient}), \quad (52)$$

$$J = \mathcal{S}(\rho_0) \quad (\text{symmetry energy at } \rho = \rho_0), \quad (53)$$

$$L_0 = 3\rho_0 \left. \left(\frac{\partial \mathcal{S}}{\partial \rho} \right) \right|_{\rho=\rho_0} \quad (\text{slope of } \mathcal{S}), \quad (54)$$

$$K_{\text{sym}}^0 = 9\rho_0^2 \left. \left(\frac{\partial^2 \mathcal{S}}{\partial \rho^2} \right) \right|_{\rho=\rho_0} \quad (\text{curvature of } \mathcal{S}), \quad (55)$$

$$Q_{\text{sym}}^0 = 27\rho_0^3 \left. \left(\frac{\partial^3 \mathcal{S}}{\partial \rho^3} \right) \right|_{\rho=\rho_0} \quad (\text{skewness of } \mathcal{S}), \quad (56)$$

$$K_{\tau,v}^0 = \left(K_{\text{sym}}^0 - 6L_0 - \frac{Q_0}{K_0} L_0 \right) \quad (\text{volume part of the isospin incompressibility}), \quad (57)$$

where ρ_0 is the saturation density; see Ref. [37].

In Appendix A we explicitly calculate some of the quantities defined above as a function of density for RMF models of types 4, 5, and 6 at zero temperature. In the finite-temperature regime, the integrals in $\rho_{p,n}$, $\rho_{s,p,n}$, $\mathcal{E}_{\text{kin}}^{p,n}$, and $P_{\text{kin}}^{p,n}$ should be replaced by those extending from zero to infinity and taking into account the Fermi-Dirac distributions for particles and antiparticles [38].

The saturation properties of all 263 RMF parametrizations analyzed in this work are displayed in Table VII of Appendix B, with the corresponding references.

III. RESULTS AND DISCUSSIONS

A. Previous constraints: SET1

We next present two sets of constraints used to analyze 263 relativistic models. First, we take the same 11 constraints previously used to analyze the Skyrme-type parameterizations. Each individual constraint is explained in detail also in Ref. [5]. Here we summarize them by stressing that they are closely related to properties (i) of SNM: the incompressibility (SM1), skewness coefficient (SM2), density dependence of pressure in the ranges of $2 < \frac{\rho}{\rho_0} < 4.6$ (SM3) and $1.2 < \frac{\rho}{\rho_0} < 2.2$ (SM4); (ii) of pure neutron matter (PNM): the density dependence of energy per particle (PNM1) and pressure (PNM2); (iii) involving both SNM and PNM: the symmetry energy (MIX1), its slope (MIX2), and the volume part of the isospin incompressibility (MIX3), all of them evaluated at the saturation density, the ratio of the symmetry energy at $\rho_0/2$ to its value at ρ_0 (MIX4), and the ratio of $3P_{\text{PNM}}(\rho_0)$ to $L_0\rho_0$ (MIX5). This set of constraints, named here as SET1, is shown in Table I with its respective range of validity.

Regarding specifically pure neutron matter, the related equation of state (EoS) is of a particular interest, because PNM is a realistic first approximation to the baryonic matter

that composes neutron stars. Most properties of neutron stars cannot be studied in terrestrial laboratories and theoretical models, based on effective forces, must be used. However, at low densities, experiments with cold Fermi atoms yield information on strongly interacting fluids, very similar to the low-density neutron matter at neutron-star crusts [47]. Different density regimes can be tuned by the magnitude of the neutron Fermi momentum k_F relative to the effective range r_o of the NN interaction in the system [48]. The ground-state energy per particle can be expressed as $E_{\text{PNM}}/E_{\text{PNM}}^o = \xi$, where $E_{\text{PNM}} = \mathcal{E}_{\text{PNM}}/\rho$ and E_{PNM}^o is the kinetic part of E_{PNM} . In the dilute degenerate Fermi gas regime ($k_F r_o \ll 1$), ξ is a constant [49]. This restricts the density below about $10^{-3} \rho_0$, the density at which neutrons become unbound in neutron stars. At higher densities, below $\sim 0.1 \rho_0$, where $k_F r_o \approx 1$, ξ has to be replaced by a system-dependent function $\xi(k_F, r_o)$. Likewise, in Ref. [5], we adopt here the expression $E_{\text{PNM}}/E_{\text{PNM}}^o$ by Epelbaum *et al.* [50], based on next-to-leading order in lattice chiral effective field theory (NLO₃) and including corrections owing to finite scattering length, nonzero effective range, and higher-order corrections,

$$\frac{E_{\text{PNM}}}{E_{\text{PNM}}^o} = \xi - \frac{\xi_1}{k_F a_o} + c_1 k_F r_o + c_2 k_F^2 m_\pi^{-2} + c_3 k_F^3 m_\pi^{-3} + \dots, \quad (58)$$

where m_π is the pion mass. The dimensionless universal constant ξ has been determined from trapped cold-atom experiments with ⁶Li and ⁴⁰K, which yield a variety of values: 0.32_{-13}^{+10} [51], $0.51(4)$ [52], 0.46_{-05}^{+12} [53], and $0.39(2)$ [54]. Values of ξ_1 in the literature are in the range 0.8–1.0 ([50] and references therein). Epelbaum *et al.*, using a simple Hamiltonian and only few particles in their system, took $\xi = 0.31$ and $\xi_1 = 0.81$ and fitted two sets of constants, namely ($c_1 = 0.27, c_2 = -0.44, c_3 = 0.0$) and ($c_1 = 0.17, c_2 = 0.0, c_3 = -0.26$), and obtained a very similar quality fit to their NLO₃. We used the constraint on energy per particle of PNM in the range of densities $0.01 - 0.1 \rho_0$ showed in Figs. 1(c) and 3(c) with $\xi_1 = 0.81$ and the two sets (c_1, c_2, c_3). The band is obtained by taking $0.2 < \xi < 0.6$, which allows for the spread in experimental values. This is the constraint named as PNM1.

TABLE I. List of the macroscopic constraints of SET1 and the range of their experimental and empirical (exp/emp) values, density region in which they are valid, and the corresponding range obtained using the approved RMF models (CRMF).

Constraint	Quantity	Density region	Range of constraint (exp/emp) (MeV)	Range of constraint from CRMF (MeV)	Reference
SM1	K_0	ρ_0 (fm ⁻³)	200–260	271.0	[39]
SM2	$K' = -Q_0$	ρ_0 (fm ⁻³)	200–1200	733.6	[40]
SM3	$P(\rho)$	$2 < \frac{\rho}{\rho_0} < 4.6$	Band region	see Fig. 1	[41]
SM4	$P(\rho)$	$1.2 < \frac{\rho}{\rho_0} < 2.2$	Band region	see Fig. 1	[42]
PNM1	$\mathcal{E}_{\text{PNM}}/\rho$	$0.017 < \frac{\rho}{\rho_0} < 0.108$	Band region	see Fig. 1	[5]
PNM2	$P(\rho)$	$2 < \frac{\rho}{\rho_0} < 4.6$	Band region	see Fig. 1	[41]
MIX1	J	ρ_0 (fm ⁻³)	30–35	33.8–34.0	[43]
MIX2	L_0	ρ_0 (fm ⁻³)	40–76	70.9–73.9	[44]
MIX3	$K_{\tau,v}^0$	ρ_0 (fm ⁻³)	−760 to −372	−388.5 to −388.4	[10]
MIX4	$\frac{S(\rho_0/2)}{L_0\rho_0}$	ρ_0 (fm ⁻³)	0.57–0.86	0.58	[45]
MIX5	$\frac{3P_{\text{PNM}}}{L_0\rho_0}$	ρ_0 (fm ⁻³)	0.90–1.10	1.05–1.06	[46]

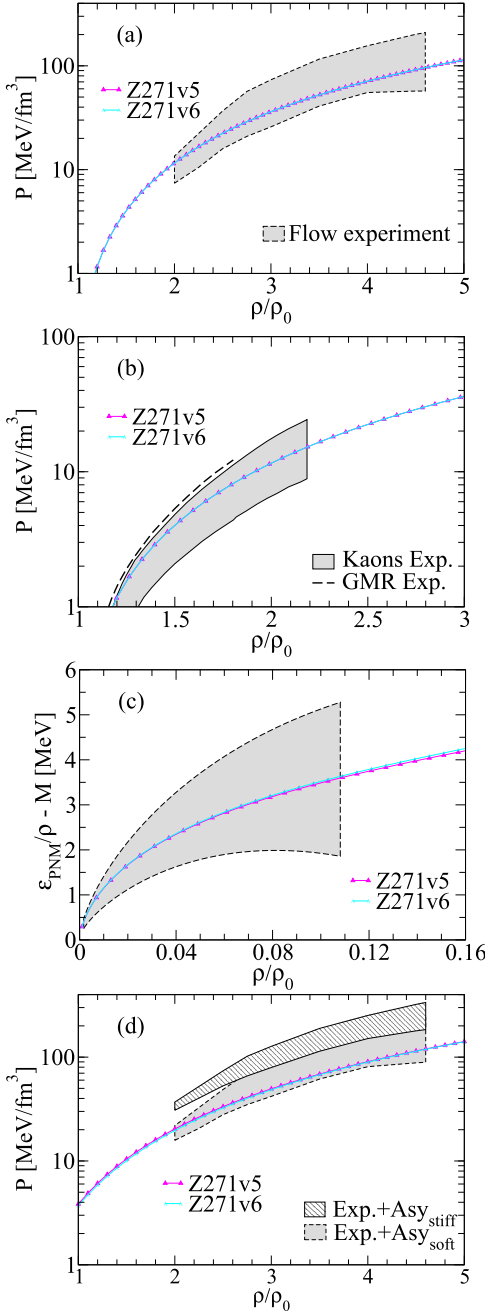


FIG. 1. (Color online) Density dependence of the approved models Z271v5 and Z271v6 in the (a) SM3, (b) SM4, (c) PNM1, and (d) PNM2 constraints related to SET1. The shaded bands were extracted from Ref. [41], where flow experimental data is compared with results obtained for (a) symmetric matter and (d) pure neutron matter, (b) Ref. [42], where pressure in symmetric matter is compared with data extracted from kaon production, and (c) Ref. [5], as explained in the text.

As in Ref. [5], a model is considered approved in a numerical constraint if its deviation, given as

$$\text{dev} = \frac{Q_{\text{mod}} - Q_{\text{const}}}{\Delta}, \quad (59)$$

TABLE II. List of parametrizations that fail in only one constraint of SET1.

Model	Model value (MeV)	Deviation
Constraint not satisfied: SM1 ($200 \leq K_0 \leq 260$ MeV)		
Z271v5	271.00	1.37
Z271v6	271.00	1.37
Constraint not satisfied: MIX3 ($-760 \leq K_{\tau,v}^0 \leq -372$ MeV)		
BSR15	-252.54	1.62
BSR16	-258.75	1.58
FSUGold	-276.07	1.49
FSUGZ06	-259.47	1.58
FSUGold4	-205.59	1.86
FSU-III	-341.03	1.16
FSU-IV	-210.68	1.83
TW99	-332.32	1.20
DD-F	-285.54	1.45
DD-ME δ	-258.28	1.59

obeys the relation $|\text{dev}| \leq 1$, with Q_{mod} being the value of the quantity calculated in the model, Q_{const} the central value of the related constraint, and Δ the error related to Q_{const} . Specifically for the MIX1, MIX3, and MIX4 constraints, we define their central values as $Q_{\text{const}} = (x_2 + x_1)/2$ and the error as $\Delta = x_2 - Q_{\text{const}} = Q_{\text{const}} - x_1$, because they are given in the form of $x_1 \leq X \leq x_2$. However, a graphic constraint is satisfied if the model is inside the corresponding band in 95% or more of the density region.

We also present in the fifth column of Table I the range of the quantities used in each constraint obtained from the approved models which are designated by consistent relativistic mean field (CRMF). This range is defined from the smaller and larger values of the respective quantity chosen among the selected models. For instance, the range of the slope of the symmetry energy, $70.9 \leq L_0 \leq 73.9$, is constructed by noting that $L_0^{\text{Z271v6}} = 70.9$ MeV and $L_0^{\text{Z271v5}} = 73.9$ MeV. For the graphic constraints, we analyze the density dependence of the Z271v5 and Z271v6 parameterizations in Fig. 1.

By applying the constraints of SET1 to the RMF parametrizations, we obtain the result that *none of the models* satisfies all constraints simultaneously. However, there are 12 parametrizations that do not satisfy only one individual constraint; i.e., they are consistent with the 10 remaining ones. We specify such parametrizations in Table II, including the constraint they do not satisfy and the respective deviation obtained from Eq. (59).

In these 12 parametrizations, 2 specific ones, models of type 4 (cross-terms models), namely, Z271v5 and Z271v6, fall outside the limits of the SM1 constraint (the one not satisfied only for these two models) by less than 5%; i.e., their incompressibilities, $K_0^{\text{Z271v5}} = K_0^{\text{Z271v6}} = 271$ MeV, exceed the highest value of the SM1 constraint, $K_{0,\text{SM1}}^{\text{max}} = 260$ MeV, by 11 MeV and the ratio of this excess to $K_{0,\text{SM1}} = 230$ MeV is less than 5%. For such cases, we apply the same criterion of Ref. [5] and define these models as included in the CRMF parameterizations, i.e., the ones satisfying the constraints of SET1.

TABLE III. Number of approved models (among 263) in each constraint of SET1.

Constraints	SM1	SM2	SM3	SM4	PNM1	PNM2	MIX1	MIX2	MIX3	MIX4	MIX5
No. of models	146	174	104	153	193	101	162	59	124	65	258

For the sake of completeness, we provide in Table III the number of the RMF approved models for each constraint of SET1.

It is worth noting that the MIX5 constraint is the “weakest” one, while the constraint defined by the slope of the symmetry energy, MIX2, is the “strongest” among all of them, because only 58 of 263 parametrizations present L_0 in the range of $L_0 = 58 \pm 18$ MeV.

B. Updated constraints: SET2a and SET2b

It is well known that some of the validity ranges are different if obtained for Skyrme-type or relativistic models. Several studies involving both RMF models and nonrelativistic models have shown that although both sets of models verify the same correlations, the parameter distribution of each set is not completely overlapping; see, for instance, Refs. [15,27,37]. This is a consequence of the different structure of these models, namely, the existence of a scalar density completely absent in the nonrelativistic models which gives contributions corresponding to many-body effects [55]. In fact, the constraints imposed within each of the sets are not measured directly, but they result from the analysis of raw data, which involves model assumptions. As an example, we refer that the incompressibility derived from GMR using Skyrme interactions is around 230 MeV, but many of the RMF models predict higher values (see, e.g., Ref. [10]). In a similar way, a value $J = 32.5 \pm 0.5$ MeV is found by fitting a large set of experimental data in the finite-range droplet-model (FRDM) [56]. The extrapolation of the various fits for the nonrelativistic models (Skyrme and Gogny) yield typical values of J in the region of 27 to 38 MeV. Also, for such a quantity, the various RMF parametrizations yield higher values; see Fig. 18 of Ref. [43] for a clear comparison. Based on this phenomenology, we have opted for other sets of constraints that are somewhat more adequate to analyze the RMF models. In these new sets, named hereafter as SET2a and SET2b, we also intend to take into account new theoretical, experimental, and empirical information concerning the quantities related to the constraints used in this work.

First of all, we discuss the SM1 constraint, related to the incompressibility of infinite nuclear matter. In the recent study of Refs. [11,12], the authors investigated the density dependence of the incompressibility in various relativistic and nonrelativistic models, finding a crossing point around a density of $\rho_c = 0.7\rho_0$. They pointed out the existence of this crossing also in other bulk properties such as the symmetry energy [23] and the energy density of pure neutron matter [57]. In fact, phenomenological models are generally fitted to finite nuclei which provide fitting constraints at a density slightly below saturation, making ρ_c more suitable to characterize nuclear finite systems. In this perspective, the authors have shown that the quantity $M_c = 3\rho_c \frac{\partial K(\rho)}{\partial \rho} \Big|_{\rho=\rho_c}$ is more strongly

correlated with E_{GMR} than $K_0 = K(\rho_0)$ and claimed to use this relation to first constrain M_c and after to infer the value of K_0 (E_{GMR} is the centroid energy of the isoscalar giant monopole resonance). This is an alternative to the often-used method of constraining K_0 directly from its correlation with E_{GMR} . Following this new approach, and by using experimental data of E_{GMR} for ^{208}Pb , $^{112-124}\text{Sn}$ isotopes, ^{90}Zr , and ^{144}Sm , the linear correlation of E_{GMR} and M_c shown in Refs. [11,12] was used to constrain M_c to the range $M_c = 1100 \pm 70$ MeV. Thereby, a new range of K_0 was proposed by noting that K_0 and M_c are also linearly correlated [11,12]. In our new set of updated constraints, we use this range of values for K_0 as our new SM1 constraint, in this case given by $K_0 = 230 \pm 40$ MeV. Notice that this new constraint is slightly less restrictive than the old one given by $K_0 = 230 \pm 30$ MeV.

Although interesting, we note that the new constraint is based on theory and a specific selection of Skyrme forces (with the exception of FSUGold, DDME2, and D1S which seem to cluster just at the low M_c values). The selection of experimental E_{GMR} is also limited; there are many more values E_{GMR} in the literature which would have to be used to verify the conclusion of Fig. 3 (Fig. 2) in Ref. [11] (Ref. [12]). For example, there are three different sets of the experimental E_{GMR} in ^{208}Pb which differ outside errors: 13.91 ± 0.11 MeV, 13.90 ± 0.30 MeV, 14.24 MeV, 14.17 ± 0.28 MeV, 14.18 ± 0.11 MeV (see discussion in Ref. [39]), 13.96 ± 0.20 MeV [58], 13.4 ± 0.2 MeV [59], and 13.5 ± 0.2 MeV [60]. If the lowest value, 13.2 MeV, allowed by the error was used, the constraint on M_c would be different. Also, the error on E_{GMR} ^{120}Sn is 200 keV, not 100 keV (15.4 ± 0.2 MeV) [28,61].

Another constraint directly established from a correlation with the incompressibility is the SM2 one. In Ref. [40], the authors used the leptodermous expansion for the incompressibility of a finite nucleus of mass number A and radius R ,

$$K(A, y) = K_0 + K_{\text{surf}} A^{-1/3} + K_{\text{curv}} A^{-2/3} + K_{\tau,v}^0 (1 - 2y)^2 + K_{\text{coul}} \frac{Z^2}{A^{4/3}} + \dots, \quad (60)$$

and its relation with E_{GMR} through

$$K(A, y) = (M/\hbar^2) \langle R^2 \rangle E_{\text{GMR}}^2, \quad (61)$$

to find the range of $K' = 700 \pm 500$ MeV [the volume part of the isospin incompressibility, $K_{\tau,v}^0$, is written in terms of $K' = -Q_0$ in Eq. (57)]. This constraint was obtained from the range predicted for the incompressibility, $K_0 = 215 \pm 15$ MeV, extracted from the comparison of experimental values of E_{GMR} and those calculated from theoretical models. However, the analysis of Ref. [40] was entirely based on parameterizations of the nonrelativistic Skyrme model. For this reason, and because of the difference between K_0 found in Ref. [40] and the one defined in our new SM1 constraint,

we have decided here to eliminate the SM2 constraint from SET2 and, consequently, from the updated analysis of the RMF parametrizations.

The SM3 constraint is related to the limits of the density dependence of the pressure of INM. In the previous work [5], we have taken these limits as defined by Danielewicz and coauthors in Ref. [41]. In that work, the authors established such limits from analysis of transverse and elliptical flows of the ejected particles in the $^{197}\text{Au} + ^{197}\text{Au}$ collisions.

In a recent study [62], Steiner *et al.* extracted the radius r of a $1.4M_{\odot}$ neutron star in the range $10.4 \leq r \leq 12.9$ km, generating a new constraint that equations of state must satisfy for the mass-radius relation of neutron stars. Their analysis was based on observational data of (i) bursting neutron stars showing photospheric radius expansion and of (ii) transiently accreting neutron stars in quiescence. As a consequence, the authors also established a new range of validity for the density dependence of the pressure of infinity nuclear matter, consistent with the previous SM3 constraint proposed in Ref. [41] in the lower pressure region. In the high-pressure region, however, the new constraint is broader than the former. To take into account this new phenomenology, we use here the SM3 constraint in two different levels, namely, the SM3a, in which we consider the band in the density dependence of pressure increased by 20% in its upper limit, and the SM3b, in which we use the band exactly as in the SM3 constraint of SET1. It is worth noting that the SM3a constraint is a less restrictive version of the SM3 one used in SET1.

We note that very recently the radius of a $1.4M_{\odot}$ neutron star [62] has been updated by Lattimer and Steiner [63] to be 11.15–12.66 km (with 95% confidence) if a nucleon-only equation of state is considered and 10.45–12.45 km for an equation of state with *exotic* components. Their analysis was performed on exactly the same five objects as the analysis reported by Guillot *et al.* [64], who found the radius of a wide range of neutron-star masses to be $9.1^{+1.3}_{-1.5}$ km (with 90% confidence). Further observation and analysis would be desirable to refine constraints related to mass radius of cold neutron stars.

In Ref. [41], Danielewicz *et al.*, also proposed a constraint on the density dependence of the pressure in pure neutron matter. They made an extrapolation of data concerning transversal and elliptical flow of the previous case by including asymmetry terms with strong and weak density dependence in the pressure. This constraint, named PNM2, was used in Ref. [5] and also in SET1. However, in SET2 we decide not to consider it, by understanding that no new experimental information on heavy-ion collisions is present in such an extrapolation. Therefore, the PNM2 constraint is absent from SET2.

Concerning the constraints on the symmetry energy at the saturation density (J), we decide to consider in SET2 the fact that effective hadronic models present values for J in a broader range than that used in SET1, namely, $30 \leq J \leq 35$ MeV. We consider here a small modification in the lower limit of this range, giving rise to our MIX1a constraint in which $25 \leq J \leq 35$ MeV. By the same token, we modify the range of the slope of the symmetry energy at ρ_0 (L_0) to the new one given by $25 \leq L_0 \leq 115$ MeV. This constraint is named MIX2a. However, we call the reader's attention to the fact that

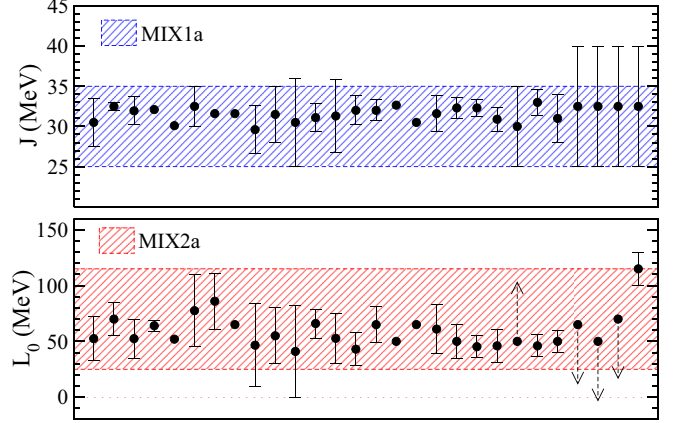


FIG. 2. (Color online) Comparison between the limits used in MIX1a and MIX2a constraints and those from 28 different experimental and observational data collected in Ref. [65].

the new limits established for MIX1a and MIX2a are totally compatible with experimental values available in the literature. To make this clear, we present in Fig. 2, a set of 28 J and L values extracted from Ref. [65], in which the authors collected from the literature data obtained from analyses of different terrestrial nuclear experiments and astrophysical observations. They include analyses of isospin diffusion, neutron skins, pygmy dipole resonances, α and β decays, transverse flow, the mass-radius relation of neutron stars, and torsional crust oscillations of neutron stars. As one can see in Fig. 2, the new constraints encompass all experimental and observational data.

The reader is reminded that this comparison, based on searching for an overlap of the outcome of many experimental and observational methods, inherently implies that all of them have the same weight, which may not be in consensus in the literature. However, we wish to make clear that this comparison has been used in this work only as a guideline, to take into account the more recent data regarding the possible ranges of validity for J and L .

We also compare the broader range of J with our previous one of Ref. [5], named in SET2 as MIX1b, and, for the sake of completeness, we also compare the new range of L_0 with a combination of the ranges recently given in Refs. [18,66]. We name this more restrictive range for L_0 , namely, $30 \leq L_0 \leq 80$ MeV, as MIX2b.

To finish the list of updated constraints, we make several remarks concerning the limits of the quantity $K_{\tau,v}^0$. First of all, we point out here that such a quantity is extremely relevant in our study, because it represents the volume part of the isospin incompressibility. It is important to analyze the values that RMF models predict for this observable, in the sense that such an investigation can offer a clue for the improvement of the isospin part of effective RMF interactions. According to the literature, there are at least three methods for finding a constraint on the value of K_{τ} , defined as $K_{\tau} = K_{\tau,v}^0 + K_{\tau,s}$, where the last term is related to the surface part of the isospin incompressibility. In Ref. [26], the authors used an isospin- and momentum-dependent transport model to obtain the degree of isospin diffusion in the $^{124}\text{Sn} + ^{112}\text{Sn}$, $^{124}\text{Sn} + ^{124}\text{Sn}$, and

TABLE IV. The same as in Table I, now taking into account the following updated constraints: SM1, SM3a, SM3b, MIX1a, MIX1b, MIX2a, MIX2b, and MIX3. The SM4, PNM1, and MIX4 constraints are the same as in SET1. The SM2, PNM2, and MIX5 constraints were removed. These new constraints are used to generate two new sets, namely, SET2a and SET2b (see the text for their definitions).

Constraint	Quantity	Density region	Range of constraint (exp/emp) (MeV)	Range of constraint from CRMF (MeV)	Ref.
SM1	K_0	ρ_0 (fm $^{-3}$)	190–270	225.2–232.4	[11,12]
SM3a		The same as SM3b plus 20% on upper limit		see Fig. 3	[62]
SM3b	$P(\rho)$	$2 < \frac{\rho}{\rho_0} < 5$	Band region	see Fig. 3	[41]
SM4	$P(\rho)$	$1.2 < \frac{\rho}{\rho_0} < 2.2$	Band region	see Fig. 3	[42]
PNM1	$\mathcal{E}_{\text{PNM}}/\rho$	$0.017 < \frac{\rho}{\rho_0} < 0.108$	Band region	see Fig. 3	[5]
MIX1a	J	ρ_0 (fm $^{-3}$)	25–35	33.2–34.2	
MIX1b	J	ρ_0 (fm $^{-3}$)	30–35	33.2–34.0	[43]
MIX2a	L_0	ρ_0 (fm $^{-3}$)	25–115	77.9–84.8	
MIX2b	L_0	ρ_0 (fm $^{-3}$)	30–80	77.9–78.8	
MIX3	$K_{\tau,v}^0$	ρ_0 (fm $^{-3}$)	–700 to –400	–421.6(a)/–414.3(b) to –382.5 MeV	[18,66]
MIX4	$\frac{\mathcal{S}(\rho_0/2)}{J}$	ρ_0 (fm $^{-3}$)	0.57–0.86	0.57(a)/0.59(b)–0.59	[45]

$^{112}\text{Sn} + ^{112}\text{Sn}$ collisions, at energies of 50 MeV/nucleon and impact parameter of 6 fm. The correlation between this degree of diffusion and the isospin incompressibility led to the constraint of -500 ± 50 MeV for K_τ . However, Centelles *et al.* found in Ref. [27] that $c_{\text{sym}}(\rho \simeq 0.1 \text{ fm}^{-3}) = a_{\text{sym}}(A)$, where $c_{\text{sym}}(\rho) \simeq J - L_0 \epsilon + \frac{1}{2} K_{\tau,v}^0 \epsilon^2$ (with $\epsilon = \frac{\rho_0 - \rho}{3\rho_0}$) and the symmetry energy coefficient of finite nuclei is $a_{\text{sym}}(A) = J/[1 + (9J/4Q)A^{1/3}]$ (Q is the surface stiffness). From this relation, and using that $a_{\text{sym}}(A)$ is a linear function of the neutron skin thickness, the authors estimated a range of $K_\tau = -500^{+125}_{-100}$ MeV by analyzing the neutron skin thickness of 26 antiprotonic atoms. Finally, in Ref. [28], the authors used an expression for $K(A, y)$ similar to Eq. (60) to obtain the value of $K_\tau = -550 \pm 100$ MeV from data of E_{GMR} .

Regarding the theoretical calculations for K_τ , it is also important to mention here that mean-field models predict only its volume term, i.e., $K_{\tau,v}^0$. However, as it is rather tricky to separate the volume from the surface term (although it has been done several times; see, e.g., Ref. [10] and references therein), and as the volume term seems to be dominant, we have opted to constrain the calculated volume term with K_τ values obtained from experiment; i.e., we have assumed $K_{\tau,v}^0 \approx K_\tau$ for the RMF models. Finally, to take into account all aforementioned procedures for the estimation of K_τ , we define here our new constraint MIX3 as $K_\tau = -550 \pm 150$ MeV.

Finally, we stress here that the MIX5 constraint was also removed from our new analysis because it is a very “weak” constraint, in the sense that practically all models are approved in its range; see Table III. Thus, we do not consider it as a good model selector.

The list of the updated constraints together with those not modified from SET1 is given in Table IV.

From these updated constraints we define two distinct sets: one of them composed by the constraints in which their ranges are broader, SET2a, and other one in which they are more stringent, namely, SET2b. Specifically, SET2a (SET2b) is defined by the SM1, SM3a (SM3b), SM4, PNM1, MIX1a (MIX1b), MIX2a (MIX2b), MIX3, and MIX4 constraints.

The application of the constraints of SET2a to the 263 RMF parametrizations collected in our work leads to

only *two models* satisfying all constraints simultaneously. They are the type 4 models BSR12 and BKA24. In addition, 24 parametrizations satisfy all constraints of SET2a except one; i.e., they are approved in seven of the eight constraints. In this group, the BSR11 and BKA22 models, also of type 4, fell outside the range of the unsatisfied constraint (in this case, MIX3) by less than 5%. Therefore, as we have done in Ref. [5], and in the previous analysis of SET1, we consider these *four models* as belonging to the CRMF models of SET2a.

When considering the SET2b, the more stringent one, we found no significant changes in the results. In such an analysis, *only* the BSR12 model, among 263, satisfies all SET2b simultaneously, and 22 parametrizations satisfy seven of the eight constraints. Two such models fell outside the range of the unsatisfied constraint by less than 5%, namely, BSR11 and BKA22, the same as in the SET2a analysis. The MIX3 constraint is again the one not satisfied for these two models. In summary, we have, in total, *three models* consistent with the SET2b analysis.

It is worth noting that the difference between the two analyses regarding SET2a and SET2b is the absence of the BKA24 model in the CRMF approved models of SET2b, in comparison to those approved in SET2a. The reason for this absence is the slope of the symmetry energy of the BKA24 model, $L_0 = 84.8$ MeV, clearly outside the MIX2b range, given by $L_0 = 55 \pm 25$ MeV, by more than 5%.

As in the previous section, we present in the fifth column of Table IV the range of the constraints of SET2, defined by the CRMF models. In the cases of MIX3 and MIX4 constraints, the boundary models are different for both sets, namely, SET2a and SET2b. Therefore, we included the letter (a) or (b) in the values to identify the corresponding set. The density dependence of the approved models in both analyses is shown in Fig. 3.

Also regarding our analysis of SET2a and SET2b, in Table V we present the number of approved models in each constraint.

We also provide in Table VIII of Appendix C the information whether each model of the 263 ones is approved (+) or not (–) in the constraints of SET2. In Table IX of Appendix D,

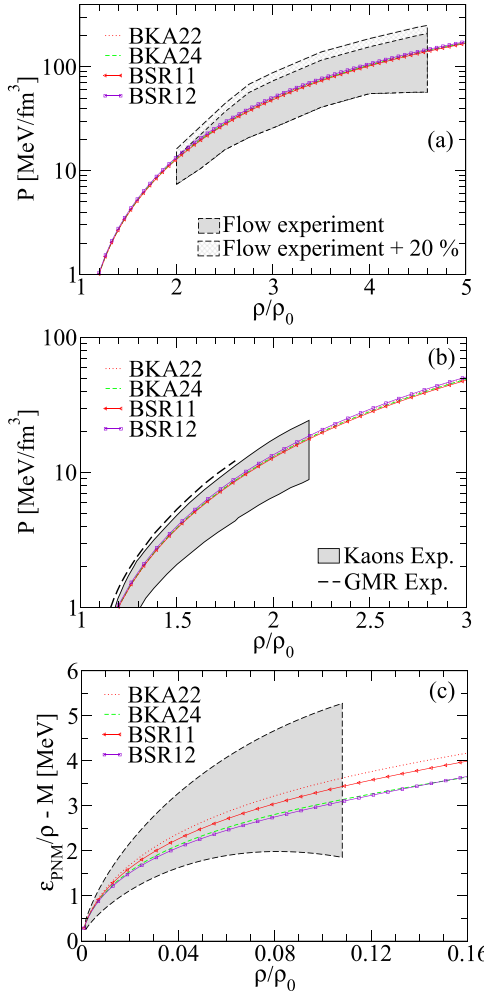


FIG. 3. (Color online) Density dependence of approved models in the (a) SM3, (b) SM4, and (c) PNM1 constraints related to SET2a and SET2b. Shaded bands extracted from (a) Ref. [41], where flow experimental data are compared with results obtained for symmetric matter, (b) Ref. [42], where pressure in symmetric matter is compared with data extracted from kaon production, and (c) Ref. [5], as explained in the text.

we give the deviation as calculated in Eq. (59) for the numerical constraints, as well as those obtained for the graphic constraints, all of them related to SET2.

To finish the analysis of SET2, we point out that our work concerns only nuclear matter. Owing to the translational invariance, rotational symmetry, and rotational invariance around the third axis in isospin space of the latter, we can constrain only some features of the Lagrangian and the approved models cannot guarantee successful predictions for

finite nuclei. From our analysis, one can see from Table VIII that the models FSUGold, FSUZG03, DD-ME δ , and IU-FSU are consistent with all constraints except MIX3, a constraint applicable in the region of saturation density (it applies only to SET2a for the IU-FSU model). These parameter sets provide quite good global fits to binding energies, charge radii, isotopic shifts, and neutron skin thicknesses.

For the sake of completeness, we display in Table VI several nuclear matter properties, at the saturation density, of the approved models in all sets analyzed here, namely, SET1, SET2a, and SET2b.

C. Excluding MIX3 constraint

The results presented in the previous section pointed to a small number of RMF models consistent to all constraints simultaneously, namely, four in the SET2a analysis and three for the SET2b analysis. However, these numbers change significantly if we simply discard the MIX3 constraint from SET2a and SET2b. By excluding this constraint, the new results for the SET2a analysis become the following: 25 *models* are consistent with all seven constraints. They are: BKA20, BKA22, BKA24, BSR8, BSR9, BSR10, BSR11, BSR12, BSR15, BSR16, BSR17, BSR18, BSR19, DD-ME δ , DD-F, DDH δ , FSU-III, FSU-IV, FSUGold, FSUGold4, FSUGZ03, FSUGZ06, G2*, IU-FSU, and TW99. Moreover, 48 models satisfy all but one of the constraints. In this group, 10 models fall outside the range of the constraint by less than 5%. They are BSR20, FA3, Z271s2, Z271s3, Z271s4, Z271s5, Z271s6, Z271v4, Z271v5, and Z271v6. By also including such models in the CRMF parameterizations, one has 35 *models* consistent with the SET2a analysis.

For the SET2b, we have 22 *models* consistent with all constraints. These are the same models approved in SET2a, except for the BKA24, IU-FSU, and DDH δ models. Moreover, 14 models satisfy only seven constraints, and by applying the 5% criterion, 8 more models are approved. They are the same as in the corresponding case of SET2a, except for the BSR20 and FA3 models. Therefore, one has in the SET2b analysis a total of 30 *models* in the group of approved models.

D. Additional new constraints

After the work presented in this paper has been completed, new constraints from reanalysis of data on GMR energies became available [10], suggesting that the SM1 constraint would span to somewhat higher values, 250–315 MeV (SM1-new) and MIX3 would be between –620 and –370 MeV (MIX3-new). We reanalysed the data introducing the two additional constraints with the following results.

TABLE V. Number of approved models (among 263) in each constraint of SET2.

SET2											
Constraints	SM1	SM3a	SM3b	SM4	PNM1	MIX1a	MIX1b	MIX2a	MIX2b	MIX3	MIX4
No. of models	153	129	104	153	193	174	162	216	72	96	65

TABLE VI. Nuclear matter properties at the saturation density ρ_0 of the RMF models consistent with the macroscopic constraints.

Model	Approved in SET	ρ_0 (fm $^{-3}$)	E_0 (MeV)	K_0 (MeV)	m^*	K' (MeV)	J (MeV)	L_0 (MeV)	$K_{\tau,v}^0$ (MeV)	$\frac{S(\rho_0/2)}{J}$
BKA22	2a and 2b	0.147	-15.91	225.24	0.61	283.29	33.17	78.79	-382.46	0.59
BKA24	2a	0.147	-15.95	227.06	0.60	273.58	34.19	84.80	-421.55	0.57
BSR11	2a and 2b	0.147	-16.08	226.75	0.61	312.37	33.69	78.78	-388.86	0.59
BSR12	2a and 2b	0.147	-16.10	232.35	0.61	290.31	34.00	77.90	-414.30	0.59
Z271v5	1	0.148	-16.24	271.00	0.80	733.59	34.04	73.90	-388.52	0.58
Z271v6	1	0.148	-16.24	271.00	0.80	733.59	33.80	70.94	-388.36	0.58

1. Analysis considering MIX3-new in SET2

- (i) SET2a (SM1-new, SM3a, SM4, PNM1, MIX1a, MIX2a, MIX3-new, and MIX4): Four models approved, namely, Z271v4, Z271v5, Z271v6, and FA3; 24 models not satisfying only one constraint. Even with 5% tolerance, no further model approved.
- (ii) SET2b (SM1-new, SM3b, SM4, PNM1, MIX1b, MIX2b, MIX3-new, and MIX4): Three models approved, namely, Z271v4, Z271v5, and Z271v6; 12 models not satisfying only one constraint. Even with 5% tolerance, no further model approved.

2. Analysis discarding MIX3-new in SET2

- (i) SET2a (SM1-new, SM3a, SM4, PNM1, MIX1a, MIX2a, and MIX4): Nine models approved, namely, Z271v4, Z271v5, Z271v6, Z271s2, Z271s3, Z271s4, Z271s5, Z271s6, and FA3; 45 models not satisfying only one constraint. Even with 5% tolerance, no further model approved.
- (ii) SET2b (SM1-new, SM3b, SM4, PNM1, MIX1b, MIX2b, and MIX4): Eight models approved, namely, Z271v4, Z271v5, Z271v6, Z271s2, Z271s3, Z271s4, Z271s5, and Z271s6; 26 models not satisfying only one constraint. Even with 5% tolerance, no further model approved.

IV. SUMMARY AND CONCLUSIONS

In this work we submitted 263 parametrizations of the widely used RMF hadronic models to three different sets of constraints. One of them (SET1) is composed exactly of the same constraints used in the extensive study of Ref. [5] in which 240 parametrizations of the nonrelativistic Skyrme model were examined. The second one, named SET2, was divided in two other sets, in which updated constraints were taken into account and some of them removed from our analysis. The first set, SET2a, contains a broader version of the constraints and the second, SET2b, a more stringent one. In summary, all sets present constraints regarding information of SNM, pure neutron matter (PNM), and those in which these two frameworks are considered simultaneously (MIX), i.e., constraints derived from the symmetry energy at the saturation density.

We have organized the RMF models in seven different groups regarding their Lagrangian density structure, namely, linear (type 1), $\sigma^3 + \sigma^4$ (type 2), $\sigma^3 + \sigma^4 + \omega_0^4$ (type 3),

$\sigma^3 + \sigma^4 + \omega_0^4 +$ cross terms (type 4), density-dependent (type 5), point-coupling (type 6), and δ meson (type 7) models. Their saturation properties are displayed in Table VII of Appendix B.

The application of the SET1 constraints to the models leads to the impressive result of only the Z271v5 and Z271v6 parametrizations being classified as consistent RMF (CRMF) models. This result is still more stringent than that found in Ref. [5] in which among 240 Skyrme parametrizations, only 16 were approved in the analysis regarding SET1. If we consider our analysis based on the constraints of SET2a, a more updated version in comparison with SET1, the results do not change significantly. In this case, BKA22, BKA24, BSR11, and BSR12 are the CRMF models, and, except for the BKA24 model, this is the same result when we use the SET2b, a more stringent one in comparison with the updated SET2a. The saturation properties of these models are summarized in Table VI. Also, the density dependence of the properties used to construct the graphic constraints are shown in Figs. 1 and 3.

As an interesting feature concerning our analysis, we point out that in all sets of constraints, the approved models are of type 4, i.e., models presenting cross terms between the mesonic fields σ , ω_μ , and ρ_μ . In particular, these interactions include a density dependence of the symmetry energy that goes beyond the almost linear behavior of models of the types 1, 2, and 3. Moreover, models BKA22 and BKA24 yield a neutron-skin thickness in the ^{208}Pb nucleus, respectively, of 0.22 and 0.24 fm and were found to be consistent with most of the constraints included in sets 2a and 2b [67]. This means that models of type 4, those that include the cross-term interactions, favor the reproduction of the expected behavior of the properties defined in each individual constraint. To satisfy the constraints used in this work, new parameterizations of the RMF models must take into account the density dependence of the symmetry energy through the inclusion of cross terms between the isoscalar mesons and the vector-isovector meson or other means.

We also highlight that such results change dramatically if we simply neglect from our analysis in SET2a and SET2b the constraint regarding the volume part of the isospin incompressibility, $K_{\tau,v}^0 \approx K_\tau = -550 \pm 150$ MeV. By applying the seven remaining constraints of SET2a, we found the following 35 approved models: BKA20, BKA22, BKA24, BSR8, BSR9, BSR10, BSR11, BSR12, BSR15, BSR16, BSR17, BSR18, BSR19, DD-ME δ , DD-F, DDH δ , FSU-III, FSU-IV, FSUGold, FSUGold4, FSUGZ03, FSUGZ06, G2*, IU-FSU, TW99, BSR20, FA3, Z271s2, Z271s3, Z271s4, Z271s5, Z271s6, Z271v4, Z271v5, and Z271v6. Notice that, besides the

cross-term models, other types of models are consistent with the SET2a constraints, namely, two density-dependent (DD-F, TW99), one point-coupling (FA3), and two δ meson models (DD-ME δ , DDH δ). The common feature of these models is that they do not include the simple symmetry energy density dependence present in all type 1, 2, and 3 models. The use of isospin-dependent properties in the fit procedure is essential to get a reasonable parametrization. For SET2b, the analysis leads to the same group of approved models excluding the BKA24, IU-FSU, DDH δ , BSR20, and FA3 models, totaling 30 consistent parametrizations. Notice that in this more restrictive set, one of the δ meson (DDH δ) models and the point-coupling model are excluded from the CRMF models. However, the density-dependent models DD-F and TW99 remain approved.

In the present work we have used the known physics of nuclear matter at densities around the saturation value to constrain relativistic models. However, these models have been extensively used to describe compact star constituents and macroscopic properties, such as radii and masses, and for this purpose have been extended to much higher densities. In this respect, the inclusion of other degrees of freedom, such as the lightest eight baryons, is energetically favored, but the onset of hyperons softens the equations of state and consequently reduces the maximum stellar masses [68]. Having in mind the description of two recently detected neutron stars with masses of the order of $2M_{\odot}$ [69,70], appropriate equations of state with the inclusion of hyperons were shown to strongly depend on the choice of the models and also on the hyperon-meson coupling constants [71–73]. After the comprehensive analyses performed in the present work, we suggest that the models that passed all tests be used in further studies involving the inclusion of hyperons in astrophysical applications.

We remark that there is still another class of relativistic models known as quark-meson-coupling models [74], in which baryons are described as a system of nonoverlapping MIT bags interacting through intermediate mesons. In these models, quark degrees of freedom are explicitly taken into account and the couplings are determined at the quark level. These models will also be examined according to the constraints proposed in the present work in a future investigation.

Finally, we reinforce that our work represents a unique effort to qualify the current RMFs and their usefulness for modeling of nuclear matter, which has never been done before. At present it is impossible to critically compare published results, obtained with a different selection of RMF models because nuclear matter properties are model dependent. Consistent use of a narrowed selection of approved RMF model should allow to improve the situation. Furthermore, the failure of many RMF models to satisfy the most up-to-date constraints should stimulate search for missing physics, which, when included, should lead to improvement of the models and their predictive power.

As a final remark concerning the analysis performed in the present work (RMF models), and in the previous one (nonrelativistic Skyrme models [5]), we highlight that it would be desirable to establish a unique protocol to study the predictive power of mean-field models (both relativistic and nonrelativistic) to deal not only with nuclear matter but also with finite nuclei. Actually, Stone and Reinhard outlined

a possible protocol for the Skyrme interaction in Sec. 5 of their review [43] by indicating the finite nuclei constraints that should be used to select Skyrme parametrizations, such as charge rms radius, spin-orbit splittings, neutron radii isotopic shifts, excitation properties, and others. Despite the fact that this procedure was developed for nonrelativistic models, it should also be applicable to RMF ones. Some of the entries should be updated, but the basic philosophy remains the same. One of the positive outcomes of such a work would be to learn more about surface properties of finite nuclei. It is well known that the crucial difference between finite nuclei and nuclear matter is the presence (or absence) of the nuclear surface, which plays a very important role, but is not yet well understood. Comparison of the properties of nuclear matter around saturation density and those of finite nuclei could yield valuable information in this direction. A preliminary study involving these ideas was performed in Ref. [75] for the Skyrme parametrizations selected in Ref. [5]. A more detailed study, also taking into account the selected RMF models presented here, will be addressed in a future work.

ACKNOWLEDGMENTS

This work was partially supported by CNPq (Brazil), CAPES (Brazil), and FAPESP (Brazil) under Project No. 2009/00069-5 and FAPESC (Brazil) under Project No. 2716/2012,TR 2012000344; by COMPETE/FEDER and FCT (Portugal) under Grant No. PTDC/FIS/113292/2009; and by NEW COMPSTAR, a COST initiative. M.D. acknowledges the hospitality at ITA/CTA and D.P.M. acknowledges the hospitality at the Universidad de Alicante, where parts of this work were carried out. S.T. is grateful for the support by the Helmholtz Association (HGF) through the Nuclear Astrophysics Virtual Institute (Grant No. VH-VI-417). J.R.S. wishes to thank D.M.’s group at Universidade Federal de Santa Catarina for its hospitality during her stay, made possible by CNPq Processo (Grant No. 401593/2009-6), when this project was initiated. O.L. acknowledges support from FAPESP.

APPENDIX A: ANALYTICAL EXPRESSIONS FOR INFINITE NUCLEAR MATTER QUANTITIES

In this Appendix, we show the analytical expressions of some quantities at $y = 1/2$ used to analyze the constraints of Sec. III related to RMF models of types 4 (nonlinear finite range), 5 (density dependent), and 6 (NLPC). The quantities are obtained at zero temperature and generalized to any density.

1. Finite-range models

The incompressibility is obtained as

$$\begin{aligned} K_{\text{NL}} &= 9 \left(\frac{\partial P_{\text{NL}}}{\partial \rho} \right)_{y=1/2} \\ &= 9 \left[g_{\omega} \rho \frac{\partial \omega_0}{\partial \rho} + \frac{k_F^2}{3(k_F^2 + M^{*2})^{1/2}} \right. \\ &\quad \left. + \frac{\rho M^{*}}{(k_F^2 + M^{*2})^{1/2}} \frac{\partial M^{*}}{\partial \rho} \right], \end{aligned} \quad (\text{A1})$$

where

$$\frac{\partial M^*}{\partial \rho} = -g_\sigma \frac{\partial \sigma}{\partial \rho}. \quad (\text{A2})$$

The skewness coefficient is

$$\begin{aligned} Q_{\text{NL}} &= 27\rho^3 \frac{\partial^3(\mathcal{E}_{\text{NL}}/\rho)}{\partial \rho^3} \Big|_{y=1/2} \\ &= 27\rho^3 \left[\frac{1}{\rho} \frac{\partial^3 \mathcal{E}_{\text{NL}}}{\partial \rho^3} - \frac{3}{\rho^2} \frac{\partial^2 \mathcal{E}_{\text{NL}}}{\partial \rho^2} + \frac{6}{\rho^3} \frac{\partial \mathcal{E}_{\text{NL}}}{\partial \rho} - \frac{6\mathcal{E}_{\text{NL}}}{\rho^4} \right] \Big|_{y=1/2}, \end{aligned} \quad (\text{A3})$$

with

$$\frac{\partial \mathcal{E}_{\text{NL}}}{\partial \rho} = (k_F^2 + M^{*2})^{1/2} + g_\omega \omega_0, \quad (\text{A4})$$

$$\frac{\partial^2 \mathcal{E}_{\text{NL}}}{\partial \rho^2} = g_\omega \frac{\partial \omega_0}{\partial \rho} + \frac{1}{2E_F^*} \left(\frac{\pi^2}{k_F} + 2M^* \frac{\partial M^*}{\partial \rho} \right), \quad \text{and} \quad (\text{A5})$$

$$\begin{aligned} \frac{\partial^3 \mathcal{E}_{\text{NL}}}{\partial \rho^3} &= g_\omega \frac{\partial^2 \omega_0}{\partial \rho^2} - \frac{1}{4E_F^{*3}} \left(\frac{\pi^2}{k_F} + 2M^* \frac{\partial M^*}{\partial \rho} \right)^2 \\ &\quad + \frac{1}{2E_F^*} \left[-\frac{\pi^4}{2k_F^4} + 2 \left(\frac{\partial M^*}{\partial \rho} \right)^2 + 2M^* \frac{\partial^2 M^*}{\partial \rho^2} \right]. \end{aligned} \quad (\text{A6})$$

The quantities \mathcal{E}_{NL} , $\frac{\partial \mathcal{E}_{\text{NL}}}{\partial \rho}$, $\frac{\partial^2 \mathcal{E}_{\text{NL}}}{\partial \rho^2}$, and $\frac{\partial^3 \mathcal{E}_{\text{NL}}}{\partial \rho^3}$ are evaluated at $y = 1/2$.

The slope and curvature of symmetry energy are given, respectively, by

$$L_{\text{NL}} = 3\rho \left(\frac{\partial \mathcal{S}_{\text{NL}}}{\partial \rho} \right) = \frac{k_F^2}{3E_F^*} - \frac{k_F^4}{6E_F^{*3}} \left(1 + \frac{2M^* k_F}{\pi^2} \frac{\partial M^*}{\partial \rho} \right) + \frac{3g_\rho^2}{8m_\rho^{*2}} \rho - \frac{3g_\rho^2}{8m_\rho^{*4}} \frac{\partial m_\rho^{*2}}{\partial \rho} \rho^2 \quad (\text{A7})$$

and

$$\begin{aligned} K_{\text{sym}}^{\text{NL}} &= 9\rho^2 \left(\frac{\partial^2 \mathcal{S}_{\text{NL}}}{\partial \rho^2} \right) = 9\rho^2 \left\{ -\frac{\pi^2}{12E_F^{*3}k_F} \left(\frac{\pi^2}{k_F} + 2M^* \frac{\partial M^*}{\partial \rho} \right) - \frac{\pi^4}{12E_F^*k_F^4} - \frac{g_\rho^2}{4m_\rho^{*4}} \frac{\partial m_\rho^{*2}}{\partial \rho} \right. \\ &\quad - \left[\frac{\pi^4}{24E_F^{*3}k_F^2} - \frac{k_F \pi^2}{8E_F^{*5}} \left(\frac{\pi^2}{k_F} + 2M^* \frac{\partial M^*}{\partial \rho} \right) \right] \left(1 + \frac{2M^* k_F}{\pi^2} \frac{\partial M^*}{\partial \rho} \right) + \frac{g_\rho^2}{4m_\rho^{*6}} \left(\frac{\partial m_\rho^{*2}}{\partial \rho} \right)^2 \rho \\ &\quad \left. - \frac{k_F \pi^2}{12E_F^{*3}} \left[\frac{M^*}{k_F^2} \frac{\partial M^*}{\partial \rho} + \frac{2k_F}{\pi^2} \left(\frac{\partial M^*}{\partial \rho} \right)^2 + \frac{2k_F M^*}{\pi^2} \frac{\partial^2 M^*}{\partial \rho^2} \right] - \frac{g_\rho^2}{8m_\rho^{*4}} \frac{\partial^2 m_\rho^{*2}}{\partial \rho^2} \rho \right\}. \end{aligned} \quad (\text{A8})$$

For SNM, where $y = 1/2$ and $\bar{\rho}_{0(3)} = 0$, the density derivatives of σ and ω_0 are given by

$$\frac{\partial \sigma}{\partial \rho} = \frac{a_1 b_2 + a_2 b_3}{a_1 b_1 - a_3 b_3} \quad \text{and} \quad \frac{\partial \omega_0}{\partial \rho} = \frac{a_2 b_1 + a_3 b_2}{a_1 b_1 - a_3 b_3}, \quad (\text{A9})$$

where

$$a_1 = m_\omega^2 + 3cg_\omega^4 \omega_0^2 + g_\sigma g_\omega^2 \sigma (2\alpha_1 + \alpha'_1 g_\sigma \sigma), \quad (\text{A10})$$

$$a_2 = g_\omega, \quad (\text{A11})$$

$$a_3 = -2g_\sigma g_\omega^2 \omega_0 (\alpha_1 + \alpha'_1 g_\sigma \sigma), \quad (\text{A12})$$

$$b_1 = m_\sigma^2 + 2A\sigma + 3B\sigma^2 - g_\sigma^2 g_\omega^2 \omega_0^2 \alpha'_1$$

$$+ 3g_\sigma^2 \left(\frac{\rho_s}{M^*} - \frac{\rho}{E_F^*} \right), \quad (\text{A13})$$

For the sake of completeness, we also present the proton and neutron chemical potentials,

$$\begin{aligned} \mu_p^{\text{NL}} &= \frac{\partial \mathcal{E}_{\text{NL}}}{\partial \rho_p} = (k_F^2 + M^{*2})^{1/2} + g_\omega \omega_0 \\ &\quad + \frac{g_\rho}{2} \bar{\rho}_{0(3)} \quad \text{and} \end{aligned} \quad (\text{A16})$$

$$\mu_n^{\text{NL}} = \frac{\partial \mathcal{E}_{\text{NL}}}{\partial \rho_n} = (k_F^2 + M^{*2})^{1/2} + g_\omega \omega_0 - \frac{g_\rho}{2} \bar{\rho}_{0(3)}, \quad (\text{A17})$$

both at any density and proton fraction y .

2. Density-dependent models

The incompressibility is

$$\begin{aligned} K_{\text{DD}} &= 9 \left(\frac{\partial P_{\text{DD}}}{\partial \rho} \right)_{y=1/2} \\ &= 9 \left[\rho \frac{\partial \Sigma_R}{\partial \rho} + \omega_0 \rho \frac{\partial \Gamma_\omega}{\partial \rho} + \Gamma_\omega \rho \frac{\partial \omega_0}{\partial \rho} + \frac{k_F^2}{3(k_F^2 + M^{*2})^{1/2}} + \frac{\rho M^*}{(k_F^2 + M^{*2})^{1/2}} \frac{\partial M^*}{\partial \rho} \right] \\ &= 9 \left[\rho \frac{\partial \Sigma_R}{\partial \rho} + \frac{2\Gamma_\omega \rho^2}{m_\omega^2} \frac{\partial \Gamma_\omega}{\partial \rho} + \frac{\Gamma_\omega^2 \rho}{m_\omega^2} + \frac{k_F^2}{3(k_F^2 + M^{*2})^{1/2}} + \frac{\rho M^*}{(k_F^2 + M^{*2})^{1/2}} \frac{\partial M^*}{\partial \rho} \right], \end{aligned} \quad (\text{A18})$$

with

$$\frac{\partial M^*}{\partial \rho} = - \left(\Gamma_\sigma \frac{\partial \sigma}{\partial \rho} + \sigma \frac{\partial \Gamma_\sigma}{\partial \rho} \right) \quad \text{and} \quad (\text{A19})$$

$$\frac{\partial \sigma}{\partial \rho} = \frac{\left[\rho_s - 3 \left(\frac{\rho_s}{M^*} - \frac{\rho}{E_F^*} \right) \Gamma_\sigma \sigma \right] \frac{\partial \Gamma_\sigma}{\partial \rho} + \frac{\Gamma_\sigma M^*}{E_F^*}}{m_\sigma^2 + 3 \left(\frac{\rho_s}{M^*} - \frac{\rho}{E_F^*} \right) \Gamma_\sigma^2}, \quad (\text{A20})$$

observing that $\omega_0 = \frac{\Gamma_\omega \rho}{m_\omega^2}$ and $\sigma = \frac{\Gamma_\sigma \rho_s}{m_\sigma^2}$.

The skewness coefficient is

$$Q_{\text{DD}} = 27\rho^3 \frac{\partial^3(\mathcal{E}_{\text{DD}}/\rho)}{\partial \rho^3} \Big|_{y=1/2} = 27\rho^3 \left[\frac{1}{\rho} \frac{\partial^3 \mathcal{E}_{\text{DD}}}{\partial \rho^3} - \frac{3}{\rho^2} \frac{\partial^2 \mathcal{E}_{\text{DD}}}{\partial \rho^2} + \frac{6}{\rho^3} \frac{\partial \mathcal{E}_{\text{DD}}}{\partial \rho} - \frac{6\mathcal{E}_{\text{DD}}}{\rho^4} \right]_{y=1/2}, \quad (\text{A21})$$

with

$$\frac{\partial \mathcal{E}_{\text{DD}}}{\partial \rho} = (k_F^2 + M^{*2})^{1/2} + \frac{\Gamma_\omega^2}{m_\omega^2} \rho + \bar{\Sigma}_R, \quad (\text{A22})$$

$$\frac{\partial^2 \mathcal{E}_{\text{DD}}}{\partial \rho^2} = \frac{1}{2E_F^*} \left(\frac{\pi^2}{k_F} + 2M^* \frac{\partial M^*}{\partial \rho} \right) + \frac{\Gamma_\omega^2}{m_\omega^2} + \frac{2\Gamma_\omega \rho}{m_\omega^2} \frac{\partial \Gamma_\omega}{\partial \rho} + \frac{\partial \bar{\Sigma}_R}{\partial \rho}, \quad \text{and} \quad (\text{A23})$$

$$\begin{aligned} \frac{\partial^3 \mathcal{E}_{\text{DD}}}{\partial \rho^3} &= -\frac{1}{4E_F^{*3}} \left(\frac{\pi^2}{k_F} + 2M^* \frac{\partial M^*}{\partial \rho} \right)^2 + \frac{1}{2E_F^*} \left[-\frac{\pi^4}{2k_F^4} + 2 \left(\frac{\partial M^*}{\partial \rho} \right)^2 + 2M^* \frac{\partial^2 M^*}{\partial \rho^2} \right] \\ &\quad + \frac{2\Gamma_\omega \rho}{m_\omega^2} \frac{\partial^2 \Gamma_\omega}{\partial \rho^2} + \frac{2\rho}{m_\omega^2} \left(\frac{\partial \Gamma_\omega}{\partial \rho} \right)^2 + \frac{4\Gamma_\omega}{m_\omega^2} \frac{\partial \Gamma_\omega}{\partial \rho} + \frac{\partial^2 \bar{\Sigma}_R}{\partial \rho^2}, \end{aligned} \quad (\text{A24})$$

where

$$\bar{\Sigma}_R = \Sigma_R(y=1/2) = \frac{\Gamma_\omega \rho^2}{m_\omega^2} \frac{\partial \Gamma_\omega}{\partial \rho} - \frac{\Gamma_\sigma \rho_s^2}{m_\sigma^2} \frac{\partial \Gamma_\sigma}{\partial \rho}, \quad (\text{A25})$$

$$\frac{\partial^2 M^*}{\partial \rho^2} = - \left(\Gamma_\sigma \frac{\partial^2 \sigma}{\partial \rho^2} + \sigma \frac{\partial^2 \Gamma_\sigma}{\partial \rho^2} \right) - 2 \frac{\partial \Gamma_\sigma}{\partial \rho} \frac{\partial \sigma}{\partial \rho}, \quad (\text{A26})$$

$$\begin{aligned} \frac{\partial^2 \sigma}{\partial \rho^2} &= \left[(\rho_s - \mathcal{J} \Gamma_\sigma \sigma) \frac{\partial^2 \Gamma_\sigma}{\partial \rho^2} + \left(\frac{\partial \rho_s}{\partial \rho} - \Gamma_\sigma \sigma \frac{\partial \mathcal{J}}{\partial \rho} - \mathcal{J} \sigma \frac{\partial \Gamma_\sigma}{\partial \rho} - \mathcal{J} \Gamma_\sigma \frac{\partial \sigma}{\partial \rho} \right) \frac{\partial \Gamma_\sigma}{\partial \rho} + \frac{M^*}{E_F^*} \frac{\partial \Gamma_\sigma}{\partial \rho} \right. \\ &\quad \left. + \frac{\Gamma_\sigma}{E_F^*} \frac{\partial M^*}{\partial \rho} - \frac{\Gamma_\sigma M^*}{E_F^{*2}} \frac{\partial E_F^*}{\partial \rho} \right] (m_\sigma^2 + \mathcal{J} \Gamma_\sigma^2)^{-1} - \left[(\rho_s - \mathcal{J} \Gamma_\sigma \sigma) \frac{\partial \Gamma_\sigma}{\partial \rho} + \frac{\Gamma_\sigma M^*}{E_F^*} \right] \left[\frac{\partial \mathcal{J}}{\partial \rho} \Gamma_\sigma^2 + 2\mathcal{J} \Gamma_\sigma \frac{\partial \Gamma_\sigma}{\partial \rho} \right] (m_\sigma^2 + \mathcal{J} \Gamma_\sigma^2)^{-2}, \end{aligned} \quad (\text{A27})$$

$$\mathcal{J} = 3 \left(\frac{\rho_s}{M^*} - \frac{\rho}{E_F^*} \right), \quad (\text{A28})$$

$$\frac{\partial E_F^*}{\partial \rho} = \frac{\pi^2}{2E_F^* k_F} \left(1 + \frac{2M^* k_F}{\pi^2} \frac{\partial M^*}{\partial \rho} \right), \quad (\text{A29})$$

$$\begin{aligned} \frac{\partial^2 \bar{\Sigma}_R}{\partial \rho^2} = & \frac{\Gamma_\omega \rho^2}{m_\omega^2} \frac{\partial^3 \Gamma_\omega}{\partial \rho^3} + \frac{4\Gamma_\omega \rho}{m_\omega^2} \frac{\partial^2 \Gamma_\omega}{\partial \rho^2} + \frac{3\rho^2}{m_\omega^2} \frac{\partial \Gamma_\omega}{\partial \rho} \frac{\partial^2 \Gamma_\omega}{\partial \rho^2} + \frac{4\rho}{m_\omega^2} \left(\frac{\partial \Gamma_\omega}{\partial \rho} \right)^2 + \frac{2\Gamma_\omega}{m_\omega^2} \frac{\partial \Gamma_\omega}{\partial \rho} \\ & - \frac{\Gamma_\sigma \rho_s^2}{m_\sigma^2} \frac{\partial^3 \Gamma_\sigma}{\partial \rho^3} - \frac{4\Gamma_\sigma \rho_s}{m_\sigma^2} \frac{\partial \rho_s}{\partial \rho} \frac{\partial^2 \Gamma_\sigma}{\partial \rho^2} - \frac{3\rho_s^2}{m_\sigma^2} \frac{\partial \Gamma_\sigma}{\partial \rho} \frac{\partial^2 \Gamma_\sigma}{\partial \rho^2} - \frac{4\rho_s}{m_\sigma^2} \frac{\partial \rho_s}{\partial \rho} \left(\frac{\partial \Gamma_\sigma}{\partial \rho} \right)^2 \\ & - \frac{2\Gamma_\sigma}{m_\sigma^2} \left(\frac{\partial \rho_s}{\partial \rho} \right)^2 \frac{\partial \Gamma_\sigma}{\partial \rho} - \frac{2\Gamma_\sigma \rho_s}{m_\sigma^2} \frac{\partial^2 \rho_s}{\partial \rho^2} \frac{\partial \Gamma_\sigma}{\partial \rho}, \end{aligned} \quad (\text{A30})$$

$$\frac{\partial \rho_s}{\partial \rho} = \frac{M^*}{E_F^*} - \mathcal{J} \left(\sigma \frac{\partial \Gamma_\sigma}{\partial \rho} + \Gamma_\sigma \frac{\partial \sigma}{\partial \rho} \right), \quad (\text{A31})$$

and

$$\frac{\partial^2 \rho_s}{\partial \rho^2} = \frac{1}{E_F^*} \frac{\partial M^*}{\partial \rho} - \frac{M^*}{E_F^{*2}} \frac{\partial E_F^*}{\partial \rho} - \mathcal{J} \left(\sigma \frac{\partial^2 \Gamma_\sigma}{\partial \rho^2} + 2 \frac{\partial \Gamma_\sigma}{\partial \rho} \frac{\partial \sigma}{\partial \rho} + \Gamma_\sigma \frac{\partial^2 \sigma}{\partial \rho^2} \right) - \frac{\partial \mathcal{J}}{\partial \rho} \left(\sigma \frac{\partial \Gamma_\sigma}{\partial \rho} + \Gamma_\sigma \frac{\partial \sigma}{\partial \rho} \right). \quad (\text{A32})$$

The slope and curvature of \mathcal{S}_{DD} are

$$L_{\text{DD}} = 3\rho \left(\frac{\partial \mathcal{S}_{\text{DD}}}{\partial \rho} \right) = \frac{k_F^2}{3E_F^*} - \frac{k_F^4}{6E_F^{*3}} \left(1 + \frac{2M^* k_F}{\pi^2} \frac{\partial M^*}{\partial \rho} \right) + \frac{3\Gamma_\rho^2}{8m_\rho^2} \rho + \frac{3\Gamma_\rho}{4m_\rho^2} \frac{\partial \Gamma_\rho}{\partial \rho} \rho^2 \quad (\text{A33})$$

and

$$\begin{aligned} K_{\text{sym}}^{\text{DD}} = 9\rho^2 \left(\frac{\partial^2 \mathcal{S}_{\text{DD}}}{\partial \rho^2} \right) = & 9\rho^2 \left\{ -\frac{\pi^2}{12E_F^{*3}k_F} \left(\frac{\pi^2}{k_F} + 2M^* \frac{\partial M^*}{\partial \rho} \right) - \frac{\pi^4}{12E_F^* k_F^4} + \frac{\Gamma_\rho}{2m_\rho^2} \frac{\partial \Gamma_\rho}{\partial \rho} \right. \\ & - \left[\frac{\pi^4}{24E_F^{*3}k_F^2} - \frac{k_F \pi^2}{8E_F^{*5}} \left(\frac{\pi^2}{k_F} + 2M^* \frac{\partial M^*}{\partial \rho} \right) \right] \left(1 + \frac{2M^* k_F}{\pi^2} \frac{\partial M^*}{\partial \rho} \right) + \frac{\rho}{4m_\rho^2} \left(\frac{\partial \Gamma_\rho}{\partial \rho} \right)^2 \\ & \left. - \frac{k_F \pi^2}{12E_F^{*3}} \left[\frac{M^* \partial M^*}{k_F^2 \partial \rho} + \frac{2k_F}{\pi^2} \left(\frac{\partial M^*}{\partial \rho} \right)^2 + \frac{2k_F M^* \partial^2 M^*}{\pi^2 \partial \rho^2} \right] + \frac{\Gamma_\rho \rho}{4m_\rho^2} \frac{\partial^2 \Gamma_\rho}{\partial \rho^2} \right\}. \end{aligned} \quad (\text{A34})$$

The chemical potentials for any proton fraction are

$$\mu_p^{\text{DD}} = \frac{\partial \mathcal{E}_{\text{DD}}}{\partial \rho_p} = (k_F^2 + M^{*2})^{1/2} + \Gamma_\omega \omega_0 + \frac{\Gamma_\rho}{2} \bar{\rho}_{0(3)} + \Sigma_R \quad \text{and} \quad (\text{A35})$$

$$\mu_n^{\text{DD}} = \frac{\partial \mathcal{E}_{\text{DD}}}{\partial \rho_n} = (k_F^2 + M^{*2})^{1/2} + \Gamma_\omega \omega_0 - \frac{\Gamma_\rho}{2} \bar{\rho}_{0(3)} + \Sigma_R. \quad (\text{A36})$$

3. Point-coupling models

For NLPC models, the incompressibility reads

$$\begin{aligned} K_{\text{NLPC}} = 9 \left(\frac{\partial P_{\text{NLPC}}}{\partial \rho} \right)_{y=1/2} = & 9 \left[\alpha_V \rho + 3\gamma_V \rho^3 + \frac{k_F^2}{3(k_F^2 + M^{*2})^{1/2}} + \frac{\rho M^*}{(k_F^2 + M^{*2})^{1/2}} \frac{\partial M^*}{\partial \rho} \right. \\ & \left. + 2(\eta_1 + 2\eta_2 \rho_s) \rho_s \rho + 2(\eta_1 + 2\eta_2 \rho_s) \rho^2 \frac{\partial \rho_s}{\partial \rho} \right], \end{aligned} \quad (\text{A37})$$

where

$$\frac{\partial M^*}{\partial \rho} = \frac{2(\eta_1 + 2\eta_2 \rho_s) \rho + \frac{M^*}{E_F^*} (\alpha_s + 2\beta_s \rho_s + 3\gamma_s \rho_s^2 + 2\eta_2 \rho^2)}{1 - 3(\alpha_s + 2\beta_s \rho_s + 3\gamma_s \rho_s^2 + 2\eta_2 \rho^2) \left(\frac{\rho_s}{M^*} - \frac{\rho}{E_F^*} \right)}, \quad (\text{A38})$$

$$\frac{\partial \rho_s}{\partial \rho} = \frac{M^*}{(k_F^2 + M^{*2})^{1/2}} + 3 \left(\frac{\rho_s}{M^*} - \frac{\rho}{E_F^*} \right) \frac{\partial M^*}{\partial \rho}. \quad (\text{A39})$$

The skewness coefficient is

$$\begin{aligned} Q_{\text{NLPC}} &= 27\rho^3 \frac{\partial^3(\mathcal{E}_{\text{NLPC}}/\rho)}{\partial\rho^3} \Big|_{y=1/2} \\ &= 27\rho^3 \left[\frac{1}{\rho} \frac{\partial^3\mathcal{E}_{\text{NLPC}}}{\partial\rho^3} - \frac{3}{\rho^2} \frac{\partial^2\mathcal{E}_{\text{NLPC}}}{\partial\rho^2} + \frac{6}{\rho^3} \frac{\partial\mathcal{E}_{\text{NLPC}}}{\partial\rho} - \frac{6\mathcal{E}_{\text{NLPC}}}{\rho^4} \right]_{y=1/2}, \end{aligned} \quad (\text{A40})$$

with

$$\frac{\partial\mathcal{E}_{\text{NLPC}}}{\partial\rho} = (k_F^2 + M^{*2})^{1/2} + \alpha_V\rho + \gamma_V\rho^3 + 2(\eta_1 + \eta_2\rho_s)\rho_s\rho, \quad (\text{A41})$$

$$\begin{aligned} \frac{\partial^2\mathcal{E}_{\text{NLPC}}}{\partial\rho^2} &= \frac{1}{2E_F^*} \left(\frac{\pi^2}{k_F} + 2M^* \frac{\partial M^*}{\partial\rho} \right) + \alpha_V + 3\gamma_V\rho^2 + 2(\eta_1 + 2\eta_2\rho_s)\rho \frac{\partial\rho_s}{\partial\rho} \\ &\quad + 2(\eta_1 + \eta_2\rho_s)\rho_s, \quad \text{and} \end{aligned} \quad (\text{A42})$$

$$\begin{aligned} \frac{\partial^3\mathcal{E}_{\text{NLPC}}}{\partial\rho^3} &= -\frac{1}{4E_F^{*3}} \left(\frac{\pi^2}{k_F} + 2M^* \frac{\partial M^*}{\partial\rho} \right)^2 + \frac{1}{2E_F^*} \left[-\frac{\pi^4}{2k_F^4} + 2 \left(\frac{\partial M^*}{\partial\rho} \right)^2 + 2M^* \frac{\partial^2 M^*}{\partial\rho^2} \right] \\ &\quad + 6\gamma_V\rho + 4(\eta_1 + 2\eta_2\rho_s) \frac{\partial\rho_s}{\partial\rho} + 4\eta_2\rho \left(\frac{\partial\rho_s}{\partial\rho} \right)^2 + 2(\eta_1 + 2\eta_2\rho_s)\rho \frac{\partial^2\rho_s}{\partial\rho^2}. \end{aligned} \quad (\text{A43})$$

The slope and curvature of $\mathcal{S}_{\text{NLPC}}$ are

$$\begin{aligned} L_{\text{NLPC}} &= 3\rho \left(\frac{\partial\mathcal{S}_{\text{NLPC}}}{\partial\rho} \right) \\ &= \frac{k_F^2}{3E_F^*} - \frac{k_F^4}{6E_F^{*3}} \left(1 + \frac{2M^*k_F}{\pi^2} \frac{\partial M^*}{\partial\rho} \right) + \frac{3}{2}\alpha_{\text{TV}}\rho + 3\eta_3\rho_s\rho + 3\eta_3\rho^2 \frac{\partial\rho_s}{\partial\rho} \end{aligned} \quad (\text{A44})$$

and

$$\begin{aligned} K_{\text{sym}}^{\text{NLPC}} &= 9\rho^2 \left(\frac{\partial^2\mathcal{S}_{\text{NLPC}}}{\partial\rho^2} \right) = 9\rho^2 \left\{ -\frac{\pi^2}{12E_F^{*3}k_F} \left(\frac{\pi^2}{k_F} + 2M^* \frac{\partial M^*}{\partial\rho} \right) - \frac{\pi^4}{12E_F^*k_F^4} + 2\eta_3 \frac{\partial\rho_s}{\partial\rho} \right. \\ &\quad - \left[\frac{\pi^4}{24E_F^{*3}k_F^2} - \frac{k_F\pi^2}{8E_F^{*5}} \left(\frac{\pi^2}{k_F} + 2M^* \frac{\partial M^*}{\partial\rho} \right) \right] \left(1 + \frac{2M^*k_F}{\pi^2} \frac{\partial M^*}{\partial\rho} \right) + \eta_3\rho \frac{\partial^2\rho_s}{\partial\rho^2} \\ &\quad \left. - \frac{k_F\pi^2}{12E_F^{*3}} \left[\frac{M^*}{k_F^2} \frac{\partial M^*}{\partial\rho} + \frac{2k_F}{\pi^2} \left(\frac{\partial M^*}{\partial\rho} \right)^2 + \frac{2k_FM^*}{\pi^2} \frac{\partial^2 M^*}{\partial\rho^2} \right] \right\}. \end{aligned} \quad (\text{A45})$$

The chemical potentials for any proton fraction are

$$\begin{aligned} \mu_p^{\text{NLPC}} &= \frac{\partial\mathcal{E}_{\text{NLPC}}}{\partial\rho_p} \\ &= (k_F^2 + M^{*2})^{1/2} + \alpha_V\rho + \gamma_V\rho^3 + \alpha_{\text{TV}}\rho_3 + \gamma_{\text{TV}}\rho_3^3 + 2\eta_1\rho_s\rho + 2\eta_2\rho_s^2\rho + 2\eta_3\rho_s\rho_3, \end{aligned} \quad (\text{A46})$$

$$\begin{aligned} \mu_n^{\text{NLPC}} &= \frac{\partial\mathcal{E}_{\text{NLPC}}}{\partial\rho_n} \\ &= (k_F^2 + M^{*2})^{1/2} + \alpha_V\rho + \gamma_V\rho^3 - \alpha_{\text{TV}}\rho_3 - \gamma_{\text{TV}}\rho_3^3 + 2\eta_1\rho_s\rho + 2\eta_2\rho_s^2\rho - 2\eta_3\rho_s\rho_3. \end{aligned} \quad (\text{A47})$$

APPENDIX B: SATURATION PROPERTIES

TABLE VII. Saturation properties of all RMF models used in this work. All quantities are given in MeV, except for the dimensionless effective mass, $m^* = M^*/M$, and the saturation density ρ_0 , given in fm $^{-3}$. Here $K' = -Q_0$.

Model	ρ_0	E_0	K_0	m^*	K'	J	L_0	K_{sym}^0	Q_{sym}^0	$K_{\tau,v}^0$
Linear finite-range models (type 1)										
H1 [76]	0.148	-15.75	546.81	0.54	-2152.62	25.93	88.38	93.56	-538.40	-784.64
L1 [77]	0.177	-18.52	625.56	0.53	-2229.20	21.68	75.64	81.88	-786.15	-641.56
L2 [77]	0.142	-16.78	578.49	0.53	-2323.13	19.07	68.81	97.43	-605.30	-591.73
L3 [77]	0.134	-18.24	624.53	0.52	-2568.70	18.86	69.52	102.17	-709.63	-600.92
LBF [78]	0.152	-17.01	584.18	0.53	-2261.30	46.92	151.91	92.59	-640.84	-1406.85
LHS [77]	0.148	-15.79	548.10	0.54	-2157.94	34.99	115.60	93.62	-541.51	-1055.08
LW [77]	0.194	-15.75	545.55	0.56	-1877.70	22.11	74.44	74.96	-604.39	-627.91
LZ [77]	0.149	-17.07	586.34	0.53	-2296.35	48.84	157.90	94.34	-638.92	-1471.42
RMF201 [79]	0.153	-16.30	577.84	0.54	-2160.72	32.50	108.36	92.22	-607.65	-963.16
RMF202 [79]	0.153	-16.30	571.55	0.54	-2169.45	32.50	108.29	92.16	-598.81	-968.59
RMF203 [79]	0.153	-16.30	565.30	0.54	-2178.08	32.50	108.21	92.10	-590.05	-974.11
RMF204 [79]	0.153	-16.30	559.08	0.54	-2186.61	32.50	108.14	92.03	-581.37	-979.73
RMF205 [79]	0.153	-16.30	552.90	0.54	-2195.05	32.50	108.06	91.95	-572.77	-985.43
RMF206 [79]	0.153	-16.30	546.75	0.54	-2203.39	32.50	107.99	91.87	-564.24	-991.23
$\sigma^3 + \sigma^4$ models (type 2)										
CS [80]	0.150	-16.17	187.21	0.58	292.63	40.91	131.42	136.68	514.05	-446.40
E [80]	0.150	-16.13	221.43	0.58	-20.87	38.58	124.57	132.12	381.38	-627.06
ER [80]	0.149	-16.16	220.49	0.58	24.93	39.42	126.60	127.62	377.17	-617.67
FAMA1 [21]	0.148	-16.00	200.05	0.60	303.20	38.01	120.53	113.22	403.17	-427.27
FAMA2 [21]	0.148	-16.00	225.07	0.60	117.70	38.01	120.28	107.02	314.30	-551.75
FAMA3 [21]	0.148	-16.00	250.08	0.60	-52.65	38.01	120.03	100.99	233.23	-644.48
FAMA4 [21]	0.148	-16.00	275.09	0.60	-208.08	38.01	119.79	95.11	159.52	-714.23
FAMA5 [21]	0.148	-16.00	300.09	0.60	-348.82	38.01	119.54	89.40	92.81	-766.83
FAMB1 [21]	0.148	-16.00	200.03	0.70	593.95	37.01	108.39	33.10	157.33	-295.40
FAMB2 [21]	0.148	-16.00	225.05	0.70	465.50	37.01	108.20	29.15	115.82	-396.24
FAMB3 [21]	0.148	-16.00	250.05	0.70	355.71	37.01	108.01	25.36	80.03	-469.06
FAMB4 [21]	0.148	-16.00	275.06	0.70	264.20	37.01	107.82	21.70	49.50	-521.67
FAMB5 [21]	0.148	-16.00	300.06	0.70	190.59	37.01	107.64	18.19	23.84	-559.26
FAMC1 [21]	0.148	-16.00	200.03	0.70	593.95	28.01	81.38	33.10	157.33	-213.55
FAMC2 [21]	0.148	-16.00	225.05	0.70	465.50	28.01	81.19	29.15	115.82	-290.06
FAMC3 [21]	0.148	-16.00	250.05	0.70	355.71	28.01	81.01	25.36	80.03	-345.45
FAMC4 [21]	0.148	-16.00	275.06	0.70	264.20	28.00	80.82	21.70	49.50	-385.58
FAMC5 [21]	0.148	-16.00	300.06	0.70	190.59	28.00	80.63	18.19	23.84	-414.39
GL1 [68]	0.153	-16.30	199.97	0.70	618.94	32.49	94.66	33.06	161.40	-241.92
GL2 [68]	0.153	-16.30	200.04	0.75	608.35	32.51	91.54	8.75	100.11	-262.10
GL3 [68]	0.153	-16.31	200.07	0.80	580.33	32.51	89.06	-8.43	73.41	-284.44
GL4 [68]	0.153	-16.31	250.07	0.70	380.57	32.51	94.34	25.25	82.58	-397.20
GL5 [68]	0.153	-16.31	250.11	0.75	454.87	32.51	91.22	2.64	54.13	-378.79
GL6 [68]	0.153	-16.31	250.06	0.80	547.49	32.51	88.75	-12.93	54.23	-351.11
GL7 [68]	0.153	-16.31	300.09	0.75	384.54	32.51	90.88	-2.91	25.94	-431.71
GL8 [68]	0.153	-16.31	300.07	0.80	610.91	32.51	88.45	-16.84	48.32	-367.47
GL82 [81]	0.145	-16.00	285.74	0.77	450.64	36.23	101.31	-8.06	35.32	-456.14
GL9 [68]	0.153	-16.31	210.08	0.78	564.87	32.51	89.91	-3.37	73.17	-301.09
GM1 [82]	0.153	-16.33	300.50	0.70	215.66	32.52	94.02	17.98	25.01	-478.64
GM2 [82]	0.153	-16.31	300.10	0.78	506.35	32.51	89.35	-12.00	37.19	-397.34
GM3 [82]	0.153	-16.30	240.04	0.78	512.46	32.51	89.72	-6.46	55.69	-353.24
GPS [83]	0.150	-15.96	299.59	0.80	590.98	32.49	88.57	-16.41	46.81	-373.11
Hybrid [84]	0.148	-16.24	230.01	0.60	71.51	37.30	118.62	110.94	314.21	-563.91
MS2 [85]	0.148	-15.75	249.92	0.60	-75.88	35.00	111.00	100.85	228.29	-598.88
NL-VT1 [86]	0.150	-16.09	179.03	0.60	488.02	39.03	123.63	117.72	483.16	-287.07
NL ρ [87]	0.160	-16.05	240.76	0.75	464.60	30.37	84.60	3.36	61.34	-341.00

TABLE VII. (*Continued.*)

Model	ρ_0	E_0	K_0	m^*	K'	J	L_0	K_{sym}^0	Q_{sym}^0	$K_{\tau,v}^0$
NL06 [78]	0.147	-16.05	195.09	0.60	367.03	39.33	124.14	110.85	412.35	-400.47
NL065 [78]	0.150	-16.37	256.86	0.65	220.00	38.98	117.77	55.86	132.74	-549.91
NL07 [78]	0.150	-16.49	276.45	0.70	296.13	38.52	112.30	21.58	51.65	-531.94
NL075 [78]	0.151	-16.64	281.12	0.75	418.96	38.96	110.44	-0.54	35.98	-498.61
NL1 [77]	0.152	-16.42	211.09	0.57	32.69	43.46	140.07	142.68	444.67	-676.04
NL1J4 [88]	0.152	-16.42	211.70	0.57	-3.91	40.00	130.06	146.26	448.71	-636.53
NL1J5 [88]	0.152	-16.42	211.70	0.57	-3.91	50.00	160.06	146.26	448.71	-817.08
NL2 [77]	0.146	-17.03	399.37	0.67	-68.42	43.86	129.66	20.10	-51.87	-780.04
NL3 [89]	0.148	-16.24	271.53	0.60	-202.91	37.40	118.53	100.88	181.31	-698.85
NL3-II [89]	0.149	-16.26	271.72	0.59	-222.71	37.70	119.71	103.43	183.75	-712.92
NL3* [90]	0.150	-16.31	258.25	0.59	-122.04	38.68	122.63	105.56	223.95	-688.19
NL4 [91]	0.148	-16.16	270.34	0.60	-193.75	36.24	114.92	99.72	180.84	-672.14
NLB [92]	0.148	-15.77	421.02	0.61	-727.93	35.01	108.26	54.94	-132.35	-781.79
NLB1 [77]	0.162	-15.79	280.44	0.62	-108.61	33.04	102.51	76.15	107.80	-578.59
NLB2 [77]	0.163	-15.79	245.58	0.55	-542.60	33.10	111.30	158.94	289.13	-754.77
NLC [92]	0.148	-15.77	224.46	0.63	278.13	35.02	107.97	76.91	235.59	-437.12
NLD [93]	0.148	-15.77	343.21	0.70	75.49	35.01	101.52	13.53	-12.22	-573.26
NLM [88]	0.160	-16.00	200.00	0.70	600.49	30.00	87.02	33.20	161.25	-227.65
NLM2 [88]	0.160	-17.00	200.00	0.70	675.54	30.00	86.95	33.27	170.92	-194.74
NLM3 [88]	0.145	-16.00	200.00	0.70	591.82	30.00	87.45	33.01	156.01	-232.93
NLM4 [88]	0.160	-16.00	300.00	0.70	196.02	30.00	86.25	17.69	22.57	-443.46
NLM5 [88]	0.160	-16.00	200.00	0.55	-216.98	30.00	103.18	179.44	524.64	-551.60
NLM6 [88]	0.160	-16.00	200.00	0.70	600.49	40.00	117.02	33.20	161.24	-317.57
NLRA [94]	0.157	-16.25	320.48	0.63	-216.23	38.90	119.09	62.11	26.63	-732.77
NLRA1 [95]	0.147	-16.15	285.23	0.60	-279.28	36.45	115.38	95.72	139.44	-709.55
NLS [96]	0.150	-16.44	262.94	0.60	-57.53	42.07	131.59	94.22	195.27	-724.10
NLSH [89]	0.146	-16.36	355.65	0.60	-602.90	36.13	113.68	79.83	-23.79	-795.00
NLZ [86]	0.151	-16.18	172.84	0.58	422.59	41.72	133.91	140.19	577.02	-335.86
NLZ2 [86]	0.151	-16.06	172.23	0.58	412.31	39.01	125.82	140.62	577.35	-313.10
P-067 [97]	0.157	-16.31	231.63	0.67	413.34	41.07	122.33	46.33	151.24	-469.38
P-070 [97]	0.163	-16.25	245.07	0.70	396.44	41.85	122.35	27.75	93.48	-508.45
P-075 [97]	0.173	-16.51	271.29	0.75	439.84	42.95	121.48	-1.98	43.56	-533.91
P-080 [97]	0.162	-15.84	259.93	0.80	529.34	39.63	109.78	-14.16	52.52	-449.29
Q1 [98]	0.148	-16.10	241.86	0.60	-8.70	36.44	115.71	105.65	266.72	-592.77
RMF301 [79]	0.153	-16.30	253.86	0.78	489.08	32.50	89.87	-6.25	49.30	-372.34
RMF302 [79]	0.153	-16.30	249.71	0.78	502.35	32.50	89.66	-7.35	51.33	-364.94
RMF303 [79]	0.153	-16.30	248.88	0.78	504.91	32.50	89.62	-7.57	51.73	-363.46
RMF304 [79]	0.153	-16.30	248.04	0.78	507.43	32.50	89.57	-7.78	52.13	-361.98
RMF305 [79]	0.153	-16.30	246.37	0.78	512.37	32.50	89.49	-8.21	52.92	-359.04
RMF306 [79]	0.153	-16.30	244.69	0.79	517.18	32.50	89.41	-8.63	53.72	-356.09
RMF307 [79]	0.153	-16.30	243.84	0.79	519.54	32.50	89.37	-8.84	54.11	-354.63
RMF308 [79]	0.153	-16.30	242.99	0.79	521.85	32.50	89.32	-9.04	54.50	-353.15
RMF309 [79]	0.153	-16.30	241.30	0.79	526.40	32.50	89.24	-9.45	55.28	-350.22
RMF310 [79]	0.153	-16.30	238.75	0.79	532.98	32.50	89.12	-10.04	56.45	-345.82
RMF311 [79]	0.153	-16.30	237.89	0.79	535.10	32.50	89.08	-10.24	56.83	-344.35
RMF312 [79]	0.153	-16.30	237.03	0.79	537.20	32.50	89.04	-10.44	57.22	-342.89
RMF313 [79]	0.153	-16.30	235.31	0.80	541.28	32.50	88.96	-10.82	57.98	-339.96
RMF314 [79]	0.153	-16.30	234.43	0.80	543.28	32.50	88.92	-11.01	58.36	-338.47
RMF315 [79]	0.153	-16.30	234.01	0.80	544.27	32.50	88.91	-11.10	58.55	-337.76
RMF316 [79]	0.153	-16.30	233.57	0.80	545.22	32.50	88.89	-11.20	58.74	-337.02
RMF317 [79]	0.153	-16.30	232.70	0.80	547.17	32.50	88.85	-11.38	59.12	-335.55
RMF401 [79]	0.153	-16.30	229.99	0.71	477.86	32.50	93.79	23.04	100.51	-344.81
RMF402 [79]	0.153	-16.30	231.99	0.71	469.28	32.50	93.77	22.74	97.75	-350.20
RMF403 [79]	0.153	-16.30	229.99	0.72	486.57	32.50	93.13	18.06	90.88	-343.67
RMF404 [79]	0.153	-16.30	231.99	0.72	478.64	32.50	93.11	17.78	88.39	-348.78
RMF405 [79]	0.153	-16.30	233.99	0.72	470.83	32.50	93.10	17.50	85.94	-353.76

TABLE VII. (*Continued.*)

Model	ρ_0	E_0	K_0	m^*	K'	J	L_0	K_{sym}^0	Q_{sym}^0	$K_{\tau,v}^0$
RMF406 [79]	0.153	-16.30	233.99	0.78	520.06	32.50	89.75	-5.80	58.72	-344.85
RMF407 [79]	0.153	-16.30	229.99	0.73	493.83	32.50	92.50	13.42	82.67	-342.96
RMF408 [79]	0.153	-16.30	231.99	0.73	486.58	32.50	92.48	13.15	80.44	-347.78
RMF409 [79]	0.153	-16.30	233.99	0.73	479.45	32.50	92.47	12.88	78.25	-352.46
RMF410 [79]	0.153	-16.30	235.99	0.73	472.46	32.50	92.46	12.62	76.09	-357.02
RMF411 [79]	0.153	-16.30	229.99	0.74	500.11	32.50	91.90	9.09	75.82	-342.47
RMF412 [79]	0.153	-16.30	231.99	0.74	493.59	32.50	91.89	8.84	73.85	-346.98
RMF413 [79]	0.153	-16.30	233.99	0.74	487.20	32.50	91.87	8.58	71.90	-351.36
RMF414 [79]	0.153	-16.30	235.99	0.74	480.94	32.50	91.86	8.33	69.99	-355.62
RMF415 [79]	0.153	-16.30	229.98	0.75	505.92	32.50	91.33	5.06	70.28	-342.01
RMF416 [79]	0.153	-16.30	231.98	0.75	500.17	32.50	91.32	4.82	68.54	-346.19
RMF417 [79]	0.153	-16.30	233.99	0.75	494.57	32.50	91.30	4.58	66.84	-350.26
RMF418 [79]	0.153	-16.30	235.98	0.75	489.09	32.50	91.29	4.34	65.16	-354.20
RMF419 [79]	0.153	-16.30	229.99	0.76	511.79	32.50	90.79	1.31	65.98	-341.39
RMF420 [79]	0.153	-16.30	231.99	0.76	506.88	32.50	90.78	1.09	64.47	-345.23
RMF421 [79]	0.153	-16.30	233.99	0.76	502.11	32.50	90.76	0.86	62.99	-348.96
RMF422 [79]	0.153	-16.30	229.99	0.77	518.27	32.50	90.27	-2.17	62.86	-340.38
RMF423 [79]	0.153	-16.30	231.99	0.77	514.26	32.50	90.26	-2.38	61.57	-343.86
RMF424 [79]	0.153	-16.30	245.99	0.79	523.99	32.50	89.21	-9.88	53.59	-355.12
RMF425 [79]	0.153	-16.30	247.99	0.79	523.21	32.50	89.20	-10.06	52.90	-357.07
RMF426 [79]	0.153	-16.30	249.99	0.79	522.57	32.50	89.19	-10.24	52.23	-358.93
RMF427 [79]	0.153	-16.30	235.98	0.80	546.20	32.50	88.83	-11.67	58.05	-339.04
RMF428 [79]	0.153	-16.30	237.98	0.80	545.82	32.50	88.81	-11.85	57.43	-341.04
RMF429 [79]	0.153	-16.30	239.99	0.80	545.60	32.50	88.80	-12.02	56.84	-342.95
RMF430 [79]	0.153	-16.30	241.99	0.80	545.53	32.50	88.79	-12.19	56.26	-344.77
RMF431 [79]	0.153	-16.30	243.98	0.80	545.62	32.50	88.78	-12.36	55.71	-346.50
RMF432 [79]	0.153	-16.30	245.98	0.80	545.86	32.50	88.77	-12.53	55.19	-348.16
RMF433 [79]	0.153	-16.30	247.99	0.80	546.26	32.50	88.76	-12.70	54.68	-349.73
RMF434 [79]	0.153	-16.30	249.99	0.80	546.81	32.50	88.74	-12.87	54.19	-351.22
RSk1* [88]	0.160	-15.77	216.60	0.79	529.69	30.03	81.75	-7.42	66.77	-297.98
S271 [17]	0.148	-16.24	271.08	0.70	295.30	36.48	106.26	22.29	55.84	-499.50
SMFT1 [99]	0.158	-13.80	173.14	0.63	456.57	17.57	55.94	87.28	351.11	-100.85
SMFT2 [99]	0.162	-13.78	211.31	0.66	270.11	17.38	52.73	60.27	187.74	-188.71
SRK3M5 [100]	0.150	-16.00	299.86	0.55	-966.33	23.49	82.45	146.76	96.88	-613.65
SRK3M7 [100]	0.150	-16.00	299.95	0.75	363.93	28.73	79.69	-2.56	24.62	-384.00
VT [80]	0.153	-16.09	172.74	0.59	482.84	39.72	126.83	130.05	542.92	-276.41
$\sigma^3 + \sigma^4 + \omega_0^4$ models (type 3)										
BM-A [101]	0.179	-15.17	188.32	0.61	436.32	19.62	51.88	-18.05	-36.02	-209.14
BM-B [101]	0.156	-13.47	170.77	0.64	504.54	17.42	45.46	-15.61	-5.33	-154.06
BM-C [101]	0.142	-12.36	163.10	0.65	547.19	16.01	41.49	-14.20	7.05	-123.94
DJM [101]	0.172	-14.81	244.73	0.57	-147.54	20.21	62.95	32.66	-302.43	-383.00
DJM-C [101]	0.181	-15.67	329.44	0.54	-229.30	21.89	68.46	17.17	-468.73	-441.27
EMFT1 [99]	0.159	-13.56	166.12	0.59	-3.47	18.60	56.58	30.48	-165.49	-310.17
HD [102]	0.177	-16.22	284.18	0.67	101.75	35.69	105.93	44.58	93.60	-553.09
LB [102]	0.184	-15.26	316.76	0.59	51.67	31.92	96.73	27.18	-268.79	-537.44
MB [102]	0.190	-15.07	341.71	0.59	1375.71	32.49	89.97	-28.08	-32.74	-205.68
MS1 [103]	0.148	-15.75	249.97	0.60	161.37	35.00	106.75	38.56	-150.95	-533.03
MS3 [104]	0.148	-15.75	249.98	0.60	563.90	35.00	102.38	-0.20	-111.15	-383.52
NLSV1 [105]	0.149	-16.26	270.15	0.61	74.63	37.30	114.68	58.97	-27.80	-597.46
NLSV2 [105]	0.147	-16.23	291.65	0.62	174.88	36.76	111.52	39.50	-100.07	-562.74
PK1 [106]	0.148	-16.27	282.69	0.61	27.82	37.64	115.88	55.30	-87.79	-628.58
TM1 [107]	0.145	-16.26	281.16	0.63	285.22	36.89	110.79	33.62	-66.54	-518.75
TM2 [107]	0.132	-16.16	343.82	0.57	-265.60	35.98	113.03	56.07	-237.87	-709.40
TMA [108]	0.147	-16.02	318.15	0.63	572.12	30.66	90.14	10.75	-108.74	-367.99
Z271 [17]	0.148	-16.24	270.99	0.80	733.54	35.92	98.86	-16.40	49.00	-341.94

TABLE VII. (*Continued.*)

Model	ρ_0	E_0	K_0	m^*	K'	J	L_0	K_{sym}^0	Q_{sym}^0	$K_{\tau,v}^0$
$\sigma^3 + \sigma^4 + \omega^4 + \text{cross-terms models (type 4)}$										
BKA20 [67]	0.146	-15.93	237.95	0.64	464.66	32.24	75.38	-15.04	198.38	-320.11
BKA22 [67]	0.147	-15.91	225.24	0.61	283.29	33.17	78.79	-8.80	134.05	-382.46
BKA24 [67]	0.147	-15.95	227.06	0.60	273.58	34.19	84.80	-14.95	112.40	-421.55
BSR1 [109]	0.148	-16.02	239.89	0.61	35.68	31.04	59.41	12.96	468.10	-334.65
BSR2 [109]	0.149	-16.03	239.93	0.61	48.06	31.50	62.02	-3.14	403.21	-362.81
BSR3 [109]	0.150	-16.09	230.55	0.60	114.72	32.74	70.45	-7.76	397.59	-395.42
BSR4 [109]	0.150	-16.08	238.57	0.61	-4.00	33.17	73.23	-20.71	420.06	-461.34
BSR5 [109]	0.151	-16.12	235.71	0.61	10.96	34.46	83.37	-14.16	346.84	-510.53
BSR6 [109]	0.149	-16.13	235.75	0.60	7.59	35.62	85.68	-49.55	352.00	-560.86
BSR7 [109]	0.149	-16.18	231.80	0.60	19.80	37.26	99.14	-16.97	198.47	-603.32
BSR8 [109]	0.147	-16.04	230.95	0.61	290.85	31.08	60.25	-0.74	238.23	-286.36
BSR9 [109]	0.147	-16.07	232.50	0.60	297.11	31.61	63.89	-11.32	202.86	-313.03
BSR10 [109]	0.147	-16.06	227.41	0.60	255.13	32.72	70.83	-16.51	205.04	-362.04
BSR11 [109]	0.147	-16.08	226.75	0.61	312.37	33.69	78.78	-24.72	172.54	-388.86
BSR12 [109]	0.147	-16.10	232.35	0.61	290.31	34.00	77.90	-44.23	324.15	-414.30
BSR13 [109]	0.147	-16.13	228.64	0.60	294.46	35.82	91.07	-41.68	138.98	-470.82
BSR14 [109]	0.147	-16.18	235.47	0.61	317.10	36.32	93.85	-41.95	112.53	-478.66
BSR15 [109]	0.146	-16.03	226.82	0.61	512.29	30.97	61.79	-21.36	128.26	-252.54
BSR16 [109]	0.146	-16.05	224.98	0.61	503.17	31.24	62.33	-24.17	152.29	-258.75
BSR17 [109]	0.146	-16.05	221.67	0.61	489.45	31.98	67.44	-31.58	176.65	-287.31
BSR18 [109]	0.146	-16.05	221.13	0.61	485.73	32.74	72.65	-42.24	199.39	-318.55
BSR19 [109]	0.147	-16.08	220.83	0.61	484.25	33.78	79.47	-50.13	194.70	-352.70
BSR20 [109]	0.146	-16.09	223.25	0.61	507.75	34.54	88.03	-39.90	82.74	-367.86
BSR21 [109]	0.145	-16.12	220.32	0.60	468.20	35.96	92.94	-46.01	67.45	-406.16
C1 [98]	0.146	-16.19	303.97	0.66	132.68	32.03	94.62	26.60	-11.72	-499.83
FSU-I [110]	0.148	-16.28	229.54	0.61	523.95	37.42	109.62	2.64	-101.71	-404.87
FSU-II [110]	0.148	-16.28	229.54	0.61	523.95	35.49	87.39	-68.37	156.81	-393.23
FSU-III [110]	0.148	-16.28	229.54	0.61	523.95	33.89	71.72	-74.40	398.23	-341.03
FSU-IV [110]	0.148	-16.28	229.54	0.61	523.95	31.43	52.16	-16.78	249.99	-210.68
FSU-V [110]	0.148	-16.28	229.54	0.61	523.95	30.96	49.46	5.37	79.77	-178.50
FSUGold [111]	0.148	-16.28	229.54	0.61	523.93	32.56	60.44	-51.40	425.72	-276.07
FSUGold4 [112]	0.147	-16.40	229.56	0.61	538.33	31.40	51.74	-16.49	253.33	-205.59
FSUGold5 [112]	0.148	-16.79	233.18	0.61	555.05	30.55	45.61	23.11	-91.83	-141.96
FSUGZ00 [113]	0.149	-16.03	240.00	0.61	47.74	31.43	62.16	-3.46	402.48	-364.05
FSUGZ03 [113]	0.147	-16.07	232.48	0.60	297.13	31.54	63.98	-11.66	203.43	-313.79
FSUGZ06 [113]	0.146	-16.05	225.06	0.61	503.17	31.18	62.42	-24.49	153.31	-259.47
G1 [98]	0.153	-16.14	214.83	0.63	361.91	38.48	123.19	96.87	95.59	-434.73
G2 [98]	0.154	-16.07	214.77	0.66	438.68	36.39	100.67	-7.48	47.62	-405.89
G2* [114]	0.154	-16.07	214.77	0.66	438.68	30.39	69.68	-21.93	197.52	-297.69
HC [102]	0.169	-15.75	231.91	0.68	390.71	31.01	58.53	-99.04	933.54	-351.62
IU-FSU [115]	0.155	-16.40	231.33	0.61	290.28	31.30	47.21	28.53	370.71	-195.46
LA [102]	0.179	-15.46	301.59	0.60	145.52	33.48	78.67	-61.77	264.62	-495.82
MA [102]	0.179	-15.93	347.40	0.61	1279.91	32.39	71.47	-74.53	265.76	-240.04
NL3v1 [116]	0.148	-16.24	271.59	0.59	-204.06	36.07	101.25	0.69	129.02	-682.91
NL3v2 [116]	0.148	-16.24	271.59	0.59	-204.06	34.98	87.77	-46.15	442.19	-638.69
NL3v3 [116]	0.148	-16.24	271.59	0.59	-204.06	34.48	82.08	-56.12	632.86	-610.24
NL3v4 [116]	0.148	-16.24	271.59	0.59	-204.06	34.02	76.96	-59.87	819.51	-579.46
NL3v5 [116]	0.148	-16.24	271.59	0.59	-204.06	33.16	68.24	-52.95	1128.57	-513.65
NL3v6 [116]	0.148	-16.24	271.59	0.59	-204.06	32.39	61.14	-33.68	1323.38	-446.44
S271v1 [116]	0.148	-16.24	271.00	0.70	295.64	35.73	95.93	-44.06	-53.63	-514.99
S271v2 [116]	0.148	-16.24	271.00	0.70	295.64	35.06	86.87	-90.33	14.94	-516.79
S271v3 [116]	0.148	-16.24	271.00	0.70	295.64	34.42	78.86	-121.00	180.94	-508.12

TABLE VII. (*Continued.*)

Model	ρ_0	E_0	K_0	m^*	K'	J	L_0	K_{sym}^0	Q_{sym}^0	$K_{\tau,v}^0$
S271v4 [116]	0.148	-16.24	271.00	0.70	295.64	33.83	71.76	-139.52	390.88	-491.78
S271v5 [116]	0.148	-16.24	271.00	0.70	295.64	33.27	65.44	-148.63	609.90	-469.88
S271v6 [116]	0.148	-16.24	271.00	0.70	295.64	32.74	59.81	-150.45	815.93	-444.07
SIG-OM [117]	0.149	-16.30	265.33	0.62	233.77	37.01	111.97	41.15	-48.89	-532.02
SVI-1 [118]	0.149	-16.30	263.90	0.62	490.57	37.05	116.54	95.84	208.24	-386.76
SVI-2 [118]	0.149	-16.31	271.49	0.62	455.15	37.04	116.05	91.36	199.04	-410.37
TM1* [119]	0.145	-16.34	281.53	0.63	541.57	36.89	101.76	-13.79	25.05	-428.61
XS [104]	0.148	-16.30	229.98	0.60	702.85	31.83	54.97	-28.80	128.26	-190.62
Z271* [114]	0.148	-16.24	270.96	0.80	733.47	40.25	83.57	-198.47	306.00	-473.66
Z271s1 [116]	0.148	-16.24	271.00	0.80	733.59	34.95	86.86	-64.86	144.67	-350.90
Z271s2 [116]	0.148	-16.24	271.00	0.80	733.59	34.08	76.62	-92.28	301.43	-344.61
Z271s3 [116]	0.148	-16.24	271.00	0.80	733.59	33.27	67.81	-104.58	457.51	-327.87
Z271s4 [116]	0.148	-16.24	271.00	0.80	733.59	32.53	60.18	-106.04	580.42	-304.23
Z271s5 [116]	0.148	-16.24	271.00	0.80	733.59	31.84	53.57	-99.81	655.09	-276.22
Z271s6 [116]	0.148	-16.24	271.00	0.80	733.59	31.20	47.81	-88.22	676.74	-245.65
Z271v1 [116]	0.148	-16.24	271.00	0.80	733.59	35.34	90.86	-66.37	-17.49	-365.58
Z271v2 [116]	0.148	-16.24	271.00	0.80	733.59	34.80	83.61	-104.84	15.41	-380.19
Z271v3 [116]	0.148	-16.24	271.00	0.80	733.59	34.54	80.23	-120.39	57.82	-384.59
Z271v4 [116]	0.148	-16.24	271.00	0.80	733.59	34.29	77.00	-133.76	112.71	-387.31
Z271v5 [116]	0.148	-16.24	271.00	0.80	733.59	34.04	73.90	-145.15	177.12	-388.52
Z271v6 [116]	0.148	-16.24	271.00	0.80	733.59	33.80	70.94	-154.74	248.50	-388.36
Density-dependent models (type 5)										
DD [120]	0.149	-16.02	239.99	0.56	-134.65	31.64	55.98	-95.30	576.86	-462.57
DD-F [121]	0.147	-16.04	223.32	0.56	758.73	31.63	56.00	-139.80	467.35	-285.54
DD-ME1 [122]	0.152	-16.20	244.72	0.58	-316.66	33.06	55.45	-101.05	705.59	-505.50
DD-ME2 [123]	0.152	-16.14	250.92	0.57	-478.75	32.30	51.25	-87.19	776.91	-492.45
DD2 [124]	0.149	-16.02	242.72	0.56	-168.65	31.67	55.04	-93.23	598.138	-461.69
PKDD [106]	0.150	-16.27	262.19	0.57	118.73	36.79	90.21	-80.55	24.36	-580.97
TW99 [31]	0.153	-16.25	240.27	0.55	539.79	32.77	55.31	-124.71	538.50	-332.32
Point-coupling models (type 6)										
FA2 [125]	0.150	-16.03	287.24	0.60	812.70	33.53	99.38	-3.17	-245.96	-318.27
FA3 [125]	0.152	-16.02	275.79	0.68	487.11	29.69	29.09	-274.99	577.83	-398.14
FA4 [125]	0.152	-16.09	294.31	0.68	166.20	29.78	30.62	-257.95	730.06	-424.40
FZ0 [125]	0.140	-16.14	559.34	0.53	-2267.00	39.40	129.53	97.99	-551.13	-1204.15
FZ1 [125]	0.149	-15.95	381.37	0.70	-286.97	32.57	95.18	22.97	-10.73	-619.71
FZ2 [125]	0.150	-16.00	327.94	0.67	307.36	31.83	73.70	-102.07	-52.65	-475.19
FZ3 [125]	0.151	-15.93	294.71	0.74	364.21	29.93	33.93	-261.59	424.03	-423.24
FZ4 [125]	0.151	-15.85	302.83	0.74	136.60	30.00	36.61	-241.23	544.22	-444.36
PC-F1 [126]	0.151	-16.17	254.57	0.61	289.97	37.75	117.04	74.55	78.70	-494.39
PC-F3 [126]	0.151	-16.18	254.67	0.61	288.23	38.24	118.51	74.67	78.49	-502.28
VA2 [125]	0.149	-15.90	285.10	0.60	805.10	34.89	125.69	116.53	-376.72	-282.67
VA3 [125]	0.149	-16.07	298.68	0.63	100.92	39.22	186.06	401.48	-770.96	-652.02
VA4 [125]	0.151	-16.11	322.41	0.66	-668.03	34.56	125.32	190.20	50.99	-821.39
VZ0 [125]	0.145	-16.29	563.38	0.54	-2243.19	37.93	124.93	95.78	-571.95	-1151.19
VZ1 [125]	0.148	-15.86	379.55	0.70	-288.93	32.72	95.68	23.21	-9.55	-623.69
VZ2 [125]	0.149	-15.99	324.20	0.60	435.61	34.79	127.33	133.57	-390.54	-459.32
VZ3 [125]	0.150	-16.04	297.70	0.62	75.77	34.60	123.95	154.81	-195.99	-557.32
VZ4 [125]	0.151	-15.90	305.48	0.65	-286.33	32.70	97.38	62.70	335.81	-612.88
δ meson models (type 7)										
DD-ME δ [127]	0.152	-16.08	219.60	0.61	748.31	32.18	51.43	-124.96	843.03	-258.28
DDH δ [128]	0.153	-16.25	240.18	0.55	539.59	25.34	45.33	52.91	783.21	-117.22
GDFM [32]	0.178	-17.66	323.80	0.68	-2783.75	33.05	67.89	75.08	491.06	-915.98
NL δ [129]	0.160	-16.00	240.17	0.75	463.63	30.60	101.46	117.03	227.51	-295.86
NL3 δ [89]	0.148	-16.24	269.94	0.60	-198.33	37.67	149.98	393.86	1484.30	-616.21

APPENDIX C: PLUS-MINUS TABLE

TABLE VIII. Status of each RMF model; approved (+) or not (−) under SET2a and SET2b constraints. SET2a (SET2b): SM1, SM3a (SM3b), SM4, PNMI, MIX1a (MIX1b), MIX2a (MIX2b), MIX3, and MIX4.

Model	SM1	SM3a	SM3b	SM4	PNMI	MIX1a	MIX1b	MIX2a	MIX2b	MIX3	MIX4	SM1	SM3a	SM3b	SM4	PNMI	MIX1a	MIX1b	MIX2a	MIX2b	MIX3	MIX4
Linear finite-range models																						
H1	−	−	−	−	+	+	−	−	−	LZ	−	−	−	+	−	−	−	−	−	−	−	
L1	−	−	−	−	−	−	−	+	+	−	RMF201	−	−	−	+	+	−	+	−	−	−	
L2	−	−	−	−	−	−	−	−	+	−	RMF202	−	−	−	+	+	−	−	−	−	−	
L3	−	−	−	−	−	−	−	−	−	−	RMF203	−	−	−	+	+	−	−	−	−	−	
LBF	−	−	−	−	−	−	−	−	−	−	RMF204	−	−	−	+	+	−	−	−	−	−	
LHS	−	−	−	−	−	+	+	−	−	−	RMF205	−	−	−	+	+	−	−	−	−	−	
LW	−	−	−	−	−	+	−	+	+	−	RMF206	−	−	−	+	+	−	−	−	−	−	
CS	−	−	−	−	−	−	−	−	−	−	$\sigma^3 + \sigma^4$ models											
E	+	−	−	−	−	−	−	−	−	−	NLZ2	−	−	−	+	+	−	−	−	−	−	
ER	+	−	−	−	−	−	−	−	−	−	P-067	+	−	−	P-070	+	−	−	−	−	−	
FAMA1	+	−	−	−	−	−	−	−	−	−	P-075	−	−	−	P-080	+	−	−	−	−	−	
FAMA2	+	−	−	−	−	−	−	−	−	−	Q1	+	−	−	+	+	−	−	−	−	−	
FAMA3	+	−	−	−	−	−	−	−	−	−	RMF301	+	−	−	RMF302	+	−	−	−	−	−	
FAMA4	−	−	−	−	−	−	−	−	−	−	RMF303	+	−	−	RMF304	+	−	−	−	−	−	
FAMA5	−	−	−	−	−	−	−	−	−	−	RMF305	+	−	−	RMF306	+	−	−	−	−	−	
FAMB1	+	−	−	−	−	−	−	−	−	−	RMF307	+	−	−	RMF308	+	−	−	−	−	−	
FAMB2	+	−	−	−	−	−	−	−	−	−	RMF309	+	−	−	RMF310	+	−	−	−	−	−	
FAMB3	+	−	−	−	−	−	−	−	−	−	RMF310	+	−	−	RMF310	+	−	−	−	−	−	
FAMB4	−	−	−	−	−	−	−	−	−	−	RMF310	+	−	−	RMF310	+	−	−	−	−	−	
FAMB5	−	−	−	−	−	−	−	−	−	−	RMF310	+	−	−	RMF310	+	−	−	−	−	−	
FAMC1	+	−	−	−	−	−	−	−	−	−	RMF310	+	−	−	RMF310	+	−	−	−	−	−	
FAMC2	+	−	−	−	−	−	−	−	−	−	RMF310	+	−	−	RMF310	+	−	−	−	−	−	
FAMC3	+	−	−	−	−	−	−	−	−	−	RMF310	+	−	−	RMF310	+	−	−	−	−	−	

TABLE VIII. (*Continued.*)

Model	SM1	SM3a	SM3b	SM4	PNM1	MIX1a	MIX1b	MIX2a	MIX2b	MIX3	MIX4	Model	SM1	SM3a	SM3b	SM4	PNM1	MIX1a	MIX1b	MIX2a	MIX2b	MIX3	MIX4
FAMC4	-	-	-	-	-	-	-	-	-	-	-	RMF311	-	-	-	-	-	-	-	-	-	-	
FAMC5	-	-	-	-	-	-	-	-	-	-	-	RMF312	-	-	-	-	-	-	-	-	-	-	
GL1	+	+	+	+	+	+	+	+	+	+	+	RMF313	+	+	+	+	+	+	+	+	+	+	
GL2	+	+	+	+	+	+	+	+	+	+	+	RMF314	+	+	+	+	+	+	+	+	+	+	
GL3	+	+	+	+	+	+	+	+	+	+	+	RMF315	+	+	+	+	+	+	+	+	+	+	
GL4	+	+	+	+	+	+	+	+	+	+	+	RMF316	+	+	+	+	+	+	+	+	+	+	
GL5	+	+	+	+	+	+	+	+	+	+	+	RMF317	+	+	+	+	+	+	+	+	+	+	
GL6	+	+	+	+	+	+	+	+	+	+	+	RMF401	+	+	+	+	+	+	+	+	+	+	
GL7	+	+	+	+	+	+	+	+	+	+	+	RMF402	+	+	+	+	+	+	+	+	+	+	
GL8	+	+	+	+	+	+	+	+	+	+	+	RMF403	+	+	+	+	+	+	+	+	+	+	
GL82	+	+	+	+	+	+	+	+	+	+	+	RMF404	+	+	+	+	+	+	+	+	+	+	
GL9	+	+	+	+	+	+	+	+	+	+	+	RMF405	+	+	+	+	+	+	+	+	+	+	
GM1	+	+	+	+	+	+	+	+	+	+	+	RMF406	+	+	+	+	+	+	+	+	+	+	
GM2	+	+	+	+	+	+	+	+	+	+	+	RMF407	+	+	+	+	+	+	+	+	+	+	
GM3	+	+	+	+	+	+	+	+	+	+	+	RMF408	+	+	+	+	+	+	+	+	+	+	
GPS	+	+	+	+	+	+	+	+	+	+	+	RMF409	+	+	+	+	+	+	+	+	+	+	
Hybrid	+	+	+	+	+	+	+	+	+	+	+	RMF410	+	+	+	+	+	+	+	+	+	+	
MS2	+	+	+	+	+	+	+	+	+	+	+	RMF411	+	+	+	+	+	+	+	+	+	+	
NL-VT1	-	-	-	-	-	-	-	-	-	-	-	RMF412	+	+	+	+	+	+	+	+	+	+	
NL06	+	+	+	+	+	+	+	+	+	+	+	RMF413	+	+	+	+	+	+	+	+	+	+	
NL065	-	-	-	-	-	-	-	-	-	-	-	RMF414	+	+	+	+	+	+	+	+	+	+	
NL07	-	-	-	-	-	-	-	-	-	-	-	RMF415	+	+	+	+	+	+	+	+	+	+	
NL075	-	-	-	-	-	-	-	-	-	-	-	RMF416	+	+	+	+	+	+	+	+	+	+	
NL1	+	+	+	+	+	+	+	+	+	+	+	RMF417	+	+	+	+	+	+	+	+	+	+	
NL1J4	-	-	-	-	-	-	-	-	-	-	-	RMF418	+	+	+	+	+	+	+	+	+	+	
NL1J5	-	-	-	-	-	-	-	-	-	-	-	RMF419	+	+	+	+	+	+	+	+	+	+	
NL2	-	-	-	-	-	-	-	-	-	-	-	RMF420	+	+	+	+	+	+	+	+	+	+	
NL3	-	-	-	-	-	-	-	-	-	-	-	RMF421	+	+	+	+	+	+	+	+	+	+	
NL3-II	-	-	-	-	-	-	-	-	-	-	-	RMF422	+	+	+	+	+	+	+	+	+	+	
NL3*	+	+	+	+	+	+	+	+	+	+	+	RMF423	+	+	+	+	+	+	+	+	+	+	

TABLE VIII. (*Continued.*)

Model	SM1	SM3a	SM3b	SM4	PNM1	MIX1a	MIX1b	MIX2a	MIX2b	MIX3	MIX4	Model	SM1	SM3a	SM3b	SM4	PNM1	MIX1a	MIX1b	MIX2a	MIX2b	MIX3	MIX4
NL4	-	-	-	-	-	-	-	-	-	-	-	RMF424	+	-	-	-	-	-	-	-	-	-	
NLB	-	-	-	-	-	-	-	-	-	-	-	RMF425	+	-	-	-	-	-	-	-	-	-	
NLB1	-	-	-	-	-	-	-	-	-	-	-	RMF426	+	-	-	-	-	-	-	-	-	-	
NLB2	-	-	-	-	-	-	-	-	-	-	-	RMF427	+	-	-	-	-	-	-	-	-	-	
NLC	-	-	-	-	-	-	-	-	-	-	-	RMF428	+	-	-	-	-	-	-	-	-	-	
NLD	-	-	-	-	-	-	-	-	-	-	-	RMF429	+	-	-	-	-	-	-	-	-	-	
NLM	-	-	-	-	-	-	-	-	-	-	-	RMF430	+	-	-	-	-	-	-	-	-	-	
NLM2	-	-	-	-	-	-	-	-	-	-	-	RMF431	+	-	-	-	-	-	-	-	-	-	
NLM3	-	-	-	-	-	-	-	-	-	-	-	RMF432	+	-	-	-	-	-	-	-	-	-	
NLM4	-	-	-	-	-	-	-	-	-	-	-	RMF433	+	-	-	-	-	-	-	-	-	-	
NLM5	-	-	-	-	-	-	-	-	-	-	-	RMF434	+	-	-	-	-	-	-	-	-	-	
NLM6	-	-	-	-	-	-	-	-	-	-	-	RSk1*	-	-	-	-	-	-	-	-	-	-	
NLRA	-	-	-	-	-	-	-	-	-	-	-	S271	-	-	-	-	-	-	-	-	-	-	
NLRA1	-	-	-	-	-	-	-	-	-	-	-	SMFT1	-	-	-	-	-	-	-	-	-	-	
NLrho	-	-	-	-	-	-	-	-	-	-	-	SMFT2	+	-	-	-	-	-	-	-	-	-	
NLS	-	-	-	-	-	-	-	-	-	-	-	SRK3M5	-	-	-	-	-	-	-	-	-	-	
NLSH	-	-	-	-	-	-	-	-	-	-	-	SRK3M7	-	-	-	-	-	-	-	-	-	-	
NLZ	-	-	-	-	-	-	-	-	-	-	-	VT	-	-	-	-	-	-	-	-	-	-	
													$\sigma^3 + \sigma^4 + \omega^4$ models										
BM-A	-	-	-	-	-	-	-	-	-	-	-	MS1	+	-	-	-	-	-	-	-	-	-	
BM-B	-	-	-	-	-	-	-	-	-	-	-	MS3	+	-	-	-	-	-	-	-	-	-	
BM-C	-	-	-	-	-	-	-	-	-	-	-	NLSV1	+	-	-	-	-	-	-	-	-	-	
DIM	-	-	-	-	-	-	-	-	-	-	-	NLSV2	-	-	-	-	-	-	-	-	-	-	
DIM-C	-	-	-	-	-	-	-	-	-	-	-	PK1	-	-	-	-	-	-	-	-	-	-	
EMFT1	-	-	-	-	-	-	-	-	-	-	-	TM1	-	-	-	-	-	-	-	-	-	-	
HD	-	-	-	-	-	-	-	-	-	-	-	TM2	-	-	-	-	-	-	-	-	-	-	
LB	-	-	-	-	-	-	-	-	-	-	-	TMA	-	-	-	-	-	-	-	-	-	-	
MB	-	-	-	-	-	-	-	-	-	-	-	Z271	-	-	-	-	-	-	-	-	-	-	

TABLE VIII. (*Continued.*)

Model	SM1	SM3a	SM3b	SM4	PNM1	MIX1a	MIX1b	MIX2a	MIX2b	MIX3	MIX4	Model	$\sigma^3 + \sigma^4 + \omega^4 +$ mixing terms models
BKA20	+	-	-	-	-	-	-	-	-	-	-	-	-
BKA22	+	-	-	-	-	-	-	-	-	-	-	-	-
BKA24	+	-	-	-	-	-	-	-	-	-	-	-	-
BSR1	++	++	++	++	++	++	++	++	++	++	++	-	G2
BSR2	++	++	++	++	++	++	++	++	++	++	++	-	G2*
BSR3	++	++	++	++	++	++	++	++	++	++	++	-	HC
BSR4	++	++	++	++	++	++	++	++	++	++	++	-	IU-FSU
BSR5	++	++	++	++	++	++	++	++	++	++	++	-	LA
BSR6	++	++	++	++	++	++	++	++	++	++	++	-	MA
BSR7	++	++	++	++	++	++	++	++	++	++	++	-	NL3v1
BSR8	++	++	++	++	++	++	++	++	++	++	++	-	NL3v2
BSR9	++	++	++	++	++	++	++	++	++	++	++	-	NL3v3
BSR10	++	++	++	++	++	++	++	++	++	++	++	-	NL3v4
BSR11	++	++	++	++	++	++	++	++	++	++	++	-	NL3v5
BSR12	++	++	++	++	++	++	++	++	++	++	++	-	NL3v6
BSR13	++	++	++	++	++	++	++	++	++	++	++	-	S271v1
BSR14	++	++	++	++	++	++	++	++	++	++	++	-	S271v2
BSR15	++	++	++	++	++	++	++	++	++	++	++	-	S271v3
BSR16	++	++	++	++	++	++	++	++	++	++	++	-	S271v4
BSR17	++	++	++	++	++	++	++	++	++	++	++	-	S271v5
BSR18	++	++	++	++	++	++	++	++	++	++	++	-	S271v6
BSR19	++	++	++	++	++	++	++	++	++	++	++	-	SIG-OM
BSR20	++	++	++	++	++	++	++	++	++	++	++	-	SVI-1
BSR21	++	++	++	++	++	++	++	++	++	++	++	-	SVI-2
C1	-	-	-	-	-	-	-	-	-	-	-	-	TM1*
FSU-I	-	-	-	-	-	-	-	-	-	-	-	-	Xs
FSU-II	-	-	-	-	-	-	-	-	-	-	-	-	Z271*
FSU-III	-	-	-	-	-	-	-	-	-	-	-	-	Z271s1
FSU-IV	-	-	-	-	-	-	-	-	-	-	-	-	Z271s2
FSU-V	-	-	-	-	-	-	-	-	-	-	-	-	Z271s3
FSUGold	-	-	-	-	-	-	-	-	-	-	-	-	Z271s4
	-	-	-	-	-	-	-	-	-	-	-	-	Z271s5
	-	-	-	-	-	-	-	-	-	-	-	-	Z271s6
	-	-	-	-	-	-	-	-	-	-	-	-	Z271v1

TABLE VIII. (*Continued.*)

Model	SM1	SM3a	SM3b	SM4	PNM1	MIX1a	MIX1b	MIX2a	MIX2b	MIX3	MIX4	Model	SM1	SM3a	SM3b	SM4	PNM1	MIX1a	MIX1b	MIX2a	MIX2b	MIX3	MIX4
FSUGold4	+	+	+	+	+	+	+	-	+	Z271v2	-	+	+	+	+	+	-	-	-	-	-		
FSUGold5	+	+	+	-	+	+	+	-	+	Z271v3	-	+	+	+	+	+	-	-	-	-	-		
FSUGZ00	+	-	-	-	-	-	-	-	+	Z271v4	-	+	+	+	+	+	-	-	-	-	-		
FSUGZ03	+	-	-	-	-	-	-	-	+	Z271v5	-	+	+	+	+	+	-	-	-	-	-		
FSUGZ06	+	-	-	-	-	-	-	-	+	Z271v6	-	+	+	+	+	+	-	-	-	-	-		
G1	+	-	-	-	-	-	-	-	-	-	-	-	-	-	-	-	-	-	-	-	-		
DD	+	-	-	-	-	-	-	-	-	-	-	-	-	-	-	-	-	-	-	-	-		
DD-F	+	+	-	-	-	-	-	-	-	-	-	-	-	-	-	-	-	-	-	-	-		
DD-ME1	+	-	-	-	-	-	-	-	-	-	-	-	-	-	-	-	-	-	-	-	-		
DD-ME2	+	-	-	-	-	-	-	-	-	-	-	-	-	-	-	-	-	-	-	-	-		
FA2	-	-	-	-	-	-	-	-	-	-	-	-	-	-	-	-	-	-	-	-	-		
FA3	-	-	+	-	-	-	-	-	-	-	-	-	-	-	-	-	-	-	-	-	-		
FA4	-	-	-	-	-	-	-	-	-	-	-	-	-	-	-	-	-	-	-	-	-		
FZ0	-	-	-	-	-	-	-	-	-	-	-	-	-	-	-	-	-	-	-	-	-		
FZ1	-	-	-	-	-	-	-	-	-	-	-	-	-	-	-	-	-	-	-	-	-		
FZ2	-	-	-	-	-	-	-	-	-	-	-	-	-	-	-	-	-	-	-	-	-		
FZ3	-	-	-	-	-	-	-	-	-	-	-	-	-	-	-	-	-	-	-	-	-		
FZ4	-	-	-	-	-	-	-	-	-	-	-	-	-	-	-	-	-	-	-	-	-		
PC-F1	+	-	-	-	-	-	-	-	-	-	-	-	-	-	-	-	-	-	-	-	-		
DD-ME δ	+	+	+	+	+	+	+	+	+	+	+	+	+	+	+	+	+	+	+	+	+		
DDH δ	+	+	+	+	+	+	+	+	+	+	+	+	+	+	+	+	+	+	+	+	+		
GDFM	-	-	-	-	-	-	-	-	-	-	-	-	-	-	-	-	-	-	-	-	-		

APPENDIX D: DEVIATION TABLE

TABLE IX. List of the RMF parametrizations and their compliance with macroscopic constraints used in this work. For SM1 and MIX1-4 we give the standard deviation; the constraint is satisfied if the standard deviation is less than or equal to one. For SM3, SM4, and PNM1 we give the fraction of the full density range in % in which the constraint is not satisfied. A letter L (H) indicates that the RMF prediction starts to fail at the beginning (end) of the density range. No letter indication means that the model fails in the middle of the density range. For models that fail in 100% of the range, the letter U (D) indicates that its curve is above (below) the band defined by the constraint. For more details, see the text.

Model	SM1	SM3a (%)	SM3b (%)	SM4 (%)	PNM1 (%)	MIX1a	MIX1b	MIX2a	MIX2b	MIX3	MIX4
Linear finite-range models											
H1	7.92	100U	100U	100U	0	-0.81	-2.63	0.41	1.34	-1.56	-1.62
L1	9.89	100U	100U	100U	0	-1.66	-4.33	0.13	0.83	-0.61	-1.69
L2	8.71	100U	100U	100U	58.6H	-2.19	-5.37	-0.03	0.55	-0.28	-1.69
L3	9.86	100U	100U	100U	75.6H	-2.23	-5.46	-0.01	0.58	-0.34	-1.77
LBF	8.85	100U	100U	100U	0	3.38	5.77	1.82	3.88	-5.71	-1.62
LHS	7.95	100U	100U	100U	0	1.00	1.00	1.01	2.42	-3.37	-1.62
LW	7.89	100U	100U	100U	.4L	-1.58	-4.16	0.10	0.78	-0.52	-1.54
LZ	8.91	100U	100U	100U	0	3.77	6.54	1.95	4.12	-6.14	-1.62
RMF201	8.66	100U	100U	100U	0	0.50	0.00	0.85	2.13	-2.82	-1.62
RMF202	8.52	100U	100U	100U	0	0.50	0.00	0.85	2.13	-2.83	-1.62
RMF203	8.38	100U	100U	100U	0	0.50	0.00	0.85	2.13	-2.84	-1.62
RMF204	8.24	100U	100U	100U	0	0.50	0.00	0.85	2.13	-2.85	-1.62
RMF205	8.10	100U	100U	100U	0	0.50	0.00	0.85	2.12	-2.85	-1.62
RMF206	7.96	100U	100U	100U	0	0.50	0.00	0.84	2.12	-2.86	-1.62
$\sigma^3 + \sigma^4$ models											
CS	-1.07	100U	100U	54.6H	39.2	2.18	3.36	1.36	3.06	0.69	-1.54
E	-0.21	100U	100U	71.4H	36.0	1.72	2.43	1.21	2.78	-0.51	-1.54
ER	-0.24	100U	100U	67.8H	13.2	1.88	2.77	1.26	2.86	-0.45	-1.54
FAMA1	-0.75	100U	100U	45.6H	50.2	1.60	2.20	1.12	2.62	0.82	-1.54
FAMA2	-0.12	100U	100U	58.3H	0	1.60	2.20	1.12	2.61	-0.01	-1.54
FAMA3	0.50	100U	100U	73.8H	0	1.60	2.20	1.11	2.60	-0.63	-1.54
FAMA4	1.13	100U	100U	89.9H	0	1.60	2.20	1.11	2.59	-1.09	-1.54
FAMA5	1.75	100U	100U	100U	0	1.60	2.20	1.10	2.58	-1.45	-1.54
FAMB1	-0.75	8.0H	36.4H	0	0	1.40	1.80	0.85	2.14	1.70	-1.38
FAMB2	-0.12	9.3H	39.9H	0	0	1.40	1.80	0.85	2.13	1.03	-1.38
FAMB3	0.50	11.6H	17.6L/51.1H	0	0	1.40	1.80	0.84	2.12	0.54	-1.38
FAMB4	1.13	8.5L/14.4H	26.2L/63.7H	0	0	1.40	1.80	0.84	2.11	0.19	-1.38
FAMB5	1.75	15.4L/17.3H	100U	2.9L/19.2/39.2H	0	1.40	1.80	0.84	2.11	-0.06	-1.38
FAMC1	-0.75	8.0H	36.4H	0	82.2H	-0.40	-1.80	0.25	1.06	2.24	-1.31
FAMC2	-0.12	9.3H	39.9H	0	77.6H	-0.40	-1.80	0.25	1.05	1.73	-1.31
FAMC3	0.50	11.6H	17.6L/51.1H	0	70.6H	-0.40	-1.80	0.24	1.04	1.36	-1.31
FAMC4	1.13	8.5L/14.4H	26.2L/63.7H	0	45.6	-0.40	-1.80	0.24	1.03	1.10	-1.31
FAMC5	1.75	15.4L/17.3H	100U	2.9L/19.2/39.2H	0	-0.40	-1.80	0.24	1.03	0.90	-1.31
GL1	-0.75	13.1H	38.7H	0	75.0H	0.50	0.00	0.55	1.59	2.05	-1.38
GL2	-0.75	0	0	0	75.0H	0.50	0.00	0.48	1.46	1.92	-1.31
GL3	-0.75	0	0	0	75.8H	0.50	0.00	0.42	1.36	1.77	-1.23
GL4	0.50	17.3H	19.6L/57.4H	0	0	0.50	0.00	0.54	1.57	1.02	-1.38
GL5	0.50	0	2.3L	0	0	0.50	0.00	0.47	1.45	1.14	-1.31
GL6	0.50	0	0	0	0	0.50	0.00	0.42	1.35	1.33	-1.23
GL7	1.75	3.5L	17.2L	3.7L/1.0	0	0.50	0.00	0.46	1.44	0.79	-1.31
GL8	1.75	0	7.5L	1.0L	0	0.50	0.00	0.41	1.34	1.22	-1.23
GL82	1.39	0	6.5L	0	0	1.25	1.49	0.70	1.85	0.63	-1.31
GL9	-0.50	0	0	0	70.8H	0.50	0.00	0.44	1.40	1.66	-1.31
GM1	1.76	17.3L/23.3H	100U	100U	0	0.50	0.01	0.53	1.56	0.48	-1.38
GM2	1.75	0	11.5L	1.6L/.8	0	0.50	0.00	0.43	1.37	1.02	-1.23
GM3	0.25	0	0	0	0	0.50	0.00	0.44	1.39	1.31	-1.23
GPS	1.74	0	6.3L	0	0	0.50	0.00	0.41	1.34	1.18	-1.23

TABLE IX. (*Continued.*)

Model	SM1	SM3a (%)	SM3b (%)	SM4 (%)	PNM1 (%)	MIX1a	MIX1b	MIX2a	MIX2b	MIX3	MIX4
Hybrid	0.00	100U	100U	63.7H	42.2	1.46	1.92	1.08	2.54	-0.09	-1.54
MS2	0.50	100U	100U	74.3H	0	1.00	1.00	0.91	2.24	-0.33	-1.54
NL-VT1	-1.27	100U	100U	37.2H	60.2	1.81	2.61	1.19	2.75	1.75	-1.54
NL06	-0.87	100U	100U	40.3H	37.8	1.87	2.73	1.20	2.77	1.00	-1.54
NL065	0.67	100U	100U	37.2H	0	1.80	2.59	1.06	2.51	0.00	-1.46
NL07	1.16	8.9L/15.8H	26.5L/65.2H	0	0	1.70	2.41	0.94	2.29	0.12	-1.38
NL075	1.28	0	12.4L	0	0	1.79	2.58	0.90	2.22	0.34	-1.31
NL1	-0.47	100U	100U	70.8H	0	2.69	4.38	1.56	3.40	-0.84	-1.54
NL1J4	-0.46	100U	100U	72.7H	47.2	2.00	3.00	1.33	3.00	-0.58	-1.54
NL1J5	-0.46	100U	100U	72.7H	0	4.00	7.00	2.00	4.20	-1.78	-1.54
NL2	4.23	100U	100U	100U	0	2.77	4.54	1.33	2.99	-1.53	-1.46
NL3	1.04	100U	100U	88.5H	0	1.48	1.96	1.08	2.54	-0.99	-1.54
NL3-II	1.04	100U	100U	90.1H	0	1.54	2.08	1.10	2.59	-1.09	-1.54
NL3*	0.71	100U	100U	82.7H	0	1.74	2.47	1.17	2.71	-0.92	-1.54
NL4	1.01	100U	100U	86.8H	0	1.25	1.50	1.00	2.40	-0.81	-1.54
NLB	4.78	100U	100U	100U	0	1.00	1.00	0.85	2.13	-1.55	-1.46
NLB1	1.26	100U	100U	100U	0	0.61	0.22	0.72	1.90	-0.19	-1.46
NLB2	0.39	100U	100U	100U	68.0H	0.62	0.24	0.92	2.25	-1.37	-1.62
NLC	-0.14	100U	100U	37.2H	25.8	1.00	1.01	0.84	2.12	0.75	-1.46
NLD	2.83	23.1L/27.2H	100U	100U	0	1.00	1.00	0.70	1.86	-0.16	-1.38
NLM	-0.75	21.0H	45.5H	0	74.0H	0.00	-1.00	0.38	1.28	2.15	-1.31
NLM2	-0.75	19.4H	41.6H	0	81.4H	0.00	-1.00	0.38	1.28	2.37	-1.31
NLM3	-0.75	2.7H	33.7H	0	81.0H	0.00	-1.00	0.39	1.30	2.11	-1.38
NLM4	1.75	21.4L/35.0H	100U	100U	0	0.00	-1.00	0.36	1.25	0.71	-1.31
NLM5	-0.75	100U	100U	82.5H	83.4H	0.00	-1.00	0.74	1.93	-0.01	-1.62
NLM6	-0.75	21.0H	45.5H	0	0	2.00	3.00	1.04	2.48	1.55	-1.38
NLRA	2.26	100U	100U	100U	0	1.78	2.56	1.09	2.56	-1.22	-1.46
NLRA1	1.38	100U	100U	1.7L/98.3H	0	1.29	1.58	1.01	2.42	-1.06	-1.54
NLrho	0.27	0	2.7L	0	0	0.07	-0.85	0.32	1.18	1.39	-1.31
NLS	0.82	100U	100U	80.6H	0	2.41	3.83	1.37	3.06	-1.16	-1.54
NLSH	3.14	100U	100U	100U	0	1.23	1.45	0.97	2.35	-1.63	-1.54
NLZ	-1.43	100U	100U	49.7H	43.0	2.34	3.69	1.42	3.16	1.43	-1.54
NLZ2	-1.44	100U	100U	49.9H	72.6	1.80	2.60	1.24	2.83	1.58	-1.54
P-067	0.04	16.2L/62.3H	100U	0	0	2.21	3.43	1.16	2.69	0.54	-1.38
P-070	0.38	2.1L/33.5H	28.5L/70.8H	0	0	2.37	3.74	1.16	2.69	0.28	-1.38
P-075	1.03	5.3L	18.7L/16.7H	19.0L/5.0	0	2.59	4.18	1.14	2.66	0.11	-1.31
P-080	0.75	0	3.0L	0	0	1.93	2.85	0.88	2.19	0.67	-1.31
Q1	0.30	100U	100U	69.5H	26.6	1.29	1.58	1.02	2.43	-0.29	-1.54
RMF301	0.60	0	0	0	0	0.50	0.00	0.44	1.39	1.18	-1.31
RMF302	0.49	0	0	0	0	0.50	0.00	0.44	1.39	1.23	-1.23
RMF303	0.47	0	0	0	0	0.50	0.00	0.44	1.38	1.24	-1.23
RMF304	0.45	0	0	0	0	0.50	0.00	0.43	1.38	1.25	-1.23
RMF305	0.41	0	0	0	0	0.50	0.00	0.43	1.38	1.27	-1.23
RMF306	0.37	0	0	0	0	0.50	0.00	0.43	1.38	1.29	-1.23
RMF307	0.35	0	0	0	0	0.50	0.00	0.43	1.37	1.30	-1.23
RMF308	0.32	0	0	0	0	0.50	0.00	0.43	1.37	1.31	-1.23
RMF309	0.28	0	0	0	0	0.50	0.00	0.43	1.37	1.33	-1.23
RMF310	0.22	0	0	0	0	0.50	0.00	0.42	1.36	1.36	-1.23
RMF311	0.20	0	0	0	0	0.50	0.00	0.42	1.36	1.37	-1.23
RMF312	0.18	0	0	0	0	0.50	0.00	0.42	1.36	1.38	-1.23
RMF313	0.13	0	0	0	0	0.50	0.00	0.42	1.36	1.40	-1.23
RMF314	0.11	0	0	0	0	0.50	0.00	0.42	1.36	1.41	-1.23
RMF315	0.10	0	0	0	0	0.50	0.00	0.42	1.36	1.41	-1.23
RMF316	0.09	0	0	0	0	0.50	0.00	0.42	1.36	1.42	-1.23
RMF317	0.07	0	0	0	0	0.50	0.00	0.42	1.35	1.43	-1.23
RMF401	0.00	.4H	34.2H	0	52.8	0.50	0.00	0.53	1.55	1.37	-1.31
RMF402	0.05	.5H	34.6H	0	49.2	0.50	0.00	0.53	1.55	1.33	-1.31

TABLE IX. (*Continued.*)

Model	SM1	SM3a (%)	SM3b (%)	SM4 (%)	PNM1 (%)	MIX1a	MIX1b	MIX2a	MIX2b	MIX3	MIX4
RMF403	0.00	0	21.7H	0	49.8	0.50	0.00	0.51	1.53	1.38	-1.31
RMF404	0.05	0	22.1H	0	45.6	0.50	0.00	0.51	1.52	1.34	-1.31
RMF405	0.10	0	22.5H	0	41.2	0.50	0.00	0.51	1.52	1.31	-1.31
RMF406	0.10	0	0	0	0	0.50	0.00	0.44	1.39	1.37	-1.31
RMF407	0.00	0	8.2H	0	46.6	0.50	0.00	0.50	1.50	1.38	-1.31
RMF408	0.05	0	8.7H	0	42.0	0.50	0.00	0.50	1.50	1.35	-1.31
RMF409	0.10	0	9.3H	0	37.0	0.50	0.00	0.50	1.50	1.32	-1.31
RMF410	0.15	0	9.8H	0	31.2	0.50	0.00	0.50	1.50	1.29	-1.31
RMF411	0.00	0	0	0	43.6	0.50	0.00	0.49	1.48	1.38	-1.31
RMF412	0.05	0	0	0	38.2	0.50	0.00	0.49	1.48	1.35	-1.31
RMF413	0.10	0	0	0	32.4	0.50	0.00	0.49	1.47	1.32	-1.31
RMF414	0.15	0	0	0	25.0	0.50	0.00	0.49	1.47	1.30	-1.31
RMF415	0.00	0	0	0	40.0	0.50	0.00	0.47	1.45	1.39	-1.31
RMF416	0.05	0	0	0	34.2	0.50	0.00	0.47	1.45	1.36	-1.31
RMF417	0.10	0	0	0	27.0	0.50	0.00	0.47	1.45	1.33	-1.31
RMF418	0.15	0	0	0	16.8	0.50	0.00	0.47	1.45	1.31	-1.31
RMF419	0.00	0	0	0	36.2	0.50	0.00	0.46	1.43	1.39	-1.31
RMF420	0.05	0	0	0	29.2	0.50	0.00	0.46	1.43	1.37	-1.31
RMF421	0.10	0	0	0	19.6	0.50	0.00	0.46	1.43	1.34	-1.31
RMF422	0.00	0	0	0	31.4	0.50	0.00	0.45	1.41	1.40	-1.31
RMF423	0.05	0	0	0	22.2	0.50	0.00	0.45	1.41	1.37	-1.31
RMF424	0.40	0	0	0	0	0.50	0.00	0.43	1.37	1.30	-1.23
RMF425	0.45	0	0	0	0	0.50	0.00	0.43	1.37	1.29	-1.23
RMF426	0.50	0	0	0	0	0.50	0.00	0.43	1.37	1.27	-1.23
RMF427	0.15	0	0	0	0	0.50	0.00	0.42	1.35	1.41	-1.23
RMF428	0.20	0	0	0	0	0.50	0.00	0.42	1.35	1.39	-1.23
RMF429	0.25	0	0	0	0	0.50	0.00	0.42	1.35	1.38	-1.23
RMF430	0.30	0	0	0	0	0.50	0.00	0.42	1.35	1.37	-1.23
RMF431	0.35	0	0	0	0	0.50	0.00	0.42	1.35	1.36	-1.23
RMF432	0.40	0	0	0	0	0.50	0.00	0.42	1.35	1.35	-1.23
RMF433	0.45	0	0	0	0	0.50	0.00	0.42	1.35	1.34	-1.23
RMF434	0.50	0	0	0	0	0.50	0.00	0.42	1.35	1.33	-1.23
RSk1*	-0.34	0	0	0	50.8	0.01	-0.99	0.26	1.07	1.68	-1.23
S271	1.03	5.6L/13.3H	24.7L/60.1H	0	0	1.30	1.59	0.81	2.05	0.34	-1.38
SMFT1	-1.42	100U	100U	18.8H	85.0H	-2.49	-5.97	-0.31	0.04	2.99	-1.38
SMFT2	-0.47	100U	100U	27.0H	78.4H	-2.52	-6.05	-0.38	-0.09	2.41	-1.31
SRK3M5	1.75	100U	100U	100U	84.6H	-1.30	-3.60	0.28	1.10	-0.42	-1.62
SRK3M7	1.75	1.5L	16.3L	1.2L	0	-0.25	-1.51	0.22	0.99	1.11	-1.31
VT	-1.43	100U	100U	43.9H	56.6	1.94	2.89	1.26	2.87	1.82	-1.54
$\sigma^3 + \sigma^4 + \omega^4$ models											
BM-A	-1.04	0	0	0	88.8H	-2.08	-5.15	-0.40	-0.12	2.27	-1.15
BM-B	-1.48	8.2	8.2	0	84.6H	-2.52	-6.03	-0.55	-0.38	2.64	-1.15
BM-C	-1.67	90.7L	90.7L	5.8H/1.8	80.4H	-2.80	-6.60	-0.63	-0.54	2.84	-1.15
DJM	0.37	16.6L	28.2L	.1L/87.2H	80.2H	-1.96	-4.92	-0.16	0.32	1.11	-1.46
DJM-C	2.49	26.9L	100U	100U	66.2H	-1.62	-4.24	-0.03	0.54	0.72	-1.54
EMFT1	-1.60	0	0	0	88.8H	-2.28	-5.56	-0.30	0.06	1.60	-1.38
HD	1.35	91.1L	100U	100U	0	1.14	1.28	0.80	2.04	-0.02	-1.38
LB	2.17	26.2L	100U	100U	0	0.38	-0.23	0.59	1.67	0.08	-1.46
MB	2.79	1.7L	12.1L	55.7L/9.1	100D	0.50	0.00	0.44	1.40	2.30	-1.31
MS1	0.50	0	16.8L	0	0	1.00	1.00	0.82	2.07	0.11	-1.46
MS3	0.50	0	0	0	0	1.00	1.00	0.72	1.90	1.39	-1.46
NLSV1	1.00	24.0L	100U	58.8H	0	1.46	1.92	0.99	2.39	1.11	-1.46
NLSV2	1.54	11.6L	24.2L	37.2H	0	1.35	1.70	0.92	2.26	-0.32	-1.46
PK1	1.32	21.5L	100U	76.0H	0	1.53	2.06	1.02	2.44	-0.08	-1.46
TM1	1.28	1.1L	17.3L	0	0	1.38	1.76	0.91	2.23	-0.52	-1.46
TM2	2.85	20.7L	49.6L	100U	0	1.20	1.39	0.96	2.32	0.21	-1.54
TMA	2.20	0	9.3L	3.8L	0	0.13	-0.74	0.45	1.41	-1.06	-1.38
Z271	1.02	0	0	0	0	1.18	1.37	0.64	1.75	1.21	-1.31

TABLE IX. (*Continued.*)

Model	SM1	SM3a (%)	SM3b (%)	SM4 (%)	PNM1 (%)	MIX1a	MIX1b	MIX2a	MIX2b	MIX3	MIX4
$\sigma^3 + \sigma^4 + \omega^4 +$ mixing-terms models											
BKA20	0.20	0	0	0	0	0.45	-0.10	0.12	0.82	1.53	-0.85
BKA22	-0.12	0	0	0	0	0.63	0.27	0.20	0.95	1.12	-0.85
BKA24	-0.07	0	0	0	0	0.84	0.68	0.33	1.19	0.86	-1.00
BSR1	0.25	1.00	100U	37.2H	0	100	-0.58	0.18	1.44	1.44	1.00
BSR2	0.25	16.8L/27.9H	100U	37.2H	0	0.30	-0.40	-0.18	0.28	1.25	-0.38
BSR3	0.01	14.0L/18.9H	100U	6.6H	0	0.55	0.10	0.01	0.62	1.03	-0.62
BSR4	0.21	27.8L/69.0H	100U	37.2H	0	0.63	0.27	0.07	0.73	0.59	-0.69
BSR5	0.14	100U	100U	38.5H	0	0.89	0.78	0.30	1.13	0.26	-0.92
BSR6	0.14	26.0L/63.4H	100U	37.2H	0	1.12	1.25	0.35	1.23	-0.07	-1.00
BSR7	0.05	100U	100U	38.3H	0	1.45	1.90	0.65	1.77	-0.36	-1.23
BSR8	0.02	0	1.5L	0	0	0.22	-0.57	-0.22	0.21	1.76	-0.31
BSR9	0.06	0	0	0	0	0.32	-0.36	-0.14	0.36	1.58	-0.38
BSR10	-0.06	0	0	0	0	0.54	0.09	0.02	0.63	1.25	-0.62
BSR11	-0.08	0	0	0	0	0.74	0.48	0.20	0.95	1.07	-0.85
BSR12	0.06	0	.5L	0	0	0.80	0.60	0.18	0.92	0.90	-0.85
BSR13	-0.03	0	0	0	0	1.16	1.33	0.47	1.44	0.53	-1.08
BSR14	0.14	0	0	0	0	1.26	1.53	0.53	1.55	0.48	-1.15
BSR15	-0.08	0	0	0	0	0.19	-0.61	-0.18	0.27	1.98	-0.38
BSR16	-0.13	0	0	0	0	0.25	-0.50	-0.17	0.29	1.94	-0.38
BSR17	-0.21	0	0	0	0	0.40	-0.21	-0.06	0.50	1.75	-0.54
BSR18	-0.22	0	0	0	0	0.55	0.10	0.06	0.71	1.54	-0.77
BSR19	-0.23	0	0	0	0	0.76	0.51	0.21	0.98	1.32	-0.92
BSR20	-0.17	0	0	0	0	0.91	0.82	0.40	1.32	1.21	-1.08
BSR21	-0.24	0	0	0	0	1.19	1.38	0.51	1.52	0.96	-1.15
C1	1.85	17.6L/20.6H	100U	3.0L/88.1H	0	0.41	-0.19	0.55	1.58	0.33	-1.38
FSU-I	-0.01	0	0	0	0	1.48	1.97	0.88	2.18	0.97	-1.46
FSU-II	-0.01	0	0	0	0	1.10	1.20	0.39	1.30	1.05	-1.08
FSU-III	-0.01	0	0	0	0	0.78	0.56	0.04	0.67	1.39	-0.77
FSU-IV	-0.01	0	0	0	0	0.29	-0.43	-0.40	-0.11	2.26	0.00
FSU-V	-0.01	0	0	0	48.4H	0.19	-0.62	-0.46	-0.22	2.48	0.15
FSUGold	-0.01	0	0	0	0	0.51	0.02	-0.21	0.22	1.83	-0.38
FSUGold4	-0.01	0	0	0	0	0.28	-0.44	-0.41	-0.13	2.30	0.00
FSUGold5	0.08	0	0	0	99.4H	0.11	-0.78	-0.54	-0.38	2.72	0.38
FSUGZ00	0.25	16.9L/28.0H	100U	37.2H	0	0.29	-0.43	-0.17	0.29	1.24	-0.38
FSUGZ03	0.06	0	0	0	0	0.31	-0.38	-0.13	0.36	1.57	-0.46
FSUGZ06	-0.12	0	0	0	0	0.24	-0.53	-0.17	0.30	1.94	-0.38
G1	-0.38	6.5	25.9L	0	33.0	1.70	2.39	1.18	2.73	0.77	-1.54
G2	-0.38	0	0	0	0	1.28	1.56	0.68	1.83	0.96	-1.31
G2*	-0.38	0	0	0	0	0.08	-0.84	-0.01	0.59	1.68	-0.77
HC	0.05	18.8L/64.6H	100U	6.4H	0	0.20	-0.60	-0.25	0.14	1.32	-0.62
IU-FSU	0.03	0	11.5L	0	0	0.26	-0.48	-0.51	-0.31	2.36	0.23
LA	1.79	20.6L	50.5L	100U	0	0.70	0.39	0.19	0.95	0.36	-1.00
MA	2.93	.2L	11.2L	50.2L/5.5	100D	0.48	-0.04	0.03	0.66	2.07	-0.85
NL3v1	1.04	100U	100U	88.7H	0	1.21	1.43	0.69	1.85	-0.89	-1.31
NL3v2	1.04	100U	100U	88.7H	0	1.00	0.99	0.39	1.31	-0.59	-1.15
NL3v3	1.04	100U	100U	88.7H	0	0.90	0.79	0.27	1.08	-0.40	-1.00
NL3v4	1.04	100U	100U	88.7H	0	0.80	0.61	0.15	0.88	-0.20	-0.92
NL3v5	1.04	100U	100U	88.7H	0	0.63	0.26	-0.04	0.53	0.24	-0.69
NL3v6	1.04	100U	100U	88.7H	0	0.48	-0.04	-0.20	0.25	0.69	-0.54
S271v1	1.02	5.5L/13.2H	24.6L/60.0H	0	0	1.15	1.29	0.58	1.64	0.23	-1.23
S271v2	1.02	5.5L/13.2H	24.6L/60.0H	0	0	1.01	1.02	0.37	1.27	0.22	-1.15
S271v3	1.02	5.5L/13.2H	24.6L/60.0H	0	0	0.88	0.77	0.20	0.95	0.28	-1.00
S271v4	1.02	5.5L/13.2H	24.6L/60.0H	0	0	0.77	0.53	0.04	0.67	0.39	-0.92
S271v5	1.02	5.5L/13.2H	24.6L/60.0H	0	0	0.65	0.31	-0.10	0.42	0.53	-0.77
S271v6	1.02	5.5L/13.2H	24.6L/60.0H	0	0	0.55	0.10	-0.23	0.19	0.71	-0.69
SIG-OM	0.88	12.2L/0.3H	28.4L/69.9H	5.0H/6.8	0	1.40	1.80	0.93	2.28	0.12	-1.46

TABLE IX. (*Continued.*)

Model	SM1	SM3a (%)	SM3b (%)	SM4 (%)	PNM1 (%)	MIX1a	MIX1b	MIX2a	MIX2b	MIX3	MIX4
SVI-1	0.85	100U	100U	44.0H	0	1.41	1.82	1.03	2.46	1.09	-1.46
SVI-2	1.04	100U	100U	45.0H	0	1.41	1.82	1.02	2.44	0.93	-1.46
TM1*	1.29	0	2.1L	0	0	1.38	1.76	0.71	1.87	0.81	-1.31
XS	0.00	0	0	0	73.8H	0.37	-0.27	-0.33	0.00	2.40	-0.08
Z271*	1.02	0	0	0	0	2.05	3.10	0.30	1.14	0.51	-0.92
Z271s1	1.02	0	0	0	0	0.99	0.98	0.37	1.27	1.33	-1.08
Z271s2	1.02	0	0	0	0	0.82	0.63	0.15	0.86	1.37	-0.92
Z271s3	1.02	0	0	0	0	0.65	0.31	-0.05	0.51	1.48	-0.77
Z271s4	1.02	0	0	0	0	0.51	0.01	-0.22	0.21	1.64	-0.54
Z271s5	1.02	0	0	0	0	0.37	-0.26	-0.37	-0.06	1.83	-0.38
Z271s6	1.02	0	0	0	0	0.24	-0.52	-0.49	-0.29	2.03	-0.15
Z271v1	1.02	0	0	0	0	1.07	1.14	0.46	1.43	1.23	-1.15
Z271v2	1.02	0	0	0	0	0.96	0.92	0.30	1.14	1.13	-1.08
Z271v3	1.02	0	0	0	0	0.91	0.82	0.23	1.01	1.10	-1.08
Z271v4	1.02	0	0	0	0	0.86	0.72	0.16	0.88	1.08	-1.00
Z271v5	1.02	0	0	0	0	0.81	0.62	0.09	0.76	1.08	-0.92
Z271v6	1.02	0	0	0	0	0.76	0.52	0.02	0.64	1.08	-0.92
Density-dependent models											
DD	0.25	22.0L/37.7H	100U	37.2H	0	0.33	-0.34	-0.31	0.04	0.59	-0.46
DD-F	-0.17	0	0	0	0	0.33	-0.35	-0.31	0.04	-0.21	-0.54
DD-ME1	0.37	100U	100U	69.0H	0	0.61	0.22	-0.32	0.02	1.76	-0.31
DD-ME2	0.52	100U	100U	82.3H	0	0.46	-0.08	-0.42	-0.15	0.30	-0.23
DD2	0.32	24.3L/40.7H	100U	41.5H	0	0.33	-0.33	-0.33	0.00	1.45	-0.38
PKDD	0.80	15.7L/18.0H	100U	37.2H	0	1.36	1.72	0.45	1.41	0.38	-1.08
TW99	0.26	0	0	0	0	0.55	0.11	-0.33	0.01	0.58	-0.38
Point-coupling models											
FA2	1.43	91.9L	91.9L	0	0	0.71	0.41	0.65	1.78	0.70	-1.46
FA3	1.14	0	15.5L	0	0	-0.06	-1.12	-0.91	-1.04	0.37	-0.08
FA4	1.61	100U	100U	100U	0	-0.04	-1.09	-0.88	-0.98	0.32	-0.08
FZ0	8.23	100U	100U	100U	0	1.88	2.76	1.32	2.98	0.84	-1.62
FZ1	3.78	100U	100U	100U	0	0.51	0.03	0.56	1.61	-4.36	-1.38
FZ2	2.45	4.0L	14.8L/10.0H	46.1L/10.5	0	0.37	-0.27	0.08	0.75	-0.46	-1.00
FZ3	1.62	10.4L	25.9L	.8L/10.4	0	-0.01	-1.03	-0.80	-0.84	0.50	-0.15
FZ4	1.82	100U	100U	100U	0	0.00	-1.00	-0.74	-0.74	0.85	-0.23
PC-F1	0.61	24.8L	51.7L	46.2H	0	1.55	2.10	1.05	2.48	1.54	-1.46
PC-F3	0.62	25.0L	51.9L	46.8H	0	1.65	2.30	1.08	2.54	1.01	-1.46
VA2	1.38	92.3L	92.3L	0	0	0.98	0.96	1.24	2.83	0.60	-1.92
VA3	1.72	27.9L	73.6L	100U	83.2H	1.84	2.69	2.58	5.24	-0.05	-2.62
VA4	2.31	100U	100U	100U	0	0.91	0.82	1.23	2.81	-0.42	-1.77
VZ0	8.33	100U	100U	100U	0	1.59	2.17	1.22	2.80	1.78	-1.62
VZ1	3.74	100U	100U	100U	0	0.54	0.09	0.57	1.63	-0.68	-1.38
VZ2	2.35	5.4L/64.7H	5.4L/64.7H	20.8L	0	0.96	0.92	1.27	2.89	-1.81	-1.92
VZ3	1.69	31.7L	73.3L	100U	0	0.92	0.84	1.20	2.76	-4.01	-1.77
VZ4	1.89	100U	100U	100U	0	0.54	0.08	0.61	1.70	-0.49	-1.38
δ meson models											
DD-ME δ	-0.26	0	0	0	0	0.44	-0.13	-0.41	-0.14	1.94	-0.31
DDH δ	0.25	0	0	0	0	-0.93	-2.86	-0.55	-0.39	-2.44	-0.08
GDFM	2.35	100U	100U	90.4L	11.8L	0.61	0.22	-0.05	0.52	-0.44	-0.31
NL δ	0.25	2.2L	2.2L	0	68.8L	0.12	-0.76	0.70	1.86	2.89	-1.62
NL3 δ	1.00	100U	100U	86.4L	71.1L	1.53	2.07	1.78	3.80	1.69	-1.92

- [1] C. F. von Weizsäcker, *Z. Phys.* **96**, 431 (1935).
- [2] T. H. R. Skyrme, *Philos. Mag.* **1**, 1043 (1956).
- [3] D. Vautherin and D. M. Brink, *Phys. Rev. C* **5**, 626 (1972).
- [4] J. D. Walecka, *Ann. Phys.* **83**, 491 (1974).
- [5] M. Dutra, O. Lourenço, J. S. Sá Martins, A. Delfino, J. R. Stone, and P. D. Stevenson, *Phys. Rev. C* **85**, 035201 (2012).
- [6] J. M. Pearson, N. Chamel, and S. Goriely, *Phys. Rev. C* **82**, 037301 (2010).
- [7] E. Lipparini and S. Stringari, *Phys. Rep.* **175**, 103 (1989).
- [8] J. P. Blaizot and B. Grammaticos, *Nucl. Phys. A* **265**, 315 (1976).
- [9] S. Shlomo, V. M. Kolomietz, and G. Colo, *Eur. Phys. J. A* **30**, 23 (2006); T. Sil, S. Shlomo, B. K. Agrawal, and P. G. Reinhard, *Phys. Rev. C* **73**, 034316 (2006); B. K. Agrawal, S. Shlomo, and V. Kim Au, *ibid.* **68**, 031304 (2003).
- [10] J. R. Stone, N. J. Stone, and S. A. Moszkowski, *Phys. Rev. C* **89**, 044316 (2014).
- [11] E. Khan, J. Margueron, and I. Vidaña, *Phys. Rev. Lett.* **109**, 092501 (2012).
- [12] E. Khan and J. Margueron, *Phys. Rev. C* **88**, 034319 (2013).
- [13] M. B. Tsang, Y. Zhang, P. Danielewicz, M. Famiano, Z. Li, W. G. Lynch, and A. W. Steiner, *Phys. Rev. Lett.* **102**, 122701 (2009); Z. Kohley *et al.*, *Phys. Rev. C* **83**, 044601 (2011).
- [14] A. Klimkiewicz *et al.*, *Phys. Rev. C* **76**, 051603(R) (2007); O. Wieland *et al.*, *Phys. Rev. Lett.* **102**, 092502 (2009).
- [15] A. Carbone, G. Colo, A. Bracco, L.-G. Cao, P. F. Bortignon, F. Camera, and O. Wieland, *Phys. Rev. C* **81**, 041301 (2010).
- [16] P. Danielewicz and J. Lee, *AIP Conf. Proc.* **1423**, 29 (2012).
- [17] C. J. Horowitz and J. Piekarewicz, *Phys. Rev. Lett.* **86**, 5647 (2001).
- [18] M. B. Tsang, J. R. Stone, F. Camera, P. Danielewicz, S. Gandolfi, K. Hebeler, C. J. Horowitz, J. Lee, W. G. Lynch, Z. Kohley, R. Lemmon, P. Moller, T. Murakami, S. Riordan, X. Roca-Maza, F. Sammarruca, A. W. Steiner, I. Vidaña, and S. J. Yennello, *Phys. Rev. C* **86**, 015803 (2012).
- [19] A. Krugmann, D. Martin, P. von Neumann-Cosel, N. Pietralla, and A. Tamii for the E350 Collaboration, *EPJ Web Conf.* **66**, 02060 (2014).
- [20] C. Providência, S. S. Avancini, R. Cavagnoli, S. Chiacchiera, C. Ducoin, F. Grill, J. Margueron, D. P. Menezes, A. Rabhi, and I. Vidaña, *Eur. Phys. J. A* **50**, 44 (2014).
- [21] J. Piekarewicz, *Phys. Rev. C* **66**, 034305 (2002).
- [22] J. Piekarewicz, *Phys. Rev. C* **69**, 041301 (2004).
- [23] C. Ducoin, J. Margueron, C. Providência, and I. Vidaña, *Phys. Rev. C* **83**, 045810 (2011).
- [24] J. M. Lattimer and Y. Lim, *Astrophys. J.* **771**, 51 (2013).
- [25] B. M. Santos, M. Dutra, O. Lourenço, and A. Delfino, *Phys. Rev. C* **90**, 035203 (2014).
- [26] L. W. Chen, C. M. Ko, and B.-A. Li, *Phys. Rev. Lett.* **94**, 032701 (2005); *Phys. Rev. C* **72**, 064309 (2005); B.-A. Li, L. W. Chen, and C. M. Ko, *Phys. Rep.* **464**, 113 (2008).
- [27] M. Centelles, X. Roca-Maza, X. Viñas, and M. Warda, *Phys. Rev. Lett.* **102**, 122502 (2009).
- [28] T. Li *et al.*, *Phys. Rev. Lett.* **99**, 162503 (2007).
- [29] B. D. Lackey, M. Nayyar, and B. J. Owen, *Phys. Rev. D* **73**, 024021 (2006).
- [30] J. Boguta and A. R. Bodmer, *Nucl. Phys. A* **292**, 413 (1977).
- [31] S. Typel and H. H. Wolter, *Nucl. Phys. A* **656**, 331 (1999).
- [32] P. Görglein, E. N. E. van Dalen, C. Fuchs, and H. Müther, *Phys. Rev. C* **77**, 025802 (2008).
- [33] S. S. Avancini, L. Brito, Ph. Chomaz, D. P. Menezes, and C. Providência, *Phys. Rev. C* **74**, 024317 (2006).
- [34] B. A. Nikolaus, T. Hoch, and D. G. Madland, *Phys. Rev. C* **46**, 1757 (1992).
- [35] G. Gelmini and B. Ritz, *Phys. Lett. B* **357**, 431 (1995); A. Delfino, M. Malheiro, and T. Frederico, *Braz. J. Phys.* **31**, 518 (2001).
- [36] O. Lourenço, R. L. P. G. Amaral, M. Dutra, and A. Delfino, *Phys. Rev. C* **80**, 045206 (2009); O. Lourenço, M. Dutra, A. Delfino, and R. L. P. G. Amaral, *Int. J. Mod. Phys. E* **16**, 3037 (2007).
- [37] I. Vidaña, C. Providência, A. Polls, and A. Rios, *Phys. Rev. C* **80**, 045806 (2009).
- [38] J. B. Silva, O. Lourenço, A. Delfino, J. S. Sá Martins, and M. Dutra, *Phys. Lett. B* **664**, 246 (2008); J. B. Elliott, P. T. Lake, L. G. Moretto, and L. Phair, *Phys. Rev. C* **87**, 054622 (2013).
- [39] D. H. Youngblood, H. L. Clark, and Y.-W. Lui, *Phys. Rev. Lett.* **82**, 691 (1999).
- [40] M. Farine, J. M. Pearson, and F. Tondeur, *Nucl. Phys. A* **615**, 135 (1997).
- [41] P. Danielewicz, R. Lacey, and W. G. Lynch, *Science* **298**, 1592 (2002).
- [42] W. G. Lynch, M. B. Tsang, Y. Zhang, P. Danielewicz, M. Famiano, Z. Li, and A. W. Steiner, *Prog. Part. Nucl. Phys.* **62**, 427 (2009).
- [43] J. R. Stone and P. G. Reinhard, *Prog. Part. Nucl. Phys.* **58**, 587 (2007).
- [44] L. W. Chen, C. M. Ko, Bao-An Li, and J. Xu, *Phys. Rev. C* **82**, 024321 (2010).
- [45] P. Danielewicz, *Nucl. Phys. A* **727**, 233 (2003).
- [46] J. Piekarewicz, *Phys. Rev. C* **76**, 064310 (2007).
- [47] A. Gezerlis and J. Carlson, *Phys. Rev. C* **77**, 032801 (2008).
- [48] A. Schwenk and C. J. Pethick, *Phys. Rev. Lett.* **95**, 160401 (2005).
- [49] J. Carlson, S.-Y. Chang, V. R. Pandharipande, and K. E. Schmidt, *Phys. Rev. Lett.* **91**, 050401 (2003).
- [50] E. Epelbaum, H. Krebs, D. Lee, and U.-G. Meissner, *Eur. Phys. J. A* **40**, 199 (2009).
- [51] M. Bartenstein, A. Altmeyer, S. Riedl, S. Jochim, C. Chin, J. H. Denschlag, and R. Grimm, *Phys. Rev. Lett.* **92**, 120401 (2004).
- [52] J. Kinast, A. Turlapov, J. E. Thomas, Q. Chen, J. Stajic, and K. Levin, *Science* **307**, 1296 (2005).
- [53] J. T. Stewart, J. P. Gaebler, C. A. Regal, and D. S. Jin, *Phys. Rev. Lett.* **97**, 220406 (2006).
- [54] L. Luo and J. E. Thomas, *J. Low Temp. Phys.* **154**, 1 (2009).
- [55] L. Brito, Ph. Chomaz, D. P. Menezes, and C. Providência, *Phys. Rev. C* **76**, 044316 (2007).
- [56] P. Möller, W. D. Meyers, W. J. Swiatecki, and J. Treiner, *At. Data Nucl. Data Tables* **39**, 225 (1988).
- [57] B. A. Brown, *Phys. Rev. Lett.* **85**, 5296 (2000).
- [58] D. H. Youngblood, Y. W. Lui, H. L. Clark, B. John, Y. Tokimoto, and X. Chen, *Phys. Rev. C* **69**, 034315 (2004).
- [59] M. Uchida *et al.*, *Phys. Rev. C* **69**, 051301 (2004).
- [60] M. Uchida *et al.*, *Phys. Lett. B* **557**, 12 (2003).
- [61] T. Li *et al.*, *Phys. Rev. C* **81**, 034309 (2010).
- [62] A. W. Steiner, J. M. Lattimer, and E. F. Brown, *Astrophys. J. Lett.* **765**, L5 (2013).
- [63] J. M. Lattimer and A. W. Steiner, *Astrophys. J.* **784**, 123 (2014).
- [64] S. Guillot, M. Servillat, N. A. Webb, and R. E. Rutledge, *Astrophys. J.* **772**, 7 (2013).

- [65] B.-A. Li and X. Han, *Phys. Lett. B* **727**, 276 (2013).
- [66] B.-A. Li *et al.*, *J. Phys.: Conf. Ser.* **312**, 042006 (2011).
- [67] B. K. Agrawal, *Phys. Rev. C* **81**, 034323 (2010).
- [68] N. K. Glendenning, *Compact Stars: Nuclear Physics, Particle Physics, and General Relativity*, 2nd ed. (Springer, New York, 2000).
- [69] P. B. Demorest *et al.*, *Nature (London)* **467**, 1081 (2010).
- [70] J. Antoniadis *et al.*, *Science* **340**, 1233232 (2013).
- [71] S. Weissenborn, D. Chatterjee, and J. Schaffner-Bielich, *Phys. Rev. C* **85**, 065802 (2012); *Nucl. Phys. A* **881**, 62 (2012).
- [72] R. Cavagnoli, D. P. Menezes, and C. Providência, *Phys. Rev. C* **84**, 065810 (2011); C. Providência and A. Rabhi, *ibid.* **87**, 055801 (2013).
- [73] L. L. Lopes and D. P. Menezes, *Phys. Rev. C* **89**, 025805 (2014).
- [74] P. A. M. Guichon, *Phys. Lett. B* **200**, 235 (1988); K. Saito and A. W. Thomas, *ibid.* **327**, 9 (1994); J. R. Stone, P. A. Guichon *et al.*, *Nucl. Phys. A* **792**, 341 (2007); P. K. Panda, D. P. Menezes, and C. Providência, *Phys. Rev. C* **89**, 045803 (2014).
- [75] P. D. Stevenson, P. M. Goddard, J. R. Stone, and M. Dutra, *AIP Conf. Proc.* **1529**, 262 (2013).
- [76] S. Haddad, *Europhys. Lett.* **48**, 505 (1999).
- [77] P.-G. Reinhard, *Rep. Prog. Phys.* **52**, 439 (1989).
- [78] Internal discussion notes, ORNL, University of Erlangen, University of Frankfurt, University of Tennessee Knoxville, University of Oxford, Vanderbilt University, and University of Warsaw (private communication).
- [79] A. A. Dadi, *Phys. Rev. C* **82**, 025203 (2010).
- [80] M. Rufa, P.-G. Reinhard, J. A. Maruhn, W. Greiner, and M. R. Strayer, *Phys. Rev. C* **38**, 390 (1988).
- [81] N. K. Glendenning, *Phys. Lett. B* **114**, 392 (1982).
- [82] N. K. Glendenning and S. A. Moszkowski, *Phys. Rev. Lett.* **67**, 2414 (1991).
- [83] S. K. Ghosh, S. C. Phatak, and P. K. Sahu, *Z. Phys. A* **352**, 457 (1995).
- [84] J. Piekarewicz and M. Centelles, *Phys. Rev. C* **79**, 054311 (2009).
- [85] H. Müller and B. D. Serot, *Nucl. Phys. A* **606**, 508 (1996).
- [86] M. Bender, K. Rutz, P. G. Reinhard, J. A. Maruhn, and W. Greiner, *Phys. Rev. C* **60**, 034304 (1999).
- [87] B. Liu, V. Greco, V. Baran, M. Colonna, and M. DiToro, *Phys. Rev. C* **65**, 045201 (2002).
- [88] M. Centelles, M. D. Estal, and X. Viñas, *Nucl. Phys. A* **635**, 193 (1998).
- [89] G. A. Lalazissis, J. König, and P. Ring, *Phys. Rev. C* **55**, 540 (1997).
- [90] G. A. Lalazissis *et al.*, *Phys. Lett. B* **671**, 36 (2009).
- [91] B. Nerlo-Pomorska and J. Sykut, *Int. J. Mod. Phys. E* **13**, 75 (2004).
- [92] B. D. Serot and J. D. Walecka, *Int. J. Mod. Phys. E* **6**, 515 (1997).
- [93] B. D. Serot, *Rep. Prog. Phys.* **55**, 1855 (1992).
- [94] K. C. Chung *et al.*, *Eur. Phys. J. A* **9**, 453 (2000).
- [95] M. Rashdan, *Phys. Rev. C* **63**, 044303 (2001).
- [96] P.-G. Reinhard, *Z. Phys. A* **329**, 257 (1988).
- [97] A. Sulaksono, T. Mart, and C. Bahri, *Phys. Rev. C* **71**, 034312 (2005).
- [98] R. J. Furnstahl, B. D. Serot, and H. B. Tang, *Nucl. Phys. A* **615**, 441 (1997).
- [99] S. Gmuca, *Z. Phys. A* **342**, 387 (1992).
- [100] M. Centelles *et al.*, *Nucl. Phys. A* **537**, 486 (1992).
- [101] S. Gmuca, *Nucl. Phys. A* **547**, 447 (1992).
- [102] J. K. Bunta and S. Gmuca, *Phys. Rev. C* **68**, 054318 (2003).
- [103] H. Müller and B. D. Serot, *Phys. Rev. C* **52**, 2072 (1995).
- [104] F. J. Fattoyev and J. Piekarewicz, *Phys. Rev. C* **82**, 025805 (2010).
- [105] M. M. Sharma, A. R. Farhan, and S. Mythili, *Phys. Rev. C* **61**, 054306 (2000).
- [106] W. Long, J. Meng, N. VanGiai, and S. G. Zhou, *Phys. Rev. C* **69**, 034319 (2004).
- [107] Y. Sugahara and H. Toki, *Nucl. Phys. A* **579**, 557 (1994).
- [108] H. Toki *et al.*, *Nucl. Phys. A* **588**, 357 (1995).
- [109] S. K. Dhiman, R. Kumar, and B. K. Agrawal, *Phys. Rev. C* **76**, 045801 (2007).
- [110] B.-J. Cai and L.-W. Chen, *Phys. Rev. C* **85**, 024302 (2012).
- [111] B. G. Todd-Rutel and J. Piekarewicz, *Phys. Rev. Lett.* **95**, 122501 (2005).
- [112] J. Piekarewicz and S. P. Weppner, *Nucl. Phys. A* **778**, 10 (2006).
- [113] R. Kumar, B. K. Agrawal, and S. K. Dhiman, *Phys. Rev. C* **74**, 034323 (2006).
- [114] A. Sulaksono and T. Mart, *Phys. Rev. C* **74**, 045806 (2006).
- [115] F. J. Fattoyev, C. J. Horowitz, J. Piekarewicz, and G. Shen, *Phys. Rev. C* **82**, 055803 (2010).
- [116] C. J. Horowitz and J. Piekarewicz, *Phys. Rev. C* **66**, 055803 (2002).
- [117] M. M. Haidari and M. M. Sharma, *Nucl. Phys. A* **803**, 159 (2008).
- [118] M. M. Sharma, *Phys. Lett. B* **666**, 140 (2008).
- [119] M. DelEstal, M. Centelles, X. Viñas, and S. K. Patra, *Phys. Rev. C* **63**, 024314 (2001).
- [120] S. Typel, *Phys. Rev. C* **71**, 064301 (2005).
- [121] T. Klähn *et al.*, *Phys. Rev. C* **74**, 035802 (2006).
- [122] T. Nikšić, D. Vretenar, P. Finelli, and P. Ring, *Phys. Rev. C* **66**, 024306 (2002).
- [123] G. A. Lalazissis, T. Nikšić, D. Vretenar, and P. Ring, *Phys. Rev. C* **71**, 024312 (2005).
- [124] S. Typel, G. Röpke, T. Klähn, D. Blaschke, and H. H. Wolter, *Phys. Rev. C* **81**, 015803 (2010).
- [125] J. J. Rusnak and R. J. Furnstahl, *Nucl. Phys. A* **627**, 495 (1997).
- [126] T. Bürvenich, D. G. Madland, J. A. Maruhn, and P.-G. Reinhard, *Phys. Rev. C* **65**, 044308 (2002).
- [127] X. Roca-Maza, X. Viñas, M. Centelles, P. Ring, and P. Schuck, *Phys. Rev. C* **84**, 054309 (2011).
- [128] T. Gaitanos, M. Di Toro, S. Typel, V. Baran, C. Fuchs, V. Greco, and H. H. Wolter, *Nucl. Phys. A* **732**, 24 (2004).
- [129] D. P. Menezes and C. Providência, *Phys. Rev. C* **70**, 058801 (2004).